

### **Durham E-Theses**

### Early Universe Particle Physics at Finite Temperature: Mysteries at the dawn of time

BHATNAGAR, ANSH

#### How to cite:

BHATNAGAR, ANSH (2025) Early Universe Particle Physics at Finite Temperature: Mysteries at the dawn of time, Durham theses, Durham University. Available at Durham E-Theses Online: http://etheses.dur.ac.uk/16296/

#### Use policy



This work is licensed under a Creative Commons Attribution Non-commercial Share Alike  $3.0~({\rm CC~BY\text{-}NC\text{-}SA})$ 

# Early Universe Particle Physics at Finite Temperature

Mysteries at the dawn of time

### Ansh Bhatnagar

A Thesis presented for the degree of Doctor of Philosophy



Institute for Particle Physics Phenomenology
Department of Physics
Durham University
United Kingdom

October 2025

# Early Universe Particle Physics at Finite Temperature

Mysteries at the dawn of time

#### Ansh Bhatnagar

Submitted for the degree of Doctor of Philosophy
October 2025

**Abstract:** The early universe provides a high energy lab for particle physics phenomenology, with messengers such as gravitational waves providing an insight into the events of that era. Mysteries at the dawn of time include the origin of the Baryon Asymmetry of the Universe (BAU), and the nature of the electroweak phase transition (EWPT). A first order EWPT could provide the out-of-equilibrium conditions necessary for baryogenesis, and is a natural consequence of many Standard Model extensions. An alternative source of out-of-equilibrium conditions are the decays of heavy right handed neutrinos in the early universe, as defines the leptogenesis scenario. However, vanilla leptogenesis requires fine tuning in the Higgs and neutrino sectors in order to generate the BAU. We present a model of 'Hot Leptogenesis', where a hot sector provides a factor  $\sim 50$  enhancement in the BAU, resulting in a novel model that does not demand fine tuning. We proceed to investigate the EWPT in the Two Higgs Doublet Model (2HDM), in light of the reported 95 GeV di-tau and di-gamma excess. Using a dimensional reduction method to calculate the thermal potential at 1-loop with 2-loop matching, we find regions of parameter space with a first order EWPT. However, the strongest signal-to-noise ratios for the LISA experiment are too weak to provide a detection.

$\mathbf{A}$	bstra	$\operatorname{ct}$	3
Li	${ m st}$ of	Figures	11
Li	${ m st}$ of	Tables	17
Li	$\operatorname{st}$ of	Abbreviations	19
1	Intr	oduction	29
	1.1	Paradigms and Revolutions	29
	1.2	The Crisis	30
	1.3	The Early Universe	32
2	The	Standard Model	35
	2.1	QFT and Symmetries	36
	2.2	Fermions	37
		2.2.1 Fermionic Masses	37
		2.2.2 Quarks	38
		2.2.3 Leptons	39
	2.3	Gauge bosons	39
		2.3.1 Gauge couplings	41

	2.4	Higgs	sector	•	•	•	•	•	•	•	•	٠	•	٠	41
		2.4.1	Yukawa couplings									•			42
		2.4.2	Spontaneous Symmetry Breaking			•	•	•				•			44
		2.4.3	Fermionic Masses Revisited .			•	•	•			•	•	•		47
	2.5	The St	tandard Model Lagrangian									•			47
	2.6	Calcul	ations in the SM			•	•	•			•	•	•	•	48
		2.6.1	Perturbation Theory			•	•	•			•	•	•		48
		2.6.2	Renormalisation			•									51
	2.7	Beyon	d the Standard Model			•	•	•			•	•	•		55
		2.7.1	Neutrino Masses		•					•					56
3	Earl	ly Uni	verse Cosmology												59
	3.1	Genera	al Relativity			•	•	•			•	•	•	•	60
	3.2	Standa	ard Model (of Cosmology)			•	•	•				•	•		60
	3.3	Timeli	ne of the Early Universe			•	•	•			•	•	•	•	63
		3.3.1	Inflation									•			64
		3.3.2	Electroweak Phase Transition .												68
		3.3.3	Big Bang Nucleosynthesis									•			69
		3.3.4	Recombination									•			70
	3.4	Therm	nal Statistics			•									71
		3.4.1	Relativistic Dynamics			•	•	•							73
		3.4.2	Non-Relativistic Dynamics												73
	3.5	Baryog	genesis												74
		3.5.1	Sakharov Conditions	•					•			•			75
		3.5.2	Electroweak Baryogenesis			•				•	•				76

	3.6	Leptog	genesis									78
		3.6.1	Type I Seesaw									78
		3.6.2	Boltzmann Equations									79
		3.6.3	Washout regimes									82
		3.6.4	Flavour effects	•				•				84
		3.6.5	Calculating $\eta_B$	•				•				84
		3.6.6	Naturalness and Resonant Leptogenesis	•				•	•			84
	3.7	Effecti	ve Potential	•				•				86
		3.7.1	Zero Temperature									87
		3.7.2	Matsubara Formalism									89
		3.7.3	Daisy Resummation		•							92
		3.7.4	Dimensional Reduction									95
	3.8	Gravit	ational Waves from FOPTs									97
		3.8.1	Gravitational Waves									97
		3.8.2	First Order Phase Transitions	•				•	•			99
		3.8.3	Gravitational Wave Sources and Spectra	•				•	•			100
		3.8.4	LISA					•				100
4	Hot	Lepto	genesis									103
	4.1	•	uction									
	4.2		eptogenesis from Inflaton Decays									
	4.3		del of Hot Leptogenesis									
		4.3.1	Kinetic and Chemical Equilibria	•	•	•	•	•	•	•	•	112
		4.3.2	Cosmology of the Scalar $\phi$	•				•	•		٠	119
		4.3.3	Summary									120

	4.4	Tracki	ng the Evolution of the Hot and SM Sectors .	•	•	•	•	•	•	121
		4.4.1	${\cal N}_1$ in Kinetic and Chemical Equilibrium				•		•	123
		4.4.2	$N_1$ in Kinetic Equilibrium Only							125
	4.5	Fine-T	uning		•	•				127
	4.6	Result	s							128
		4.6.1	$N_1$ in Kinetic Equilibrium Only							131
		4.6.2	$N_1$ in Kinetic and Chemical Equilibrium							136
		4.6.3	Further Scenarios							138
	4.7	Conclu	isions		•	•				139
5	Pha	ise Tra	nsition Phenomenology of the 95 GeV Res	ടറ	ทล	nc	e i	n	t.h.	P
0			s Doublet Model	J <b>O</b> .					011	141
		33	uction							
	5.1									
	5.2	The T	wo Higgs Doublet Model	•		•	•			144
	5.3	Therm	nal Potential	•			•		•	149
		5.3.1	The Dimensionally Reduced Effective Potential							150
		5.3.2	Higher Orders in the Effective Potential						•	151
	5.4	Phase	Transition and GW signature				•		•	152
		5.4.1	Bubble Nucleation							153
		5.4.2	Phase Transition Parameters							157
		5.4.3	Gravitational Wave Spectrum							159
		5.4.4	LISA signal to noise ratios							164
		5.4.5	From the Effective Potential to Gravitational V	Va	ves	S				165
	5.5	Result	s							166
	5.6	Concli	isions							172

6	Conclusion	175
$\mathbf{A}$	Cross-Sections, Decay Rates and Thermal Averaging	177
	A.1 Cross-Sections and Decay Rates	177
	A.2 Thermal Averaging	179
В	Renormalisation of the 2HDM	181
	B.1 Running and $\beta$ -functions	181
	B.2 Relations between $\overline{\text{MS}}\text{-parameters}$ and physical observables	183
$\mathbf{C}$	Integration of the DR EFT into PhaseTracer2	185
Bi	bliography	187

# List of Figures

2.1	The particles of the Standard Model, with mass values given to 3 s.f.	
	and taken from Ref. [33]. Neutrino masses are given with bounds; see	
	Section 2.7.1	36
2.2	The 'Mexican hat' potential of the Higgs after SSB. The Higgs mode	
	is shown as the massive oscillations around the broken phase radially	
	outwards from the origin, whereas the massless Goldstone mode is	
	the motion around the brim of the hat	45
2.3	Feynman diagrams of the $\phi^4$ theory contributing to the matrix element	
	up to NLO	49
3.1	The inflaton in its potential, slowly rolling towards the minimum. At	
	the minimum, it behaves like a simple harmonic oscillator and this	
	results in the reheating of the universe	66
3.2	Feynman diagrams of the $\phi^4$ theory contributing to the matrix element	
	up to NLO	82
3.3	1-loop correction to the Higgs propagator in the Type I Seesaw mech-	
	anism	85
3.4	An illustration of bubbles of a new phase nucleating and expanding	
	in a volume of the old phase. The bubbles can collide, inducing	
	anisotropic stress in spacetime, and thus producing gravitational waves.	99

4.1 Field content and the temperatures of the sectors in hot leptogenesis, along with whether they are in kinetic and chemical equilibrium (K.E. and C.E.) or only kinetic equilibrium (K.E.) around the time of  $N_1$  decay. The dominant coupling connecting the two sectors is taken to be the one responsible for  $N_1$  decay. The scalar field  $\phi$ , which keeps  $N_1$  in kinetic equilibrium, may also mediate a coupling between  $N_1$  and  $N_{2,3}$  (and also between  $N_1$  and the SM Higgs, not shown). Particles of the scalar field  $\phi$  may or may not be present at the time of  $N_1$  decay, depending on whether  $m_{\phi}$  is much greater than  $T_{N_1}$  or not 105

4.4 Feynman diagrams showing the processes which may put  $N_1$  into kinetic equilibrium with itself ((a) with i=1, (b) and (c)) and with the SM bath ((a) with  $i\in\{2,3\}$ ), which would set  $T_{\rm SM}=T_{N_1}$ . . . 114

List of Figures 13

4.5	Minimal value of $y_{\phi}^{1}$ such that the various interaction rates are greater	
	than Hubble around the time of decay, $T_{N_1}=m_{N_1}=10^7\mathrm{GeV}$ . We	
	have assumed that Hubble is dominated by the SM as it is right	
	after the decays and that $\lambda = 0.8$ . Assuming $y_{\phi}^{1} = y_{\phi}^{2}$ , the scattering	
	process $N_1N_2 \leftrightarrow N_1N_2$ will thermalise the SM and hot sectors in	
	the blue region above the dashed blue contour. To the right of the	
	black line the $\phi$ abundance will deplete with the $N_1$ abundance; the	
	region to the right of it is excluded. The region outside of the green	
	area is where the kinetic equilibrium assumption breaks down, and	
	our analysis no longer holds. To the left of the blue line (labelled	
	"cannibal $\phi$ ") the cannibal process $2\phi\leftrightarrow 3\phi$ is effective. The pink	
	(green) stars indicate example points in the toy model parameter space	
	where kinetic and chemical (only kinetic) equilibrium can be achieved,	
	where open stars require $y_{\phi}^2, y_{\phi}^3 \ll y_{\phi}^1$ . The white star shows a point	
	where the cosmology of $\phi$ would need to be carefully considered.	117
4.6	Feynman diagrams showing processes which could keep $N_1$ in chemical	
	equilibrium with the hot sector.	117
4.7	Evolution of $ \eta_B $ , $N_{N_1}$ and $\kappa$ for initial $\kappa_{\rm in}=10$ when $N_1$ is only in	
	kinetic equilibrium in the hot sector, for our benchmark point. When	
	the number density approaches zero, $\kappa$ is set to 1 (dashed line). The	
	green band indicates the baryon-to-photon ratio at the $3\sigma$ level	131
4.8	The final baryon asymmetry $ \eta_B $ as a function of the initial tem-	
	perature ratio $\kappa_{\rm in} = T_{N_1}/T_{\rm SM}$ at $a=1$ . The blue line indicates the	
	benchmark point. In the burgundy and orange curves we vary the	
	RHN mass scale and splittings (see text for details), while the dashed	

(dotted) blue curves indicate non-equilibrium initial abundances of

4.9	Values of $\eta_B$ for standard leptogenesis (left) and hot leptogenesis
	(right) for $\kappa_{\rm in}=10$ produced with the RHN in kinetic equilibrium
	only. The green dashed contours corresponding to $\eta_B$ produced at
	$(5.8-6.3)\times 10^{-10}~[53,180]$ and the red cross indicates our benchmark
	point. The greyed-out region represents when the non-thermalisation
	assumption no longer holds, such that hot leptogenesis may not be
	viable. $\Delta_H \sim 10.4\%$ and $\Delta_{\nu} \sim 855\%$ throughout the plot 135

4.10 Values of  $\eta_B$  for standard leptogenesis (left) and hot leptogenesis (right) for  $\kappa_{\rm in}=10$  produced with the RHN in kinetic and chemical equilibrium. The green dashed contours corresponding to  $\eta_B$  produced at  $(5.8-6.3)\times 10^{-10}$  [53,180] and the red cross indicates our benchmark point. The greyed out region represents when the non-thermalisation assumption no longer holds, such that hot leptogenesis may not be viable.  $\Delta_H \sim 10.4\%$  and  $\Delta_\nu \sim 855\%$  throughout the plot. . . . 137

5.2 Computed phase transitions with a light pseudoscalar  $m_A = 95$  GeV in the region seen in Fig. 5 of Ref. [204]. We have fixed  $m_H = 160$  GeV and  $\cos(\beta - \alpha) = -0.2$ , with the other fixed values as in Table 5.1.

List of Figures 15

5.3	<b>Top Left Panel:</b> First order phase transitions in the $m_H$ - $\cos(\beta - \alpha)$	
	plane, with the colour showing the value of the largest $ v_c/T_C $ for	
	that parameter point. Regions of two step (2S) and one step (1S)	
	first order phase transitions are labelled, along with the region that	
	has crossovers. Top Right Panel: As for top left, showing the peak	
	amplitude $\Omega_{\rm gw}h^2(f_{\rm gw})$ instead. Bottom Left Panel: As for top left,	
	showing the peak frequency $f_{\rm gw}$ instead. Bottom Right Panel:	
	Computed phase transitions for different parameter points plotted	
	against transition parameters $\bar{\alpha}$ and $\bar{\beta}/H_*$ . Only a randomly sampled	
	selection (1 in 4) is chosen to be shown on the plot to make the trends	
	clear. The value of $\cos(\beta - \alpha)$ for each point is shown by the colour,	
	whereas the value of $m_H$ is shown by the size of the circle. We show	
	LISA SNR curves for an ansatz transition temperature of 160 GeV,	
	and an ansatz $v_W = 0.63$	169
5.4	Illustrative phase diagrams for the benchmark points 1S and 2S in	
	Table 5.2, with regions that contain 1S and 2S shown in Fig. 5.3	171

## List of Tables

3.1	EOS parameter $w$ , energy density $\rho(a)$ and scale factor $a(t)$ scaling	
	for various types of energy.	62
4.1	Degree of fine-tuning for the best-fit points found in Ref. [156] and for	
	our benchmark point (see Table 4.2), using the fine-tuning measures	
	given in Section 4.5. Smaller numbers indicate a larger degree of	
	fine-tuning, with some degree of fine-tuning for numbers smaller than	
	$\sim 10\%$ .	129
4.2	Input parameters in the Casas-Ibarra parametrisation for our bench-	
	mark point, see text for details	130
5.1	Fixed inputs for our scan identifying $A, H$ with the resonance respect-	
	ively	168
5.2	The transition strength parameter $\bar{\alpha}$ and relative errors for Bench-	
	marks 2S and 1S at (2-loop improved) 1-loop [3D@NLO $V_3$ @LO] and	
	2-loop [3D@NLO $V_3$ @NLO]. Other parameters are fixed according to	
	Table 5.1	170

### List of Abbreviations

**QFT** Quantum Field Theory

SM / BSM Standard Model / Beyond the Standard Model

GR General Relativity

**ΛCDM** Lambda Cold Dark Matter

FLRW Friedmann-Lemaître-Robertson-Walker

LHC Large Hadron Collider

HL-LHC High-Luminosity Large Hadron Collider

**ATLAS** A Toroidal LHC Apparatus

CMS Compact Muon Solenoid

LEP Large Electron-Positron Collider

LISA Laser Interferometer Space Antenna

LIGO Laser Interferometer Gravitational-Wave Observatory

LO / NLO Leading Order / Next to Leading Order

MS / MS Minimal Subtraction / Minimal Subtraction (Modified)

**1PI** One Particle Irreducible

IR Infrared

UV Ultraviolet

BAU Baryon Asymmetry of the Universe

RHN Right Handed Neutrino

vev Vacuum Expectation Value

**d.o.f.** Degrees of Freedom

**EOS** Equation of State

**s.f.** Significant Figures

SSB Spontaneous Symmetry Breaking

EWSB Electroweak Symmetry Breaking

**EWPT** Electroweak Phase Transition

FOPT First Order Phase Transition

**DR** Dimensional Reduction

**EFT** Effective Field Theory

RG/RGE Renormalisation Group / Renormalisation Group Equations

**2HDM** Two Higgs Doublet Model

LTE Local Thermal Equilibrium

**GW** Gravitational Waves

SNR Signal-to-noise ratio

CMB Cosmic Microwave Background

BBN Big Bang Nucleosynthesis

**CKM** Cabibbo-Kobayashi-Maskawa

PMNS Pontecorvo-Maki-Nakagawa-Sakata

KMS Kubo-Martin-Schwinger

WIMP Weakly Interacting Massive Particle

SVD Singular Value Decomposition

FCNC Flavour Changing Neutral Current

GUT Grand Unified Theory

MSSM Minimally Supersymmetric Standard Model

### **Declaration**

The work in this thesis is based on research carried out in the Department of Physics at Durham University. No part of this thesis has been submitted elsewhere for any degree or qualification.

Research presented in this thesis is based on joint work.

- Chapter 4 is based on [1]: Michael J. Baker, Ansh Bhatnagar, Djuna Croon,
   Jessica Turner. Hot leptogenesis. Journal of High Energy Physics 2025, 82
   (2025). arXiv:2409.09113
- Chapter 5 is based on [2]: Ansh Bhatnagar, Djuna Croon, Philipp Schicho. Interpreting the 95 GeV resonance in the Two Higgs Doublet Model: Implications for the Electroweak Phase Transition, (2025). arXiv:2506.20716

#### Copyright © 2025 Ansh Bhatnagar.

The copyright of this thesis rests with the author. No quotation from it should be published without the author's prior written consent and information derived from it should be acknowledged.

### Acknowledgements

This thesis is the culmination of almost four years of work, and many people have helped along the way. Firstly, thank you to my supervisor Djuna Croon, who has supported me throughout and has been incredibly understanding of my circumstances such as my medical condition. Researching the mysteries of the universe with you has been a delight.

I would also like to thank all the postgraduate researchers at the IPPP over the years, and the inhabitants of OC118 in particular (Deppy, Livia, Edwin), for making work much more fun than it otherwise would have been. Thank you to Helen, Rollo, James, Mia, and Jack for all the D&D nights. And a special thank you to Mia, Elliot, Ery, Deppy, Dhruv, and Eleanor for proofreading my thesis.

Thank you to my collaborators over the years (Jessica Turner, Michael Baker, Philipp Schicho, Rachel Houtz, and Eleanor Hall) for the projects that were completed and even those that were not. I have learnt so much from you all.

I would also like to thank Trudy, Joanne, Adam, and Paul for all the administrative and computational support over the years; our PhDs wouldn't be possible without them.

Thank you to the UCU and all the PGR activists who helped me create the PGRs Against Low Pay campaign. We managed to take on the Government during a cost of living crisis, and win.

Thank you to the Parliamentary Office of Science and Technology, and my advisor Devyani Gajjar, for hosting me as a PhD Research Fellow in 2023, and STFC for funding the fellowship and production of Ref. [3].

Thank you to the teams at the University Hospital of North Durham and the Royal Victoria Infirmary for looking after me while I was in the North, in particular Mel who has always been kind and helped me substantially with medical matters.

Thank you to my family: my mum, Rekha, my dad, Sameer, and my brother, Ayush, for all the love and support over the years.

Finally, thank you to my partner Eleanor who made the final year of my PhD so special.

The Road goes ever on and on,

Down from the door where it began.

Now far ahead the Road has gone,

And I must follow, if I can.

— from *The Lord of the Rings* by J.R.R. Tolkien

# $This\ thesis\ is\ dedicated\\ to$

### PGRs Against Low Pay

The Postgraduate Researchers who stood up for better pay and conditions in 2022

### Chapter 1

### Introduction

The voices of the Ainur, like unto harps and lutes, and pipes and trumpets, and viols and organs, and like unto countless choirs singing with words, began to fashion the theme of Ilúvatar to a great music; and a sound arose of endless interchanging melodies woven in harmony that passed beyond hearing into the depths and into the heights...

from Ainulindalë by J.R.R. Tolkien

Particle physics is at a crossroads; with the discovery of the Higgs boson in 2012 [4,5] finalising the Standard Model as our 'theory of *most* things', the attention of the community was turned to physics at the TeV scale (which is 10x higher in energy than the Higgs mass). Yet the Large Hadron Collider (LHC), after years of upgrades and runs, has turned up empty handed. Beyond some minor discrepancies with the Standard Model, *no new fundamental particles* have been discovered at the LHC.

#### 1.1 Paradigms and Revolutions

The philosopher of science Thomas S. Kuhn characterised scientific progress as episodic, taking place in periods of time where there is a reigning, hegemonic, paradigm [6]. This paradigm is the framework accepted by the scientific community,

and all scientific progress within that era is done incrementally, developing that framework further. For example, in the 17th, 18th, and 19th centuries, the framework for fundamental physics was classical mechanics, formed by principles such as Galilean relativity [7], Newton's laws of motion [8], and eventually Maxwell's equations for electromagnetism [9]. These theories are all:

- deterministic, meaning that initial conditions and the principle of least action can in principle determine precisely the future evolution of the system,
- definite, meaning that the fields and particles are in a specific state at any given time.

Yet, as we are well aware, these principles once thought to be fundamental were soon found out to be merely emerging macroscopic approximations of underlying fundamental laws. In the Kuhnian view, discrepancies accumulate under a reigning paradigm until that paradigm is made untenable. A crisis occurs, which sparks a revolution and the creation of a new paradigm that is able to resolve those discrepancies. This happened at the turn of the 20th century with the quantum revolution [10,11], and led to the development of the Standard Model as we know it today.

#### 1.2 The Crisis

Now we are at a new crisis point, and the paradigm of the Standard Model is reaching its limits. Some discrepancies that exist are:

- We have not probed energies higher than  $\sqrt{s} = 13.6 \,\text{GeV}$  at particle colliders, so presumably there are particles with higher mass than this that may be coupled to the Higgs. Why then is the Higgs mass at a much lower scale than those particles, leading to a hierarchy problem?
- Galactic rotation curves [12] and cosmological observations show that there is a mysterious 'dark matter' that exists. Yet no particle in the Standard Model can account for this. What is the nature of dark matter?

1.2. The Crisis 31

• If we wish to describe physics at small scales and high energies, we need to unify quantum mechanics and general relativity. Yet efforts to create a quantum field theory of gravity have proven futile. What is the language of quantum gravity and the 'theory of everything'?

• Why does the universe have more matter than antimatter? As the overwhelming majority of matter in the universe is made up of baryons (bound particles made up of three quarks), we will instead refer to a baryon asymmetry of the universe, and baryogenesis as the process which created it.

We will elaborate on these issues and more in Section 2.7, but for now let's turn to a solution that hoped to resolve these issues: supersymmetry [13]. The idea was that each boson (or fermion) in the Standard Model would have a fermionic (bosonic) 'superpartner'. The contributions to the Higgs mass from these partners could cancel out leaving the Higgs mass stable at the electroweak scale and resolving the hierarchy problem [14]. Supersymmetry also provided the community with the 'WIMP' miracle, the idea that weakly interacting massive particles predicted by supersymmetry could be a perfect dark matter candidate [15]. Supersymmetry is also a low energy consequence of superstring theory, which is a popular candidate for a theory of everything. Finally, the extra particles in supersymmetry modify the Higgs potential, such that a first order phase transition is made possible where there can be a departure from equilibrium dynamics, spawning more baryons than anti-baryons [16].

This all sounds very promising. Yet, as aforementioned, no supersymmetric partners have been discovered at the LHC [17]. The WIMP never showed up [18]. The particle physics community bet heavily on supersymmetry, and has now been left with more questions than answers. Where do we go now for new fundamental physics?

#### 1.3 The Early Universe

Many issues raised with the Standard Model relate to high energy phenomena. One way to tackle these is to recreate these conditions in the lab, such as in particle colliders. However, it seems like the LHC, and the upcoming high luminosity (HL-LHC) upgrade [19], is unlikely to find any new physics; the best use of colliders for now might be precision studies of known physics [20]. But what if we could gain information from a part of the universe where these conditions exist naturally? What if we turned the hot early universe into our lab?

This may point towards a solution to the crisis. Through gravitational wave experiments such as the European Space Agency's LISA [21, 22], we could measure gravitational waves originating from the early universe [23–25], enlightening us on many high energy particle physics conundrums. The electroweak phase transition could be a source of these gravitational waves, if it were first order. Observing this signal would mean that the out-of-equilibrium requirement for the baryon asymmetry is satisfied, thus helping us to answer questions despite the roadblock on the collider front. However, the Standard Model Higgs potential only provides a smooth phase transition, not a first order one [26–28]. Therefore, any hope for a first order electroweak phase transition rests on physics beyond the Standard Model.

An alternative source of non-equilibrium dynamics for baryogenesis are the out-of-equilibrium decays of heavy particles that are hypothesised to exist in the early universe. A popular model for this is leptogenesis, the idea that the out-of-equilibrium decays of heavy neutrinos created a lepton asymmetry, which was then subsequently converted into a baryon asymmetry [29]. Vanilla leptogenesis models however require the heavy neutrinos to have incredibly large masses, such that they lead to a hierarchy problem for the Higgs boson [30].

In this thesis, we will explore these tangentially related early universe phenomena through well motivated models. We begin with the theoretical background in Chapters 2 and 3. In Chapter 2, we will summarise the Standard Model: its quantum

field theoretic language, its particle content, forces, and symmetries. We will briefly review the techniques used to calculate observables, such as perturbation theory and renormalisation. The chapter concludes with a discussion on physics beyond the Standard Model, and neutrino masses. In Chapter 3, we review early universe physics and cosmology. We briefly summarise general relativity and the ΛCDM model of cosmology, as well as a rough timeline of the early universe until recombination. We review quantum thermal statistics, which is important background for the introductions to baryogenesis and leptogenesis which follow after. We finish the chapter by reviewing finite temperature techniques for calculating the thermal effective potential, as well as gravitational waves from first order phase transitions.

In Chapter 4, we introduce a model of 'Hot Leptogenesis' [1], which aims to resolve fine-tuning issues in vanilla leptogenesis such as the aforementioned hierarchy problem. We outline the model's origin from inflaton decay, its particle content, the conditions necessary for chemical and/or kinetic equilibrium to be maintained, and an exploration of its parameter space.

In Chapter 5, we investigate the nature of an electroweak phase transition in a model with an extra Higgs-like particle that has a mass of 95GeV [2]. This is motivated by reported excesses in final states with two photons  $\gamma\gamma$  and two taus  $\tau\tau$  at the LHC. A new scalar in the Type I Two Higgs Doublet Model (2HDM) is seen as the most promising candidates compatible with constraints. We summarise these constraints, and outline our approach to calculating the phase transition parameters, before presenting scans in the Type I 2HDM parameter space. We explore whether or not first order phase transitions in this model could be detectable by the LISA experiment.

Finally, we conclude this thesis in Chapter 6.

### A Quick Note on Convention

Throughout this thesis, we make use of natural units where  $\hbar=c=1$ , and typically refer to particle masses and energy scales in units of eV. The gravitational constant G is usually written explicitly.

### Chapter 2

### The Standard Model

They saw with amazement the coming of the Children of Ilúvatar, and the habitation that was prepared for them; and they perceived that they themselves in the labour of their music had been busy with the preparation of this dwelling, and yet knew not that it had any purpose beyond its own beauty.

from  $Ainulindal\ddot{e}$  by J.R.R. Tolkien

The Standard Model of Particle Physics is the current hegemonic theory of High Energy Physics. With the discovery of the Higgs Boson in 2012 [4,5], the Standard Model was considered 'completed' as its most major outstanding prediction was confirmed by experiment [31]. Despite the successes of the Standard Model, we are also aware of its shortcomings and inability to explain observations such as neutrino oscillations [32] and dark matter [12].

In this chapter, we will break down and discuss the language and components of the Standard Model (summarised in Fig. 2.1), and finish by briefly discussing open questions on physics beyond the Standard Model. Much of this review can be found in textbooks such as by Schwartz [34] and Peskin and Schroeder [35]. A basic understanding of Quantum Field Theory is presumed.

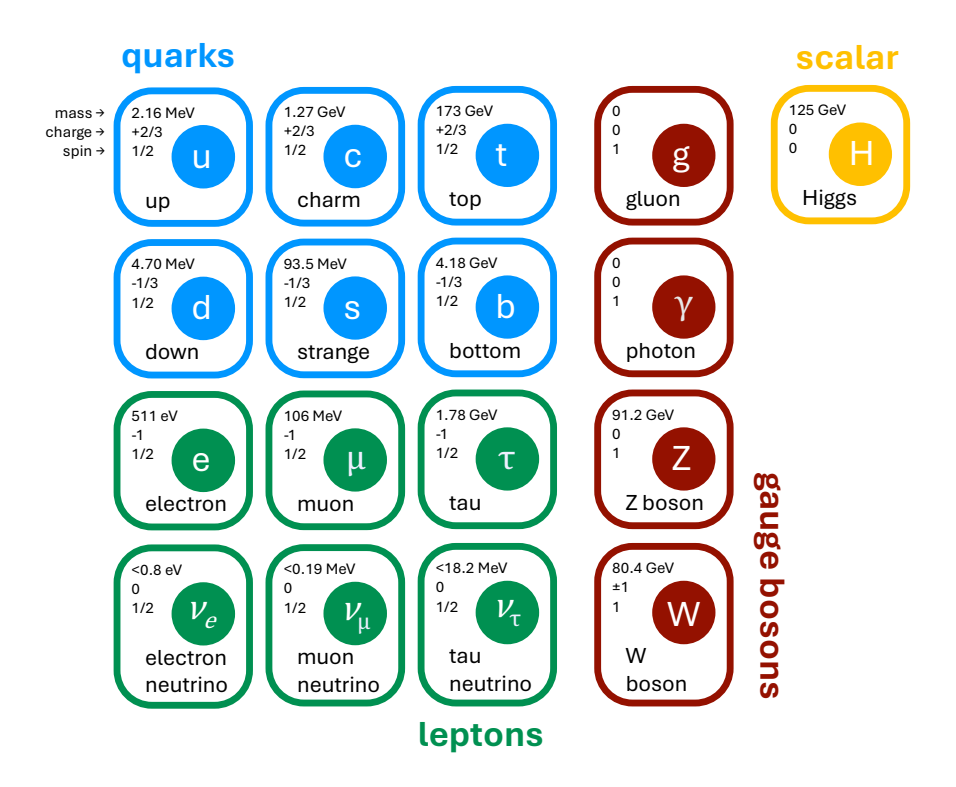


Figure 2.1: The particles of the Standard Model, with mass values given to 3 s.f. and taken from Ref. [33]. Neutrino masses are given with bounds; see Section 2.7.1.

# 2.1 QFT and Symmetries

The Standard Model has a Quantum Field Theoretic description, where fundamental particles are described by fields that are irreducible unitary representations of the Poincaré Group (the isometry group of flat, Minkowski spacetime).

The irreducibility of the representation corresponds to the fundamental nature of the fields, and the unitarity requirement arises from the desire to ensure that the inner product is preserved by the group transformations. Inner products on the Hilbert space of quantum states correspond to physical quantities, which should remain the same regardless of the reference frame they are computed in.

Therefore, it is clear that irreducible unitary representations of the Poincaré Group represent the types of fields, and thus the types of fundamental particles, that can exist in the SM.

According to Wigner's classification [36, 37], these representations are infinite dimen-

2.2. Fermions 37

sional and are thus best described by fields. These fields can be uniquely classified by a non-negative mass m and non-negative half-integer spin J.

It is because of this quantisation of spin, as well as the spin-statistics theorem, that fields in the SM can be classified as bosons (integer spin) or fermions (half-integer spin). They are further classified by their representations in the Standard Model gauge group,  $SU(3)_c \times SU(2)_L \times U(1)_Y$ , with  $SU(3)_c$  corresponding to the strong interaction and  $SU(2)_L \times U(1)_Y$  corresponding to the electroweak interaction. A field's representation under the SM gauge group is often written as  $(R_2, R_3)_Y$  where  $R_2$  and  $R_3$  refer to the  $SU(2)_L$  and  $SU(3)_c$  representations respectively, and Y refers to the  $U(1)_Y$  charge.

## 2.2 Fermions

The SM fermions are fundamental particles with half-integer spin, sometimes informally referred to as 'matter particles'. They are described by Weyl spinors, which are chiral projections of the Dirac spinor, due to the evidenced chiral nature of the electroweak force [38].

### 2.2.1 Fermionic Masses

If Dirac spinors are used instead of Weyl spinors, it is natural to include a mass term  $m\bar{\psi}\psi$  in the Lagrangian.

A Dirac spinor can be decomposed using the chiral projection operators  $P_{L/R}$  on  $\psi$  as

$$\psi = \psi_L + \psi_R = P_L \psi_L + P_R \psi_R, \qquad (2.2.1)$$

as it is also true that  $P_{L/R}\psi_{L/R}=\psi_{L/R}$ . Noting that  $\bar{P}_L=P_R$ , we find

$$\bar{\psi} = \bar{\psi}_L P_R + \bar{\psi}_R P_L \,. \tag{2.2.2}$$

Therefore, by noting that  $P_{R/L}\psi_{L/R}=0$ , the mass term becomes

$$m\bar{\psi}\psi = m(\bar{\psi}_L P_R + \bar{\psi}_R P_L)(P_L \psi_L + P_R \psi_R) = m(\bar{\psi}_L \psi_R + \bar{\psi}_R \psi_L)$$
 (2.2.3)

which would be the mass term in the Weyl spinor representation. Here, we run into a problem. The mass term necessitates the mixing of left and right handed Weyl spinors, which means they are unable to evolve independently in compliance with observations of the chiral nature of the electroweak force.

Thus, in the SM, fermions are described by massless Weyl spinors, meaning it has a chiral symmetry. This symmetry is generally composed of a vector symmetry, which acts on the spinors equally, and a U(1) axial symmetry which corresponds to a phase rotation of the left and right handed components in opposing directions:

$$\psi_L \to e^{-i\theta} \psi_L \tag{2.2.4}$$

$$\psi_R \to e^{i\theta} \psi_R \,. \tag{2.2.5}$$

However, this axial symmetry is broken in the SM by quantum corrections, which we do not discuss further here. Later, we will describe how fermions acquire mass through the Higgs mechanism.

### 2.2.2 Quarks

Quarks are fermions that are charged under the strong interaction (a property referred to as 'colour'), and also under the electroweak interaction.

Left-handed quarks are written as electroweak doublets

$$Q_L = \begin{pmatrix} u_L \\ d_L \end{pmatrix} \,, \tag{2.2.6}$$

and are in the  $(2,3)_{1/6}$  representation. The up-type and down-type right-handed quarks are electroweak singlets  $u_R$  and  $d_R$  and have the  $(1,3)_{2/3}$  and  $(1,3)_{-1/3}$  representations respectively.

There are three generations of the up-type and down-type quarks. For up-type, we have the up (u), charm (c), and top (t) quarks, and for the down-type we have down (d), strange (s), and bottom (b) quarks. The generations differ only in their mass.

Thus the quark kinetic contribution to the SM Lagrangian, for one generation, is

$$\mathcal{L} \ni i\bar{Q}_L \not\!\!\!D Q_L + i\bar{u}_R \not\!\!\!D u_R + i\bar{d}_R \not\!\!\!D d_R. \tag{2.2.7}$$

where  $D = \gamma^{\mu} D_{\mu}$  is the covariant derivative of the quarks summed with the Dirac matrices.

### 2.2.3 Leptons

Leptons are fermions that are not charged under the strong interaction, but are under the electroweak interaction. Left-handed leptons can be written as electroweak doublets

$$L_L = \begin{pmatrix} \nu_L \\ e_L \end{pmatrix}, \tag{2.2.8}$$

in the  $(2,1)_{-1/2}$  representation. Right-handed leptons are written as electroweak singlets  $e_R$  in the  $(1,1)_{-1}$  representation. The leptons are divided into the electromagnetically neutral neutrinos  $\nu_L$ , which only exist as left-handed Weyl spinors in the SM, and the electromagnetically charged leptons of type  $e_{L/R}$ . There are three generations of leptons, referred to as the electron (e), muon  $(\mu)$ , and tau  $(\tau)$ , and their associated neutrinos.

Thus the leptonic kinetic contribution to the SM Lagrangian, for one generation, is

$$\mathcal{L} \ni i\bar{L}_L \not\!\!\!D L_L + i\bar{e}_R \not\!\!\!D e_R \,. \tag{2.2.9}$$

# 2.3 Gauge bosons

A gauge symmetry is a localised symmetry of the Lagrangian, i.e. it depends on spacetime position  $x^{\mu}$ , as opposed to a global symmetry which is independent of position. As mentioned previously, the SM gauge group is the product group  $SU(3)_c \times SU(2)_L \times U(1)_Y$ .

Under the gauge group, the covariant derivative for a field is written as

$$D_{\mu} = \partial_{\mu} - ig_s G_{\mu}^a T^a - igW_{\mu}^a \tau^a - ig'B_{\mu}Y, \qquad (2.3.1)$$

where  $G_{\mu} = G_{\mu}^{a} T^{a}$ ,  $W_{\mu} = W_{\mu}^{a} \tau^{a}$  and  $B_{\mu}$  refer to the gauge vector fields of  $SU(3)_{c}$ ,  $SU(2)_{L}$  and  $U(1)_{Y}$  respectively.  $T^{a} = \frac{1}{2}\lambda^{a}$  and  $\tau^{a} = \frac{1}{2}\sigma^{a}$  represent the  $SU(3)_{c}$  and  $SU(2)_{L}$  generators respectively, with  $\lambda^{a}$  representing the Gell-Mann matrices and  $\sigma^{a}$  representing the Pauli matrices.

An N-dimensional special unitary group SU(N) has  $N^2-1$  generators. Thus, the  $SU(3)_c$  vector field  $G^{\mu}$  has 8 degrees of freedom, representing the 8 gluons (g) of the strong force.  $W^{\mu}$  has 3 degrees of freedom. Their associated groups are non-Abelian, meaning their elements do not commute.

 $B^{\mu}$  has 1 degree of freedom. The 4 degrees of freedom of the electroweak interaction, after Spontaneous Symmetry Breaking (SSB), correspond to the weak force bosons  $W^{\pm}$ , Z, and the photon  $\gamma$ .

The field strength tensor for a generic gauge group with gauge vector  $A_{\mu} = A_{\mu}^{a} t^{a}$ and covariant derivative  $D_{\mu} = \partial_{\mu} - igA_{\mu}$  is written as [39]

$$F_{\mu\nu} = D_{[\mu}A_{\nu]} = D_{\mu}A_{\nu} - D_{\nu}A_{\mu}, \qquad (2.3.2)$$

which can be expanded as

$$F_{\mu\nu} = \partial_{\mu}A_{\nu} - \partial_{\nu}A_{\mu} - ig[A_{\mu}, A_{\nu}] \tag{2.3.3}$$

$$= \partial_{\mu}A_{\nu} - \partial_{\nu}A_{\mu} + gf^{abc}A^{b}_{\mu}A^{c}_{\mu}t^{a}, \qquad (2.3.4)$$

where  $f^{abc}$  are the structure constants of the relevant Lie group.

Terms that are permitted under the gauge symmetry include the trace of the gauge field strength tensors, written as

$$-\frac{1}{2}\operatorname{Tr}(F^{\mu\nu}F_{\mu\nu}) = -\frac{1}{4}F^{\mu\nu,a}F^{a}_{\mu\nu}, \qquad (2.3.5)$$

Thus, the gauge kinetic term of the Lagrangian is written as,

$$\mathcal{L} \ni -\frac{1}{2} \operatorname{Tr} \left( G^{\mu\nu} G_{\mu\nu} \right) - \frac{1}{2} \operatorname{Tr} \left( W^{\mu\nu} W_{\mu\nu} \right) - \frac{1}{4} B^{\mu\nu} B_{\mu\nu}$$
 (2.3.6)

where  $G_{\mu\nu}$ ,  $W_{\mu\nu}$  and  $B_{\mu\nu}$  refer to the  $SU(3)_c$ ,  $SU(2)_L$  and  $U(1)_Y$  field strength tensors respectively.

### 2.3.1 Gauge couplings

The interactions between the gauge bosons and other fields arise from the covariant derivative in (2.3.1). For example,  $L_L$  is an electroweak doublet, not charged under the strong force, with a hypercharge of Y = -1/2. This means that the first term of the covariant derivative (corresponding to the  $SU(3)_c$  symmetry) will not apply to it, while the other two terms will. Therefore, the covariant derivatives in the 'kinetic' terms actually introduce interactions between the gauge bosons and the fermions/Higgs boson, which are the force interactions.

# 2.4 Higgs sector

Finally, to finish the SM, we must include a complex spin 0 (scalar) boson called the Higgs boson, which was introduced in the 1960s [40–42] to account for fermion and vector boson masses. The Higgs sector contributes to the SM Lagrangian the following terms for the Higgs doublet  $\Phi$ :

$$\mathcal{L} \ni (D_{\mu}\Phi)^{\dagger}D_{\mu}\Phi + \mu^{2}\Phi^{\dagger}\Phi - \frac{1}{2}\lambda(\Phi^{\dagger}\Phi)^{2}, \qquad (2.4.1)$$

where  $\mu$  represents the mass of the field, and  $\lambda$  is the quartic Higgs coupling. The Higgs exists in the  $(2,1)_{1/2}$  representation.

### 2.4.1 Yukawa couplings

Yukawa couplings are couplings between scalars and spinors of the type  $g\phi\bar{\psi}\psi$  for scalars and  $ig\phi\bar{\psi}\gamma^5\psi$  for pseudoscalars.

In the SM, Yukawa couplings between fermions and the Higgs are permitted, and they take the form

$$y(\bar{\psi}_L \Phi \psi_R + \text{h.c.}) \tag{2.4.2}$$

which is the only term allowed that preserves  $SU(2)_L \times U(1)_Y$  symmetry. This can be seen by the fact that in the SM, left-handed fermions exist as  $SU(2)_L$  doublets and transform as  $\psi_L \to M\psi_L$ , whereas right-handed fermions are  $SU(2)_L$  singlets. Thus the Yukawa term transforms as

$$\bar{\psi}_L \Phi \psi_R \to e^{i\theta/2} \bar{\psi}_L M^{\dagger} M e^{i\theta/2} \Phi e^{-i\theta} \psi_R = \bar{\psi}_L \Phi \psi_R,$$
 (2.4.3)

and is electroweak invariant.

### Lepton Yukawa Terms

Looking at the lepton sector, generically there are  $3 \times 3 \times 2 = 18$  free parameters in the Yukawa matrix due to the mixings between the three generations and the complex nature of the Yukawa couplings. The Yukawa terms take the form,

$$\mathcal{L} \ni -\sum_{a,b} \left( y_l^{ab} \bar{L}_L^a \Phi L_R^b + (y_l^{ab})^* \bar{L}_R^b \Phi^{\dagger} L_L^a \right) , \qquad (2.4.4)$$

where a and b are lepton generation labels.

However, a complex matrix  $y_l^{ab}$  can be multiplied by two unitary matrices  $U_L$  and  $U_R$  such that  $U_L^{\dagger}y_lU_R$  is real and diagonal. Thus the lepton basis can be rotated and we can write the Yukawa terms as a diagonalised sum,

$$\mathcal{L} \ni -\sum_{f} y_l^f \left( \bar{L}_L^f \Phi L_R^f + \bar{L}_R^f \Phi^{\dagger} L_L^f \right) , \qquad (2.4.5)$$

where  $f=e,\mu,\tau$  is the fermion generation label.

#### Quark Yukawa Terms

For quarks, the Yukawa terms for the down-type quarks follow a similar form to those of the leptons. However, for up type quarks,  $\Phi$  does not have the right hypercharge for a similarly constructed term to be electroweak invariant. This is because up type and down type quarks have different hypercharges in order to arrive at the correct electric charges after SSB. Thus, the Yukawa terms have to be structured differently in order to have invariant terms for both quark types.

We introduce the doublet  $\tilde{\Phi} = i\sigma_2 \Phi^*$ , which is in the  $(2,1)_{-1/2}$  representation of the SM group. This doublet is used in place of  $\Phi$  for the up type quark Yukawa terms. Thus, we arrive at the quark Yukawa terms

$$\mathcal{L} \ni -\sum_{a,b} \left( y_d^{ab} \bar{Q}_L^a \Phi d_R^b + (y_d^{ab})^* \bar{d}_R^b \Phi^{\dagger} Q_L^a + y_u^{ab} \bar{Q}_L^a \tilde{\Phi} u_R^b + (y_u^{ab})^* \bar{u}_R^b \tilde{\Phi}^{\dagger} Q_L^a \right) , \quad (2.4.6)$$

where a, b are quark generation labels.

#### Flavour Mixing

Performing a similar diagonalisation procedure for leptons, we can transform the quarks into their flavour basis,

$$\mathcal{L} \ni -\sum_{f} y_{d}^{f} \left( \bar{Q}_{L}^{f} \Phi d_{R}^{f} + \bar{d}_{R}^{f} \Phi^{\dagger} Q_{L}^{f} \right) - \sum_{f} y_{u}^{f} \left( \bar{Q}_{L}^{f} \tilde{\Phi} u_{R}^{f} + \bar{u}_{R}^{f} \tilde{\Phi}^{\dagger} Q_{L}^{f} \right) , \qquad (2.4.7)$$

where f is the flavour label. However, as up and down type quarks are rotated differently,

$$u_{L/R}^a \to \sum_b U_{u,L/R}^{ab} u_{L/R}^b$$
 (2.4.8)

$$d_{L/R}^a \to \sum_b U_{d,L/R}^{ab} d_{L/R}^b \,,$$
 (2.4.9)

all terms in the SM Lagrangian remain invariant except the quark kinetic term  $i\bar{Q}_L \not\!\!\!D Q_L$ . Specifically, after spontaneous symmetry breaking (which we elaborate on in Section 2.4.2), the  $W^{\pm}$  coupling terms that emerge from the quark kinetic term

transform as

$$i\bar{Q}_L \not\!\!D Q_L \ni -\frac{g}{\sqrt{2}} \sum_f \left( \bar{u}_L^f \gamma^\mu W_\mu^+ d_L^f + \bar{d}_L^f \gamma^\mu W_\mu^- u_L^f \right)$$
 (2.4.10)

$$\rightarrow -\frac{g}{\sqrt{2}} \sum_{f,g} \left( \bar{u}_L^f V_{\rm CKM}^{fg} \gamma^{\mu} W_{\mu}^+ d_L^g + \bar{d}_L^g (V_{\rm CKM}^{\dagger})^{gf} \gamma^{\mu} W_{\mu}^- u_L^f \right)$$
 (2.4.11)

where g is the weak gauge coupling, and  $V_{\text{CKM}} = U_{u,L}^{\dagger} U_{d,L}$  is the Cabibbo-Kobayashi-Maskawa (CKM) matrix. Thus the weak interaction, specifically the  $W^{\pm}$  bosons can change quark flavour, and the non-zero off-diagonal entries of the CKM matrix describe the mixing strength of the quark flavours.

### 2.4.2 Spontaneous Symmetry Breaking

The Higgs mechanism was introduced to explain how massless fermions and vector bosons can acquire mass while retaining the chiral nature of the weak force [40–42]. The structure of the zero temperature Higgs potential illustrates this; for positive  $\mu$  in

$$V(\Phi) = -\mu^2 \Phi^{\dagger} \Phi + \frac{1}{2} (\Phi^{\dagger} \Phi)^2, \qquad (2.4.12)$$

we find that the minima exists for field values that satisfy  $\Phi^{\dagger}\Phi = \mu^2/\lambda$ , thus there is a ring of minima in this so-called 'Mexican hat potential', as shown in Fig. 2.2. The Higgs doublet  $\Phi$  can be parametrised as,

$$\langle \Phi \rangle = \frac{1}{\sqrt{2}} \begin{pmatrix} 0 \\ v+h \end{pmatrix} \tag{2.4.13}$$

where  $v = \sqrt{2\mu^2/\lambda} \approx 246\,\text{GeV}$  is the Higgs Vacuum Expectation Value (vev)<sup>1</sup>, and h is a real field: the physical Higgs boson.

Thus, when the Higgs takes this vev, using the covariant derivative of the Higgs with Y=1/2 as

$$D_{\mu}\Phi = \partial_{\mu}\Phi - igW_{\mu}^{a}\tau^{a}\Phi - \frac{i}{2}g'B_{\mu}\Phi \qquad (2.4.14)$$

Note that sometimes there is a convention that the  $\sqrt{2}$  factor is absorbed into the definition of v, i.e.  $v \approx 246/\sqrt{2} \, \text{GeV} \approx 174 \, \text{GeV}$ . In this thesis we will make clear when this convention is being used instead.

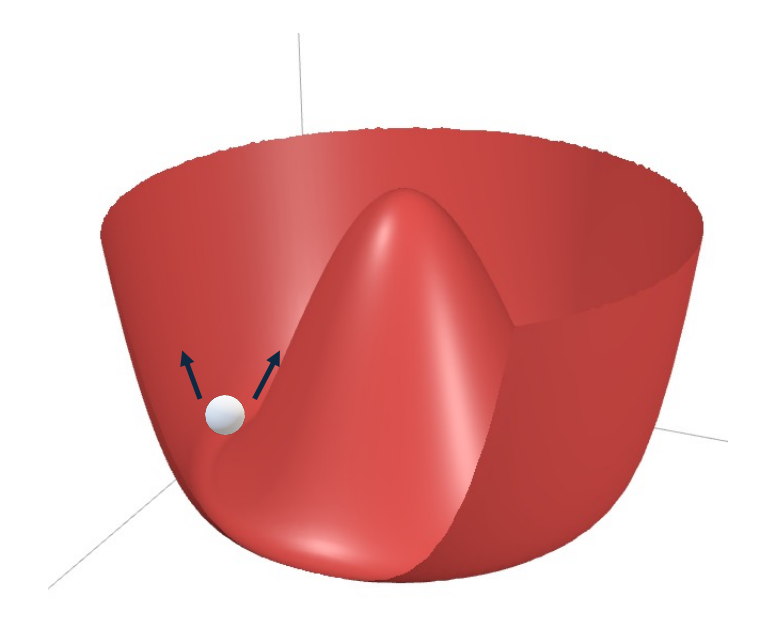


Figure 2.2: The 'Mexican hat' potential of the Higgs after SSB. The Higgs mode is shown as the massive oscillations around the broken phase radially outwards from the origin, whereas the massless Goldstone mode is the motion around the brim of the hat.

we can rewrite the Higgs kinetic term as

$$(D_{\mu}\Phi)^{\dagger}D_{\mu}\Phi = \frac{1}{2}\partial_{\mu}h\partial^{\mu}h$$

$$+ \frac{g^{2}}{8}(v+h)^{2}\left(0 \quad 1\right) \begin{pmatrix} W_{\mu}^{3} + \frac{g'}{g}B_{\mu} & W_{\mu}^{1} - iW_{\mu}^{2} \\ W_{\mu}^{1} + iW_{\mu}^{2} & W_{\mu}^{3} - \frac{g'}{g}B_{\mu} \end{pmatrix}^{2} \begin{pmatrix} 0 \\ 1 \end{pmatrix}$$

$$= \frac{1}{2}\partial_{\mu}h\partial^{\mu}h + \frac{g^{2}}{8}(v+h)^{2}\left((W_{\mu}^{1} + iW_{\mu}^{2})(W_{\mu}^{1} - iW_{\mu}^{2}) + (W^{3} - \frac{g'}{g}B)^{2}\right).$$

$$(2.4.16)$$

$$= \frac{1}{2}\partial_{\mu}h\partial^{\mu}h + \frac{g^{2}}{8}(v+h)^{2}\left((W_{\mu}^{1} + iW_{\mu}^{2})(W_{\mu}^{1} - iW_{\mu}^{2}) + (W^{3} - \frac{g'}{g}B)^{2}\right).$$

$$(2.4.17)$$

We see here that there are mass terms for the gauge fields which can be re-defined in the mass basis as

$$W_{\mu}^{\pm} \equiv \frac{1}{\sqrt{2}} (W_{\mu}^{1} \pm iW_{\mu}^{2}) \tag{2.4.18}$$

$$Z_{\mu} \equiv \frac{1}{\sqrt{g^2 + g'^2}} (gW_{\mu}^3 - g'B_{\mu}),$$
 (2.4.19)

such that the mass terms are

$$\mathcal{L} \ni \left(\frac{gv}{2}\right)^2 W_{\mu}^+ W^{-\mu} + \frac{v^2}{8} \left(g^2 + g'^2\right) Z_{\mu} Z^{\mu} \tag{2.4.20}$$

where the masses can be read off as  $m_W = gv/2$  and  $m_Z = v\sqrt{g^2 + g'^2}/2$ .

In this basis, we find that we can define the weak mixing angle

$$\cos(\theta_W) = \frac{m_W}{m_Z} = \frac{g}{\sqrt{g^2 + g'^2}},$$
 (2.4.21)

and parametrise the the Z mode as  $Z_{\mu} = \cos(\theta_W)W_{\mu}^3 - \sin(\theta_W)B_{\mu}$ . Similarly, we can define the massless mode perpendicular to this as  $A_{\mu} = \cos(\theta_W)B_{\mu} + \sin(\theta_W)W_{\mu}^3$ , which we identify as the photon of quantum electrodynamics.

This allows us to rewrite the gauge derivative in Eq. 2.4.14 as [34]

$$D_{\mu} = \partial_{\mu}\Phi + ig'\cos(\theta_W)(\tau^3 + Y)A_{\mu} \tag{2.4.22}$$

$$+i(g\cos(\theta_W)\tau^3 - g'\sin(\theta_W)Y)Z_{\mu} \tag{2.4.23}$$

$$+i\frac{g}{\sqrt{2}}(W_{\mu}^{+}\tau^{+}+W_{\mu}^{-}\tau^{-}), \qquad (2.4.24)$$

where  $\tau^{\pm} = \tau^1 \pm i\tau^2$ . The gauge coupling of the photon,  $e = g'\cos(\theta_W)$ , can be defined as the electromagnetic coupling strength.  $Q = \tau^3 + Y$  is the unbroken generator of the residual symmetry group, which is  $U(1)_{\rm EM}$ . The massless degree of freedom associated with this residual symmetry group is the photon.

We can think of motion around the three-dimensional 'brim' of the Mexican hat (see Fig. 2.2) as representing massless degrees of freedom. These are the three Goldstone bosons that are subsequently absorbed by the W and Z bosons, giving them mass.

Thus, the SM has undergone spontaneous symmetry breaking of the form,

$$SU(2)_L \times U(1)_Y \to U(1)_{EM}$$
, (2.4.25)

which is also referred to as electroweak symmetry breaking (EWSB).

The cosmological event associated with this symmetry breaking is the electroweak phase transition, which is discussed further in Chapter 3.

### 2.4.3 Fermionic Masses Revisited

SSB transforms the Yukawa terms. Focusing on the lepton Yukawa terms in Eq. 2.4.5, for one generation, we see that they transform into

$$\frac{y_l}{\sqrt{2}} \left( \begin{pmatrix} \bar{\nu}_L & \bar{e}_L \end{pmatrix} \begin{pmatrix} 0 \\ v \end{pmatrix} e_R + \bar{e}_R \begin{pmatrix} 0 & v \end{pmatrix} \begin{pmatrix} \nu_L \\ e_L \end{pmatrix} \right) = \frac{1}{\sqrt{2}} y_l v (\bar{e}_L e_R + \bar{e}_R e_L) . \tag{2.4.26}$$

Here, we see that we have arrived at the Weyl fermion mass term in Eq. 2.2.3, with the lepton mass  $m_l = y_l v / \sqrt{2}$ . The derivation follows analogously for the quark masses. We see here also that the neutrinos  $\nu_l$  drop out of the Yukawa terms and are left massless, as in the SM they do not have a right-handed partner.

Thus, with the Higgs mechanism, we are able to construct a theory that is compatible with the evidenced chiral nature of fermions at high energy [38], while also ensuring that fermions are massive at low energy.

# 2.5 The Standard Model Lagrangian

We finally arrive at the full Standard Model Lagrangian, which is given by

$$\mathcal{L} = -\frac{1}{2} \operatorname{Tr} \left( G^{\mu\nu} G_{\mu\nu} \right) - \frac{1}{2} \operatorname{Tr} \left( W^{\mu\nu} W_{\mu\nu} \right) - \frac{1}{4} B^{\mu\nu} B_{\mu\nu}$$
 (2.5.1)

$$+ (D_{\mu}\Phi)^{\dagger}D_{\mu}\Phi + \mu^{2}\Phi^{\dagger}\Phi - \frac{1}{2}\lambda(\Phi^{\dagger}\Phi)^{2}$$

$$(2.5.2)$$

$$+i\sum_{f}\left(\bar{Q}_{L}\not\!\!\!DQ_{L}+\bar{u}_{R}\not\!\!\!Du_{R}+\bar{d}_{R}\not\!\!\!Dd_{R}+\bar{L}_{L}\not\!\!\!DL_{L}+\bar{e}_{R}\not\!\!\!De_{R}\right) \tag{2.5.3}$$

$$-\sum_{f} y_l^f \left( \bar{L}_L^f \Phi L_R^f + \bar{L}_R^f \Phi^{\dagger} L_L^f \right) \tag{2.5.4}$$

$$-\sum_{a,b} \left( y_d^{ab} \bar{Q}_L^a \Phi d_R^b + (y_d^{ab})^* \bar{d}_R^b \Phi^{\dagger} Q_L^a + y_u^{ab} \bar{Q}_L^a \tilde{\Phi} u_R^b + (y_u^{ab})^* \bar{u}_R^b \tilde{\Phi}^{\dagger} Q_L^a \right)$$
(2.5.5)

where 2.5.1 refers to the gauge kinetic terms, 2.5.2 refers to the Higgs sector, 2.5.3 has the fermion kinetic terms, and 2.5.4 and 2.5.5 are the lepton and quark Yukawa terms respectively.

The SM obeys the discrete CPT symmetry, which is made up of:

- Charge conjugation (C), e.g.  $e^- \rightarrow e^+$ ,
- Parity (P), or mirror inversion defined by  $x^{\mu} \to -x^{\mu}$  for the spatial indices  $\mu = 1, 2, 3$ ,
- Time (T), defined by  $t \to -t$ .

C, P, and T symmetries can be individually violated in the SM. A source of CP asymmetry is found in the complex phases of the CKM matrix.

The SM has 19 free parameters, given by the 3 gauge couplings  $g, g', g_S$ , the Higgs mass  $\mu^2$ , the Higgs quartic coupling  $\lambda$ , the 3 lepton Yukawa couplings  $y_l^f$ , 10 parameters in the quark Yukawa matrices  $y_{d,u}$  and the strong CP angle  $\theta$ . They have been experimentally measured and the theory has withstood rigorous testing. Examples of SM precision tests include the anomalous magnetic moment of the electron, which has been measured to an accuracy of 1 part in 10 billion [43] and agrees with the theoretical prediction to at least 10 significant figures [44].

## 2.6 Calculations in the SM

# 2.6.1 Perturbation Theory

Calculating precision observables in the SM requires the use of perturbation theory, which is valid for weakly interacting theories. The basic idea is that the theory can be treated as a free theory to first order, and higher order corrections from interaction can be treated as perturbations to the free theory. Here, we briefly outline the loop expansion form of perturbation theory, where the leading order (LO) contribution is given at 'tree level', and a diagram with n loops contributes at next to leading order (N<sup>(n)</sup>LO).

As a model theory to illustrate the loop expansion, we use a  $\phi^4$  theory,

$$\mathcal{L} = \frac{1}{2}\partial_{\mu}\phi\partial^{\mu}\phi + \frac{1}{2}m^{2}\phi^{2} - \frac{1}{4!}\lambda\phi^{4}, \qquad (2.6.1)$$

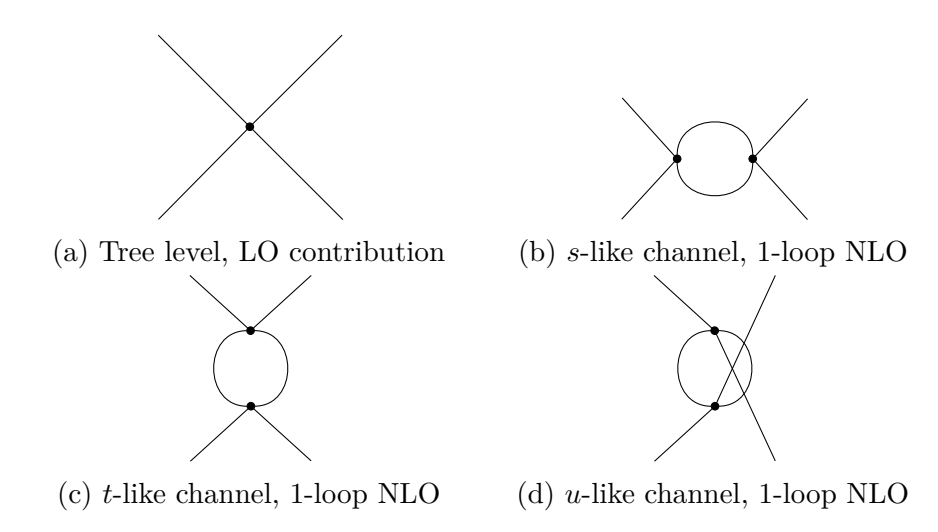


Figure 2.3: Feynman diagrams of the  $\phi^4$  theory contributing to the matrix element up to NLO.

which is similar to the Higgs Lagrangian in Eq. 2.4.1.

The scattering amplitude between the initial state of a system  $|i\rangle$  and a final state  $|f\rangle$  is given by  $\langle f|\hat{S}|i\rangle$ , where  $\hat{S}$  is defined as the scattering matrix. By taking  $\hat{S}$  as a perturbation around the free theory, defined by the identity matrix, we find  $\hat{S} = 1 + i\hat{T}$  where  $\hat{T}$  is the transfer matrix and encodes the results of interactions.

Thus, with explicit momentum conservation we find

$$\langle f | \hat{T} | i \rangle = (2\pi)^4 \delta^{(4)} \left( \sum_i p_i \right) \mathcal{M}$$
 (2.6.2)

where  $\mathcal{M}$  is referred to as the matrix element. It is calculated perturbatively, requiring couplings that are small enough such that the loop expansion converges. We can draw Feynman diagrams of all possible ways an interaction can happen which are then summed together at a certain order in the loop expansion. Feynman rules provide the factors that need to be put together for a given theory, such that a Feynman diagram gives a well-defined contribution to  $\mathcal{M}$ .

As an example, we provide the 1-loop expansion for 2-2 scattering in the  $\phi^4$  theory in Fig. 2.3. All diagrams are summed over. The Feynman rules for this theory are

as follows

$$=-i\lambda \qquad \longrightarrow = D_0(p) = \frac{i}{p^2 - m^2 + i\epsilon} \qquad (2.6.3)$$

where  $D_0(p)$  is the tree-level propagator, and the Feynman  $i\epsilon$  prescription is a tool to perform Euclidean momenta integrals which we will not discuss further here. Momenta are conserved at the vertices, and any undetermined momenta q in loops are integrated over with  $\int d^4q/(2\pi)^4$ , which we compute in Section 2.6.2.

Some measurable quantities that can be computed with  $\mathcal{M}$  in a general theory include the decay width of a particle,  $\Gamma$ , and the cross section  $\sigma$  of a  $2 \to n$  scattering. The formula for the decay rate of a particle of mass m is given by

$$\Gamma = \frac{1}{2m} \sum_{f} \int |\mathcal{M}_f|^2 d\Pi^n$$
 (2.6.4)

where we sum over all final possible states f of the decay, and  $d\Pi^n$  is the phase space element. The partial decay width,  $\Gamma_i$ , is the width for a single decay process.

The cross section of a  $2 \to n$  scattering is given by

$$\sigma = \frac{1}{4\sqrt{(p_1 \cdot p_2)^2 - m_1^2 m_2^2}} \int |\mathcal{M}|^2 d\Pi^n$$
 (2.6.5)

where  $p_i, m_i$  are the 4-momenta and masses of the particle i. The Lorentz-invariant phase space element for n particles is given by

$$d\Pi^{n} = (2\pi)^{4} \delta^{(4)} \left( \sum_{i=1}^{n+2} p_{i} \right) \prod_{j=1}^{n} \frac{d^{3} \mathbf{p}_{j}}{2\pi^{3} (2E_{j})}$$
 (2.6.6)

where  $\mathbf{p}_j$  is the 3-momentum for outgoing particle j. The sum in the delta function goes to n+2 as we sum over incoming and outgoing momenta to ensure momentum conservation.

A complete set of Feynman rules for the SM can be found in Ref. [45].

### 2.6.2 Renormalisation

We turn our attention to the undetermined momenta in the 1-loop diagrams. These involve integrating over all possible values of the loop momentum q, up to infinite momentum. Thus, the integrals are of the form  $\int d^4q/q^4$ , and they diverge logarithmically. The way to handle these divergences is the process of renormalisation.

We start off by redefining the quantities in the Lagrangian in Eq. 2.6.1 as the 'bare' quantities with labels  $\phi_B, m_B, \lambda_B$ . We can rewrite the Lagrangian as

$$\mathcal{L} = \frac{1}{2} Z_{\phi} \partial_{\mu} \phi_{R} \partial^{\mu} \phi_{R} - \frac{1}{2} Z_{\phi} Z_{m} m_{R}^{2} \phi_{R}^{2} - \frac{1}{4!} Z_{\phi}^{2} Z_{\lambda} \lambda_{R} \phi_{R}^{4}$$
(2.6.7)

$$= \frac{1}{2} \partial_{\mu} \phi_{R} \partial^{\mu} \phi_{R} - \frac{1}{2} m_{R}^{2} \phi_{R}^{2} - \frac{1}{4!} \lambda_{R} \phi_{R}^{4}$$
 (2.6.8)

$$+ \delta_{\phi} \left( \frac{1}{2} \partial_{\mu} \phi_{R} \partial^{\mu} \phi_{R} \right) - \delta_{m} \left( \frac{1}{2} m_{R}^{2} \phi_{R}^{2} \right) - \delta_{\lambda} \left( \frac{1}{4!} \lambda_{R} \phi_{R}^{4} \right) , \qquad (2.6.9)$$

where we defined the renormalised field  $\phi_R = \phi_B/\sqrt{Z_\phi}$ , mass  $m_R = m_B/\sqrt{Z_m}$ , and quartic coupling  $\lambda_R = \lambda_B/Z_\lambda$ . The counterterms are given by  $\delta_\phi = (Z_\phi - 1)$ ,  $\delta_m = (Z_\phi Z_m - 1)$ ,  $\delta_\lambda = (Z_\phi^2 Z_\lambda - 1)$  and are calculated such that they cancel out the divergences that emerge at higher loop order. In effect, this means that one can use the tree-level Feynman rules with the renormalised fields, masses, and couplings in order to calculate quantities, as the loop effects are already baked in to those quantities. Thus renormalisation is a powerful tool for QFT calculations.

To illustrate the calculation of the renormalised quantities, we compute the 1-loop expansion of the propagator D(p)

where the first diagram gives the tree-level  $D_0(p)$ , the second gives the 1-loop contribution, and the third and fourth diagrams are the 2-loop contributions.

We can rewrite the propagator using the self-energy  $i\Sigma$ , which is the sum of all 1 Particle Irreducible (1PI) diagrams. These diagrams are ones that cannot be separated by making a single cut through a line. For example, the fourth diagram can be cut between the two loops, meaning that as it can be made from two copies of the 1-loop contribution, it does not provide any new information about the renormalisation of the propagator and is not 1PI. The third diagram is a 1PI contribution at 2-loop, and is included in the self energy  $i\Sigma$ .

A propagator can thus be formed by chaining together the 1PI diagrams with the tree-level propagator connecting between them, such that

$$D(p) = D_0(p) + D_0(p)(i\Sigma)D_0(p) + D_0(p)(i\Sigma)D_0(p)(i\Sigma)D_0(p) + \cdots$$
 (2.6.11)

$$= D_0(p) \sum_{n=0}^{\infty} \left[ i \Sigma D_0(p) \right]^n$$
 (2.6.12)

which gives a finite result if perturbativity applies,

$$D(p) = \frac{D_0(p)}{1 - i\Sigma D_0(p)} = \frac{i}{p^2 - m^2 + \Sigma}.$$
 (2.6.13)

Thus, we see that the higher order effects are all captured by the self-energy  $\Sigma$ . At 1-loop, we can use the  $\phi^4$  Feynman rules on the second diagram in Eq. 2.6.10 to calculate the self-energy contribution

$$i\Sigma = -i\lambda \int \frac{d^4q}{(2\pi)^4} \frac{i}{q^2 - m^2},$$
 (2.6.14)

which we already know has a divergence. One way to get around the divergence is to use dimensional regularisation, where we perform our calculation in  $D=4-\epsilon$  dimensions, where  $\epsilon$  is a perturbation away from the 4D, and write the dimensionless coupling  $\bar{\lambda} = \mu^{D-4}\lambda = \mu^{-\epsilon}\lambda$  as  $\lambda$  acquires dimension when  $D \neq 4$ . Here, we have introduced an arbitrary mass scale  $\mu$ .

Our self-energy integral is now

$$i\Sigma = -i\mu^{\epsilon}\bar{\lambda} \int \frac{d^{D}q}{(2\pi)^{D}} \frac{i}{q^{2} - m^{2}}, \qquad (2.6.15)$$

and we can perform a Wick rotation to imaginary time  $(t \to i\tau)$  and we end up with

the Euclidean integral

$$i\Sigma = -i\mu^{\epsilon}\bar{\lambda} \int \frac{d^D q_E}{(2\pi)^D} \frac{i}{q_E^2 + m^2}$$
(2.6.16)

$$= \frac{\mu^{\epsilon} \bar{\lambda}}{(2\pi)^D} \int_0^\infty \frac{dq_E}{q_E^2 + m^2} q_E^{D-1} \int d\Omega_D$$
 (2.6.17)

where we have transformed to spherical coordinates with radius  $q_E$ , and  $d\Omega_D$  is the surface area of a D-sphere, given by

$$d\Omega_D = \frac{2\pi^{D/2}}{\Gamma\left(\frac{D}{2}\right)}. (2.6.18)$$

In the Euclidean Lagrangian, the potential has a positive sign, which is why the sign for the  $m^2$  term has become positive. It is straightforward to now evaluate the radial integral, to find

$$i\Sigma = i\frac{\bar{\lambda}m^2}{16\pi^2} \left[ \frac{2}{\epsilon} + 1 + \ln(4\pi) - \gamma_E - \ln\left(\frac{m^2}{\mu^2}\right) \right], \qquad (2.6.19)$$

where  $\gamma_E$  is the Euler-Mascheroni constant. We can see clearly that there is a divergent part  $\propto 1/\epsilon$ , a logarithmic term dependent on the renormalisation mass scale  $\mu$ , and a finite part.

We can finally write down the propagator, using the renormalised theory such that  $p^2 \to (1 + \delta_{\phi})p^2$ ,  $m^2 \to (1 + \delta_m)m_R^2$ , and  $\bar{\lambda} \to \bar{\lambda}_R$  to give us

$$i [D(p)]^{-1} = (1 + \delta_{\phi})p^{2} - (1 + \delta_{m})m_{R}^{2} + \frac{\bar{\lambda}_{R}m_{R}^{2}}{16\pi^{2}} \left[ \frac{2}{\epsilon} + 1 + \ln(4\pi) - \gamma_{E} - \ln\left(\frac{m_{R}^{2}}{\mu^{2}}\right) \right].$$
(2.6.20)

A finite propagator requires that the counterterms cancel out the divergences. In this specific case, this requires that

$$\delta_m = \frac{\bar{\lambda}_R}{8\pi^2} \frac{1}{\epsilon} + c \,, \tag{2.6.21}$$

where c is a finite constant which we are free to choose, and  $\delta_{\phi} = 0$  as there are no divergences proportional to  $p^2$ . In the Minimal Subtraction (MS) scheme c = 0, whereas in the modified MS scheme ( $\overline{\text{MS}}$ ) c absorbs the term proportional to  $(\ln(4\pi) - \gamma_E)$ .

Therefore, as  $Z_{\phi} = 1$  and thus  $m_R = m_B/\sqrt{1 + \delta_m}$ , we can expand the renormalised mass around the coupling  $\bar{\lambda}_R$  to find

$$m_R = m_B \left[ 1 - \frac{\bar{\lambda}_R}{32\pi^2} \left( \frac{2}{\epsilon} + \ln(4\pi) - \gamma_E \right) + \mathcal{O}(\bar{\lambda}_R^2) \right]. \tag{2.6.22}$$

This relation allows for the divergence to be absorbed into the bare mass m, and for  $m_R$  to remain finite. Thus we have renormalised our theory.

One issue is that, even after taking  $\epsilon \to 0$ , there is a logarithmic dependence of the self-energy on the scale  $\mu$ . Thus our renormalised theory and the quantities  $\{\phi_R, m_R^2, \lambda_R\}$  have a scale dependence. We must ensure that the bare parameters  $\{\phi_B, m_B^2, \lambda_B\}$  are scale invariant, which results in the condition

$$\frac{d\{\phi_B, m_B, \lambda_B\}}{d \ln \mu} = 0. {(2.6.23)}$$

This uniquely determines the dependence of the renormalised parameters on the renormalisation scale

$$\frac{d\{\phi_R, m_R^2, \lambda_R\}}{d \ln \mu} = \left\{ \frac{\gamma_\phi}{\phi_R}, \frac{\gamma_m}{m_R^2}, \beta_\lambda \right\} , \qquad (2.6.24)$$

giving us the Renormalisation Group Equations (RGEs) at 1-loop. The beta function<sup>1</sup> is defined as the RGE for the coupling  $\lambda$ , and the anomalous dimensions are  $\gamma_{\phi}$  and  $\gamma_{m}$ . The pre-factors ensure that  $\beta_{\lambda}$ ,  $\gamma_{\phi}$ ,  $\gamma_{m}$  have the same dimensionality. The RGEs can be solved with reference to an input scale  $\bar{\mu}$  to determine how couplings and masses vary at different energy scales. This is especially vital for this work, as in Chapter 5 we input masses measured at  $\mu = m_{Z}$  (the Z-pole) which is common for electroweak parameters, and use the beta functions/RGEs to run the parameters up to the relevant energy scale (labelled as  $\mu_{4}$  for our calculations).

<sup>&</sup>lt;sup>1</sup>Sometimes, the term 'beta functions' is used interchangeably with RGEs, although strictly they are defined for couplings only.

# 2.7 Beyond the Standard Model

While the SM has proven itself as a remarkably accurate and precise theory, there are many open questions left in fundamental physics. Some point to solutions that may extend the SM framework and continue to use the language of QFT, while other problems seem intractable with a QFT approach and require something new entirely. We summarise an inexhaustive list of open questions here, some of which are explored in this thesis.

Do the electroweak and strong forces unify at higher scales? Extensions to the SM such as supersymmetry, where SM fermions have bosonic supersymmetric partners and vice versa, lead to  $g_S$ , g, and g' beta functions that run them to the same value at a 'Grand Unified Theory' (GUT) scale of  $T \sim 10^{16}$  GeV, in the case of the Minimally Supersymmetric Standard Model (MSSM). A simple Lie group such as SU(5) or SO(10) could provide the gauge symmetry of the GUT, which then undergoes SSB to the SM gauge group. Yet the non-discovery of supersymmetric particles at the LHC brings doubt to the motivation behind GUTs.

Do all four fundamental forces unify in a theory of everything? At the Planck scale,  $T \sim M_{\rm Pl} \sim 10^{19}$  GeV, it is predicted that quantum effects from gravity become significant and a 'theory of everything' that places gravity in the same framework as the strong and electroweak forces becomes necessary. Efforts to form a theory of quantum gravity in QFT frameworks have proven futile due to the non-renormalisability of a spin 2 gauge tensor field [46], which is required for gravity.

What is dark matter? Cosmological and astrophysical observations make clear that most of the matter in the universe is not baryonic, does not interact electromagnetically, and through its gravitational attraction keeps galaxies together [12]. No particle in the SM accounts for this 'dark matter', yet some models suggest that it could be explained through composite objects such as primordial black holes. Fundamental particle solutions such as WIMPs [15] and axions [47] have been proposed.

What is dark energy? The expansion of the universe is accelerating [48, 49], and

there is a vacuum energy that is driving this expansion which cannot be explained by the SM (in fact, attempts to explain this through SM vacuum energy calculations have provided an infamous result that is wrong by 120 orders of magnitude). This dark energy  $\Lambda$  accounts for  $\sim 70\%$  of the mass-energy in the universe [50] and remains a mystery to this day.

What caused inflation? A model of rapid expansion in the very early universe, known as inflation, is required to explain cosmological observations that we explain further in Section 3.3.1. This is not explained through the SM and requires a hypothesised BSM particle called the 'inflaton'.

Is the Higgs vacuum metastable? The Higgs quartic coupling,  $\lambda$ , is predicted to run to a negative value for values of the Higgs scalar field  $h > 10^{11} \,\text{GeV}$  [51,52]. This could mean that the current Higgs vacuum is metastable and there could be a phase transition to the true vacuum of the theory in the deep future.

Why is there more matter than antimatter? Visible matter in the universe is baryonic and seemingly not anti-baryonic. If these were originally created in the same quantities then they would annihilate and lead to no matter in the universe. We explore this question further in Section 3.5.

Why do neutrinos have masses? Solar neutrinos are predicted to be electron neutrinos, yet only  $\frac{1}{3}$  of the neutrino flux has been observed to be  $\nu_e$  [32]. The rest are the muon and tau neutrinos  $\nu_{\mu}, \nu_{\tau}$ . Thus neutrinos change their flavour as they travel, in a phenomenon known as neutrino mixing. This means that they must experience time, and thus must have mass. As neutrino masses are relevant for this work, we provide a brief summary below.

#### 2.7.1 Neutrino Masses

Accounting for neutrino masses involves a minimal extension to the SM where either a Dirac-like mass term (from EWSB) or a Majorana mass term can be added.

Majorana fermions are described by the relation  $\psi^c = \mathcal{C}\bar{\psi}^T = \psi$ , where  $\mathcal{C}$  refers to the charge conjugation operation. Thus, Majorana fermions are their own antiparticles.

If we include both types of terms, our SM Lagrangian is modified with

$$\mathcal{L} \ni -\frac{1}{2}\bar{\nu}_L^c M_L \nu_L - \frac{1}{2}\bar{\nu}_R^c M_R \nu_R - \bar{\nu}_R M_D \nu_L + \text{h.c.}$$
 (2.7.1)

$$= -\frac{1}{2}\bar{\nu}^c M \nu + \text{h.c.}$$
 (2.7.2)

where the first two terms are Majorana mass terms and we have introduced the right-handed neutrinos  $\nu_R$ .  $M_L$ ,  $M_R$  are Majorana mass matrices and  $M_D$  is the Dirac mass matrix. In the illustrative case of one neutrino flavour, we write the vector  $\nu = (\nu_L, \nu_R^c)$  and find the neutrino mass matrix

$$M = \begin{pmatrix} m_L & m_D \\ m_D & m_R \end{pmatrix}, \tag{2.7.3}$$

where  $m_D$  is the Dirac mass that comes from EWSB, and  $m_{L,R,D}$  are scalars that have taken the place of the matrices  $M_{L,R,D}$ . Diagonalising M results in the matrix

$$M' = \begin{pmatrix} \frac{1}{2}(m_L + m_R) - \frac{1}{2}\sqrt{(m_L - m_R)^2 + 4m_D^2} & 0\\ 0 & \frac{1}{2}(m_L + m_R) + \frac{1}{2}\sqrt{(m_L - m_R)^2 + 4m_D^2} \end{pmatrix}$$

$$= \operatorname{diag}(m_1, m_2), \qquad (2.7.4)$$

resulting in us being left with two Majorana fermions after diagonalisation. For  $m_L = 0$ , which ensures that lepton number conservation cannot be violated by the left-handed Majorana mass term, and for  $m_R \gg m_D$ , we find that  $m_1 \approx m_D^2/m_R$ , and  $m_2 \approx m_R$ . Thus we have ended up with a situation where  $m_1 \ll m_2$  and is driven to be extremely light by the large mass of a RHN. As the bound on the sum of the neutrino masses requires them to be very light  $\sum_i m_{\nu,i} \leq 0.12 \,\text{eV}$  [50,53], this result provides motivation for the Seesaw mechanism which we explore further in Section 3.6.

<sup>&</sup>lt;sup>1</sup>Note that this upper bound comes from cosmological (CMB) observations. Terrestrial experiments provide a lower bound on the mass sum of  $\sum_i m_{\nu,i} \gtrsim 0.06 \, (0.1) \, \text{eV}$  for normal (inverted) ordering of the neutrino mass eigenstates [54, 55].

The diagonalisation procedure can be expressed through a matrix, U, by relating  $\nu_L^{\alpha} = \sum_i U_{\alpha i} \nu_i$ . This relates the mass basis  $\nu_i$ , with i = 1, 2, 3 to the flavour basis  $\nu_L^{\alpha}$  with  $\alpha = e, \mu, \tau$ . It is referred to as the Pontecorvo-Maki-Nakagawa-Sakata (PMNS) matrix and can be parametrised as [53]

$$U = \begin{pmatrix} 1 & 0 & 0 \\ 0 & c_{23} & s_{23} \\ 0 & -s_{23} & c_{23} \end{pmatrix} \begin{pmatrix} c_{13} & 0 & s_{13}e^{-i\delta} \\ 0 & 1 & 0 \\ -s_{13}e^{i\delta} & 0 & c_{13} \end{pmatrix} \begin{pmatrix} c_{12} & s_{12} & 0 \\ -s_{12} & c_{12} & 0 \\ 0 & 0 & 1 \end{pmatrix} \begin{pmatrix} e^{i\eta_{1}} & 0 & 0 \\ 0 & e^{i\eta_{2}} & 0 \\ 0 & 0 & 1 \end{pmatrix},$$

$$(2.7.5)$$

where  $\delta$  is the CP-violation phase,  $\eta_1$  and  $\eta_2$  are Majorana phases, and  $s_{ij} = \sin \theta_{ij}$ ,  $c_{ij} = \cos \theta_{ij}$  where  $\theta_{ij}$  are real angles.

# Chapter 3

# Early Universe Cosmology

Eä! Let these things Be! And I will send forth into the Void the Flame
Imperishable, and it shall be at the heart of the World, and the World shall Be.

from Ainulindalë by J.R.R. Tolkien

The early universe is an enigmatic time in our universe's history. As we go further back in time towards the Big Bang, the temperature starts to increase  $T \sim a^{-1}$ , where a is the scale factor of the universe (to be introduced later). With the universe getting hotter and smaller, high energy physics starts to gain an equal footing with cosmology, and it becomes imperative at energies approaching the Planck temperature  $T_{\rm Pl} = M_{\rm Pl} \approx 1.22 \times 10^{19} \, {\rm GeV}$  to utilise a theory of quantum gravity.

This work, fortunately, involves physics at temperatures far below  $T_{\rm Pl}$ . Yet, despite not requiring a quantum theory of gravity at these scales, there is still much we don't know about: where dark matter emerged from, the exact nature of the electroweak phase transition, and why there are more baryons than anti-baryons, to list a few unanswered questions. The research in this thesis touches on the latter two topics. Thus, this chapter aims to set the stage for these events: the early universe leading up to recombination.

# 3.1 General Relativity

The language that is used to describe cosmology is that of General Relativity [56]. Spacetime is described by a Riemannian manifold with metric  $g_{\mu\nu}$ . A useful quantity is the Riemann curvature tensor  $R^{\rho}_{\sigma\mu\nu}$  which describes the effect of parallel transporting a vector around a manifold, quantifying the curvature of the manifold. The Riemann curvature tensor is given by

$$R^{\rho}_{\sigma\mu\nu} = \partial_{\mu}\Gamma^{\rho}_{\nu\sigma} - \partial_{\nu}\Gamma^{\rho}_{\mu\sigma} + \Gamma^{\rho}_{\mu\lambda}\Gamma^{\lambda}_{\nu\sigma} - \Gamma^{\rho}_{\nu\lambda}\Gamma^{\lambda}_{\mu\sigma}, \qquad (3.1.1)$$

where the Christoffel symbols  $\Gamma^{\lambda}_{\mu\nu}$  are defined as

$$\Gamma^{\lambda}_{\mu\nu} = \frac{1}{2} g^{\lambda\rho} \left( \partial_{\mu} g_{\nu\rho} + \partial_{\nu} g_{\rho\mu} - \partial_{\rho} g_{\mu\nu} \right) . \tag{3.1.2}$$

The Ricci curvature tensor is defined through the contraction  $R_{\mu\nu} = R^{\rho}_{\mu\rho\nu}$ , and the Ricci scalar  $R = R^{\mu}_{\mu}$ .

We can then relate these quantities to the stress-energy tensor  $T_{\mu\nu}$  through the Einstein equation

$$G_{\mu\nu} \equiv R_{\mu\nu} - \frac{1}{2} R g_{\mu\nu} = 8\pi G T_{\mu\nu} ,$$
 (3.1.3)

which determines the dynamics of a manifold<sup>1</sup>. Here,  $G_{\mu\nu}$  is referred to as the Einstein tensor, and G is the gravitational constant.

It is possible to insert a cosmological constant  $\Lambda$  if the universe's expansion is accelerating, such that

$$G_{\mu\nu} + \Lambda g_{\mu\nu} = 8\pi G T_{\mu\nu} \,.$$
 (3.1.4)

# 3.2 Standard Model (of Cosmology)

Our Standard Model of Cosmology is the  $\Lambda$ CDM model, which describes the universe as having cold dark matter and dark energy  $\Lambda$  [58, 59]. It assumes that:

<sup>&</sup>lt;sup>1</sup>Wheeler summarised this equation as "Spacetime tells matter how to move; matter tells spacetime how to curve." [57], as  $T_{\mu\nu}$  involves the energy density and affects the dynamics of the manifold.

- The universe is homogeneous and isotropic, expanding in the same manner in all directions. This assumption is also known as the cosmological principle.
- Einstein's equation applies.
- The content of the universe can be approximated as a perfect fluid.

The perfect fluid assumption results in the stress energy tensor taking the form

$$T_{\mu\nu} = (\rho + p)U_{\mu}U_{\nu} + pg_{\mu\nu},$$
 (3.2.1)

where  $\rho$  is the energy density, p is the pressure, and  $U_{\mu}$  is the fluid velocity.

Spacetime is described by a manifold with the Friedmann-Lemaître-Robertson-Walker (FLRW) metric, given by

$$ds^{2} = g_{\mu\nu}dx^{\mu}dx^{\nu} = dt^{2} - a(t)^{2} \left(\frac{dr^{2}}{1 - kr^{2}} + r^{2}d\Omega^{2}\right)$$
(3.2.2)

where a(t) is the scale factor, which increases monotonically with t, k is a curvature constant, and  $d\Omega^2$  indicates the line element of a 2-sphere. As experiment has confirmed that the expansion of the universe is presently accelerating [48,49], the cosmological constant  $\Lambda$  is non-zero in this model and in Eq. 3.1.3.

We define the Hubble factor as

$$H(t) = \frac{\dot{a}}{a}.\tag{3.2.3}$$

The Hubble factor in the present day is denoted  $H_0$ . Observations of the CMB (under the  $\Lambda$ CDM assumption) by the Planck collaboration resulted in a value of  $H_0 \sim 67.4\pm0.5\,\mathrm{km\,s^{-1}Mpc^{-1}}$  [50], whereas the use of Type Ia supernovae as standard candles leads to a measurement independent of the  $\Lambda$ CDM model by the S $H_0$ ES collaboration of  $H_0 \sim 73.04\pm1.04\,\mathrm{km\,s^{-1}Mpc^{-1}}$  [60]. The incompatibility of these results is referred to as the Hubble tension and is an open question in cosmology, which we will not discuss further here.

By inserting the perfect fluid form of  $T_{\mu\nu}$  and the FLRW metric into the Eq. 3.1.3,

Energy Type	w	$\rho(a)$	a(t)
Radiation	$\frac{1}{3}$	$\propto a^{-4}$	$\propto t^{\frac{1}{2}}$
Matter	0	$\propto a^{-3}$	$\propto t^{\frac{2}{3}}$
Dark energy	-1	constant	$e^{Ht}$

Table 3.1: EOS parameter w, energy density  $\rho(a)$  and scale factor a(t) scaling for various types of energy.

we arrive at the Friedmann equations,

$$H^{2} = \frac{8\pi G}{3}\rho - \frac{k}{a^{2}} + \frac{\Lambda}{3}, \qquad (3.2.4)$$

$$\frac{\ddot{a}}{a} = -\frac{4\pi}{3}(\rho + 3p) + \frac{\Lambda}{3}.$$
 (3.2.5)

The conservation of stress energy  $\nabla_{\mu}T^{\mu\nu} = 0$ , assuming a perfect fluid form of  $T_{\mu\nu}$  as in Eq. 3.2.1, can be re-expressed as the conservation of comoving energy,

$$\dot{\rho} = -3H(\rho + p) = -3H\rho(1+w) \tag{3.2.6}$$

where  $w=p/\rho$  is the equation of state (EOS) parameter.

We can solve Eq. 3.2.6 to find

$$\rho \propto a^{-3(1+w)} \,.$$
(3.2.7)

For the time evolution of the scale factor a(t), we can now solve Eq. 3.2.4 to find

$$a(t) \propto t^{\frac{2}{3(1+w)}}$$
 (3.2.8)

In Table 3.1 we list how the energy density and scale factor scale with respect to each other, and t, for various types of energy. Radiation is defined as any relativistic mass-energy, whereas matter is specifically non-relativistic matter.

Using the Eq.3.2.4, we can define the critical density (when k=0 and  $\Lambda=0$ ) to be,

$$\rho_c = \frac{3H^2}{8\pi G},\tag{3.2.9}$$

 $<sup>^{1}\</sup>nabla_{\mu}$  refers to the covariant derivative on the manifold,  $\Delta_{\lambda}T^{\mu\nu} = \partial_{\lambda}T^{\mu\nu} + \Gamma^{\mu}_{\lambda\sigma}T^{\sigma\nu} + \Gamma^{\nu}_{\lambda\sigma}T^{\mu\sigma}$ .

which allows us to define a fractional energy density parameter

$$\Omega_i = \frac{\rho_i}{\rho_c} \tag{3.2.10}$$

for different types of energy density  $\rho_i$ . Thus, we can define  $\Omega_k = \Omega_{\text{tot}} - 1$ , where  $\Omega_k$  is the adjustment to the energy density fraction taking into account the curvature constant k.

With cosmological observations, we find that, today,

$$\Omega_{tot} = \Omega_{\gamma} + \Omega_m + \Omega_{\Lambda} + \Omega_k \,, \tag{3.2.11}$$

where the energy density of radiation is  $\Omega_{\gamma} \sim 5 \times 10^{-5}$ , the energy density of matter is  $\Omega_m \sim 0.3$ , the energy density of dark energy is  $\Omega_{\Lambda} \sim 0.7$  and  $\Omega_k \sim 0$  indicating a flat universe [61]. Thus most of the energy content today is that of dark energy, meaning that the expansion of the universe is accelerating exponentially.

As the energy density relationships in Table 3.1 show, it is evident that earlier in the universe we had a period of matter domination, and at very early times we had the era of radiation domination. As a result, the radiation domination assumption is used throughout this thesis to define the Hubble parameter, energy density evolution, and temperature evolution.

Observations find that the baryon density fraction  $\Omega_b \sim 0.05 < \Omega_m$ , implying that the majority of the matter energy density is unaccounted for. The remaining energy density is referred to as 'cold dark matter', with cold referring to the fact that it is non-relativistic. Thus we complete our brief review of the  $\Lambda$ CDM model.

# 3.3 Timeline of the Early Universe

Under our current understanding, the universe began with a hot Big Bang, expanding rapidly in all directions. For the purposes of this thesis, it is not necessary to discuss the early part of the Planck epoch, when quantum gravitational effects dominated. We skip forward to the period of inflation.

### 3.3.1 Inflation

Inflation was first proposed by Guth [62] to tackle the horizon and flatness problems in standard cosmology. Much of this review can be found in the inflation section of Ref. [33].

#### Horizon problem

The horizon problem stemmed from the fact that the Hubble horizon at the time of recombination  $H(t_{\rm rec})^{-1}$  was much smaller than we would otherwise assume by rescaling our Hubble horizon today. Using the redshift  $z=a_0/a-1$  where  $a_0$  is the scale factor today, we arrive at  $H_0^{-1}/z_{\rm rec}$  which is the size of the present day observable universe rescaled to the time of recombination using the Hubble expansion.

Taking the ratio of the circumference of our observable universe scaled to  $t_{\rm rec}$ , to the diameter of the actual observable universe at  $t_{\rm rec}$ , we arrive at a value of  $\sim 100$ , meaning there were 100 causally disconnected zones at that surface of last scattering. This would imply that these regions would not be able to thermalise, yet the Cosmic Microwave Background (CMB) that was emitted at recombination is isotropic to 1 part in  $10^5$  [33]. Thus we arrive at the horizon problem: how was the universe able to thermalise across these seemingly disconnected zones?

#### Flatness problem

As the contribution of curvature to the energy density of the universe can be expressed as  $\Omega_k$ , we can also give it an effective EOS parameter which we can calculate as w = -1/3. With this, we see that the energy density of curvature scales as  $a^{-2}$ . Referring to Table 3.1, this would imply that an era of curvature domination would appear after matter domination, and before the current era of dark energy domination.

<sup>&</sup>lt;sup>1</sup>See Section 3.3.4 for more detail.

Yet by looking at our cosmological history and through observation, we find that k is so close to zero that this period never occurred.

We can quantify this fine tuning problem by rearranging and differentiating Eq. 3.2.4 to give us,

$$\frac{d\Omega_{\text{tot}}}{da} = (1+3w)\frac{\Omega_{\text{tot}}(\Omega_{\text{tot}}-1)}{a},$$
(3.3.1)

which describes the evolution of the total fractional energy density  $\Omega_{\text{tot}}$ . If  $\Omega_{\text{tot}}(t = 0) = 1$ , then  $\Omega_{\text{tot}}$  would remain at that value until today. If it is larger, then due to the period of radiation and matter domination resulting in w > -1/3,  $\Omega_{\text{tot}}$  would be driven up. If it is smaller, then  $\Omega_{\text{tot}}$  would be driven to 0. What this means is that a small variance  $|\rho_{\text{tot}} - \rho_c| > 0$  results in the universe either exponentially expanding or collapsing, and the universe no longer being flat with k = 0.

For the universe to appear flat, at least until today, requires this initial variance to have an upper bound of  $(1 - \Omega_{\text{tot}}(t=0)) < 10^{-60}$ ; a remarkable degree of fine tuning [63]. This is the flatness problem.

#### Slow roll inflation

We assume a scalar field known as the inflaton  $\sigma$  drives inflation, with a potential  $V(\sigma)$  [33]. The equation of motion for a scalar field in an expanding flat universe is given by

$$\ddot{\sigma} + 3\frac{\dot{a}}{a}\dot{\sigma} + V'(\sigma) = 0. \tag{3.3.2}$$

The energy density and pressure are given by

$$\rho_{\sigma} = \frac{1}{2}\dot{\sigma}^2 + V(\sigma), \qquad (3.3.3)$$

$$p_{\sigma} = \frac{1}{2}\dot{\sigma}^2 - V(\sigma), \qquad (3.3.4)$$

and thus the first Friedmann equation gives

$$H^{2} = \frac{8\pi G}{3} \left( \frac{1}{2} \dot{\sigma}^{2} + V(\sigma) \right) . \tag{3.3.5}$$

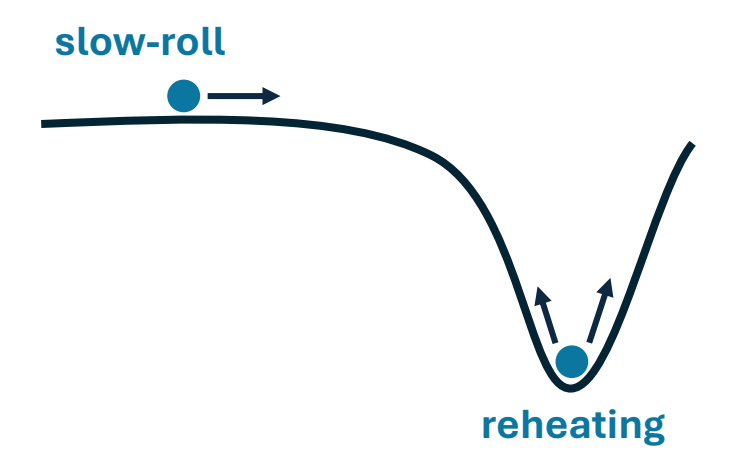


Figure 3.1: The inflaton in its potential, slowly rolling towards the minimum. At the minimum, it behaves like a simple harmonic oscillator and this results in the reheating of the universe.

We see that if  $V(\sigma) \gg \dot{\phi}^2$ , then  $p_{\sigma} \approx -p_{\sigma}$  and thus the EOS parameter for the inflaton is  $w \approx -1$ , just like dark energy. Thus, as shown in Table 3.1, the inflaton would cause exponential expansion of the universe while these assumptions remained valid. Further, Eq. 3.3.1 shows us that as a universe filled with the inflaton would have (1+3w) < 0, resulting in  $\Omega_{\rm tot}$  being driven towards unity, and thus inflation would act to 'flatten' the universe.

Thus we make the slow roll approximation, assuming that the field  $\sigma$  is in a region where the potential is close to flat, thus it is 'slowly rolling' (as shown in Fig. 3.1) and we can assume  $\ddot{\sigma} \approx 0$  and  $\dot{\sigma} \ll V(\sigma)$ . The slow roll approximation remains valid when the slow roll parameters  $|\eta|, |\epsilon| \ll 1$ , where

$$\eta = m_{\rm Pl}^2 \frac{V''}{V},$$
(3.3.6)

$$\epsilon = \frac{m_{\rm Pl}^2}{2} \left(\frac{V'}{V}\right)^2 \,, \tag{3.3.7}$$

where  $m_{\rm Pl}=(8\pi G)^{-1/2}$  is the reduced Planck mass.<sup>1</sup> We find that Eqs. 3.3.2 and 3.3.5 now give

$$3H\dot{\sigma} \approx -V'(\sigma)\,,\tag{3.3.8}$$

In this thesis, we use the capitalised  $M_{\rm Pl}=G^{-1/2}$  to refer to the normal Planck mass.

$$H^2 \approx \frac{8\pi G}{3} V(\sigma) \,. \tag{3.3.9}$$

We can integrate the first Friedmann equation to find

$$a \sim e^{\int Hdt} = e^N, \tag{3.3.10}$$

where  $H \approx \sqrt{8\pi G V(\sigma)/3}$ , and N is the number of e-foldings. We see here that, as  $\rho_k \propto a^{-2}$ , inflation aggressively dilutes away the curvature as predicted, solving the flatness problem. The horizon problem is also solved as it explains that seemingly causally disconnected regions of spacetime were in fact causally connected. It is estimated that these issues could be solved with inflation lasting for  $N \sim 60$  e-folds [33].

Inflation also provides answers for other questions. The phase transitions of Grand Unified Theories (GUTs), which unify the strong and electroweak forces, are predicted to give rise to a high density of magnetic monopoles in the universe [53,64,65]. The GUT phase transition taking place prior to inflation would mean that these magnetic monopoles are aggressively diluted away, explaining why we do not see them today. Inflation also gifts us an explanation for large scale structure. Our observable universe seems to have galaxies clustering in superclusters, like how our own galaxy, the Milky Way, is situated with other galaxies in the Laniakea supercluster [66]. Conversely, regions with a relative underdensity of galaxies such as the Boötes Void exist [67]. Quantum fluctuations in the inflaton field could have been magnified by inflation, seeding the large scale structure that we observe in the universe today [68].

#### Reheating

If inflation causes a rapid exponential expansion of the universe, driving  $\rho_k \to 0$ , then what about matter and radiation which should also be diluted away? How do we end up in a universe that has something rather than nothing?

This is answered by reheating, which signifies the end of inflation. As the inflaton field  $\sigma$  approaches the minimum of the potential  $V(\sigma)$ ,  $\ddot{\sigma}$  becomes too large causing

the slow roll approximation to no longer hold. Instead, we can ignore the  $3H\dot{\sigma}$  term in Eq. 3.3.2 to find  $\ddot{\sigma} \approx -V'(\sigma)$ , which means that the inflaton field behaves like a simple harmonic oscillator around the minimum of the potential, as depicted in Fig. 3.1.

The energy of these oscillations is eventually dumped into the SM (or BSM) sector(s) of the universe, due to model-dependent couplings of the inflaton to SM (BSM) fields. Thus, the universe is filled with matter and radiation once again through inflaton decay. Couplings between these fields can result in elastic scattering and number changing interactions, giving rise to a universe filled with a SM (BSM) sector(s) at a reheating temperature  $T_R$ .

Reheating can only occur when the Hubble expansion rate drops below the inflaton decay rate  $\Gamma$ . The first Friedmann equation tells us that  $H \sim \sqrt{\rho}/M_{\rm Pl}$ . During radiation domination,  $\rho \propto a^{-4}$ , and  $T \propto a^{-1}$ . Thus, we find that the reheating temperature is given by

$$T_R \approx \sqrt{\Gamma M_{\rm Pl}}$$
. (3.3.11)

### 3.3.2 Electroweak Phase Transition

After inflation, the universe undergoes a phase transition where the Higgs takes a vev, fermions acquire mass, and the electroweak symmetry is broken from  $SU(2)_L \times U(1)_Y \to U(1)_{EM}$ . This transition is known as the electroweak phase transition (EWPT). The events pertaining to this work take place in the period between reheating and the end of the EWPT.

Lattice calculations suggest that in the SM, the EWPT is a crossover [26, 27] that takes place at  $T \approx 160\,\text{GeV}$  [28]. A crossover is a smooth transition with no discontinuities in the order parameter which quantifies the state the system is in. For the EWPT, we use the Higgs vev  $\langle \Phi \rangle$  as the order parameter, and thus  $\langle \Phi \rangle (T, x^{\mu})$  is a continuous thermal function of spacetime.

This contrasts with a first order phase transition, where there are discontinuities

in  $\langle \Phi \rangle (T, x^{\mu})$ . BSM additions such as an extra singlet [69–75] or a second Higgs doublet [76–79] open up regions of parameter space with first order phase transitions.

Study of a potential first order EWPT is motivated by a variety of factors: it could provide the out of equilibrium conditions for baryogenesis, which we discuss in Section 3.5, and it could result in a gravitational wave signal that could be detected by space based interferometers such as LISA, which we discuss in Section 3.8.

The EWPT is then followed by the QCD phase transition at  $T \sim 200 \,\text{MeV}$ , when quarks and gluons become confined in mesons and baryons (such as protons and neutrons).

### 3.3.3 Big Bang Nucleosynthesis

After QCD confinement, and at around  $T \sim 0.1 \,\text{MeV}$ , protons (referred to as p, or sometimes in this context as  $^1\text{H}$ ) and neutrons n fuse together to form nuclei of deuterium d (or  $^2\text{H}$ ),  $^4\text{He}$ , and  $^7\text{Li}$  in appreciable quantities. This process is referred to as Big Bang Nucleosynthesis (BBN).

In order for the heavier nuclei to form, deuterons are a vital ingredient which can only exist via the reaction [80]

$$p + n \to d + \gamma \,, \tag{3.3.12}$$

which is initially in equilibrium. The equilibrium abundance of deuterons depends on the abundance of high energy photons. If they have more energy than the binding energy of the deuterons, which is  $E_d \approx 2.2 \,\mathrm{MeV}$  [81], they can photodisintegrate the deuterons back into protons and neutrons.

Using the Maxwell-Boltzmann distribution, we can approximate the number of proportion of photons that have  $E > E_d$  as

$$N_{E(\gamma)>E_d} = n_{\gamma}e^{-E_d/T}$$
 (3.3.13)

where  $n_{\gamma}$  is the number density of photons. As, in equilibrium,  $n_d n_{\gamma} = n_p n_n$ , the

ratio of deuterons to all nucleons is thus  $n_d/n_B \propto \eta_B e^{E_d/T}$ , where

$$\eta_B = \frac{n_B}{n_\gamma} \,. \tag{3.3.14}$$

Here,  $n_B$  refers to the number density of baryons/nucleons, thus  $\eta_B$  is the baryon to photon ratio, a parameter of vital relevance to this thesis, as we will see in Section 3.5.

Thus, BBN can only proceed once the temperature drops enough such that these high energy photons are not abundant, and the deuteron abundance can become significant, which happens at  $T \sim 0.1 \,\text{MeV}$ .

Through this, we see that the BBN-produced abundances of the Hydrogen, Helium and Lithium nuclei depend on the parameter  $\eta_B$ . In order for these abundances to line up with observation,  $\eta_B \sim \mathcal{O}(10^{-10})$  [80]. The current BBN based measurement of the BAU is  $\eta_B = (6.07732 \pm 0.15070) \times 10^{-10}$  [82].

### 3.3.4 Recombination

The period known as the early universe is typically held to end at recombination, when the universe cooled down enough to allow nuclei and electrons to coalesce and form neutral atoms. Prior to this, the universe was opaque to light due to photons Compton scattering with the free electrons and nuclei. The sudden transparency at the onset of recombination allowed for photons to finally travel freely.

The recombination reaction is

$$p + e^- \to H + \gamma. \tag{3.3.15}$$

A rough calculation of the recombination temperature  $T_{\rm rec}$  is presented as follows: as with the deuteron production reaction in Section 3.3.3, we require the proportion of high energy photons with  $E > E_0$ , where  $E_0 = 13.6 \,\text{eV}$  is the Hydrogen ionisation energy, to fall sufficiently. Thus, using the equilibrium condition  $n_p n_e = n_H n_\gamma$ , and the Boltzmann distribution to approximate the photon density, we find

$$\frac{x_e^2}{1+x_e} \approx (n_p + n_H)^{-1} n_\gamma e^{-E_0/T} , \qquad (3.3.16)$$

where  $x_e = n_e/(n_p + n_H)$  is the free electron fraction. As protons form the majority of baryons in the universe, we can take  $(n_p + n_H) \approx n_B$  and thus

$$\frac{x_e^2}{1+x_e} \approx \eta_B^{-1} e^{-E_0/T} \,. \tag{3.3.17}$$

Solving for a free electron fraction of  $x_e = 0.5$  and taking  $\eta \sim \mathcal{O}(10^{-10})$  gives us  $T_{\rm rec} \sim E_0/(10 \ln(10)) \approx 0.6 \,\mathrm{eV}$ , close to the observed  $T_{\rm rec} \approx 0.26 \,\mathrm{eV}$  [33].

This signal, released at a relatively late time of  $t \approx 380,000$  years, is the furthest we can look back into our universe's history through optical means. It is known as the Cosmic Microwave Background (CMB), due to the redshifting of the light into the microwave spectrum in the present day.

The CMB provides us with an independent measurement of  $\eta_B$  as the vast majority of free photons in the universe are CMB photons. The temperature of the CMB is 2.7 K, which gives us the number density of photons  $n_{\gamma}$ . We can then calculate  $\eta_B = (6.12 \pm 0.04) \times 10^{-10}$  [53], which is in remarkable agreement with the BBN based estimate.

While the electromagnetic spectrum can only provide the CMB as the earliest signal, the gravitational spectrum may provide us a glimpse far beyond the opaque fog that exists at recombination. Gravitational waves, which may have travelled from the electroweak era at  $T \gtrsim 100\,\text{GeV}$  and are practically unaffected by the opaque plasma, may be detectable with gravitational wave interferometers and tell us a lot about our early universe. We expand on this in Section 3.8.

### 3.4 Thermal Statistics

Before we proceed to discuss baryogenesis and leptogenesis, we give a brief summary of core concepts in thermal statistical mechanics. When a sector (a group of particles) is able to exchange energy quickly, it can be described by a single temperature T. Fast energy exchange depends on the elastic scattering interaction rate  $\Gamma_S > H$ . In this scenario, the sector is referred to as being in kinetic equilibrium.

If the sector also has fast number-changing interactions  $\Gamma_{\Delta N} > H$ , and thus is able to freely adjust the number of particles, then it also is in chemical equilibrium.

The combination of kinetic and chemical equilibrium is referred to in the literature as thermal equilibrium. We can define a phase space distribution for a sector in thermal equilibrium as

$$f_{\rm eq}(p) = \frac{1}{e^{(E(\mathbf{p})-\mu)/T} \pm 1},$$
 (3.4.1)

where for fermions the Fermi-Dirac distribution is given by the plus sign, and for bosons the Bose-Einstein distribution is given by the minus sign. The chemical potential  $\mu$  can be neglected in the early universe as  $|\mu| \ll T$  [83]. The energy of a particle is given by  $E(\mathbf{p}) = \sqrt{m^2 + \mathbf{p}^2}$ .

If chemical equilibrium doesn't hold and there is only kinetic equilibrium, then the phase space distribution is modified by

$$f(p) = \frac{n}{n_{\text{eq}}} f_{\text{eq}}(p),$$
 (3.4.2)

where n is the actual number density, and  $n_{\rm eq}$  is the equilibrium number density.

The number density, energy density, and pressure of a particle species i is given by [63],

$$n_i = \frac{g_i}{(2\pi)^3} \int f_i(\mathbf{p}) d^3 \mathbf{p},$$
 (3.4.3)

$$\rho_i = \frac{g_i}{(2\pi)^3} \int E(\mathbf{p}) f_i(\mathbf{p}) d^3 \mathbf{p}, \qquad (3.4.4)$$

$$p_i = \frac{g_i}{(2\pi)^3} \int \frac{|\mathbf{p}|^2}{3E(\mathbf{p})} f_i(\mathbf{p}) d^3 \mathbf{p}, \qquad (3.4.5)$$

where  $g_i$  are the number of degrees of freedom. The entropy for a particle species is

given by,

$$s = \frac{\rho + p}{T} \,, \tag{3.4.6}$$

whereas the Hubble rate is derived from Eq. 3.2.4 to be

$$H = \sqrt{\frac{8\pi G}{3}\rho} \,. \tag{3.4.7}$$

## 3.4.1 Relativistic Dynamics

In the relativistic limit, where  $T \gg m$ , we find that the number densities are given by:

$$n_i = \begin{cases} \frac{\zeta(3)}{\pi^2} g_i T^3 & \text{(bosons)}, \\ \left(\frac{3}{4}\right) \frac{\zeta(3)}{\pi^2} g_i T^3 & \text{(fermions)}, \end{cases}$$
(3.4.8)

the energy densities are given by:

$$\rho_i = \begin{cases} \frac{\pi^2}{30} g_i T^4 & \text{(bosons)}, \\ \left(\frac{7}{8}\right) \frac{\pi^2}{30} g_i T^4 & \text{(fermions)}, \end{cases}$$
(3.4.9)

and the pressures are given by  $p_i = \rho_i/3$  as the EOS parameter is w = 1/3 for radiation.

# 3.4.2 Non-Relativistic Dynamics

In the non-relativistic limit, where  $T \ll m$ , the exponential part of  $f_{\rm eq}(\mathbf{p})$  dominates over the  $\pm 1$  term, giving us the Maxwell-Boltzmann distribution

$$f_{\rm MB}(\mathbf{p}) = e^{-E(\mathbf{p})/T},$$
 (3.4.10)

which neglects quantum statistics. This gives the non-relativistic limits of [63]

$$n_i = g_i \left(\frac{m_i T}{2\pi}\right)^{3/2} e^{-m_i/T},$$
 (3.4.11)

$$\rho_i = m_i n_i \,, \tag{3.4.12}$$

$$p_i = n_i T \ll \rho_i \,. \tag{3.4.13}$$

During the era of radiation domination, which is the era that the work in this thesis is set in, the non-relativistic contributions to the Hubble expansion in Eq. 3.4.7 can be neglected.

The contribution of the relativistic degrees of freedom to the Hubble expansion in this era allows us to define the effective relativistic degrees of freedom,

$$g^* = \sum_{b} g_b + \frac{7}{8} \sum_{f} g_f, \qquad (3.4.14)$$

where we sum over b bosons and f fermions that are relativistic. When all particles in the SM are relativistic,  $g^* = 106.75$ , and this drops as degrees of freedom become non-relativistic.

# 3.5 Baryogenesis

We turn our attention to  $\eta_B$ , the baryon-to-photon ratio which we have discussed in previous sections. However, we did not discuss the fate of the anti-baryons, or antimatter more generally. What happened to the antimatter in the universe?

Observations in our solar system show that antimatter cannot exist in the present day in appreciable quantities [84]<sup>1</sup> as they would annihilate with the solar wind and provide a gamma ray signal. If entire stellar systems are composed of antimatter, their fraction in our galaxy must be less than  $10^{-4}$  [84–87]. If large scale regions in the universe existed that consisted entirely of antimatter, we would see gamma rays being emitted at the domain walls separating these region. The constraints on these observations show that these regions would have to be as large as the observable universe [85,88,89]. Thus, the evidence points to there existing a baryon asymmetry of the universe (BAU); the process that creates this asymmetry is referred to as baryogenesis. As inflation is likely to dilute away any baryon asymmetry, we know that baryogenesis must occur after inflation.

<sup>&</sup>lt;sup>1</sup>Except from those that form in trace amounts from various astrophysical events.

Due to the approximate C symmetry of the SM, we can assume that baryons and antibaryons were produced in almost equal quantities at the beginning of the universe. The baryons and anti-baryons would then annihilate, producing copious quantities of photons, until only the surplus baryons are left in the universe.

Thus, the BAU is given by

$$\eta_B = \frac{n_B - n_{\bar{B}}}{n_{\gamma}} \,, \tag{3.5.1}$$

where these quantities refer to the number densities of the baryons and anti-baryons. As anti-baryons have not survived until today, this corresponds to the present baryon-to-photon ratio we discussed in the previous section, which is why we employ the same notation.

### 3.5.1 Sakharov Conditions

As the surplus baryons make up the non-dark matter content of the universe today, the BAU is responsible for the very existence of humanity and also the large scale structure of the universe. This significance motivates us to explore the question of its origin. Sakharov's conditions are necessary and sufficient to give rise to a BAU, and they are given by [90]:

1. Baryon number (B) violation, i.e. processes such as

$$X \to B + Y \tag{3.5.2}$$

exist,

2. C and CP violation, i.e. the rates

$$\Gamma(X \to B + Y) \neq \Gamma(\bar{X} \to \bar{B} + \bar{Y}),$$
 (3.5.3)

3. Out-of-equilibrium conditions, such that

$$\Gamma(X \to B + Y) \neq \Gamma(B + Y \to X)$$
. (3.5.4)

## 3.5.2 Electroweak Baryogenesis

B violation exists in the SM through sphaleron processes, which we will elaborate on in a moment. C and CP violation also exist in the minimally extended SM as there is a small amount of CP violation sourced by the CKM and PMNS matrices. Combined with the P violation in the weak interaction, this leads to a C violation. Departure from equilibrium is trickier. While equilibrium conditions are violated through the expansion of the universe, this departure seems to be too weak to source a BAU [85]. This motivates study of a first order phase transition (see Section 3.8) as it could provide the out-of-equilibrium conditions at the bubble walls that are necessary for the BAU to be produced. Such models are referred to as electroweak baryogenesis, as the Sakharov conditions are satisfied at the electroweak scale.

#### **Sphalerons**

We return now to sphalerons. We see that we can define a global  $U(1)_B$  symmetry that rotates the phases of all quarks in the SM, as  $Q_L \to e^{i\theta/3}Q_L$ .<sup>1</sup> We can define a similar  $U(1)_L$  symmetry for the leptons. Associated with these symmetries are the classically conserved currents  $j_B^{\mu}$  and  $j_L^{\mu}$ . The baryonic current is [91–95],

$$j_B^{\mu} = \frac{1}{3} \sum_{f} \left( \bar{Q}_L^f \gamma^{\mu} Q_L^f + \bar{u}_R^f \gamma^{\mu} u_R^f + \bar{d}_R^f \gamma^{\mu} d_R^f \right) , \qquad (3.5.5)$$

where f is a sum over all the generations. As the current is conserved,  $\partial_{\mu}j_{B}^{\mu} = \partial_{\mu}j_{L}^{\mu} = 0$ . However, this doesn't hold at the quantum level. Due to loop corrections, we find that [85, 95]

$$\partial_{\mu} j_{B}^{\mu} = \partial_{\mu} j_{L}^{\mu} = \frac{n_{f}}{32\pi^{2}} \left( -2g^{2} \operatorname{Tr} \left( W_{\mu\nu} \widetilde{W}^{\mu\nu} \right) + g^{2} F_{\mu\nu} \widetilde{F}^{\mu\nu} \right)$$
(3.5.6)

where  $n_f = 3$  is the number of quark generations,  $\widetilde{W}^{\mu\nu} = \epsilon^{\mu\nu\alpha\beta}W_{\alpha\beta}$ , and likewise for  $\widetilde{F}^{\mu\nu}$ .

For the bosonic electroweak sector, there are infinite field configurations (vacua)

<sup>&</sup>lt;sup>1</sup>The 1/3 factor in the exponential is present as a quark contributes 1/3 of baryon number.

that minimise the energy functional. These vacua are distinguished by the Chern-Simons number  $N_{\rm CS}$  [85]. As the fermionic energy of a configuration depends on the bosonic background through coupling, the change of  $N_{\rm CS}$  results in the creation of fermions out of the background fields. Thus, processes that change baryon number are made possible by the transitions between these vacua [96,97]. These vacua have barriers between them, characterised by the sphaleron energy  $E_{\rm sph} \sim m_W/\alpha_W$ . The sphaleron is defined as the field configuration that gives the maximal energy along the path of least action between the two vacua, or in simple terms, the point at the 'top of the hill' between the valleys [85,98].

As we see that  $\partial_{\mu}(j_B^{\mu} - j_L^{\mu}) = 0$ , the sphaleron processes preserve B - L but violate B + L. B (and L the lepton number) are also violated individually. This violation can be quantified by [99]

$$\Delta(B+L) = 2N_f \Delta N_{\rm CS} \,, \tag{3.5.7}$$

where  $\Delta N_{\rm CS}$  is the change in  $N_{\rm CS}$  across different vacua. As  $g' = g \tan(\theta_W)$ ,  $g' \ll g$ , sphaleron processes only involve  $SU(2)_L$  doublets at leading order. This means that  $\Delta B = \Delta L = 3$  processes such as

$$\bar{\nu}_e \bar{\nu}_\mu \bar{\nu}_\tau \to u_L d_L d_L c_L b_L d_L t_L b_L b_L \tag{3.5.8}$$

are possible [94]. By balancing the chemical potentials of ingoing and outgoing particles for a rapid sphaleron process, we can derive a relation between the B asymmetry and the B-L asymmetry, given by [100]

$$B = \frac{8n_f + 4n_h}{22n_f + 13n_h} (B - L), \tag{3.5.9}$$

where  $n_f$  is once again the number of quark/lepton generations, and  $n_h$  is the number of Higgs doublets. For the Standard Model with  $n_f = 3$  and  $n_h = 1$ , we arrive at a sphaleron conversion factor of  $a_{\rm sph} = 28/79$ . Sphaleron transitions occur at a rate [94]

$$\Gamma_{\rm sph} \propto e^{-E_{\rm sph}(T)/T}$$
, (3.5.10)

which is only larger than the Hubble expansion prior to EWSB. Thus, sphalerons are exponentially suppressed and effectively shut off after the EWPT. This means that the B violation condition is no longer satisfied afterwards, and models of baryogenesis that depend on this must source the BAU prior to or during the EWPT.

# 3.6 Leptogenesis

As sphaleron processes active above the EWPT can convert a lepton asymmetry into a baryon asymmetry, it is possible to transform the question of 'where does the baryon asymmetry come from?' to 'where does the lepton asymmetry come from?'. Motivation for this comes from the fact that the CP violation in the CKM matrix alone is too weak to source the BAU [94, 101], incentivising a study of the PMNS matrix and the lepton sector as a source for sufficient CP violation. Such models are referred to as leptogenesis models, and were first proposed by Fukugita and Yanagida [29].

In leptogenesis, a heavy Majorana right handed neutrino (RHN) decays out of equilibrium into the Higgs and a light left handed neutrino. This out of equilibrium decay seeds a lepton asymmetry (specifically a B-L asymmetry) that is then converted to a baryon asymmetry through sphaleron processes [102–104].

# 3.6.1 Type I Seesaw

The model used for this interaction is typically the Type I Seesaw mechanism, which was introduced as a model for why the SM neutrinos are so light [105–108]. Incidentally, the GUT scale RHNs and their CP violating interactions introduced by the model naturally lead to leptogenesis.

The Type I Seesaw Lagrangian supplements the SM with the terms that we provide later in Eq. 4.1.1. We find the Yukawa term sources the decays  $N \to \bar{\Phi} + L (\Phi + \bar{L})$ . Individually, these are CP-violating as they are  $\Delta L = 1 (-1)$  processes. If these

decays happen at different rates and leptons are created more than anti-leptons, and if the decays happen out of equilibrium such that the inverse decays are slower than the decays, then we can seed a lepton asymmetry.

The seesaw formula provides the relation between the RHN mass matrix  $M_N$  and the light neutrino mass matrix  $M_{\nu}$  at tree level,

$$M_{\nu} \approx v^2 Y^T M_N^{-1} Y \,, \tag{3.6.1}$$

where Y is the Yukawa matrix in Eq. 4.1.1 and v is the Higgs vev. Thus, we see the origin of the moniker of this model; just like with a seesaw, the heaviness of  $M_N$ makes  $M_{\nu}$  much lighter. Leptogenesis therefore provides an elegant solution to the BAU as well as light neutrino masses.

## 3.6.2 Boltzmann Equations

In the Casas-Ibarra parametrisation of the Yukawa matrix [109],  $Y = \frac{1}{v}U\sqrt{M_{\nu}}R^{T}\sqrt{M_{N}}$ , where  $v = 174 \,\text{GeV}$  is the vacuum expectation value of the Higgs,  $^{1}U$  is the leptonic mixing matrix,  $M_{\nu}$  ( $M_{N}$ ) is the diagonal light (heavy) neutrino mass matrix and R is a complex, orthogonal matrix given by

$$R = \begin{pmatrix} 1 & 0 & 0 \\ 0 & \cos \omega_1 & \sin \omega_1 \\ 0 & -\sin \omega_1 & \cos \omega_1 \end{pmatrix} \begin{pmatrix} \cos \omega_2 & 0 & \sin \omega_2 \\ 0 & 1 & 0 \\ -\sin \omega_2 & 0 & \cos \omega_2 \end{pmatrix} \begin{pmatrix} \cos \omega_3 & \sin \omega_3 & 0 \\ -\sin \omega_3 & \cos \omega_3 & 0 \\ 0 & 0 & 1 \end{pmatrix}, (3.6.2)$$

where the  $\omega_i = x_i + iy_i$  are complex angles. We see that typically a heavier RHN gives a heavier Yukawa coupling with the SM sector. This means that, assuming a mass hierarchy where  $m_{N_2}, m_{N_3} \gg m_{N_1}$ , the heavier RHNs would be coupled more strongly to the SM and thus their decays would not deviate from equilibrium as much as  $N_1$ . Thus in vanilla leptogenesis models the dominant contribution to the B-L asymmetry comes from the out-of-equilibrium decays of the lightest RHN,  $N_1$ . These typically decay around a temperature of  $T \sim m_{N_1}$ .

<sup>&</sup>lt;sup>1</sup>Note that this definition has absorbed the  $1/\sqrt{2}$  into v.

To illustrate vanilla leptogenesis, we derive differential equations to track the number densities of the system, known as Boltzmann equations, for a simplified scenario where only  $N_1$  decays and neutrino flavour effects are ignored. This can be described by:

$$\frac{dN_{N_1}}{dt} = -\Gamma(N_1 \to L\bar{\Phi})N_{N_1} - \Gamma(N_1 \to \bar{L}\Phi)N_{N_1} 
+ \Gamma(L\bar{\Phi} \to N_1)N_LN_{\bar{\Phi}} + \Gamma(\bar{L}\Phi \to N_1)N_{\bar{L}}N_{\bar{\Phi}}$$
(3.6.3)

where  $N_{N_1}$ ,  $N_L$  and  $N_{\Phi}$  are normalised number densities for heavy neutrinos, leptons and Higgs and vice versa for the antiparticle densities. Conventionally, these are normalised such that they represent the particle numbers in a comoving volume containing a single photon at the start of the evolution.

We assume:

- 1. A thermal averaging over the statistical distributions of each incoming particle  $\psi$ , by integrating over the phase space distribution  $\int \frac{d^3 \mathbf{p}_{\psi}}{(2\pi)^2 2E_{\psi}}$ .
- 2. A Maxwell-Boltzmann distribution  $f_{\psi} \propto \exp(-E_{\psi}/T)$  instead of quantum statistics.
- 3. Kinetic equilibrium conditions, i.e.  $f_{N_1}/f_{N_1}^{eq} \approx N_{N_1}/N_{N_1}^{eq}$ , where  $N_{N_1}^{eq}$  is the number density of  $N_1$  at equilibrium.

CPT invariance allows us to equate  $|\mathcal{M}(N_1 \to L\bar{\Phi})|^2 = |\mathcal{M}(\bar{L}\Phi \to N_1)|^2$ . The exponential form of the Maxwell-Boltzmann distribution gives  $f_{N_1}^{\text{eq}} = f_L^{\text{eq}} f_{\Phi}^{\text{eq}}$ .

Using these relations, we can derive,<sup>1</sup>

$$\begin{split} \frac{dN_{N_1}}{dt} &= -\Gamma(N \to L\bar{\Phi})N_{N_1} - \Gamma(N_1 \to \bar{L}\Phi)N_{N_1} \\ &+ \Gamma(L\bar{\Phi} \to N_1)N_L^{eq}N_{\bar{\Phi}}^{eq} + \Gamma(\bar{L}\Phi \to N_1)N_{\bar{L}}^{eq}N_{\Phi}^{eq} \\ &= -\Gamma(N_1 \to L\bar{\Phi})N_{N_1} - \Gamma(N_1 \to \bar{L}\Phi)N_{N_1} \\ &+ \Gamma(N_1 \to L\bar{\Phi})N_{N_1}^{eq} + \Gamma(N_1 \to \bar{L}\Phi)N_{N_1}^{eq} \\ &= -\left(\Gamma(N_1 \to L\bar{\Phi}) + \Gamma(N_1 \to \bar{L}\Phi)\right)(N_{N_1} - N_{N_1}^{eq}) \\ &= -\Gamma_{D_1}(N_{N_1} - N_{N_1}^{eq}) \,. \end{split}$$
(3.6.4)

where

$$\Gamma_{D_1}(z) = \Gamma_{D_1}^0 \langle m_{N_1} / E_{N_1} \rangle = \Gamma_{D_1}^0 \frac{K_1(z = m_{N_1} / T)}{K_2(z = m_{N_1} / T)}$$
(3.6.5)

is the thermally averaged decay rate of the RHN, and

$$\Gamma_{D_1}^0 = \Gamma(N_1 \to L\bar{\Phi}) + \Gamma(N_1 \to \bar{L}\Phi) = \frac{\widetilde{m}_1^2 m_{N_1}^2}{8\pi v^2}$$
(3.6.6)

is the rest frame RHN decay rate [110]. Here,

$$\widetilde{m}_1 = \frac{\left(Y^{\dagger}Y\right)_{11}v^2}{m_{N_1}} \tag{3.6.7}$$

is referred to as the effective neutrino mass.

The functions  $K_1$ ,  $K_2$  are the modified Bessel functions of the second kind, and arise from the thermal averaging of a Maxwell-Boltzmann distribution. It is useful to rewrite this Boltzmann equation with respect to the scale factor a as

$$aH\frac{dN_{N_1}}{da} = -\Gamma_{D_1}(z)\left(N_{N_1} - N_{N_1}^{\text{eq}}\right). \tag{3.6.8}$$

The Feynman diagrams that contribute to the 1-loop decay rate  $N_1 \to L\bar{\Phi}$  are shown in Fig. 3.2. Interference between the tree-level amplitudes and the 1-loop amplitudes results in CP-violation in the RHN decays.

<sup>&</sup>lt;sup>1</sup>Note that the SM particles are generally assumed to be in thermal equilibrium.

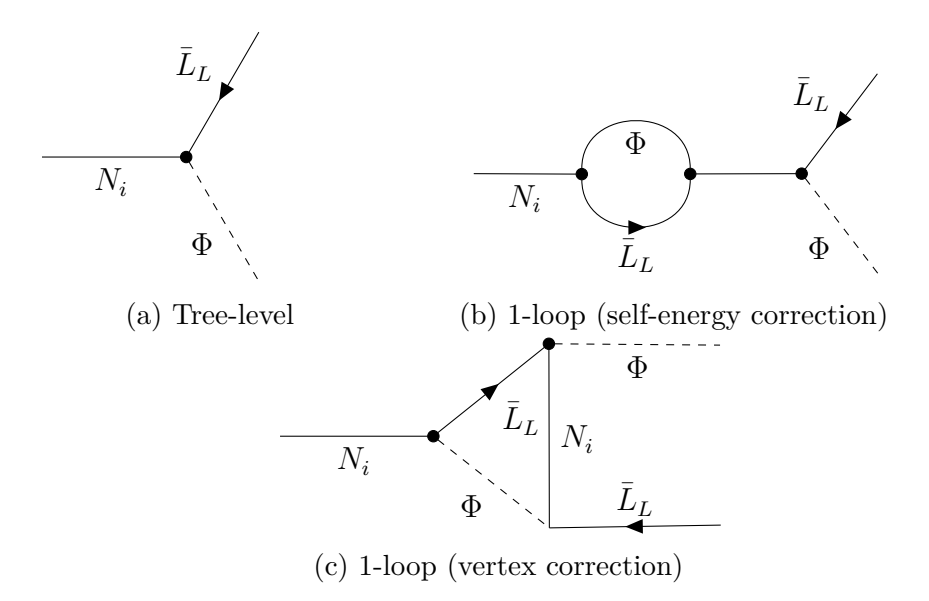


Figure 3.2: Feynman diagrams of the  $\phi^4$  theory contributing to the matrix element up to NLO.

We can derive a similar Bolzmann equation for the B-L asymmetry,

$$aH\frac{dN_{B-L}}{da} = -\epsilon_1 \Gamma_{D_1}(z) \left( N_{N_1} - N_{N_1}^{\text{eq}} \right) - W_1 N_{B-L}$$
 (3.6.9)

where the CP asymmetry parameter is given by

$$\epsilon_1 = \frac{\Gamma(N_1 \to L\bar{\Phi}) - \Gamma(N_1 \to \bar{L}\Phi)}{\Gamma(N_1 \to L\bar{\Phi}) + \Gamma(N_1 \to \bar{L}\Phi)}, \qquad (3.6.10)$$

and  $W_1$  is the 'washout' rate that can reduce the B-L asymmetry. The main process that contributes to the washout is inverse decays [111], however decays and lepton-number-violating scatterings also contribute [94].

# 3.6.3 Washout regimes

We can calculate the washout rate, assuming inverse decays as the only contributor, as [111]

$$W_1 = \frac{\Gamma_{D_1}}{2} \frac{N_{N_1}^{\text{eq}}}{N_L^{\text{eq}}} \propto K \,, \tag{3.6.11}$$

where the 'washout parameter' K is given by

$$K = \frac{\Gamma_{D_1}^0}{H(T = m_{N_1})} = \frac{\widetilde{m}_1}{m_*}.$$
 (3.6.12)

Here,  $m_*$  is the equilibrium neutrino mass given by [110]

$$m_* = \frac{16\pi^{5/2}\sqrt{g_*}v^2}{3\sqrt{5}M_{\rm Pl}} \approx 1.08 \times 10^{-3} \,\text{eV} \,.$$
 (3.6.13)

#### Weak washout

For  $K \ll 1$ , we are considered to be in the weak washout regime, where there is a strong dependence on the initial conditions [110]. Leptogenesis typically makes use of either the vanishing initial condition, where the initial  $N_{N_1}^i = 0$ , or the thermal initial condition, where  $N_{N_1}^i = N_{N_1}^{eq}$ . For the vanishing initial condition, the inverse decay rate is not fast enough to quickly populate the  $N_1$  sector, and thus it takes a longer time for  $N_{N_1}$  to reach the equilibrium number density - well after the comoving equilibrium number density has started falling, and the heavy neutrinos have become non-relativistic.

#### Strong washout

In strong washout regimes,  $K \gg 1$ , the couplings are strong enough that the inverse decays can quickly populate the  $N_1$  sector in the case of a vanishing initial condition, prior to decays and while  $N_1$  is still relativistic  $(T \gtrsim m_{N_1})$ . Thus the dependence on initial conditions disappears.

The question of initial conditions depends on the UV origin of a leptogenesis model. The vanishing initial condition is used when there is no reason for the RHNs to be already populated prior to leptogenesis. If there is inflaton decay into the RHNs and thus they are populated at the reheating temperature, then they could exist in thermal equilibrium prior to leptogenesis. This thermal equilibrium would require fast elastic scattering and number-changing interactions, which we expand on in Chapter 4.

### 3.6.4 Flavour effects

A full treatment of leptogenesis will involve the heavier RHN, as well as the flavour effects that impact on the dynamics of the number densities and  $N_{B-L}$  [100,111–115]. Sources of flavour effects include interactions that depend on charged lepton Yukawa couplings [116] which can modify the BAU by an order of magnitude [111,117,118], and differences in the heavy neutrino Yukawa couplings [119–122] that lead to an inequitable seeding of the individual lepton flavour numbers  $L_e, L_\mu, L_\tau$ . These are relevant to calculating B-L as the sphaleron processes preserve

$$\frac{1}{3}B - L_{e,\mu,\tau}$$

individually [111]. In Eq. 4.4.4 we provide a full expression for the flavour contributions to the B-L asymmetry.

## 3.6.5 Calculating $\eta_B$

The baryon asymmetry is based on the final value of the B-L asymmetry at the end of leptogenesis,  $N_{B-L}^f$ , so

$$\eta_B = a_{\rm sph} \frac{N_{B-L}^f}{N_{\gamma}^{\rm rec}} \tag{3.6.14}$$

where  $a_{\rm sph}=28/79$  is the factor for sphaleron conversion from B-L to B [100], and  $N_{\gamma}^{\rm rec}$  is the photon number density at recombination, to account for the change between the end of leptogenesis and the recombination era.

# 3.6.6 Naturalness and Resonant Leptogenesis

Models of vanilla leptogenesis result in the Davidson-Ibarra bound on the minimum mass of the  $N_1$ ,  $m_{N_1} \gtrsim 10^{7-8} \,\mathrm{GeV}$  [123], in order to generate a sufficiently high  $\eta_B$  that matches observation. However, this comes into tension with naturalness constraints such as the Vissani bound [30], which requires the 1-loop correction to the Higgs mass arising from the heavy neutrinos to not be 'too large'.

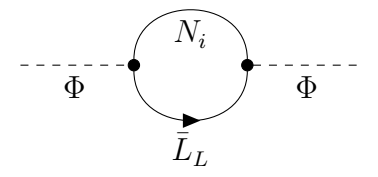


Figure 3.3: 1-loop correction to the Higgs propagator in the Type I Seesaw mechanism.

Fig. 3.3 presents the Feynman diagram for the 1-loop correction to the Higgs mass arising from the Type I Seesaw mechanism. The Higgs hierarchy problem is that, if there exist Higgs-coupled particles with masses  $T_{\rm EWSB} \ll m \ll T_{\rm GUT}$ , where  $T_{\rm GUT}$  is the energy scale of the Grand Unified Theory which is expected to supersede the SM, then those heavy particles will have a tendency to pull the Higgs mass up to scales higher than that of EWSB, yet this is not observed. The loop contributions will have at least a quadratic dependence on the mass of the new particles, based on a Higgs portal coupling similar to  $\Phi^2\phi^2$  where  $\phi$  is a new heavy particle. As the Higgs mass is not at a higher energy scale, then the tree-level mass must be almost as large as the loop correction  $\delta\mu$ , such that they finely cancel out and leave the Higgs mass at the EWSB scale  $m_H \sim \mathcal{O}(10^2\,{\rm GeV})$ .

This is an example of a fine-tuning problem, and the precise boundary between what is considered to be finely-tuned or not is arbitrary. In App. 4.5 we quantify fine-tuning using defined measures in order to make comparisons between benchmark points in different models.

However, in Ref. [30] the fine-tuning limit is taken to be one order of magnitude higher than the EWSB, at about 1 TeV,

$$\delta\mu^2 \approx \frac{m_{\nu} m_{N_1}^3}{2\pi v^2} \ln\left(\frac{q}{m_{N_1}}\right) < (1 \,\text{TeV})^2$$
 (3.6.15)

leading to the Vissani bound of  $m_{N_1} \lesssim 10^7 \,\text{GeV}$ . We see that this is incompatible with the Davidson-Ibarra bound, meaning that vanilla leptogenesis is a finely-tuned model.

Resonant leptogenesis [124] was introduced as a specific regime of leptogenesis that

alleviates this specific fine-tuning issue. This is based on the observation that for RHN mass splitting comparable to the decay widths,  $|m_{N_1} - m_{N_2}| \sim \Gamma_{D_{1,2}}^0$ , the CP-violation sourced from the self-energy contribution to the RHN decay (Fig. 3.2(b)) can be significantly enhanced [125–127]. This results in the observed BAU being able to be produced for lower RHN masses of around  $m_{N_1} \sim 10^{6-7}$  GeV, thus giving us a model of leptogenesis compatible with naturalness constraints from the Higgs sector. However, this imposes a strong constraint on the degeneracy of the neutrino masses and limits the parameter space available for leptogenesis.

## 3.7 Effective Potential

The quantity most relevant for phase transitions is the effective potential, which defines the potential energy of a field configuration in a given theory, taking loop corrections into account. The effective potential is defined with respect to the generating functional

$$Z[J] = e^{iW[J]} = \int \mathcal{D}\phi \, e^{iS[\phi] + \int d^4x J(x)\phi(x)},$$
 (3.7.1)

where J(x) is a source current coupled to the field  $\phi(x)$ , and  $\int \mathcal{D}\phi$  is a functional integral over the space of field configurations. A Legendre transform of W gives the effective action

$$\Gamma[\phi_c(x)] \equiv W[J] - \int d^4x J(x)\phi_c(x), \qquad (3.7.2)$$

where  $\phi_c(x) = \langle 0 | \phi(x) | 0 \rangle$  is referred to as the classical field. If we assume that  $\phi_c$  is a constant 'background field', we can write

$$\Gamma(\phi_c) = -\int d^4x V_{\text{eff}}(\phi_c) = -\mathcal{V}V_{\text{eff}}(\phi_c), \qquad (3.7.3)$$

where  $V_{\text{eff}}(\phi_c)$  is the effective potential.

We find that the functional derivative of the effective action gives us

$$\frac{\delta\Gamma[\phi_c]}{\delta\phi_c(x)} = -J(x), \qquad (3.7.4)$$

and in a vacuum with vanishing source J(x) = 0, we find

$$\frac{\delta\Gamma[\phi_c]}{\delta\phi_c(x)} = \frac{\partial V_{\text{eff}}}{\partial\phi_c} = 0.$$
 (3.7.5)

Thus the vacua of the theory are given by the minimum of the potential  $V_{\text{eff}}$ , making it a powerful tool for studying phase transitions. From now on, we will generally drop the subscript c on the background classical field and just refer to the effective potential as  $V(\phi)$ .

## 3.7.1 Zero Temperature

The effective potential at 1-loop is given by

$$V = V_{\text{tree}} + V_{\text{1-loop}}, \qquad (3.7.6)$$

where  $V_{\rm tree}$  is the tree-level potential. The calculation of the 1-loop contribution requires the summation of all 1-loop diagrams with zero external momenta; this is because the constant background field results in vanishing of the spatial derivatives of  $\phi$  (and thus the external momenta). As an example, the 1-loop contribution for the scalar  $\phi^4$  theory can be expressed diagrammatically as

$$V_{1-\text{loop}} = + + \cdots \qquad (3.7.7)$$

where we neglect the bubble vacuum diagrams as they are constant with respect to the field configuration  $\phi$ , thus leading to a constant shift in the potential that does not affect the dynamics.

With the  $\phi^4$  Feynman rules, we can calculate the 1-loop contribution as

$$V_{1-\text{loop}} = \sum_{n=1}^{\infty} \frac{i}{2n \cdot 2^n} \int \frac{d^4q}{(2\pi)^4} \left( \frac{(-i\lambda)\phi^2}{q^2 - m^2 + i\epsilon} \right)^n$$
 (3.7.8)

$$= \frac{i}{2} \int \frac{d^4q}{(2\pi)^4} \ln\left(1 - \frac{1}{2} \frac{\lambda \phi^2}{q^2 - m^2 + i\epsilon}\right)$$
 (3.7.9)

$$= \frac{i}{2} \int_0^{\Lambda} \frac{dq_E}{(2\pi)^4} \ln\left(\frac{q_E^2 + V_{\text{tree}}''(\phi)}{q_E^2 + m^2}\right) q_E^3 \int d\Omega_3$$
 (3.7.10)

where the symmetry factors 1/2n and  $1/2^n$  arise due to the permutation of vertices and the interchangeability of external legs at each vertex respectively [128]. We have summed over the infinite sum, and then Wick rotated into the Euclidean spherical integral as in Section 2.6.2. We have then introduced an ultraviolet cutoff  $\Lambda$  for the momentum integral, as an alternative method of renormalisation to that of dimensional regularisation. For illustrative purposes, we can take the massless case such that the 1-loop potential evaluates to [129]

$$V_{\text{1-loop}} = \frac{1}{64\pi^2} \left\{ \lambda \phi^2 \Lambda^2 + \frac{\lambda \phi^2}{4} \left[ \ln \left( \frac{\lambda \phi^2}{2\Lambda^2} - \frac{1}{2} \right) \right] \right\}. \tag{3.7.11}$$

We see that this is divergent in two senses: it has a UV divergence due to  $\Lambda$ , and an IR divergence due to the logarithmic term. We can introduce counterterms to handle the divergences

$$V(\phi) = V_{\text{tree}}(\phi) + V_{\text{1-loop}}(\phi) - \delta m^2 \phi^2 - \delta \lambda \phi^4.$$
 (3.7.12)

We can impose a renormalisation condition that ensures that the effective potential gives the tree-level mass in its vacuum, such that

$$\left. \frac{d^2V}{d\phi^2} \right|_{\phi=0} = m^2 = 0. \tag{3.7.13}$$

This results in the counterterm

$$\delta m^2 = \frac{\lambda \Lambda^2}{64\pi^2} \,. \tag{3.7.14}$$

A similar condition cannot be applied for the quartic counterterm due to the IR divergence in the logarithmic term. We instead choose a mass scale  $\mu$  so we can impose

$$\frac{d^4V}{d\phi^4}\bigg|_{\phi=\mu} = \lambda \,, \tag{3.7.15}$$

from which we can find

$$\delta\lambda = -\frac{\lambda^2}{256\pi^2} \left[ \ln\left(\frac{\Lambda^2}{\mu^2}\right) - \frac{25}{6} \right] . \tag{3.7.16}$$

giving us the renormalised form of the 1-loop effective potential for the massless  $\phi^4$ 

theory

$$V(\phi) = \frac{\lambda}{4!}\phi^4 + \frac{\lambda^2}{256\pi^2} \left[ \ln\left(\frac{\phi^2}{\mu^2}\right) - \frac{25}{6} \right] \phi^4, \qquad (3.7.17)$$

where the renormalised 1-loop contribution is the Coleman-Weinberg potential. A similar method can be used to calculate the effective potential in theories with gauge bosons, fermions, and scalars as well. For the SM Higgs background  $\phi$ , the finite part of the Coleman-Weinberg potential is [130]

$$V_{\text{CW}}(\phi) = \sum_{i} g_i \frac{m_i^4(\phi)}{64\pi^2} \left[ \ln \left( \frac{m_i^2(\phi)}{\mu^2} \right) - C_i \right], \qquad (3.7.18)$$

where  $g_i$  are the d.o.f. of Higgs interacting particles,  $m_i^2(\phi) = \partial_i^2 V(\phi)$  are the Higgs field-dependent mass terms, and

$$C_{i} = \begin{cases} \frac{5}{6} & \text{(vector bosons)} \\ \frac{3}{2} & \text{(scalars + fermions)} \end{cases}$$
 (3.7.19)

#### 3.7.2 Matsubara Formalism

At finite temperature, interactions with particles in the thermal bath induce thermal corrections at higher loop order that must be taken into account. The energy of a system is given by the Hamiltonian  $\hat{H} = S_3$ , which is the spatial sum of kinetic and potential energy of a system, and is identical to the Euclidean action in 3D. Wick rotating  $t \to i\tau$ , and integrating  $\tau \in [0, \beta)$  where  $\beta = 1/T$  is the inverse temperature, we find for the generating functional

$$Z[0] = e^{iS} = e^{-\int d\tau S_3} = e^{-\beta \hat{H}}.$$
 (3.7.20)

We denote Z[0] = Z from now on and refer to it as the partition function, in analogy with the partition function from statistical physics. Thus, the thermal expectation value of an operator  $\mathcal{O}$  is given by the thermally averaged sum over states

$$\langle \mathcal{O} \rangle = \frac{1}{Z} \sum_{n} \langle n | e^{-\beta \hat{H}} \mathcal{O} | n \rangle = \frac{1}{Z} \operatorname{Tr} \left( e^{-\beta \hat{H}} \mathcal{O} \right).$$
 (3.7.21)

Reproducing the derivation in Ref. [128], the thermal 2-point correlator function is given by,

$$\langle \psi(t, \mathbf{x}) \psi(0, \mathbf{y}) \rangle = \frac{1}{Z} \operatorname{Tr} \left( e^{-\beta \hat{H}} \psi(t, \mathbf{x}) \psi(0, \mathbf{y}) \right)$$
 (3.7.22)

$$= \frac{1}{Z} \operatorname{Tr} \left( e^{-\beta \hat{H}} \psi(t, \mathbf{x}) e^{i\hat{H}(i\beta)} \psi(-i\beta, \mathbf{y}) e^{-i\hat{H}(i\beta)} \right)$$
(3.7.23)

$$= \frac{1}{Z} \operatorname{Tr} \left( e^{-\beta \hat{H}} \psi(i\beta, \mathbf{y}) \psi(t, \mathbf{x}) \right)$$
 (3.7.24)

$$= \langle \psi(-i\beta, \mathbf{y})\psi(t, \mathbf{x})|\psi(-i\beta, \mathbf{y})\psi(t, \mathbf{x})\rangle$$
(3.7.25)

$$= \begin{cases} \langle \psi(t, \mathbf{x}) \psi(-i\beta, \mathbf{y}) | \psi(t, \mathbf{x}) \psi(-i\beta, \mathbf{y}) \rangle & \psi \text{ is a boson,} \\ -\langle \psi(t, \mathbf{x}) \psi(-i\beta, \mathbf{y}) | \psi(t, \mathbf{x}) \psi(-i\beta, \mathbf{y}) \rangle & \psi \text{ is a fermion,} \end{cases}$$
(3.7.26)

where we use the quantum time evolution  $\psi(t) = e^{i\hat{H}t}\psi(0)e^{-i\hat{H}t}$ . This is the Kubo-Martin-Schwinger (KMS) relation, and after the Wick rotation it shows that the field  $\psi(0, \mathbf{x}) = \pm \psi(\beta, \mathbf{x})$  and thus is periodic in inverse temperature. Here, we see clearly that the imaginary time  $\tau$  is identified with the inverse temperature  $\beta$ .

The frequency of these periodic modes is referred to as the Matsubara frequency [131],

$$\omega_n = \begin{cases} 2n\pi T & \text{cyclic, for bosons,} \\ (2n+1)\pi T & \text{anti-cyclic, for fermions,} \end{cases}$$
 (3.7.27)

which provides an energy contribution to the Euclidean square momentum  $p_E^2 = \omega_n^2 + \mathbf{p}^2$  due to oscillations in the time component of the field. Any 4D momentum integral can now be converted to a sum over Matsubara modes through the relation

$$\int f(q^2) d^4q = 2\pi i T \sum_{n} \int d^3 \mathbf{q} f(-\mathbf{q}^2 - \omega_n^2).$$
 (3.7.28)

We reproduce the 1-loop,  $\phi$ -dependent contribution to the effective potential for a general case [130],

$$V_{1-\text{loop}} = \frac{i}{2} \sum_{i} g_i \int \frac{d^4 q}{(2\pi)^4} \ln\left(\frac{q^2 - m_i^2(\phi)}{q^2 - m_i^2(0) + i\epsilon}\right)$$
(3.7.29)

$$= \frac{T}{2} \sum_{i} \sum_{n=-\infty}^{n=\infty} g_i \int \frac{d^3 \mathbf{q}}{(2\pi)^3} \left[ \ln \left( \mathbf{q}^2 + \omega_n^2 + m_i^2(\phi) \right) - \ln \left( \mathbf{q}^2 + \omega_n^2 + m_i^2(0) \right) \right]$$
(3.7.30)

$$\rightarrow \frac{T}{2} \sum_{i} \sum_{n=-\infty}^{n=\infty} g_i \int \frac{d^3 \mathbf{q}}{(2\pi)^3} \ln\left(\mathbf{q}^2 + \omega_n^2 + m_i^2(\phi)\right) , \qquad (3.7.31)$$

where we disregard the  $\phi$ -independent contribution in the final line, as it would provide a constant shift for the potential. In the  $T \to 0$  limit, the spacing between Matsubara modes goes to zero. Thus, the sum of modes becomes an integral over frequencies, just like in the Coleman-Weinberg case. Therefore, the temperature independent part of this simply leads to the Coleman-Weinberg potential, whereas the temperature dependent part is [130]

$$V_T = \sum_{i} \frac{g_i T^4}{2\pi^2} \int_0^\infty dq \, q^2 \ln\left(1 \mp e^{-\sqrt{q^2 + m_i^2(\phi)/T^2}}\right)$$
(3.7.32)

$$= \sum_{b} \frac{g_b T^4}{2\pi^2} J_B \left( \frac{m_b^2(\phi)}{T^2} \right) + \sum_{f} \frac{g_f T^4}{2\pi^2} J_F \left( \frac{m_f^2(\phi)}{T^2} \right) , \qquad (3.7.33)$$

where the minus sign is used for bosons, and the plus sign for fermions. In the final line we have split up the sum into bosonic and fermionic parts, and have made an implicit definition of the thermal bosonic and fermionic functions  $J_B(x)$  and  $J_F(x)$ .

In the high temperature limit  $(m/T \ll 1)$ , we find the expansion of  $J_B(x)$  gives us [132]

$$J_B\left(\frac{m^2(\phi)}{T^2}\right) = -\frac{\pi^2}{90} + \frac{1}{24}\left(\frac{m^2(\phi)}{T^2}\right) - \frac{1}{12\pi}\left(\frac{m^2(\phi)}{T^2}\right)^{\frac{3}{2}} + \mathcal{O}\left(\frac{m^4(\phi)}{T^4}\right), \quad (3.7.34)$$

whereas the expansion of  $J_F(x)$  results in

$$J_F\left(\frac{m^2(\phi)}{T^2}\right) = -\frac{7\pi^2}{8 \times 90} + \frac{1}{48}\left(\frac{m^2(\phi)}{T^2}\right) + \mathcal{O}\left(\frac{m^4(\phi)}{T^4}\right). \tag{3.7.35}$$

Therefore, we see that the bosonic thermal function provides a cubic mass term that the fermionic thermal function does not. In the SM, we know that the field-dependent masses of the gauge bosons and fermions are linearly dependent on the Higgs field (which is why the masses are  $m \propto v$  in Sec. 2.4.2). These two results mean that only bosonic contributions provide a cubic field correction, at high temperature, to the

thermal potential. It is trivial to see that a cubic term corresponds to the creation of a thermal barrier between minima in a potential [132]. Thus, a thermal barrier can be enhanced with heavier bosonic particles coupling to a scalar undergoing a phase transition. Finally, our total thermal potential at 1-loop is given by

$$V = V_{\text{tree}} + V_{\text{CW}} + V_{T}. \tag{3.7.36}$$

We finish this subsection by defining Debye masses as thermal mass corrections, which arise due to interactions with the thermal bath. These can be calculated perturbatively by modifying the integrations over loop momenta using the Matsubara formalism. The Debye mass for the scalar  $\phi$  can be calculated simply via

$$m_D^2 = \frac{\partial^2 V_T}{\partial \phi^2} \,. \tag{3.7.37}$$

Gauge bosons and fermions also acquire Debye masses, and in the next section we will see that the gauge boson Debye masses are crucial for the calculation of the Higgs effective potential. The Debye mass is acquired by the zeroeth component of the gauge boson, as it oscillates with  $\tau = \beta$  in Euclidean space, and acts as a scalar. Thus, in the literature, the Debye masses for gauge bosons are also referred to as 'temporal scalar masses'.

## 3.7.3 Daisy Resummation

Studying Eq. 3.7.32 for when  $T \gg m_i^2(\phi)$ , we see that the logarithmic part of the bosonic function

$$\ln\left(1 - e^{-\sqrt{q^2}}\right) \to \ln(0), \tag{3.7.38}$$

thus  $J_B(x)$  diverges at low energy. This means that perturbation theory breaks down for the low momentum (or long distance) modes of bosons at high temperatures, as they become highly occupied. This is Linde's infrared problem [133,134]. The source of this in the bosonic thermal function is the existence of the 'soft' zero modes with Matsubara frequency  $\omega_0 = 0$ , which do not exist for the fermions as their lowest mode is  $\omega_0 = 2\pi T$ , thus there is no IR divergence.

To investigate this further, we can split up the  $m^2$  1-loop correction in the scalar  $\phi^4$  theory as

$$= m_{1-\text{loop}}^2 + m_D^2 \,, \tag{3.7.39}$$

where  $m_{1\text{-loop}}^2$  denotes the temperature independent part of the correction, and the  $m_D^2$  denotes the Debye mass, i.e. the contribution from the Matsubara modes. This is also referred to as the hard thermal loop contribution. The hard thermal loop scales as  $m_D^2 \propto \lambda T^2$  to leading order [135, 136], which comes from the zero mode contribution at high temperature. As the Debye mass contribution can be negative, it can cancel out with the zero-temperature contribution at a certain temperature. This effect is associated with phase transitions, as it results in the high temperature restoration of a vacuum at the origin [134]. For the  $\phi^4$  theory, the associated 'critical temperature' is roughly given by solving  $m^2(T_C) = m^2 - \lambda T_C^2 = 0$  to give  $T_C \sim m/\sqrt{\lambda}$ .

However, for 'daisy' diagrams that have N-loops around the central loop, the leading order scaling in temperature is [136]

$$\lambda \frac{\lambda^{N} T^{2N-1}}{m^{2N-3}} \quad n \ge 2,$$
 (3.7.40)

where m is the tree-level mass of the theory. Near the critical temperature of a phase transition, we find that as  $T_C \sim m/\sqrt{\lambda}$ ,

$$\lambda \frac{T^2}{m^2} \sim 1, \qquad (3.7.41)$$

such that

$$\lambda^{N} \propto \left(\frac{\lambda^{N} T^{2}}{m^{2}}\right)^{N-\frac{3}{2}} \lambda^{\frac{3}{2}} T^{2} \sim \lambda^{\frac{3}{2}} T^{2}, \qquad (3.7.42)$$

and the daisy diagrams provide a contribution independent of the number of outer loops (or 'petals') N. This is an example of the breakdown of perturbation theory outlined at the beginning of this section. The origin of this is in the soft bosonic zero-modes that run in the central loop, which are 'screened' by the 'hard' non-

zero Matsubara modes running in the outer loops which then dominate at high temperature.

One way to tackle this problem is through daisy resummation, which aims to find a converging infinite sum of all N-petal daisy contributions to the effective potential. To outline this, we follow the procedure in Ref. [134] and start by splitting up the 1-loop contribution for the effective potential (Eq. 3.7.31) as

$$V_{1-\text{loop}} = \frac{T}{2} \sum_{i} \sum_{n=-\infty}^{n=\infty} g_{i} \int \frac{d^{3}\mathbf{q}}{(2\pi)^{3}} \ln\left(\mathbf{q}^{2} + \omega_{n}^{2} + m_{i}^{2}(\phi)\right)$$

$$= \frac{T}{2} \sum_{i} g_{i} \int \frac{d^{3}\mathbf{q}}{(2\pi)^{3}} \ln\left(\mathbf{q}^{2} + m_{i}^{2}(\phi)\right) + \frac{T}{2} \sum_{i} g_{i} \sum_{n=-\infty}^{n=\infty} \int \frac{d^{3}\mathbf{q}}{(2\pi)^{3}} \ln\left(\mathbf{q}^{2} + \omega_{n}^{2} + m_{i}^{2}(\phi)\right)$$

$$= V_{\text{soft}}(\{m_{i}^{2}(\phi)\}) + V_{\text{hard}}(\{m_{i}^{2}(\phi)\}),$$

$$(3.7.45)$$

where we have separated the bosonic zero mode into a soft contribution. This is in contrast to before where we split it up into the zero-temperature Coleman-Weinberg part and the temperature-dependent part, as both contributions here are temperature dependent.

By replacing the tree-level field-dependent masses with thermal masses  $(\{m_i^2(\phi)\} \rightarrow \{m_i^2(\phi) + m_D^2\})$ , we find that the soft contribution is resummed such that

$$V_{\text{soft}}(\lbrace m_i^2(\phi)\rbrace) \to V_{\text{soft}}^{\text{resummed}}(\lbrace m_i^2(\phi)\rbrace).$$
 (3.7.46)

Next, the 1-loop daisy contribution is provided by the difference between the resummed and soft contributions,

$$V_{\text{daisy}} = V_{\text{soft}}^{\text{resummed}} - V_{\text{soft}} \tag{3.7.47}$$

such that we can write the Arnold-Espinosa thermal effective potential at 1-loop [135] as

$$V = V_{\text{tree}} + V_{\text{CW}} + V_T + V_{\text{daisy}}.$$
 (3.7.48)

The subtraction of the soft contribution counteracts the one provided by  $V_{\text{CW}} + V_T = V_{\text{soft}} + V_{\text{hard}}$  such that the only soft contribution that remains is the daisy resummed

one [134].

### 3.7.4 Dimensional Reduction

The perturbative method with daisy resummation is conventionally used in numerous phase transition studies. However, this method results in significant theoretical uncertainties, primarily due to the choice of renormalisation scale [134]. It has been shown that dimensional reduction (DR), initially devised in Refs. [137–143], is an alternative method that provides a significant reduction in theoretical uncertainties [134]. The method involves perturbative calculations in a 3D effective theory of the bosonic zero-mode fields.

To motivate this, we consider first the Euclidean Lagrangian of a generic theory in the Matsubara formalism, using the notation in Ref. [144],

$$\mathcal{L} = \mathcal{L}(\phi, A_{\mu}, \psi, S, s), \qquad (3.7.49)$$

where  $\phi$  are scalars,  $A_{\mu}$  are gauge bosons and  $\psi$  are fermions. The scalar fields S and s refer to the heavy (non-zero Matsubara) and soft (zero) modes respectively, which acquire an effective mass

$$m_S \propto \pi T$$
 (3.7.50)

$$m_s \propto \begin{cases} gT & \text{gauge bosons} \\ \sqrt{\lambda}T & \text{scalar bosons} \end{cases}$$
 (3.7.51)

respectively where g represents a gauge coupling. These masses are effective masses of these modes, and can be thought of as corresponding to the energy of the oscillations in the imaginary time direction  $\tau \in [0, \beta)$ . At high temperatures, the heavy modes (from  $n \neq 0$  bosons and all fermions) can be integrated out as they correspond to small distance physical effects, which are less relevant for long distance phenomena across the potential (such as phase transitions), to give the dimensionally reduced

Lagrangian

$$\mathcal{L}^{3D} = \mathcal{L}^{3D}(\phi^{3D}, A_i^{3D}, A_0^{3D}, s^{3D}).$$
 (3.7.52)

Thus the low energy EFT can be constructed as one purely in the spatial dimensions, as we are left with zero modes that do not oscillate in the imaginary time direction.  $A_i^{\text{3D}}$  are the purely spatial gauge field modes,  $A_0^{\text{3D}}$  are the gauge temporal scalars,  $\phi_3$  and  $s_3$  are the scalars and soft scalars in 3D respectively.

A lower scale, called the ultrasoft scale at  $\sim g^2 T/\pi$ , further separates the ultra-lowenergy spatial modes  $A_i^{\rm 3D}$  from the temporal scalars  $A_0^{\rm 3D}$  with Debye masses on the order of the soft scale. The soft scalar  $s^{\rm 3D}$  is also separated from those spatial modes. Integrating out those modes leaves us with the ultrasoft Lagrangian,

$$\bar{\mathcal{L}}^{3D} = \bar{\mathcal{L}}^{3D}(\bar{\phi}^{3D}, \bar{A}_i^{3D}),$$
 (3.7.53)

which encapsulates the long distance physics. Thus, DR is well motivated for the separation of scales

$$\frac{g^2}{\pi}T \ll gT \ll \pi T. \tag{3.7.54}$$

The temperature dependence of the theory is absorbed into the mass and coupling parameters of the soft and ultrasoft theories. These parameters are obtained through matching the 3D (soft/ultrasoft) parameters to the 4D ones, such that the correlation functions of both theories give the same result. A detailed procedure for obtaining the matching relations has been outlined in Refs. [141–143], and a demonstration can be found in Ref. [145].

After performing loop corrections for the effective potential in the 3D theory, the 4D thermal effective potential can be calculated via the relation

$$V_4(\phi, T) = TV_3\left(\frac{\phi}{\sqrt{T}}, T\right), \qquad (3.7.55)$$

where the temperature dependence of the 3D theory is found in the 3D parameters.

### 3.8 Gravitational Waves from FOPTs

In Section 5.4, we describe how to calculate phase transition parameters  $\bar{\alpha}$ ,  $\bar{\beta}/H_*$  from an effective potential, as well as the gravitational wave power spectrum  $\Omega_{\rm gw}h^2(f)$ . In this section we provide more detail about gravitational waves, first order phase transitions as a GW source, and how the space-based interferometer LISA could detect them.

### 3.8.1 Gravitational Waves

We know that, in GR, c the speed of light is the speed limit of causality; any effects on the curvature of space from changes in  $T_{\mu\nu}$  are not instantaneous. Thus, the idea of perturbations in spacetime travelling as a wave naturally emerges. These waves are gravitational waves, which were first predicted shortly after the formulation of GR, and were first observed a century later by LIGO in 2015 [146].

Gravitational waves can be described by small perturbations around flat Minkowski spacetime,  $g_{\mu\nu}(x) = \eta_{\mu\nu} + h_{\mu\nu}(x)$ , where, by dropping terms of order  $h^2$  or greater, we can linearise the Einstein equation to find a perturbative solution for gravitational waves. We wish to find the solution of gravitational waves travelling through a vacuum (i.e.  $T_{\mu\nu}=0$ ), where we assume that the contribution of the gravitational waves to the stress-energy tensor are small enough to neglect. We can insert this metric into the vacuum Einstein equation, and for simplicity define the trace-reversed perturbation as  $\bar{h}_{\mu\nu} = h_{\mu\nu} - \frac{1}{2}\eta_{\mu\nu}h^{\alpha}_{\ \alpha}$ . Then, using the Lorentz gauge  $\partial_{\mu}\bar{h}^{\mu\nu} = 0$ , we find that the solution is given by [147]

$$\partial^2 \bar{h}_{\mu\nu} = 0 \,, \tag{3.8.1}$$

which is simply a wave equation. Thus

$$\bar{h}_{\mu\nu} = \operatorname{Re}\left(\epsilon_{\mu\nu}e^{ik_{\sigma}x^{\sigma}}\right), \qquad (3.8.2)$$

where  $k_{\mu}$  is a wavevector, and  $\epsilon_{\mu\nu}$  is an ansatz tensor. There is still enough redund-

ancy in the degrees of freedom that we can impose an additional gauge condition; the transverse-traceless gauge, where the perturbation can be chosen to be purely spatial and traceless such that  $h_{0i} = h_{i0} = h^{\mu}_{\mu} = 0$  [147]. This means that  $h_{\mu\nu} = \bar{h}_{\mu\nu}$ . We find that this gauge condition imposes  $\epsilon_{0i} = \epsilon_{i0} = \epsilon^{\mu}_{\mu} = 0$ , as well as  $k_i \epsilon^{ij} = 0$ . This last result shows us that gravitational waves are transverse to the direction of propagation.

For a gravitational wave with energy E travelling in the z direction such that  $k^{\mu} = (E, 0, 0, E)$ , we can write the metric perturbation as [128]

$$h_{\mu\nu} = \begin{pmatrix} 0 & 0 & 0 & 0 \\ 0 & \epsilon_{11} & \epsilon_{12} & 0 \\ 0 & \epsilon_{12} & -\epsilon_{11} & 0 \\ 0 & 0 & 0 & 0 \end{pmatrix} \cos(E(t-z)), \tag{3.8.3}$$

which reveals the existence of two polarisation states (+-type and ×-type) that make up  $\epsilon = \epsilon_{11}P_+ + \epsilon_{12}P_\times$  given by

$$P_{+} = \begin{pmatrix} 0 & 0 & 0 & 0 \\ 0 & 1 & 0 & 0 \\ 0 & 0 & -1 & 0 \\ 0 & 0 & 0 & 0 \end{pmatrix}, \quad P_{\times} = \begin{pmatrix} 0 & 0 & 0 & 0 \\ 0 & 0 & 1 & 0 \\ 0 & 1 & 0 & 0 \\ 0 & 0 & 0 & 0 \end{pmatrix}. \tag{3.8.4}$$

The energy density fraction of gravitational waves is defined as with other cosmological parameters:

$$\Omega_{\rm gw}(f) = \frac{\rho_{\rm gw}}{\rho_c} \,, \tag{3.8.5}$$

which is a function of the gravitational wave frequency f, typically in units of Hz, given by f = E/h. Redshifting due to the expansion of the universe reduces this energy between a GW source and receiver.  $\Omega_{\rm gw}h^2(f)$  is also referred to as the amplitude of the gravitational wave.

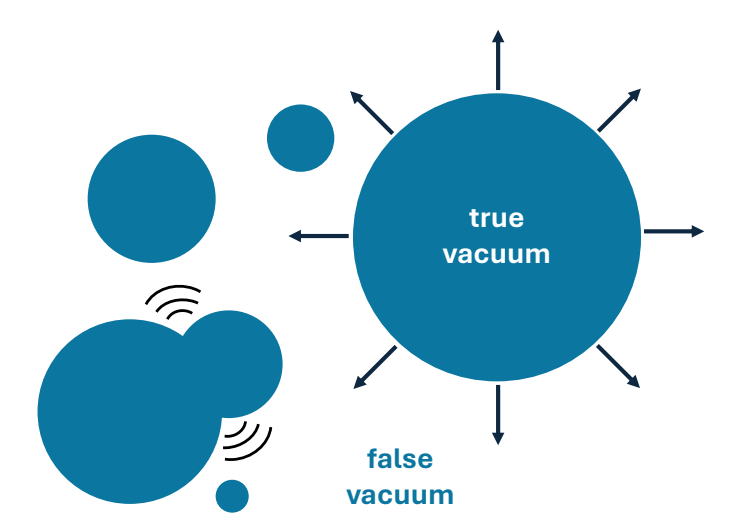


Figure 3.4: An illustration of bubbles of a new phase nucleating and expanding in a volume of the old phase. The bubbles can collide, inducing anisotropic stress in spacetime, and thus producing gravitational waves.

#### 3.8.2 First Order Phase Transitions

An effective thermal potential  $V(\phi, T)$  will have a vacuum at  $\phi_0$ , typically when the field configuration  $\phi_0 = 0$ , at high temperature. As the temperature falls down, a new vacuum with  $V'(\phi_1, T) = 0$ ,  $V''(\phi_1, T) > 0$  could emerge, which at first would be a false vacuum, with a higher potential energy  $V(\phi_1, T) > V(\phi_0, T)$ . At the critical temperature  $T_C$ , defined by  $V(\phi_1, T_C) = V(\phi_0, T_C)$ , the vacua become degenerate. As the temperature drops further, the current vacuum that the system is in may become the false vacuum.

If a potential barrier exists between the true and false vacuum, then this would result in a First Order Phase Transition (FOPT). The field configuration would either have to quantum tunnel through the barrier or thermally fluctuate above the barrier to nucleate a volume that exists in the new phase, conventionally referred to as a 'bubble', as shown in Fig. 3.4. Thermal fluctuations are the most important effect at high temperatures, so we neglect nucleation by quantum tunnelling when discussing early universe phase transitions. In Section 5.4.1, we discuss in detail how

<sup>&</sup>lt;sup>1</sup>Note that it is conventional in the literature to use 'phase', 'vacuum', and 'minimum' interchangeably in the phase transition context.

to calculate the nucleation of a bubble. The temperature at which the first bubble nucleates is the nucleation temperature,  $T_N$ , whereas the percolation temperature is defined as the temperature  $T_p$  at which a fraction of 1/e of a Hubble volume is populated by the new phase.

## 3.8.3 Gravitational Wave Sources and Spectra

The bubbles of the new phase typically expand, collide, and merge with each other. As they expand, they cause pressure waves in the plasma; shock waves for subsonic bubble wall velocities, i.e.  $v_W < 1/\sqrt{3}$ , and rarefaction waves for supersonic  $v_W > 1/\sqrt{3}$ . The collisions, sound waves, and subsequent magnetohydrodynamic turbulence of the plasma provide three sources of gravitational waves from the FOPT. Gravitational waves produced through bubble collisions are illustrated in Fig. 3.4 Each source i of gravitational waves provides a spectrum of the following shape for a source i [24,128]

$$\Omega_i h^2(f) = \Omega_i^0 \Delta_i \left(\frac{g_*}{100}\right)^{-1/3} K_i^a \left(\frac{\bar{\beta}}{H_*}\right)^{-b} S_i \left(\frac{f}{f_i}\right), \qquad (3.8.6)$$

where  $\Omega_i^0$  is a prefactor,  $\Delta_i$  is a velocity factor,  $K_i$  is the fraction of phase transition energy given to that source,  $S_i(f/f_i)$  is the spectral shape of the source and  $f_i$  is its peak frequency. The numbers a and b vary depending on the source. The parameters are calculated by fitting to the results of numerical hydrodynamical simulations for each of the three sources. We provide full formulas for the three sources in Section 5.4.3.

#### 3.8.4 LISA

While gravitational waves from compact binary mergers have been detected at LIGO, its peak sensitivity being at around  $f \sim 100\,\mathrm{Hz}$  means that it is unable to detect gravitational waves from early universe sources, which are expected to be in the mHz range. The space-based LISA (Laser Interferometer Space Antenna) experiment will

be particularly sensitive to this part of the frequency spectrum [23–25, 148, 149], taking advantage of an arm length of 5 million km and 6 laser beams to detect low frequency gravitational waves from extreme mass ratio inspirals (EMRIs) [150], compact binary star systems in the Milky Way [151, 152], supermassive black hole binary systems [153], and the stochastic gravitational wave background (SGWB) from the early universe.

Just like LIGO, LISA depends on laser interferometry: the measurement of interference between two coherent light rays. As gravitational waves pass through the arms of LISA, the path length L of the photons emitted between them changes. The interference of the photons measured at the master satellite reveals changes in the relative  $\Delta L/L$  between two arms, i.e. the characteristic strain. Studying oscillations in different frequency domains allows for the detection of gravitational wave signals, separated from noise that exists at different characteristic frequencies (such as annual variations due to the eccentric orbital pattern).

LISA has received the go ahead for launch in 2035 [152], and will be placed  $20^{\circ}$  behind Earth in its solar orbit [22].

# Chapter 4

# Hot Leptogenesis

I am a servant of the Secret Fire, wielder of the flame of Anor. You cannot pass.

The dark fire will not avail you, flame of Udûn! Go back to the Shadow. You cannot pass!

from The Lord of the Rings by J.R.R. Tolkien

## 4.1 Introduction

The observed neutrino masses can elegantly be explained by the seesaw mechanism, as we covered in Sections 2.7.1 and 3.6. To recap, in the Type-I Seesaw mechanism [105–108], at least two Majorana right-handed neutrinos (RHNs) are added to the Standard Model (SM):

$$\mathcal{L} \supset i\bar{N}_i \partial N_i - \frac{1}{2} m_{N_i} \bar{N}_i^c N_i - Y_{\alpha i} \bar{L}_{\alpha} \tilde{\Phi} N_i + \text{h.c.}, \qquad (4.1.1)$$

where  $i(\alpha)$  denotes RHN generational (lepton flavour) indices and are summed over, the Yukawa matrix is given by Y and the leptonic and Higgs doublets are given by  $L^T = (\nu_L^T, l_L^T)$  and  $\Phi$ , respectively, with  $\tilde{\Phi} = i\sigma_2\Phi$ . Once the Higgs acquires a vacuum expectation value, the light neutrino masses are generated.

Besides providing a simple explanation for light neutrino masses, the Type-I Seesaw

mechanism can also account for the observed baryon asymmetry via thermal leptogenesis [29]. In this scenario, a lepton asymmetry is produced through out-of-equilibrium and CP-violating decays of the RHNs [102–104]. This lepton asymmetry is then converted into a baryon asymmetry via electroweak sphalerons. Most leptogenesis calculations assume that the  $N_1$  particles are in kinetic equilibrium with the Standard Model bath and inherit a thermal distribution with temperature  $T_{\rm SM}$ . For parameter choices which reproduce the observed neutrino masses, the heavier right-handed neutrinos,  $N_2$  and  $N_3$ , are typically in both kinetic and chemical equilibrium with the SM thermal bath [154].

As explained in Section 3.6, while vanilla leptogenesis can successfully generate neutrino masses consistent with data along with the observed baryon asymmetry, it typically leads to a tension [155] between the Davidson-Ibarra bound [123] and the Vissani bound [30]. Furthermore, successful leptogenesis comes at the cost of an accidental cancellation between the tree and one-loop contributions to the light neutrino mass matrix [156]. Resonant leptogenesis [124], characterised by significantly lighter RHNs with a highly degenerate mass spectrum that enhances CP asymmetry during their decays, provides a way to lower the leptogenesis scale while addressing fine-tuning issues in both the Higgs and neutrino mass matrices.

In this chapter, we present an alternative solution to these tensions, where  $N_1$  has a higher temperature,  $T_{N_1}$ , than the SM particles. This leads to a larger number density of  $N_1$  particles, which generate a larger baryon asymmetry after they decay. This scenario has previously been considered in Ref. [154], where an enhancement of up to  $\sim 50$  times the standard leptogenesis baryon asymmetry can be obtained. Ref. [154] requires a connection to thermal dark matter and concludes that resonant leptogenesis is still required to produce the observed baryon asymmetry. In this work, we drop the connection to dark matter and show that non-resonant leptogenesis can produce the observed baryon asymmetry while remaining natural. Schematically,

<sup>&</sup>lt;sup>1</sup>This maximum exists because, above some temperature, the  $N_1$  particles dominate the energy density of the universe.

4.1. Introduction 105

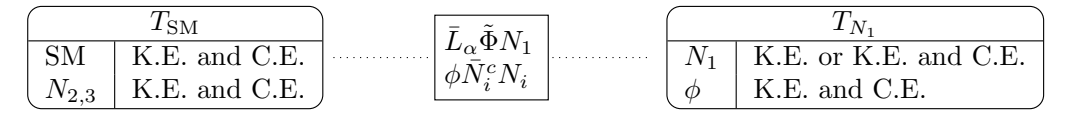


Figure 4.1: Field content and the temperatures of the sectors in hot leptogenesis, along with whether they are in kinetic and chemical equilibrium (K.E. and C.E.) or only kinetic equilibrium (K.E.) around the time of  $N_1$  decay. The dominant coupling connecting the two sectors is taken to be the one responsible for  $N_1$  decay. The scalar field  $\phi$ , which keeps  $N_1$  in kinetic equilibrium, may also mediate a coupling between  $N_1$  and  $N_{2,3}$  (and also between  $N_1$  and the SM Higgs, not shown). Particles of the scalar field  $\phi$  may or may not be present at the time of  $N_1$  decay, depending on whether  $m_{\phi}$  is much greater than  $T_{N_1}$  or not.

the scenario is depicted in Fig. 4.1. We will be interested in  $T_{\rm SM} < T_{N_1}$ , and take the dominant coupling between the two sectors to be the one responsible for  $N_1$  decay. Additional particles are needed to realise equilibrium within the hot sector. We quantitatively demonstrate that this can be realised by introducing a new scalar,  $\phi$ , which is primarily responsible for mediating the self-interactions of  $N_1$ . Within this setup, we consider two regimes. In the first,  $N_1$  is only in kinetic equilibrium during  $N_1$  decay (so  $N_1$  particles can exchange energy between themselves, but there are no number-changing processes that are sufficiently fast to realise chemical equilibrium). In the second,  $N_1$  is in both kinetic and chemical equilibrium with itself and  $\phi$  (similar to the regime considered in Ref. [154]). That is, they are both in thermal equilibrium in the hot sector during  $N_1$  decay.

In Section 4.2 we first motivate this setup, showing that it can be a consequence of inflaton decays. In Section 4.3 we determine the regions of parameter space in our toy model where the two scenarios ( $N_1$  in kinetic or kinetic and chemical equilibrium) are realised and discuss the cosmological constraints on the  $\phi$  particle. In Section 4.4 we derive the relevant Boltzmann equations to track the evolution of the sectors and compute the resulting baryon asymmetry. We present and discuss our results in Section 4.6 and conclude in Section 4.7.

# 4.2 Hot Leptogenesis from Inflaton Decays

While the mechanism of inflation is not yet determined, as a proof of principle we discuss here one plausible scenario. The origin of two sectors with similar, but different, temperatures could be explained by an inflaton that couples with different strengths to the particles within each sector. Assuming perturbative reheating, the reheating temperature in each sector is approximately,<sup>1</sup>

$$T_R \approx \sqrt{\Gamma M_{\rm Pl}}\,,$$
 (4.2.1)

where  $\Gamma$  is the inflaton decay rate to particles within that sector and  $M_{\rm Pl} \approx 1.22 \times 10^{19} \,\text{GeV}$  is the Planck mass. The decay rate of an inflaton  $\sigma$ , with mass  $m_{\sigma}$ , to decay to particle species i, with mass  $m_i$ , is approximately

$$\Gamma_i \approx \frac{y^2 m_\sigma}{8\pi} \,, \tag{4.2.2}$$

for  $m_i \ll m_{\sigma}$  and where y is the coupling of the inflaton to the particle. For an inflaton mass  $m_{\sigma} \sim 10^{13}$  GeV, the reheating temperature is then  $T_R \sim y \times 10^{15}$  GeV, and the ratio of temperatures between the two sectors is

$$\kappa \equiv \frac{T_{N_1}}{T_{\rm SM}} \approx \sqrt{\frac{\Gamma_{N_1}}{\Gamma_{\rm SM}}} \approx \frac{y_{N_1}}{y_{\rm SM}}, \qquad (4.2.3)$$

where  $y_{N_1}$  ( $y_{\rm SM}$ ) is the largest coupling of the inflaton to particles in the hot (SM) sector. As long as the two sectors cannot efficiently exchange energy,  $y_{\rm SM} < y_{N_1}$  will typically lead to  $T_{\rm SM} < T_{N_1}$ . While other factors can impact the precise value of  $\kappa$ , such as the spin of the daughter particles or other degrees of freedom with smaller couplings to  $\sigma$ , the fact that  $y_{N_1}$  and  $y_{\rm SM}$  are not constrained by experiment mean that a wide range of values of  $\kappa$  is plausible.

If there is only a weak coupling between the two sectors, they will not thermalise before the hot  $N_1$  particles decay into particles in the SM sector. A weak coupling

<sup>&</sup>lt;sup>1</sup>Note that for efficient parametric resonance reheating, the relation is more complicated. Parametric resonance reheating occurs due to the resonant oscillation of the inflaton around the minimum, leading to an extremely rapid energy transfer to bosons. This is suppressed for inflaton decays to fermions due to the Pauli exclusion principle [157].

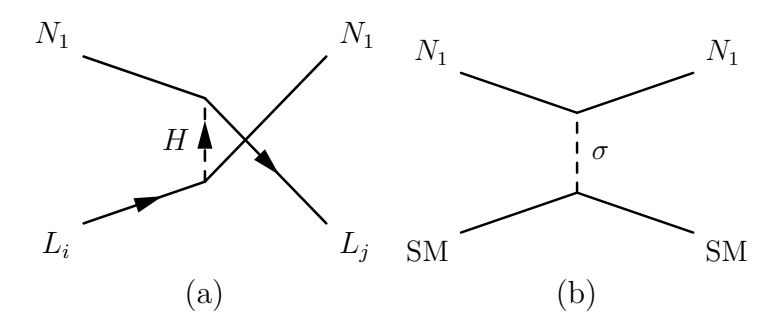


Figure 4.2: Feynman diagrams showing the (a) Higgs- and (b) inflaton-mediated processes which could thermalise the hot and SM sectors. All Standard Model particles are denoted simply by SM.

means that leptogenesis will operate in the weak washout regime and ensures that scattering processes (such as those shown in Fig. 4.2 (a)<sup>1</sup>) are out-of-equilibrium before  $N_1$  decays. In the case of strong washout, there are rapid interactions between the  $N_1$  particles and the SM sectors which would cause the two sectors to thermalise. It is also important that the inflaton itself does not thermalise the hot and SM sectors through the process shown in Fig. 4.2 (b). To avoid this, we require the scattering rate between SM particles and  $N_1$  particles to be slower than the Hubble rate. Taking a simple Yukawa coupling between the inflaton and  $N_1$ ,

$$\mathcal{L} \supset \frac{1}{2} y_{N_1} \, \sigma \bar{N}_1^c N_1 \,,$$
 (4.2.4)

and assuming that the dominant inflaton-SM coupling is a universal Yukawa coupling to all SM fermions,

$$\mathcal{L} \supset y_{\rm SM} \, \sigma \sum_{f \in \rm SM} \overline{\psi}_f \psi_f \,, \tag{4.2.5}$$

we require the interaction rate to be

$$\Gamma_{N_1 \text{ SM} \to N_1 \text{ SM}} = \max(n_{N_1}, n_{\text{SM}}) \langle \sigma v \rangle < H, \qquad (4.2.6)$$

where  $n_{N_1}$  and  $n_{\rm SM}$  are the relevant number densities and  $\langle \sigma v \rangle$  is the thermally averaged elastic cross-section between  $N_1$  and the SM fermions via an inflaton medi-

<sup>&</sup>lt;sup>1</sup>In this chapter and the relevant appendices A and 4.5, we use H to denote the physical Higgs.

ator.<sup>1</sup> When the inflaton decays, the SM particles quickly reach thermal equilibrium so  $n_{\rm SM}=n_{\rm SM}^{\rm eq}(T_{\rm SM})$ . We assume that some unspecified UV particles also allow  $N_1$  to reach thermal equilibrium with itself around the reheating temperature, so that  $n_{N_1}=3\zeta(3)g_{N_1}T_{N_1}^3/4\pi^2$  where  $g_{N_1}=2$  is the number of degrees of freedom of  $N_1$ , but that these reactions rates fall below the Hubble rate before  $N_1$  starts to decay (see Section 4.4). The cross-section for inflaton-mediated  $N_1$ -SM scatterings is

$$\sigma = \frac{y_{\rm SM}^2 y_{N_1}^2}{4\pi s^2 \left(m_{\sigma}^2 + s\right)} \left[ s \left(2m_{\sigma}^2 - 4m_{N_1}^2 + s\right) - 2\left(2m_{N_1}^2 - m_{\sigma}^2\right) \left(m_{\sigma}^2 + s\right) \log\left(\frac{m_{\sigma}^2}{m_{\sigma}^2 + s}\right) \right], \tag{4.2.7}$$

where s denotes the centre-of-mass energy,  $m_{N_1}$  the mass of  $N_1$  and we have assumed  $m_f \ll m_{N_1}, m_{\sigma}$ . The thermal averaging for this process is discussed in Appendix A.1. For a universe consisting of two decoupled relativistic sectors with temperature ratio  $\kappa$ , the Hubble rate is given by

$$H = \sqrt{\frac{8\pi^3}{90} \left(g_{\rm SM}^* + g_{N_1}^* \kappa^4\right)} \frac{T_{\rm SM}^2}{M_{\rm Pl}}, \qquad (4.2.8)$$

where  $g_{\rm SM}^*$  and  $g_{N_1}^*$  denote the effective number of degrees of freedom in the Standard Model and hot sectors, respectively. The relative sizes of  $g_{\rm SM}^*$  and  $g_{N_1}^*\kappa^4$  determine which sector dominates the energy density of the Universe. For energies above the electroweak scale, with  $g_{\rm SM}^* = 106.75 + 4$  and assuming  $g_{N_1}^* = 2$ , the SM sector dominates the Universe's energy density for  $\kappa \lesssim 2.7$ , while the hot sector dominates for  $2.7 \lesssim \kappa$ .

Given Eqs. (4.2.6) to (4.2.8), we can determine the maximum value of  $y_{\rm SM}y_{N_1}$  that ensures that the inflaton does not thermalise the two sectors. For a given  $\kappa$ , this gives an upper bound on the reheating temperature of the hot sector. For chaotic inflation<sup>2</sup>, which fixes  $m_{\sigma} \approx 10^{13} \, \text{GeV}$ . and using  $m_{N_1} = 10^7 \, \text{GeV}$  as our benchmark value, the white region of Fig. 4.3 shows the viable reheating temperatures of the hot sector as

<sup>&</sup>lt;sup>1</sup>Not to be confused with the Higgs vev v. The v that appears always in  $\langle \sigma v \rangle$  is a velocity, typically either the relativistic relative velocity of the interacting particles, or the Møller velocity. See Ref. [158] for detailed discussion.

<sup>&</sup>lt;sup>2</sup>Chaotic inflation is a model of inflation that avoids finely-tuned conditions in the early universe [159].

<sup>&</sup>lt;sup>3</sup>This result is due to the constraints from Cosmic Background Explorer (COBE) data [160].

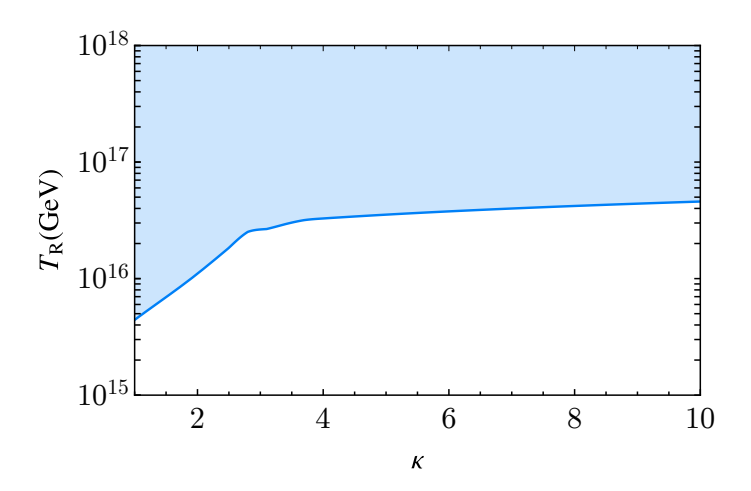


Figure 4.3: Upper bound on the reheating temperature in the hot sector from the requirement that inflaton-mediated elastic scattering does not realise kinetic equilibrium between the hot and SM sectors. In this plot we take  $m_{N_1}=10^7\,\mathrm{GeV}$  and  $m_\sigma=10^{13}\,\mathrm{GeV}$ .

a function of  $\kappa$ . In the blue region, inflaton-mediated interactions will thermalise the two sectors, so that  $T_{\rm SM} \approx T_{N_1}$  and standard leptogenesis would proceed. We find that for the two sectors to remain decoupled, we require  $T_R \lesssim 10^{17}$  GeV, with a slight reduction when  $\kappa \lesssim 3.8$  (where  $n_{\rm SM} \lesssim n_{N_1}$ ). We will be interested in  $N_1$  masses around  $10^7$  GeV, motivated by the Vissani bound limiting  $m_{N_1} \lesssim 7.4 \times 10^7$  GeV for the Higgs mass correction  $\delta \mu^2$  to remain below  $1 \, {\rm TeV}^2$  [30]. Thus, the reheating temperature in the hot sector can be well above the right-handed neutrino masses.

As mentioned above, the inflaton couplings to the different sectors are experimentally unconstrained. As such,  $\kappa$  can in principle take a wide range of values. Some limiting scenarios often studied in the literature are:

1. The inflaton decays exclusively to  $N_1$  [161–166], corresponding to an initial  $n_{\rm SM}=0$  and  $\kappa\to\infty$ . Such a scenario is typically studied in the context of non-thermal leptogenesis, where the assumption is that  $T_R\ll m_{N_1}$  and that the  $N_1$  decay happens immediately after the inflaton decay. For example, Ref. [162] assumes that perturbative inflaton decay is kinematically forbidden, i.e.,  $m_{\sigma}<2m_{N_1}$  so that the only relevant decays are through strong parametric resonance (overcoming the Pauli blocking of fermions). Ref. [163] studies perturbative

inflaton decay into  $N_1$ , but with  $100T_R \lesssim m_{N_1}$  such that the  $N_1$  particles are always out of kinetic and chemical equilibrium, making leptogenesis non-thermal. In this latter scenario,  $N_1$  and the inflaton have similar masses, which is somewhat of a coincidence of scales. The inflaton decaying exclusively to  $N_1$  was first studied away from the limit  $T_R \ll m_{N_1}$  in Ref. [166]. Without a self-interaction in the hot sector, the  $N_1$  distribution after inflaton decay is non-thermal, and the Universe becomes radiation-dominated only after  $N_1$  decay, complicating numerical analysis. In our work, we will assume  $m_{N_i} \ll T_R$  and the presence of an  $N_1$  self-interaction, so the  $N_1$  particles rapidly achieve a thermal distribution.

- 2. The inflaton decay leads to  $\kappa \approx 1$ . When we take the case that  $N_1$  are in kinetic and chemical equilibrium with themselves in Section 4.3.1, our calculations with  $\kappa = 1$  are comparable to the standard leptogenesis scenario with a thermal initial condition.
- 3. The inflaton decays only to the SM, corresponding to  $\kappa \to 0$ . This scenario corresponds to standard leptogenesis with a vanishing initial abundance of  $N_1$ . Since we are interested in increasing the baryon asymmetry compared to standard leptogenesis by increasing the number density of  $N_1$  particles in a sector that is hotter than the SM sector, we will not study  $\kappa < 1$ .

In summary, we see that it is plausible for a simple model of inflation to lead to two decoupled sectors at a similar but different temperature, with a reheating temperature that is significantly above the right-handed neutrino masses. In what follows, we will take this as a starting point and we will study two different scenarios in the regime  $1 \lesssim \kappa$ .

## 4.3 A Model of Hot Leptogenesis

While there are many possible realisations of the scenario we discuss, for concreteness we study a toy model consisting of the SM plus  $N_2$  and  $N_3$  at temperature  $T_{\rm SM}$  and a hot sector containing  $N_1$  and a real scalar  $\phi$  at temperature  $T_{N_1}$ . The lightest right-handed neutrino,  $N_1$ , will decay to produce a lepton asymmetry which ultimately produces the baryon asymmetry, while  $\phi$  will mediate interactions in the hot sector. We will consider two cases: that around the time of  $N_1$  decay either  $N_1$  is only in kinetic equilibrium with itself, or  $N_1$  is in both kinetic and chemical equilibrium with itself. In this section, we find the regions of parameter space which exhibit these two cases.

The relevant interaction Lagrangian terms in our toy model are,

$$\mathcal{L} \supset -Y_{\alpha i} \bar{L}_{\alpha} \tilde{\Phi} N_{i} + \text{h.c.}$$

$$-y_{\phi}^{i} \phi \bar{N}_{i}^{c} N_{i} - \frac{m_{\phi}^{2}}{2} \phi^{2} - \frac{\lambda_{3} m_{\phi}}{3!} \phi^{3} - \frac{\lambda}{4!} \phi^{4}, \qquad (4.3.1)$$

where  $i \in \{1, 2, 3\}$  and  $\alpha \in \{e, \mu, \tau\}$ . The Yukawa matrix,  $Y_{\alpha i}$ , is parametrised using the Casas-Ibarra parameterisation [109],  $Y = v^{-1}U\sqrt{M_{\nu}}R^{T}\sqrt{M_{N}}$  as in Section 3.6.2, where  $v = 174\,\mathrm{GeV}$  is the vacuum expectation value of the Higgs  $^{1}$ , U is the leptonic mixing matrix,  $M_{\nu}$  ( $M_{N}$ ) is the diagonal light (heavy) neutrino mass matrix and R is the complex, orthogonal matrix given in Section 3.6.2. We discuss our specific choice of benchmark point for  $Y_{\alpha i}$  in Section 4.6. We assume that the  $\phi^{3}$  term is small enough that  $\phi$  does not obtain a vacuum expectation value ( $m_{\phi}^{2} > 0$  and  $\lambda_{3} < \sqrt{3\lambda}$ ). In principle, the scalar  $\phi$  could generate the RHN masses, which is natural with diagonal couplings to the RHN mass eigenstates. However, we make the assumption that  $\phi$  does not obtain a vev as we do not wish to restrict our attention to a particular mass generation mechanism and instead pursue a more general analysis of hot leptogenesis. Sizeable non-diagonal couplings between  $\phi$  and the RHN generations could result in premature thermalisation of the two sectors,

<sup>&</sup>lt;sup>1</sup>In this chapter, we use the convention that the  $1/\sqrt{2}$  factor is absorbed into the Higgs vev v.

but we do not investigate this here. While in principle there can also be cubic and quartic couplings with the SM Higgs,  $\phi |\Phi|^2$  and  $\phi^2 |\Phi|^2$ , we assume that these are small enough to keep the two sectors out of thermal contact. Although the inflaton could potentially play the role of  $\phi$ , we do not study this possibility and instead introduce a new scalar particle. As noted in the introduction, standard leptogenesis leads to fine-tuning in the SM Higgs mass [30, 155] and/or in the light neutrino masses [156]. The relevant expressions can be found in these references and the fine-tuning measures we use are given in Section 4.5.

#### 4.3.1 Kinetic and Chemical Equilibria

We first consider the expected phase space distribution of  $N_1$  in different regions of the parameter space of this model. As stated in Section 3.4, when  $N_1$  is in kinetic and chemical equilibrium, it will have a Fermi-Dirac phase space distribution function, with zero chemical potential. When  $N_1$  is only in kinetic equilibrium, its phase space distribution assumes the same form but will be normalised so that the number density of particles,  $n_{N_1}$ , is not fixed to the equilibrium number density,

$$f_{N_1} = \frac{n_{N_1}}{n_{N_1}^{\text{eq}}} f_{N_1}^{\text{eq}}. \tag{4.3.2}$$

Another possibility is that  $N_1$  may have been in kinetic equilibrium at some point after inflaton decay but came out of kinetic equilibrium sometime before  $N_1$  decay. We do not analyse this case in detail, which would require the tracking of individual momentum modes, but we briefly discuss the expected applicability of our results to this scenario. Finally, if the  $N_1$  particles were never in kinetic equilibrium, their momentum would be spiked around half the inflaton mass. We will not consider this case here.

There are a variety of processes to consider to determine which particles are in kinetic or chemical equilibria with themselves or each other. The two sectors are necessarily coupled by the Lagrangian term responsible for  $N_1$  decay, and potentially

also by  $\phi$  mediated processes. The new scalar  $\phi$  can keep  $N_1$  in kinetic equilibrium with itself through s-, t- and u-channel scattering processes, and if  $\phi$  is not too much heavier than  $N_1$ , number-changing interactions could also keep  $N_1$  in chemical equilibrium with itself. We now find the regions of parameter space where the following conditions hold:

- 1. All elastic scattering processes between the hot and SM sectors are slower than the Hubble expansion rate.
- 2. Elastic  $N_1N_1 \leftrightarrow N_1N_1$  scattering processes are faster than the Hubble expansion rate.
- 3. Number changing processes of both  $N_1$  and  $\phi$  are faster than the Hubble expansion rate.

Condition 1 ensures that the two sectors are decoupled, allowing each sector to maintain independent temperatures. Condition 2 ensures that  $N_1$  is in kinetic equilibrium with itself, resulting in a Fermi-Dirac-shaped phase space distribution function. In our analyses, we will ensure that these two conditions always hold. If Condition 3 is satisfied,  $N_1$  will be in both kinetic and chemical equilibrium, achieving an equilibrium number density. It is important to note that chemical equilibrium requires processes that can independently change the comoving number densities of  $N_1$  and  $\phi$ ; for example, the process  $2N_1 \leftrightarrow 2\phi$  alone is not sufficient.

The Hubble rate in this model is given by

$$H = \frac{1}{\sqrt{3}M_{\rm pl}} \sqrt{\frac{\pi^2}{30} g_*^{\rm SM}(T_{\rm SM}) T_{\rm SM}^4 + \rho_{N_1} + \rho_{N_2} + \rho_{N_3} + \rho_{\phi}}, \qquad (4.3.3)$$

where for  $N_i$  and  $\phi$ 

$$\rho = \frac{n}{n^{\text{eq}}} \rho^{\text{eq}} = \frac{n}{n^{\text{eq}}} \frac{g}{2\pi^2} T^4 J_{\pm} \left(\frac{m}{T}\right) , \qquad (4.3.4)$$

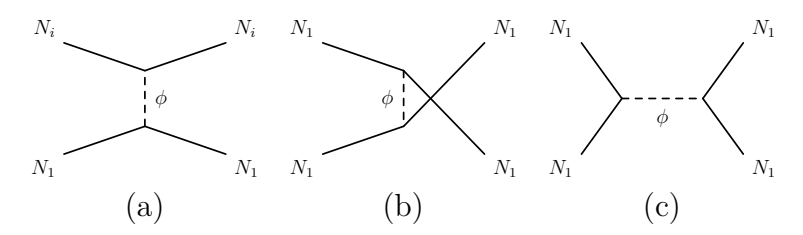


Figure 4.4: Feynman diagrams showing the processes which may put  $N_1$  into kinetic equilibrium with itself ((a) with i=1, (b) and (c)) and with the SM bath ((a) with  $i\in\{2,3\}$ ), which would set  $T_{\rm SM}=T_{N_1}$ .

where

$$J_{\pm}(z) = \int_0^\infty d\xi \frac{\xi^2 \sqrt{\xi^2 + z^2}}{\exp\left[\sqrt{\xi^2 + z^2}\right] \pm 1},$$
 (4.3.5)

with a plus sign for fermion, a negative sign for bosons and where  $\xi = |\mathbf{p}|/T_{N_1}$ . For  $N_2$  and  $N_3$ , which have a vanishing initial condition but approach their equilibrium energy densities throughout the evolution, and for computational simplicity, we approximate their contribution to the energy density as relativistic fermions in thermal equilibrium for  $m_{N_{2,3}} < T_{\rm SM}$  and we neglect their contribution otherwise. We have checked that this approximation does not affect our final results.

#### Condition 1 – Two Decoupled Sectors

For the hot sector to remain thermally decoupled from the SM sector, we require that the decay rate of  $N_1$  to SM particles is slower than the Hubble rate at  $T_{N_1} \gtrsim m_{N_1}$ . For  $m_{N_1} \approx 10^7$  GeV this gives  $Y_{\alpha 1} \lesssim 10^{-5}$ . This condition ensures leptogenesis proceeds in the weak washout regime and that the two sectors do not thermalise via inverse decays,  $N_1$ SM  $\to N_1$ SM scatterings [115, 167] or processes like  $N_1$ SM  $\to$  SM SM before  $N_1$  decays [154]. This also ensures that other processes involving  $Y_{\alpha 1}$ , such as  $N_1$  and  $N_{2,3}$  thermalisation via the Higgs, are slower than the Hubble rate, due to the extra couplings and phase space suppression factors involved.

Beyond the direct coupling of  $N_1$  with the SM plasma, it is possible that the  $\phi$ mediated coupling between  $N_1$  and the heavier  $N_2$  and  $N_3$  (which will be thermally

produced in the SM sector) may thermalise the two sectors via the scattering process shown in Fig. 4.4 (a) with  $i \in \{2,3\}$ . We need to check that the interaction rate per  $N_1$  particle and per  $N_{2,3}$  particle is slower than the Hubble rate. For  $n_{N_1} \approx n_{N_1}^{\rm eq}$  we will have  $n_{N_{2,3}} < n_{N_1}$  since  $m_{N_1} < m_{N_{2,3}}$  and  $T_{\rm SM} < T_{N_1}$ , so the rate per  $N_1$  particle is slower than the rate per  $N_{2,3}$  particle. We therefore only need to check the rate per  $N_{2,3}$  particle. The two sectors will then not thermalise as long as

$$n_{N_1} \langle \sigma v \rangle_{N_1 N_{2,3} \to N_1 N_{2,3}} < H,$$
 (4.3.6)

where the cross-section is given in Eq. (A.1.1), the thermal averaging is given in Eq. (A.2.5) and the Hubble rate is given in Eq. (4.3.3). Here, and for the remaining rate calculations, in this section we approximate  $n_{N_1}^{\text{eq}} \approx n_{N_1}$ . In principle, this could be modified when chemical equilibrium does not hold. This would lead to a proportional shift in the rates calculated here. Thus, our conclusions should be taken as a guide rather than precise statements for the kinetic equilibrium-only scenario. However, it is a good approximation for the kinetic equilibrium-only cases we consider.

We may expect the  $N_1 - \phi$  Yukawa coupling  $y_{\phi}^1$  to be a similar order to  $y_{\phi}^2$  and  $y_{\phi}^3$  since the right-handed neutrino masses are all at a similar scale (although note that we do not discuss the origin of the right-handed neutrino masses here and do not assume that  $\phi$  is a Majoron). The blue region above the dashed blue contour in Fig. 4.5 shows where the rate of this process is greater than the Hubble rate at the time of  $N_1$  decay assuming  $y_{\phi}^1 = y_{\phi}^2$ . That is, where condition 1 is not satisfied. However, this bound can be relaxed, without affecting any other phenomenology, by taking  $y_{\phi}^2 \ll y_{\phi}^1$ . Throughout this chapter, we consider the parameter space where the  $N_1 N_{2,3} \leftrightarrow N_1 N_{2,3}$  scattering rate is less than the Hubble expansion rate to ensure the two sectors do not thermalise with each other.

There are also interactions between the  $\phi$  and the Higgs that are induced at loop level via the coupling to the heavier RHN generations  $N_{2,3}$ , which typically have a larger Yukawa coupling to the Higgs than  $N_1$ . We computed the  $\phi HH$  interaction rate at one-loop level and found an interaction rate much smaller than the Hubble rate  $H \sim T^2/M_p$  for the scenarios we consider. Thus these interactions do not thermalise the two sectors.

#### Condition 2 – Kinetic Equilibrium within the Hot Sector

The processes shown in Fig. 4.4 (a) and (b) along with an extra s-channel process, Fig. 4.4 (c), will keep  $N_1$  in kinetic equilibrium with itself if condition 2 is satisfied,

$$n_{N_1} \langle \sigma v \rangle_{2N_1 \to 2N_1} > H \,, \tag{4.3.7}$$

where the cross-section in given in Eq. (A.1.2) and the thermal averaging is given by Eq. (A.2.1). The green region in Fig. 4.5 shows where condition 2, or Eq. (4.3.7), is satisfied. We see that there is a minimum value of  $y_{\phi}^1$  for a given  $m_{\phi}/m_{N_1}$ . When  $2m_{N_1} \lesssim m_{\phi}$  there is a resonant enhancement as the  $\phi$  propagator in Fig. 4.4 (c) can go on-shell.

#### Condition 3 – Chemical Equilibrium Within the Hot Sector

If there are fast number-changing interactions, such as those shown in Fig. 4.6,  $N_1$  could also be in chemical equilibrium in the hot sector. Chemical equilibrium requires processes which can increase (or decrease) both the comoving number densities of  $N_1$  and  $\phi$  at the same time. This could, for instance, be a combination of  $2N_1 \leftrightarrow \phi$  and  $2N_1 \leftrightarrow 2\phi$ , or either of those along with  $2\phi \leftrightarrow 3\phi$ . If these processes are faster than the Hubble rate we may assume that  $n_{N_1}$  is simply given by  $n_{N_1}^{\rm eq}$ , which simplifies the analysis. This is a version of the scenario considered in [154] (see, e.g., their Eq. 2.19), where the hot sector was populated by the decay of dark matter. If only one of these processes is faster than the Hubble rate, neither  $N_1$  nor  $\phi$  can be assumed to be in chemical equilibrium and their abundances should be tracked dynamically.

 $N_1$  and  $\phi$  also both need to be in chemical equilibrium in the hot sector, so we technically need to check the rate per  $N_1$  particle and the rate per  $\phi$  particle. However,

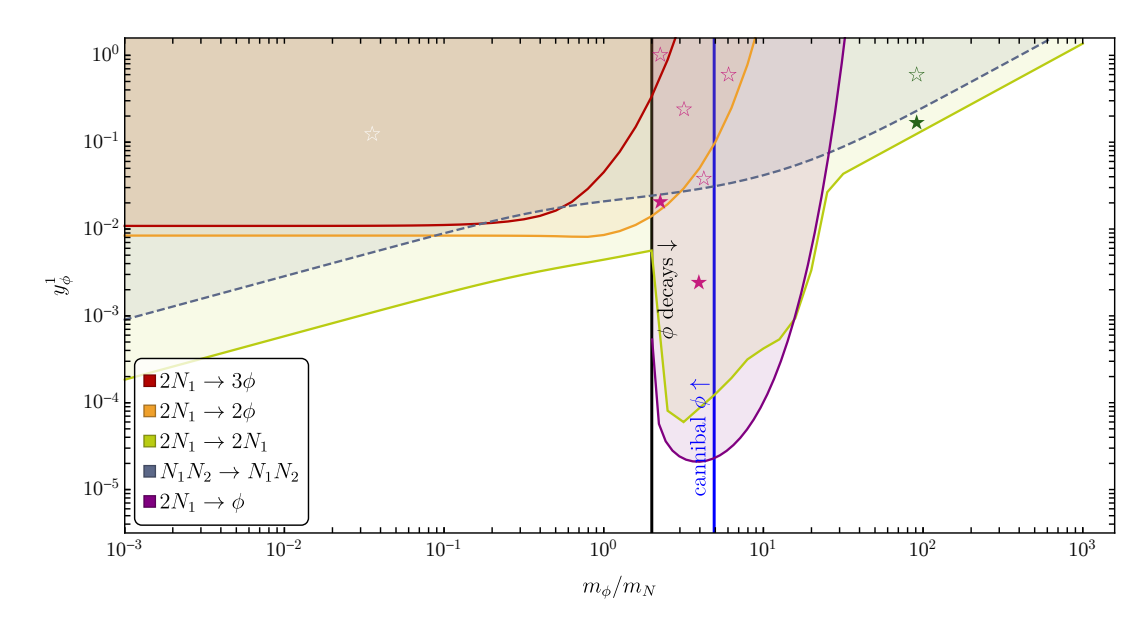


Figure 4.5: Minimal value of  $y_{\phi}^{1}$  such that the various interaction rates are greater than Hubble around the time of decay,  $T_{N_1} = m_{N_1} = 10^7 \,\text{GeV}$ . We have assumed that Hubble is dominated by the SM as it is right after the decays and that  $\lambda = 0.8$ . Assuming  $y_{\phi}^1 = y_{\phi}^2$ , the scattering process  $N_1N_2 \leftrightarrow N_1N_2$  will thermalise the SM and hot sectors in the blue region above the dashed blue contour. To the right of the black line the  $\phi$  abundance will deplete with the  $N_1$  abundance; the region to the right of it is excluded. The region outside of the green area is where the kinetic equilibrium assumption breaks down, and our analysis no longer holds. To the left of the blue line (labelled "cannibal  $\phi$ ") the cannibal process  $2\phi \leftrightarrow 3\phi$ is effective. The pink (green) stars indicate example points in the toy model parameter space where kinetic and chemical (only kinetic) equilibrium can be achieved, where open stars require  $y_{\phi}^2, y_{\phi}^3 \ll y_{\phi}^1$ . The white star shows a point where the cosmology of  $\phi$  would need to be carefully considered.

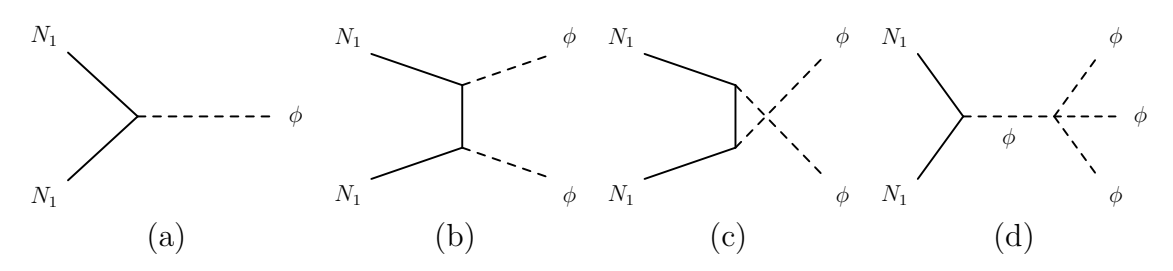


Figure 4.6: Feynman diagrams showing processes which could keep  $N_1$  in chemical equilibrium with the hot sector.

since  $n_{\phi}^{\text{eq}} < n_{N_1}^{\text{eq}}$  at  $T_{N_1} = m_{N_1}$  for all  $\phi$  masses, we only need to check the rate per  $N_1$  particle. The purple region in Fig. 4.5 shows where  $\phi \leftrightarrow 2N_1$  decays and inverse decays, Fig. 4.6 (a), occur faster than the Hubble rate,

$$\langle \Gamma_{\phi \to 2N_1} \rangle \frac{n_{\phi}^{\text{eq}}}{n_{N_1}^{\text{eq}}} = \Gamma_{\phi \to 2N_1} \frac{K_1(m_{N_1}/T_{N_1})}{K_2(m_{N_1}/T_{N_1})} \frac{n_{\phi}^{\text{eq}}}{n_{N_1}^{\text{eq}}} > H, \qquad (4.3.8)$$

where the  $\phi \to 2N_1$  decay rate is given in Eq. (A.1.3) and  $K_1$  and  $K_2$  are modified Bessel functions of the second kind. We see that in the range  $2m_{N_1} \lesssim m_{\phi} \lesssim 10m_{N_1}$  this rate is faster than the Hubble rate if  $10^{-4} \lesssim y_{\phi}^1$ , and for larger  $y_{\phi}^1$  this process can be relevant up to  $m_{\phi} \approx 30m_{N_1}$ .

Next, we consider the process  $2\phi \leftrightarrow 3\phi$ , which is independent of the coupling  $y_{\phi}^{1}$ . Choosing a representative  $\lambda = 0.8$  and  $\lambda_{3} = 0.57\sqrt{3\lambda}$ , we find that the region left of the blue vertical line satisfies

$$n_{\phi}^2 \langle \sigma v^2 \rangle_{3\phi \to 2\phi} > H$$
, (4.3.9)

where we take the thermally averaged cross-section from Ref. [169]. We see that, for these parameters, this process is faster than Hubble for  $m_{\phi} < 5m_{N_1}$ . In what follows, when we assume chemical equilibrium we will work in regions of parameter space where  $2N_1 \leftrightarrow 2N_1$ ,  $\phi \leftrightarrow 2N_1$  and  $2\phi \leftrightarrow 3\phi$  are all faster than Hubble. However, we now briefly consider some other processes that could potentially be relevant.

The orange region in Fig. 4.5 shows where the  $2N_1 \leftrightarrow 2\phi$  processes, Fig. 4.6 (b) and (c), are faster than the Hubble rate,

$$n_{N_1} \langle \sigma v \rangle_{2N_1 \to 2\phi} > H$$
, (4.3.10)

where the cross-section is given in Eq. (A.1.4) and the thermal averaging is given in Eq. (A.2.1). For  $m_{\phi} \lesssim m_{N_1}$  this process is faster than Hubble if  $10^{-2} \lesssim y_{\phi}^1$ , while for heavier  $\phi$  particles a larger coupling is required.

The process  $2N_1 \leftrightarrow 3\phi$  can occur either via t-channel-like diagrams, where the cross-

<sup>&</sup>lt;sup>1</sup>This value, which is not the result of spontaneous symmetry breaking [168], is chosen to maximise the cross section.

section is proportional to  $(y_{\phi}^1)^6$  or via an s-channel type diagram, Fig. 4.6 (d), whose cross-section is proportional  $(y_{\phi}^1)^2\lambda^2$ . Since we are mostly interested in the region  $y_{\phi}^1 \ll \lambda \approx 1$ , where the t-channel processes will be suppressed, we show in red in Fig. 4.5 the region where the s-channel process is faster than Hubble,

$$n_{N_1} \langle \sigma v \rangle_{2N_1 \to 3\phi} > H.$$
 (4.3.11)

The cross-section for this process is given by Eq. (A.1.5) and the thermal averaging is done using Eq. (A.2.1). We see that this process is only faster than Hubble when  $2N_1 \leftrightarrow 2\phi$  and  $2\phi \leftrightarrow 3\phi$  are both faster than Hubble, so it does not create any new regions where chemical equilibrium for  $N_1$  can be established (assuming similar values of  $\lambda_3$  and  $\lambda$  to those chosen here).

Another number-changing process that could be relevant is  $2\phi \to 4\phi$ . However, for an *n*-body massless particle, the phase space factor goes as

$$\Pi^n \sim \frac{1}{2(4\pi)^{2n-3}\Gamma(n)\Gamma(n-1)}$$
(4.3.12)

In comparison to the  $2\phi \to 3\phi$  cross-section, there is a phase space suppression factor of  $1/(192\pi^2)$ . Therefore the ratio of the cross-sections goes as

$$\frac{\sigma_{2\phi \to 4\phi}}{\sigma_{2\phi \to 3\phi}} \sim \frac{\lambda^2}{192\pi^2 \lambda_3^2} \,. \tag{4.3.13}$$

This implies that the  $2\phi \to 4\phi$  process is subdominant to  $2\phi \to 3\phi$  as long as  $\lambda \ll \sqrt{192}\pi\lambda_3 \approx 44\lambda_3$ .

## 4.3.2 Cosmology of the Scalar $\phi$

We finish this section with a discussion of the cosmology of the new scalar  $\phi$ . If  $m_{\phi} < 2m_{N_1}$ , the hot sector will not deplete during  $N_1$  decay and there will be a non-negligible abundance of  $\phi$ , which will freeze out relativistically. While the scalar  $\phi$  is not stable, its four-body decay (via two off-shell  $N_1$  particles) is suppressed by  $Y_{\alpha i}^4$ . If  $\phi$  couples to all three RHNs, we find that  $Y_{\alpha i}$  is typically large enough such

that the decay can be expected to deplete the sector before BBN. However, this will cause a large entropy dump which will wash out the generated asymmetry to some extent. If  $\phi$  only couples to  $N_1$ , the smallness of  $Y_{\alpha i}$  implies that  $\phi$  is stable on a cosmological timescale. Because it freezes out relativistically, its large abundance will either give rise to a large contribution to  $\Delta N_{\rm eff}$  – the number of relativistic degrees of freedom at BBN – or an overproduction of (dark) matter, depending on its mass. We conclude that in our current model  $m_{\phi}$  needs to be larger than  $2m_{N_1}$ .

#### 4.3.3 Summary

In summary, we see that there are many relevant processes and different possible regimes which can realise kinetic or kinetic and chemical equilibrium in the hot sector, even for our simple toy model. To ensure the SM and hot sectors remain decoupled we require that leptogenesis occurs in the weak washout regime, effectively limiting the size of the Yukawa coupling. From Fig. 4.5 we see that, for  $\lambda=0.8$  and  $\lambda_3\sim\sqrt{3\lambda}$ , we can assume that  $N_1$  is in kinetic and chemical equilibrium with the hot sector around the time of  $N_1$  decays if  $2\,m_{N_1}< m_\phi< 5\,m_{N_1},\ 10^{-4}\lesssim y_\phi^1$  and  $y_\phi^{2,3}\lesssim 10^{-2}$ . For  $\lambda\ll 1$  chemical equilibrium could be established through  $\phi\leftrightarrow 2N_1$  and  $2N_1\leftrightarrow 2\phi$  (which requires  $y_\phi^1\gtrsim 10^{-2}$  and typically require  $y_\phi^{2,3}\ll y_\phi^1$ ). When  $30\,m_{N_1}\lesssim m_\phi$  and  $y_\phi^{2,3}\lesssim 10^{-2}\lesssim y_\phi^1$  we can assume that  $N_1$  is only in kinetic equilibrium. Both cases can also be realised for  $m_\phi<2m_{N_1}$ , but in that case an entropy dump and/or washout would need to be carefully considered. We indicate with pink, green and white stars the regions where these conditions hold (see caption of Fig. 4.5 for details).

<sup>&</sup>lt;sup>1</sup>An alternative possibility is the existence of an additional portal coupling (for example a coupling to the SM Higgs) through which the  $\phi$  abundance can deplete. In this scenario, the washout effect from this decay needs to be carefully considered.

# 4.4 Tracking the Evolution of the Hot and SM Sectors

In the simplest formulation, the leptogenesis kinetic equations operate in the one-flavoured regime, accounting for only a single flavour of charged lepton. This is a good approximation at very high temperatures ( $T \gg 10^{12}$  GeV) when charged lepton Yukawa coupling processes are out of thermal equilibrium, resulting in a coherent superposition of the three flavour eigenstates.

However, at lower temperatures ( $10^9 \,\text{GeV} \ll T \ll 10^{12} \,\text{GeV}$ ), the interaction rates proportional to the tau Yukawa couplings come into thermal equilibrium and can cause decoherence, necessitating a description in terms of two flavour eigenstates. In our case, leptogenesis occurs at even lower temperatures ( $T < 10^9 \,\text{GeV}$ ), where interactions mediated by the muon have equilibrated. In these regimes, a density matrix formalism [116, 170–173] provides a more comprehensive description than semiclassical Boltzmann equations, which do not include flavour oscillations in the lepton asymmetry. For this reason, we solve the density matrix equations which capture the time evolution of the RHN number densities in the hot and SM sectors, and the lepton asymmetry number density (which is promoted to a density matrix,  $N_{\alpha\beta}$ ).

As discussed in Section 4.2, the Hubble expansion rate depends on the energy densities of both the hot and SM sectors. Since we track the energy density of both sectors, it will be convenient to evolve the density matrix equation as a function of the scale factor, a, which is then

$$aH\frac{dN_{N_1}}{da} = -\Gamma_{D_1}(z_{N_1})N_{N_1} + \Gamma_{D_1}(z_{SM})N_{N_1}^{eq}, \qquad (4.4.1)$$

$$aH\frac{dN_{N_2}}{da} = -\Gamma_{D_2}(z_{N_2}) \left( N_{N_2} - N_{N_2}^{\text{eq}} \right) , \qquad (4.4.2)$$

$$aH\frac{dN_{N_3}}{da} = -\Gamma_{D_3}(z_{N_3}) \left( N_{N_3} - N_{N_3}^{\text{eq}} \right) , \qquad (4.4.3)$$

$$aH\frac{dN_{\alpha\beta}}{da} = \epsilon_{\alpha\beta}^{(1)} \left( \Gamma_{D_1}(z_{N_1}) N_{N_1} - \Gamma_{D_1}(z_{\rm SM}) N_{N_1}^{\rm eq} \right) - \frac{1}{2} W_1 \left\{ P^{(1)}, n \right\}_{\alpha\beta}$$

$$+\sum_{i=2}^{3} \epsilon_{\alpha\beta}^{(i)} \Gamma_{D_{i}}(z_{N_{i}}) \left(N_{N_{i}} - N_{N_{i}}^{\text{eq}}\right) - \frac{1}{2} W_{i} \left\{P^{(i)}, N\right\}_{\alpha\beta}$$

$$-\Lambda_{\tau} \begin{bmatrix} \begin{pmatrix} 1 & 0 & 0 \\ 0 & 0 & 0 \\ 0 & 0 & 0 \end{pmatrix}, \begin{bmatrix} \begin{pmatrix} 1 & 0 & 0 \\ 0 & 0 & 0 \\ 0 & 0 & 0 \end{pmatrix}, N \end{bmatrix}_{\alpha\beta}$$

$$-\Lambda_{\mu} \begin{bmatrix} \begin{pmatrix} 0 & 0 & 0 \\ 0 & 1 & 0 \\ 0 & 0 & 0 \end{pmatrix}, \begin{bmatrix} \begin{pmatrix} 0 & 0 & 0 \\ 0 & 1 & 0 \\ 0 & 0 & 0 \end{pmatrix}, N \end{bmatrix}_{\alpha\beta}, \qquad (4.4.4)$$

where i is a generation index,  $\alpha$ ,  $\beta$  are lepton flavour indices,  $N_{N_i}$  and  $N_{\alpha\beta}$  are the comoving number density of  $N_i$  and the B-L asymmetry for lepton flavour indices  $\alpha$ ,  $\beta$ , respectively,  $\Gamma_{D_i} = \Gamma_{D_i}^0 \langle m_{N_i}/E_{N_i} \rangle$  are the thermally averaged decay rates of  $N_i$  where we assume Maxwell-Boltzmann statistics with  $\langle m_{N_i}/E_{N_i} \rangle = K_1(z_{N_i})/K_2(z_{N_i})$ . For the  $N_1$  decay, we thermally average over the hot sector using the variable  $z_{N_1} = m_{N_1}/T_{N_1}$  while for the  $N_1$  inverse decays from the SM, and for  $N_2$  and  $N_3$ , we thermally average over the Standard Model sector using the variables  $z_{\rm SM} = m_{N_1}/T_{\rm SM}$  and  $z_{N_{2,3}} = m_{N_{2,3}}/T_{\rm SM}$  respectively.

The equilibrium abundance of  $N_i$  is denoted as  $N_i^{\rm eq}$  and the initial abundance of  $N_1$  is  $N_{N_1} \propto \kappa^3$ . The initial abundance for  $N_2$  and  $N_3$  are assumed to be vanishing, which is an arbitrary choice for our computation as  $N_2$  and  $N_3$  are both in the strong washout regime so reach a thermal abundance before the  $N_1$  particles decay. Thus, their initial abundance (whether thermal or vanishing) has an insignificant effect on the final results. The washout terms, which remove the lepton asymmetry produced by decays of  $N_1$  in the hot sector, are denoted by  $W_i$ . We remind the reader that when the hot and visible sectors remain decoupled before  $N_1$  decays, the washout is weak. The decay asymmetry (between RHNs decaying to leptons and the Higgs doublet, compared to the CP-conjugate process) generated by the decays of  $N_i$  is given by the CP-asymmetry matrix  $\epsilon_{\alpha\beta}^{(i)}$  [102, 171, 173, 174].  $\Lambda_{\tau}$  ( $\Lambda_{\mu}$ ) denote the thermal widths of the tau (muon) charged leptons, which is obtained from the imaginary part of the self-energy correction to the lepton propagator in the plasma.

Finally,  $P_{\alpha\beta}^{(i)} \equiv c_{i\alpha}c_{i\beta}^*$  where  $c_{i\alpha} = Y_{\alpha i}/\sqrt{(YY)_{ii}}$  denote projection matrices which describe how a given flavour of lepton is washed out.

We note that this equation describes both the decays of  $N_1$  from the hot sector into the SM and the possible inverse decays from the SM into the hot sector, as well as the SM washout processes. We note that while we include the evolution of the RHNs  $N_2$  and  $N_3$  for completeness, their contribution to the lepton asymmetry compared to  $N_1$  is small. To compute the final lepton asymmetry one solves the coupled system for  $z_{N_1} \gg 1$  and takes the trace of the  $N_{\alpha\beta}$  matrix,  $N_{B-L}^f = \text{Tr}[N_{\alpha\beta}]$ . Finally, to calculate the baryon asymmetry (as previously shown in Section 3.6), we multiply  $N_{B-L}^f$  by the sphaleron conversion factor and divide by the photon number density, to account for the change between the end of the leptogenesis era and recombination,  $\eta_B = a_{\rm sph} N_{B-L}^f / N_{\gamma}^{\rm rec}$  where  $a_{\rm sph} = 28/79$  [100].

# 4.4.1 $N_1$ in Kinetic and Chemical Equilibrium

Having established the density matrix equations which determine the matter-antimatter asymmetry in our setup, we now consider how the temperatures of the two sectors evolve with time, assuming that kinetic and chemical equilibrium can be maintained within the hot sector while  $N_1$  decays (pink stars in Fig. 4.5). We first consider the SM temperature,  $T_{\rm SM}$ , and then the hot sector temperature,  $T_{N_1}$ .

Before  $N_1$  starts to decay around  $T_{N_1} \sim m_{N_1}$ , its comoving number density  $N_{N_1}$  will remain constant,  $T_{N_1}$  will drop as  $a^{-1}$ , and the two sectors will remain decoupled. When  $N_1$  starts to decay, the hot sector transfers energy  $(Q_{N_1})$  to the SM sector at a rate

$$\frac{dQ_{N_1}}{dt} = -\frac{dQ_{SM}}{dt} = -m_{N_1} V \Gamma_{D_1}^0 \left( N_{N_1} - N_{N_1}^{eq} \right) , \qquad (4.4.5)$$

where we normalise using the volume that contains one photon when we begin tracking the abundances,  $V=1/n_{\gamma}^{eq}(a=1)$ . Note that this is exact since the thermally averaged energy transfer rate is  $\langle \Gamma_{D_1}^0 m_{N_1} E_{N_1} / E_{N_1} \rangle = m_{N_1} \Gamma_{D_1}^0$ .

As the SM sector is in thermodynamic equilibrium, we can apply the second law of thermodynamics to calculate the change in total entropy of the Standard Model,

$$dS_{\rm SM} = \frac{dQ_{\rm SM}}{T_{\rm SM}}, \qquad (4.4.6)$$

and use this to find the evolution of  $T_{\rm SM}$  with a. First we write

$$\frac{dS_{\rm SM}}{da} = \frac{d(s_{\rm SM}a^3V)}{da},\tag{4.4.7}$$

where  $s_{\rm SM}$  is the SM sector entropy density, which becomes

$$\frac{1}{T_{\rm SM}} \frac{dQ_{\rm SM}}{da} = a^3 V \frac{ds_{\rm SM}}{dT_{\rm SM}} \frac{dT_{\rm SM}}{da} + 3a^2 V s_{\rm SM}, \qquad (4.4.8)$$

when we use Eq. (4.4.6) and differentiate the right-hand side. The rate of change of the SM sector entropy density  $s_{\text{SM}}$  with respect to its temperature is

$$\frac{ds_{\rm SM}}{dT_{\rm SM}} = \frac{2\pi^2}{15} g_*(T_{\rm SM}) T_{\rm SM}^2 + \frac{2\pi^2}{45} T_{\rm SM}^3 \frac{dg_*(T_{\rm SM})}{dT_{\rm SM}}, \qquad (4.4.9)$$

where numerically we neglect the second term which only has a small change due to  $N_2$  and  $N_3$ . Finally, using Eqs. (4.4.5), (4.4.8) and (4.4.9), we find that

$$\frac{dT_{\rm SM}}{da} = \frac{m_{N_1}}{3a^4 H s_{\rm SM}} \Gamma_{D_1}^0 \left( N_{N_1} - N_{N_1}^{\rm eq} \right) - \frac{T_{\rm SM}}{a} \,. \tag{4.4.10}$$

Next, we show how we determine the evolution of  $T_{N_1}$ . When  $N_1$  is in kinetic and chemical equilibrium, the solution to Eq. (4.4.1) is the equilibrium comoving number density, which is

$$N_{N_1}^{\text{eq}} = a^3 n_{N_1}^{\text{eq}} V = a^3 V \frac{g_{N_1}}{2\pi^2} T_{N_1}^3 I_+ \left(\frac{m_{N_1}}{T_{N_1}}\right), \qquad (4.4.11)$$

where  $n_{N_1}$  is the (non-comoving) number density of  $N_1$ . We account for the quantum statistics of  $N_1$  using

$$I_{+}(z_{N_{1}}) = \int_{0}^{\infty} d\xi \frac{\xi^{2}}{\exp\left(\sqrt{\xi^{2} + z_{N_{1}}^{2}}\right) + 1},$$
 (4.4.12)

where  $\xi = |\mathbf{p}_{N_1}|/T_{N_1}$ . Thus, for a fixed  $m_{N_1}$  there is then a one-to-one relationship between  $N_{N_1} = N_{N_1}^{\text{eq}}$  and  $T_{N_1}$ , so solving Eq. (4.4.1) tells us how  $T_{N_1}$  evolves with a. Equations (4.4.1) to (4.4.4), (4.4.10) and (4.4.11) then provide a set of coupled differential equations which we solve using the numerical framework of ULYSSES [175, 176]. Once we fix an initial  $T_{\rm SM}$ ,  $\kappa = T_{N_1}/T_{\rm SM}$  and the comoving number densities, we can use these equations to track  $N_{N_i}$ ,  $T_{N_1}$ ,  $T_{\rm SM}$  and  $N_{\alpha\beta}$  as a function of a, which allows us to compute the final baryon asymmetry  $\eta_B$ . As the scalar  $\phi$  remains in kinetic and chemical equilibrium with  $N_1$ , the hot sector depletes completely as  $N_1$  decays. We do not include the contribution from  $\phi$  in the computation of the asymmetry, since for  $2m_{N_1} < m_{\phi}$  its abundance will be Boltzmann suppressed at the time of  $N_1$  decay. The  $\phi$  population will both mildly increase the generated asymmetry by producing  $N_1$ 's as it decays, and mildly decrease it as it dumps entropy into the SM sector.

# 4.4.2 $N_1$ in Kinetic Equilibrium Only

We will now explore regions of the parameter space where number-changing interactions are slower than the Hubble rate, so the assumption of chemical equilibrium no longer holds (green stars in Fig. 4.5). In this case, the density matrix equations, Eqs. (4.4.1) to (4.4.4), and the SM temperature derivative  $dT_{\rm SM}/da$ , Eq. (4.4.10), remain the same as in the previous section. However, the evolution of the temperature of the hot sector,  $T_{N_1}(a)$ , is no longer given by Eq. (4.4.11), as the lack of number-changing interactions leads to a departure from the equilibrium number density.

The phase space distribution function for  $N_1$  is  $f_{N_1} = \left(n_{N_1}/n_{N_1}^{\rm eq}\right) f_{N_1}^{\rm eq}$  where  $f_{N_1}^{\rm eq}$  is the Fermi-Dirac distribution. Neglecting quantum statistics by utilising the Maxwell-Boltzmann distribution instead, the energy density  $\rho$  and pressure p of  $N_1$  become

$$\rho_{N_1} = \left(\frac{n_{N_1}}{n_{N_1}^{\text{eq}}}\right) \rho_{N_1}^{\text{eq}}, \tag{4.4.13}$$

$$p_{N_1} = \left(\frac{n_{N_1}}{n_{N_1}^{\text{eq}}}\right) p_{N_1}^{\text{eq}}. \tag{4.4.14}$$

We can now calculate the evolution of  $T_{N_1}$  using the second law of thermodynamics

and comoving energy conservation. First, we use the second law of thermodynamics,

$$dS_{N_1} = \frac{dQ_{N_1}}{T_{N_1}}, (4.4.15)$$

to equate

$$\frac{dS_{N_1}}{da} = \frac{ds_{N_1}a^3V}{da} {4.4.16}$$

$$= \frac{d}{da} \left( \frac{\rho_{N_1} + p_{N_1}}{T_{N_1}} a^3 V \right) \tag{4.4.17}$$

$$= \frac{a^3 V}{T_{N_1}} \left( \frac{d\rho_{N_1}}{da} + \frac{dp_{N_1}}{da} - s_{N_1} \frac{dT_{N_1}}{da} + 3 \frac{s_{N_1} T_{N_1}}{a} \right), \tag{4.4.18}$$

with

$$\frac{1}{T_{N_1}} \frac{dQ_{N_1}}{da} = -\frac{m_{N_1} V}{T_{N_1}} \left( \Gamma_{D_1}^0 N_{N_1} - \Gamma_{D_1}^0 N_{N_1}^{\text{eq}} \right) . \tag{4.4.19}$$

We see that we now require expressions for the rate of change of the energy density of  $N_1$ ,  $d\rho_{N_1}/da$ , and for the rate of change of the pressure of  $N_1$ ,  $d\rho_{N_1}/da$ .

To find an expression for  $d\rho_{N_1}/da$  we can use the conservation of total comoving energy density,

$$a\frac{d\rho_{\text{tot}}}{da} + 3(\rho_{\text{tot}} + p_{\text{tot}}) = 0,$$
 (4.4.20)

where  $\rho_{\text{tot}}$  and  $p_{\text{tot}}$  are the total energy density and pressure, respectively. We see that the derivatives of the energy densities in the two sectors are related by

$$a\frac{d\rho_{N_1}}{da} = -3(\rho_{\text{tot}} + p_{\text{tot}}) - a\frac{d\rho_{\text{SM}}}{da}.$$
 (4.4.21)

For the rate of change of the pressure,  $dp_{N_1}/da$ , we differentiate Eq. (4.4.14) with respect to a to write  $dp_{N_1}/da$  in terms of  $dT_{N_1}/da$  and  $dn_{N_1}/da$ ,

$$\frac{dp_{N_1}}{da} = \frac{n_{N_1}}{n_{N_1}^{\text{eq}}} \frac{dp_{N_1}^{\text{eq}}}{da} + \frac{dn_{N_1}}{da} \frac{p_{N_1}^{\text{eq}}}{n_{N_1}^{\text{eq}}} - \frac{p_{N_1}^{\text{eq}}}{n_{N_1}^{\text{eq}}} \frac{dn_{N_1}^{\text{eq}}}{da}$$
(4.4.22)

$$= \left(\frac{n_{N_1}}{n_{N_1}^{\text{eq}}} \frac{dp_{N_1}^{\text{eq}}}{dT_{N_1}} - \frac{p_{N_1}^{\text{eq}}}{n_{N_1}^{\text{eq}}} \frac{dn_{N_1}^{\text{eq}}}{dT_{N_1}}\right) \frac{dT_{N_1}}{da} + \frac{dn_{N_1}}{da} \frac{p_{N_1}^{\text{eq}}}{n_{N_1}^{\text{eq}}}.$$
 (4.4.23)

Together, Eqs. (4.4.18), (4.4.19), (4.4.21) and (4.4.23) give an expression for  $dT_{N_1}/da$  in terms of quantities we can compute or track. This, in combination with the

density matrix equations, Eqs. (4.4.1) to (4.4.4), and the  $T_{\rm SM}$  evolution equation in the previous section, Eq. (4.4.10), can be solved with the appropriate initial conditions to find the resulting baryon asymmetry. The initial conditions we take for our benchmark point are that  $N_1$  has an equilibrium abundance while  $N_2$  and  $N_3$  have vanishing initial abundance.

This is motivated by the possibility that  $\phi$  (or another particle) mediated sufficiently fast number changing rates for  $N_1$  at higher temperatures, but that it no longer can at  $T_{N_1} \sim m_{N_1}$ . In the case where  $N_1$  is only in kinetic equilibrium with itself around its decay, the  $\phi$  abundance is heavily suppressed and does not contribute to the asymmetry generation (beyond maintaining kinetic equilibrium in the hot sector).

# 4.5 Fine-Tuning

To quantify the degree of fine-tuning present in the neutrino sector, we will adopt a fine-tuning measure that is the inverse of that used in [156]. The matrix of physical light neutrino masses  $M_{\nu}$  is

$$M_{\nu} = M_{\nu}^{\text{tree}} + M_{\nu}^{\text{1-loop}},$$
 (4.5.1)

where  $M_{\nu}^{\text{tree}}$  contains the tree-level Lagrangian neutrino masses and  $M_{\nu}^{\text{1-loop}}$  is the one-loop contribution (which is always negative) [156]. The fine-tuning can be measured using,

$$\Delta_{\nu} = \frac{\sum_{i=1}^{3} \text{SVD}[M_{\nu}]_{i}}{\sum_{i=1}^{3} \text{SVD}[M_{\nu}^{1-\text{loop}}]_{i}},$$
(4.5.2)

where SVD is the Singular Value Decomposition of the matrix, i.e., SVD[M]<sub>i</sub> is the square root of the i-th (real and positive) eigenvalue of  $M^*M$ . If the eigenvalues of M are real and positive, then the singular value decomposition of M simply gives the eigenvalues. Fine-tuning of  $\Delta_{\nu} \approx 1\%$  corresponds to, e.g.,  $M_{\nu}^{\text{tree}} \approx 100 M_{\nu}$  and  $M_{\nu}^{\text{1-loop}} \approx 100 M_{\nu}$ , so the tree- and loop-level masses would cancel to one part in 100.

Analogously for the Higgs sector, we will have

$$\mu_H^2 \approx (\mu_H^{\text{tree}})^2 - |\delta\mu^2|, \qquad (4.5.3)$$

where  $\mu_H = \frac{m_h}{\sqrt{2}} = 88 \,\text{GeV}$  is the effective Higgs mass parameter,  $\mu_H^{\text{tree}}$  is the Lagrangian Higgs parameter and  $\delta \mu^2$  is the one-loop correction to the Higgs mass parameter [155],

$$|\delta\mu^2| \approx \frac{1}{4\pi^2} \text{Tr}\left[Y M_N^2 Y^{\dagger}\right].$$
 (4.5.4)

The degree of fine-tuning in the mass parameters (not the mass squared parameters) can be measured with

$$\Delta_H = \sqrt{\frac{(\mu_H^{\text{tree}})^2 - |\delta\mu^2|}{\frac{1}{2}((\mu_H^{\text{tree}})^2 + |\delta\mu^2|)}} \approx \sqrt{\frac{\mu_H^2}{|\delta\mu^2|}},$$
(4.5.5)

where we have assumed  $\mu_H^2 \ll (\mu_H^{\rm tree})^2$ ,  $|\delta\mu^2|$ . Fine-tuning of  $\Delta_H = 10\%$  corresponds to  $|\delta\mu| = 10\mu_H = 880\,{\rm GeV}$ .

### 4.6 Results

Standard non-resonant leptogenesis, which can produce a baryon asymmetry consistent with observations using RHN masses around  $10^6$ – $10^7$  GeV, requires fine-tuning of the light neutrino masses [156] and the SM Higgs mass [30, 155]. The neutrino mass fine-tuning occurs because the tree and one-loop contributions to the light neutrino mass matrix have opposing signs [177] and standard leptogenesis requires them to be separately large, and then largely cancel, to give an overall small neutrino mass consistent with observation. Fine-tuned solutions are favoured because the specific structure of the R-matrix reduces effective Yukawa couplings, which in turn decreases washout effects and leads to successful leptogenesis, while also enabling this critical cancellation between the tree-level and one-loop contributions, keeping the light neutrino masses within experimental bounds. The SM Higgs mass is also fine-tuned as the RHNs contribute at the one-loop level, with lower RHN masses

4.6. Results 129

Benchmark	$S_1$	$S_2$	$S_3$	$\overline{S_1}$	$\overline{S_2}$	$\overline{S_3}$	$S_4$	$\overline{S_4}$	Our Benchmark
$\Delta_{\nu} \left[\%\right]$	0.2	0.3	0.2	0.6	0.7	0.4	0.2	0.5	855
$\Delta_H\left[\% ight]$	0.08	0.02	0.004	0.3	0.06	0.1	0.001	0.007	10.4

Table 4.1: Degree of fine-tuning for the best-fit points found in Ref. [156] and for our benchmark point (see Table 4.2), using the fine-tuning measures given in Section 4.5. Smaller numbers indicate a larger degree of fine-tuning, with some degree of fine-tuning for numbers smaller than  $\sim 10\%$ .

giving a smaller loop level contribution but also reducing the amount of baryon asymmetry produced.

Using the measures defined in Section 4.5, the degree of fine-tuning for both the light neutrino mass and the SM Higgs required for successful standard leptogenesis with  $m_{N_1} \sim 10^{6.5}$  GeV is given in Table 4.1, based on benchmarks from Ref. [156]. These benchmarks,  $S_i$  ( $\overline{S_i}$ ) for i=1,2,3,4, correspond to normal (inverted) ordering with the PMNS matrix parameters set to their best-fit values based on global data [178]. The remaining Casas-Ibarra parameters are fixed to ensure a viable baryon asymmetry. From Table 4.1, we see that the fine-tuning is worse than 1% for both the light neutrino mass and the SM Higgs. We present these benchmarks and their associated fine-tuning measures to evaluate how effectively hot leptogenesis can reduce fine-tuning while still producing the observed baryon asymmetry.

Here we explore two distinct scenarios of hot leptogenesis which alleviate this finetuning: one in which  $N_1$  is only in kinetic equilibrium with itself before decay and one in which chemical equilibrium is also established. The parameters that determine whether chemical and kinetic equilibrium are established are different to those that determine the baryon asymmetry (except that they determine the manner of evolution of our model – these scenarios evolve under a different set of evolution equations as described in the previous section). The parameters related to the baryon asymmetry are given in Table 4.2.

We will focus on a benchmark scenario for the neutrino parameters, where we use the Casas-Ibarra parametrisation to construct the Yukawa matrix Y [109]. The

Parameter	Unit	Benchmark point		
δ	[°]	270		
$\alpha_{21}$	[°]	50		
$\alpha_{31}$	[°]	120		
$\theta_{23}$	[0]	49.1		
$ heta_{12}$	[°]	33.41		
$ heta_{13}$	[°]	8.54		
$\overline{x_1}$	[°]	7		
$y_1$	[°]	15		
$x_2$	[°]	1		
$y_2$	[°]	2		
$x_3$	[°]	4		
$y_3$	[°]	3		
$\overline{m_1}$	[eV]	0		
$\log_{10}\left(m_{N_1}/[{ m GeV}]\right)$	[1]	7		
$\log_{10} \left( m_{N_1} / [\text{GeV}] \right) \\ \log_{10} \left( m_{N_2} / [\text{GeV}] \right)$	[1]	7.006		
$\log_{10}\left(m_{N_3}/[{ m GeV}]\right)$	[1]	7.4		
$\kappa$	[1]	10		

Table 4.2: Input parameters in the Casas-Ibarra parametrisation for our benchmark point, see text for details.

constrained light neutrino parameters  $\delta$ ,  $\theta_{12}$ ,  $\theta_{13}$  and  $\theta_{23}$  are fixed at their bestfit value from recent global fit data [179] where we assume normally ordered light neutrino masses and for simplicity assume the lightest neutrino mass  $m_1 = 0 \,\mathrm{eV}$ . While we fix the Majorana phases to be 50° and 120°, they do not significantly affect the resulting baryon asymmetry. For the right-handed neutrino masses, we choose an intermediate-mass scale  $m_{N_1} \sim 10^7 \,\mathrm{GeV}$ , commensurate with the standard case studied in Ref. [156].

We fix  $m_{N_2}$  and  $m_{N_3}$  to reduce the Higgs fine-tuning measure while ensuring that leptogenesis occurs well beyond the resonant regime (the decay widths of  $N_1$ ,  $N_2$  and  $N_3$  are approximately  $10^{-5}$  GeV,  $10^{-3}$  GeV and  $10^{-2}$  GeV, respectively, which are much smaller than the  $N_1$ – $N_2$  mass splitting of approximately  $10^5$  GeV). The remaining Casas-Ibarra parameters,  $x_i$  and  $y_i$ , are chosen to provide a reduced fine-tuning to the light neutrino masses. Finally, the benchmark has an initial ratio of temperatures of  $\kappa = T_{N_1}/T_{\rm SM} = 10$ , which gives approximately the maximum achievable baryon asymmetry. We note that if we assumed standard thermal leptogenesis,

4.6. Results 131

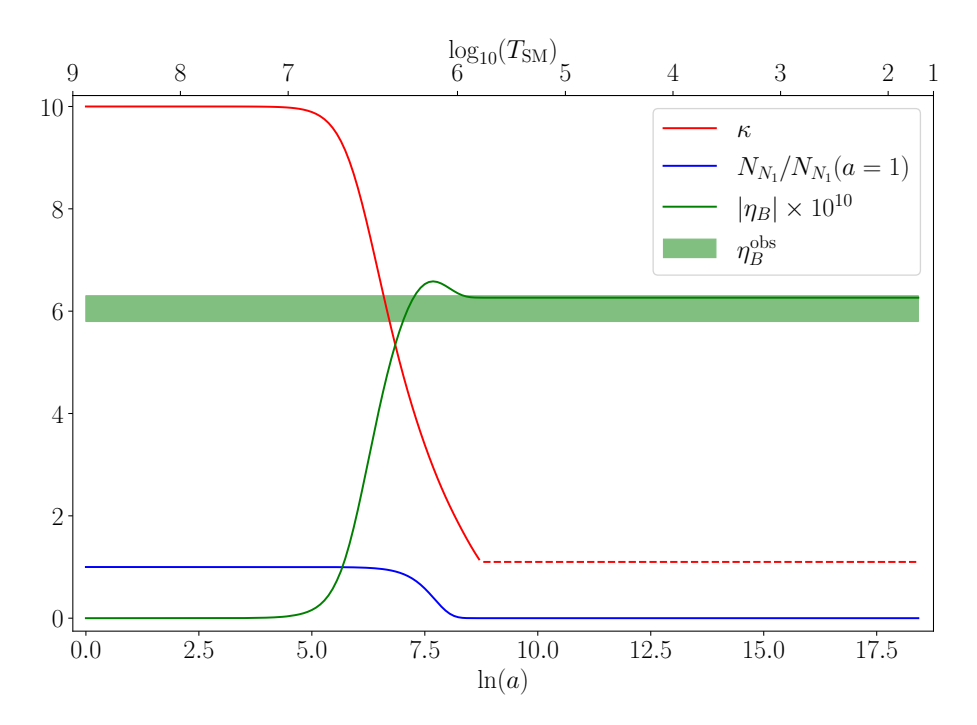


Figure 4.7: Evolution of  $|\eta_B|$ ,  $N_{N_1}$  and  $\kappa$  for initial  $\kappa_{\rm in}=10$  when  $N_1$  is only in kinetic equilibrium in the hot sector, for our benchmark point. When the number density approaches zero,  $\kappa$  is set to 1 (dashed line). The green band indicates the baryon-to-photon ratio at the  $3\sigma$  level.

in the absence of a hot sector, this benchmark point significantly under-produces the baryon asymmetry. We now numerically integrate the evolution equations, show the evolution of various quantities for this benchmark point and investigate the impact of varying one or two parameters at a time on the final baryon asymmetry.

# 4.6.1 $N_1$ in Kinetic Equilibrium Only

We first focus on the case where  $N_1$  is only in kinetic equilibrium with itself. Note that the scenario differs from that considered by Ref. [154], where  $N_1$  is in equilibrium.

In Fig. 4.7 we show the evolution of the temperature ratio  $\kappa$  (red), the number density of the lightest right-handed neutrino  $N_{N_1}$  (blue), and the baryon asymmetry  $\eta_B$  (green) as a function of  $\ln a$  (where we set a=1 at the beginning of our simulation) for the benchmark point in Table 4.2. We also show the corresponding SM temperature on the top axis.

We see that at early times before  $N_1$  has started to decay, at  $T_{\rm SM} \gtrsim 10^7\,{\rm GeV}$  and  $T_{N_1} \gtrsim 10^8\,{\rm GeV}$ , the temperature ratio, the  $N_1$  comoving number density and the baryon asymmetry remain constant. When the  $N_1$  population starts to decay, at  $T_{\rm SM} \sim 10^7\,{\rm GeV}$  and  $T_{N_1} \sim 10^8\,{\rm GeV}$ , the decay starts to put the two sectors into kinetic equilibrium and the temperature ratio  $\kappa$  begins to fall. The baryon asymmetry immediately starts rising and overshoots the observed value around halfway through the decay. It then reduces slightly due to the effect of the washout terms. The temperature ratio approaches  $\kappa=1$  as the hot sector is depleted, and at some point the  $N_1$  abundance goes below the numerical accuracy of our computation. At this point, we set  $\kappa=1$  (dashed red line) so the system can evolve while avoiding numerical errors. This procedure does not affect the final baryon asymmetry  $\eta_B$  as almost all  $N_1$  particles have decayed by this time. Note, however, that even though the two sectors are technically in kinetic equilibrium, the hot sector is essentially empty since almost all  $N_1$  particles have decayed.

We see that our benchmark point produces a baryon asymmetry within the observed  $3\sigma$  band. For these parameters we find  $\Delta_{\eta} \approx 855\%$  (indicating that the tree-level mass is  $\mathcal{O}(10)$  times larger than the loop level mass) and  $\Delta_{H} \approx 10.4\%$  (indicating that the loop level contribution is  $\sim$  TeV) so there is no fine-tuning in the light neutrino masses and very mild fine-tuning in the Higgs mass.

In Fig. 4.8 (blue curve) we show the final baryon asymmetry as a function of the initial temperature ratio  $\kappa$  for our benchmark point.

We see that  $|\eta_B|$  is far below the observed asymmetry for  $\kappa \sim 1$  and first increases with  $\kappa$ . The rate of increase reaches a maximum of around  $\kappa = 2.7$ , where the energy densities of the SM and  $N_1$  are approximately equal. After this point, the baryon asymmetry begins to level off and reaches a maximum around  $\kappa \sim 7$ . For  $1 \lesssim \kappa \lesssim 7$  the initial number density of  $N_1$  in the hot sector is larger than for  $\kappa = 1$ , which enhances the final asymmetry. For  $2.7 < \kappa$  the hot sector dominates the energy density of the universe, and so the Hubble expansion rate (Eq. (4.3.3)), which counteracts the increased asymmetry. Essentially, the energy dump from the

4.6. Results 133

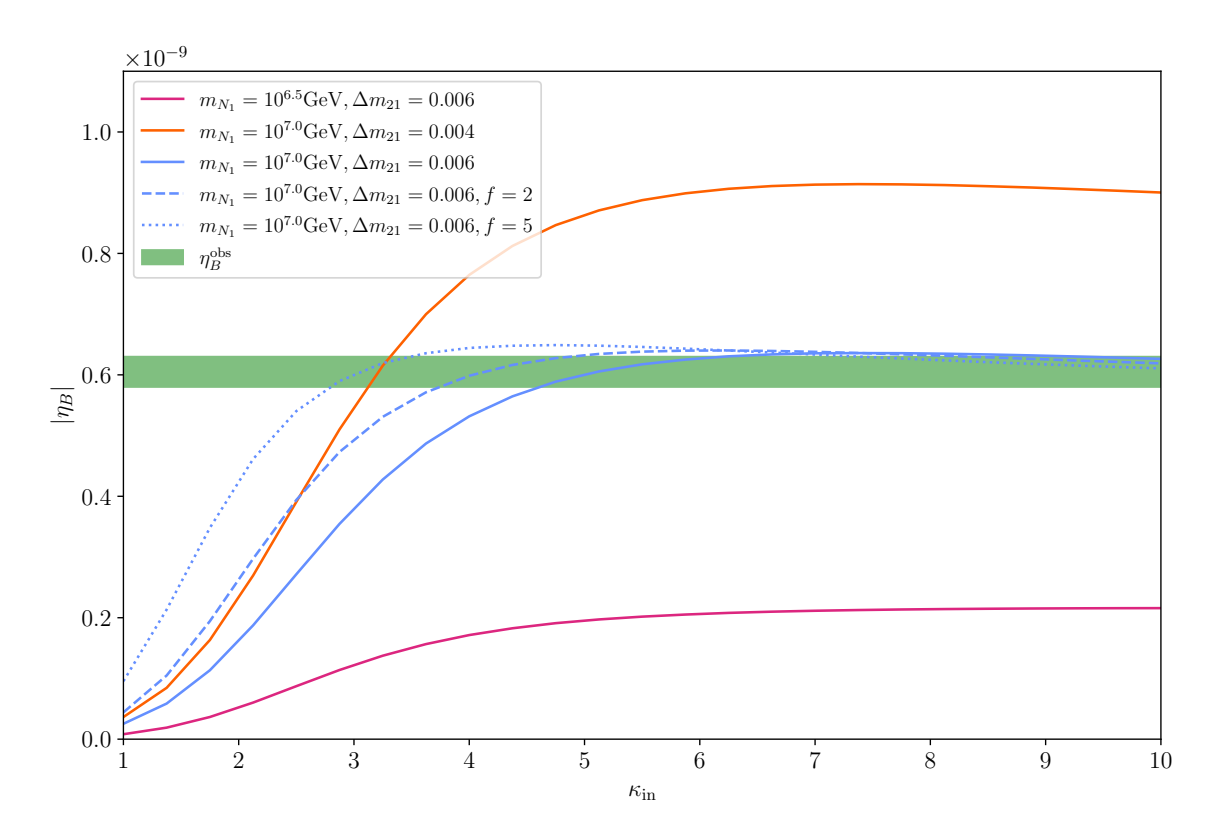


Figure 4.8: The final baryon asymmetry  $|\eta_B|$  as a function of the initial temperature ratio  $\kappa_{\rm in} = T_{N_1}/T_{\rm SM}$  at a=1. The blue line indicates the benchmark point. In the burgundy and orange curves we vary the RHN mass scale and splittings (see text for details), while the dashed (dotted) blue curves indicate non-equilibrium initial abundances of  $N_1$ ,  $f \equiv \left(n_{N_1}/n_{N_1}^{\rm eq}\right)_{\rm in}$ .

hot sector dilutes the baryon asymmetry. In Fig. 4.8 we also show the impact of varying important parameters.

We see that reducing the RHN masses by setting  $m_{N_1} = 10^{6.5}$  GeV and keeping the mass splittings fixed (burgundy curve) significantly reduces the generated asymmetry, as is typical in leptogenesis since the Yukawa matrix  $Y \propto M_N$ . The  $N_1$ – $N_2$  mass splitting is defined as  $\Delta m_{21} = \log_{10}(m_{N_2}/[\text{GeV}]) - \log_{10}(m_{N_1}/[\text{GeV}])$ , with  $\Delta m_{31}$  defined analogously and preserved at 0.4. Reducing the right-handed neutrino masses reduces the fine-tuning to  $\Delta_H = 58\%$ , which is a bit better than our benchmark point, but does not reproduce the observed baryon asymmetry.

We also see that a smaller mass splitting between  $N_1$  and  $N_2$  (orange curve) enhances the asymmetry. This also very slightly decreases the amount of fine-tuning needed in the Higgs sector to  $\Delta_H = 10.4 \%$ , because the  $N_2$  state is lighter. When fitting the light neutrino masses, the smaller  $N_1 - N_2$  mass splitting leads to a larger  $Y_{\mu 1}$  and  $Y_{\mu 3}$  and a smaller  $Y_{\mu 2}$  (with the other Yukawas remaining approximately constant). Since the  $Y_{\alpha 1}$  couplings have the largest impact on the generated asymmetry, this leads to an overall increase. If one wanted to find the minimal fine-tuning possible in this scenario, this could potentially be achieved by reducing the mass splitting further (while remaining out of the resonant leptogenesis regime), which boosts the asymmetry, while reducing the overall RHN mass scale, which reduces the asymmetry and would further improve the fine-tuning in the SM Higgs sector.

In the dashed and dotted blue lines, we show the impact of changing the initial  $N_1$  abundance to 2 and 5 times its equilibrium abundance. We see that as the initial abundance increases, the asymmetry increases faster and levels off around a similar maximum value, but at a lower  $\kappa_{\rm in}$ . Increasing the initial abundance is in many ways similar to increasing the hot sector temperature, as both lead to a higher initial number density of  $N_1$  and an increased energy density in the hot sector. While the number and energy densities scale differently with temperature, this does not lead to an increased final asymmetry at large  $\kappa_{\rm in}$ . In fact, for a higher initial abundance, the asymmetry drops slowly at large  $\kappa_{\rm in}$ .

4.6. Results 135

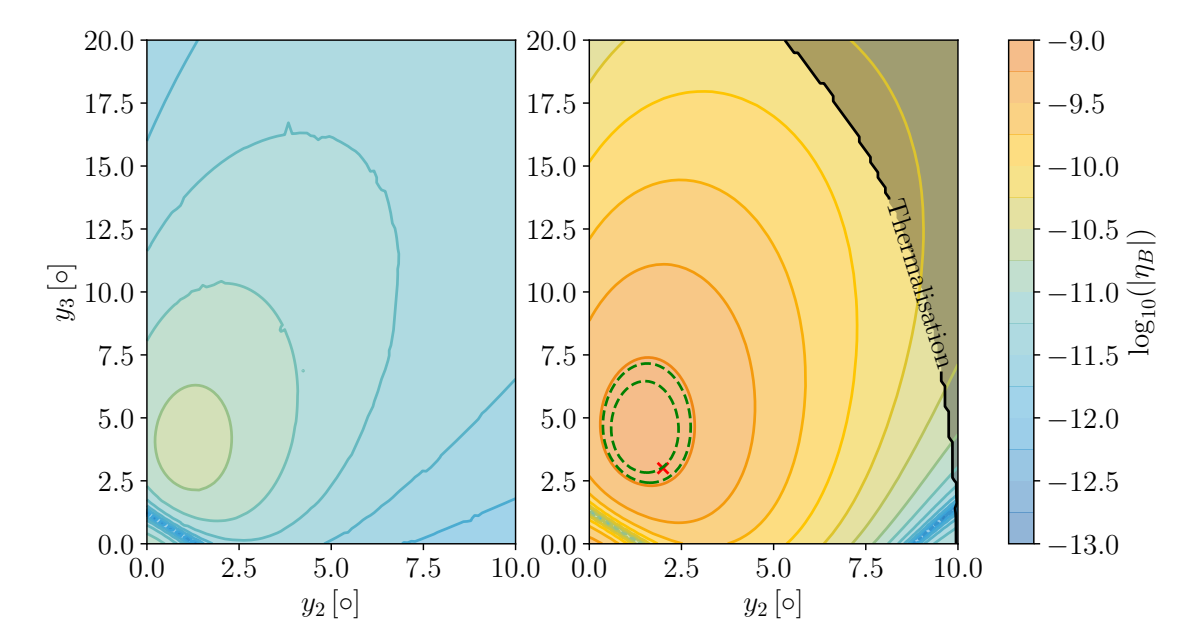


Figure 4.9: Values of  $\eta_B$  for standard leptogenesis (left) and hot leptogenesis (right) for  $\kappa_{\rm in}=10$  produced with the RHN in kinetic equilibrium only. The green dashed contours corresponding to  $\eta_B$  produced at  $(5.8-6.3) \times 10^{-10}$  [53,180] and the red cross indicates our benchmark point. The greyed-out region represents when the non-thermalisation assumption no longer holds, such that hot leptogenesis may not be viable.  $\Delta_H \sim 10.4\,\%$  and  $\Delta_{\nu} \sim 855\,\%$  throughout the plot.

Finally, in Fig. 4.9 we show the baryon asymmetry in  $y_2$  and  $y_3$ , chosen for their impact on the baryon asymmetry. On the left, we show the standard leptogenesis case where  $T_{N_1} = T_{\rm SM}$  and the  $N_1$  are in chemical equilibrium with themselves, while on the right we show the results for hot leptogenesis with an initial  $\kappa = 10$  and where  $N_1$  particles are only in kinetic equilibrium with themselves. The benchmark point is indicated by a red cross. In the left panel, we see that in this region of parameter space standard leptogenesis under-produces the baryon asymmetry by more than an order of magnitude.

In the right panel, we see that  $\eta_B$  is enhanced by a factor of  $\sim 50$  compared to the standard case and the observed baryon asymmetry can be produced in this parameter space (the dashed green contours give the  $3\sigma$  range). Importantly, this is away from the regime in the top-right where Higgs-mediated  $N_1\ell \to N_1\ell$  and lepton-mediated  $N_1H \to N_1H$  elastic scattering processes equilibrate the SM and the hot sector, indicated by the greyed-out 'Thermalisation' region. The fine-tuning in both the Higgs mass and the neutrino masses do not depend strongly on the parameters  $y_2$  and  $y_3$  so remain approximately equal to those of the benchmark point.

## 4.6.2 $N_1$ in Kinetic and Chemical Equilibrium

We now briefly turn to the scenario where the hot sector is in both kinetic and chemical equilibrium with itself. As described above, in this scenario we assume  $n_{N_1} = n_{N_1}^{\text{eq}}$  throughout and use this relation to find the evolution of the hot sector temperature  $T_{N_1}$ .

Even though we are in a different region of parameter space, pink stars in Fig. 4.5, these parameters do not strongly impact the  $N_1$  evolution and baryon asymmetry generation, which depend on the parameters in Table 4.2. Taking the initial  $N_1$  abundance to be  $N_{N_1}^{\text{eq}}$  and using the benchmark parameters in Table 4.2, we find that the  $\kappa$ ,  $N_{N_1}$  and  $\eta_B$  evolution is virtually identical to Fig. 4.7. For this reason, we do not show it, but instead just show the results of a parameter scan in  $y_2$  and

4.6. Results 137

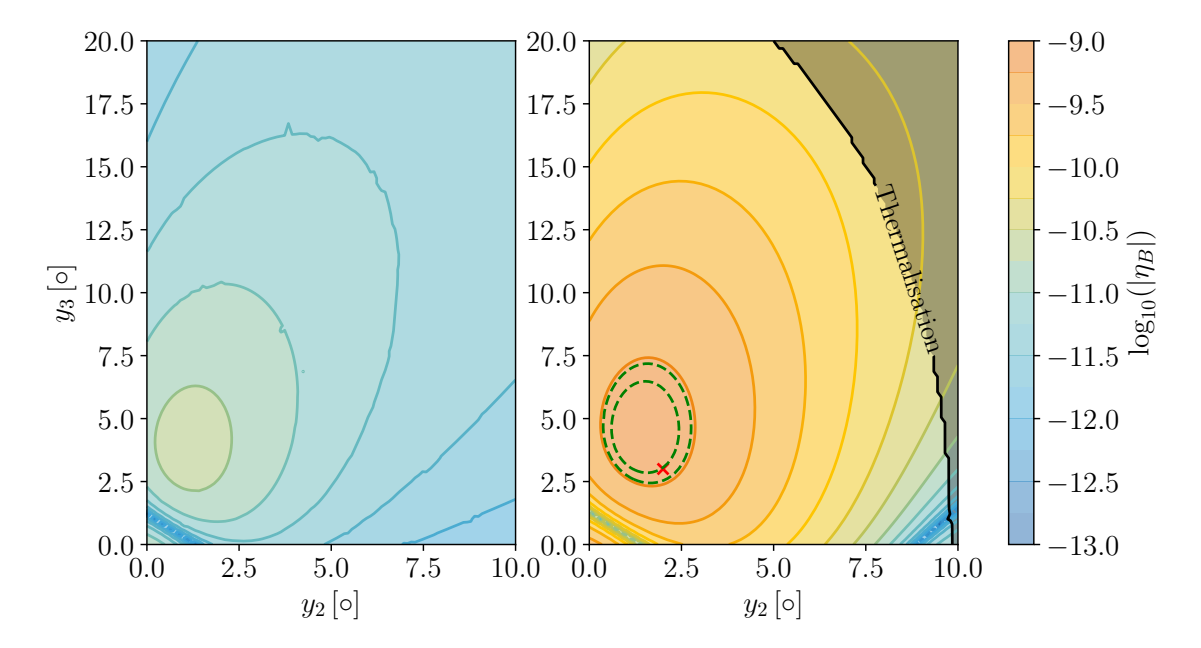


Figure 4.10: Values of  $\eta_B$  for standard leptogenesis (left) and hot leptogenesis (right) for  $\kappa_{\rm in}=10$  produced with the RHN in kinetic and chemical equilibrium. The green dashed contours corresponding to  $\eta_B$  produced at  $(5.8-6.3)\times 10^{-10}$  [53, 180] and the red cross indicates our benchmark point. The greyed out region represents when the non-thermalisation assumption no longer holds, such that hot leptogenesis may not be viable.  $\Delta_H \sim 10.4\,\%$  and  $\Delta_\nu \sim 855\,\%$  throughout the plot.

 $y_3$  in Fig. 4.10. We see that the difference with Fig. 4.9 is very small: at most a factor 4 in the baryon asymmetry near the thermalisation region, but at the percent level in the region where the observed  $\eta_B$  is produced. The thermalisation region has moved slightly to the left, indicating that it is easier for the hot sector to come into kinetic equilibrium with the SM sector in this scenario. The fine-tuning, in this case, is identical to that in Section 4.6.1.

Overall, we see that phenomenologically it does not make a significant difference whether only kinetic equilibrium, or both kinetic and chemical equilibrium, are maintained during  $N_1$  decay. Both scenarios can produce the observed baryon asymmetry while avoiding fine-tuning of the neutrino masses or the SM Higgs mass.

#### 4.6.3 Further Scenarios

We now briefly comment on two possible alternative scenarios. First, kinetic equilibrium could be established after inflaton decay but not maintained in the hot sector while  $N_1$  decays. This could, for example, occur if a heavy mediator realises fast  $2N_1 \rightarrow 2N_1$  scattering shortly after inflaton decay, but is too heavy to maintain it at  $T_{N_1} \sim m_{N_1}$ . In this scenario, one in principle has to compute the evolution for the full set of momentum modes. However, in the absence of additional processes affecting the sector, the assumption of a thermal distribution may be reasonable until the  $N_1$  start to decay. As was shown in Ref. [181], in vanilla leptogenesis the assumption of kinetic equilibrium when it is not realised underestimates the final baryon asymmetry by a tiny amount, because low momentum  $N_1$  particles are more efficiently produced than accounted for in a thermal distribution. In our present scenario, we may expect that large momentum  $N_1$  particles decay earlier, and thus the produced asymmetry is overestimated by a small amount if kinetic equilibrium is assumed.

Second, there is the possibility of  $N_2$  and  $N_3$  starting with temperature at or around  $T_{N_1}$  and with an approximately equilibrium abundance, but where all three particles

4.7. Conclusions

are weakly coupled and do not establish kinetic equilibrium with the SM. While Ref. [154] shows that the observed light neutrino masses mean that, in a Type I Seesaw scenario, the decay rate of  $N_2$  and  $N_3$  must be larger than Hubble at temperatures around their masses, we find that they do not have enough time to fully equilibrate before decay. It is therefore possible that this scenario may lead to an asymmetry which is larger by up to a factor of three compared to the results we find here, further reducing the required fine-tuning.

#### 4.7 Conclusions

In this chapter, we have studied a class of leptogenesis scenarios in which the sector containing the lightest right-handed neutrino  $(N_1)$  establishes kinetic equilibrium with itself at a temperature higher than that of the Standard Model (SM) sector. We have motivated this setup by considering the decay of the inflaton, which can lead to two sectors with similar but distinct temperatures. Higher temperatures in the  $N_1$  sector enhance the number density of  $N_1$  particles and can lead to an enhanced baryon asymmetry. With this setup, the observed baryon asymmetry can be generated without the significant fine-tuning of the light neutrino masses and the SM Higgs boson mass present in standard leptogenesis. We have checked that inflaton-mediated energy exchange between the sectors is not fast enough to equilibrate them after inflation.

In Section 4.3 we described a toy model that can realise such a scenario of hot leptogenesis, introducing a new scalar field  $\phi$  responsible for mediating self-interactions of  $N_1$  and maintaining its kinetic equilibrium. We explore two regimes: one where the hot sector containing  $N_1$  is only in kinetic equilibrium with itself and another where it is in both kinetic and chemical equilibrium. We derived the relevant evolution equations to track the relevant quantities and compute the resulting baryon asymmetry in both of these scenarios.

Our numerical analysis reveals that both scenarios can produce the observed baryon

asymmetry with minimal fine-tuning. As expected, the enhancement of the baryon asymmetry can be up to a factor of around 50, and the observed asymmetry can then be achieved for smaller right-handed neutrino masses and couplings. These scenarios therefore reduce the fine-tuning required in both the Higgs and neutrino sectors compared to the standard leptogenesis scenario. This confirms that non-resonant leptogenesis is viable and efficient in producing the observed baryon asymmetry under our model assumptions.

Comparing the numerical results in the two cases, we find that the results for kinetic only and kinetic and chemical equilibrium are similar. This can be understood from the fact that we assume  $n_{N_1} = n_{N_1}^{\text{eq}}$  as an initial condition for the former case, which is preserved until  $T \sim m_{N_1}$ , right before the decays happen. Thus, we expect that chemical equilibrium can be a reasonable approximation in the case where it is not realised or maintained.

We finally note that our computations are also likely to be a good approximation to the case where  $N_1$  are not in kinetic equilibrium with themselves when they decay and that it may be possible that  $N_2$  and  $N_3$  are present in the hot sector and could lead to an enhanced baryon asymmetry.

# Chapter 5

# Phase Transition Phenomenology of the 95 GeV Resonance in the Two Higgs Doublet Model

For the world is changing: I feel it in the water, I feel it in the earth, and I smell it in the air.

from The Lord of the Rings by J.R.R. Tolkien

## 5.1 Introduction

Following the discovery of the Higgs boson [4,5], searches at the Large Hadron Collider (LHC) have increasingly focused on exploring the structure of the Higgs sector. Motivated by numerous Beyond the Standard Model (BSM) scenarios featuring extended scalar sectors, the CMS collaboration extended its Higgs-like particle searches to include invariant masses below 110 GeV. While CMS reported an excess near 95 GeV in the diphoton channel (two photons in the final state) by combining data from 8 and 13 TeV runs with a local significance of  $2.8\sigma$  [182], recently, this result was updated using the full 13 TeV dataset. The latter shifted the excess to 95.4 GeV

with a local significance of  $2.9\sigma$  [183]. The presence of a neutral scalar decaying into two photons around 95 GeV remains compatible with the latest ATLAS results [184].

A resonance of a similar mass has also been reported by CMS in  $\tau\tau$  final state searches at around 100 GeV [185], and around 98 GeV in  $b\bar{b}$  final state searches at the Large Electron-Positron (LEP) collider in 2006 [186].

Due to the limited resolution of the CMS and LEP measurements, these measurements seem to be compatible and could point to a new scalar particle at a mass of around 95 GeV. The possibility of a lighter Higgs-like particle explaining these excesses has been explored in numerous models [187–208].

A model that has been studied extensively in the context of new Higgs-like particles is the Two Higgs Doublet Model (2HDM), a minimal extension to the Standard Model that requires the addition of an extra Higgs doublet [189,190,192,202,204–208]. This model predicts additional scalar particles, which may account for a 95 GeV resonance. Although phenomenological investigations of the 2HDM in this context have largely focused on collider observables [189,208]. the existence of new scalars coupled to the Higgs can also alter the dynamics of cosmological evolution.

In this chapter, we explore the possibility of a first-order electroweak phase transition (EWPT) in the Type I 2HDM model, identifying the 95 GeV excess with an additional pseudoscalar state. Employing state-of-the-art dimensional reduction to a three-dimensional effective field theory (3D EFT) [141, 142], we perform a broad finite temperature scan over the parameter region compatible with current collider limits.

Previous studies have explored the EWPT in the 2HDM using both perturbative and non-perturbative approaches. Early work using one-loop finite-temperature effective potentials (e.g. Refs. [77, 78, 209–213]) showed that a strong first-order EWPT is possible in Type I and Type II 2HDMs, typically requiring sizeable mass splittings among the scalar states to enhance thermal barriers generated by gauge bosons or scalar loops <sup>1</sup> (e.g. Refs. [78, 209]). These studies often focused on parameter regions

<sup>&</sup>lt;sup>1</sup>We explain why this is the case in Section 3.7.2.

5.1. Introduction 143

with heavy new scalars with mass  $m \gtrsim 300$  GeV, motivated by electroweak precision tests [214–218] and Higgs signal strength measurements.

More recently, non-perturbative studies of the dimensionally reduced 3D EFT have been employed to assess the nature of the electroweak phase transition more reliably. The model has also been studied perturbatively, including in its inert doublet realisation [225–227].

These studies have demonstrated that certain regions of 2HDM parameter space can indeed support a strong first-order electroweak phase transition, particularly when thermally induced cubic terms in the potential are sufficiently enhanced. However, such analyses typically do not account for the presence of a light scalar or pseudoscalar near 95 GeV, nor the associated phenomenological constraints.

The potential existence of such a light state can substantially alter the structure of the finite-temperature potential. In particular, it can introduce new phase transition pathways or weaken the strength of the transition by reducing the need for large mass splittings.

We find that unlike in the Standard Model, where the EWPT is a crossover [26–28, 228, 229], the transition is first order in the majority of the constrained parameter space. Moreover, depending on the parameters in the 2HDM Lagrangian, the transition can occur in a single or in two steps. <sup>3</sup> We find that the transition strength remains modest across the viable parameter space, with the order parameter not exceeding  $|v_c/T_C| \lesssim 1.3$ .

A strong first-order phase transition can leave behind a stochastic gravitational wave (GW) background, as explained in Section 3.8. However, due to the relatively modest values of the order parameter in the 2HDM, the resulting GW signal lies well

<sup>&</sup>lt;sup>1</sup>See Refs. [79,219–221] for recent analyses, or Refs. [222–224] for earlier foundational work.

<sup>&</sup>lt;sup>2</sup>The inert doublet model is a limit of the 2HDM where the extra doublet has no couplings to SM fermions.

<sup>&</sup>lt;sup>3</sup>See Ref. [230] for a non-perturbative analysis of two-step transitions in the triplet extension of the SM.

<sup>&</sup>lt;sup>4</sup>Here,  $v_c$  is the field space distance between the phases.

below the projected sensitivity of LISA [21, 24, 25] and other planned (space-based) observatories [231–233].<sup>1</sup>

Furthermore, the moderate strength of the transition also appears insufficient to support electroweak baryogenesis (see Section 3.5). Achieving successful baryogenesis would likely require additional model ingredients, such as tree-level barriers in the effective potential, to sufficiently enhance the strength of the transition and realise a sharp turn-off of the electroweak sphaleron rates inside the bubbles of true vacuum. We discuss possible extensions, including singlet scalars or higher-dimensional operators, that could enhance the transition.

# 5.2 The Two Higgs Doublet Model

The real two-Higgs-doublet model (2HDM) Type I is particularly well suited to accommodating a new  $\sim 95$  GeV state while respecting existing flavour and collider bounds. In Type I, all fermions couple directly to the same Higgs doublet. In Type III, X and Y, both doublets directly couple to all charged fermions. These induce flavour-changing neutral currents (FCNCs) at tree level [220], which are undesirable due to the observed suppression of such interactions.<sup>2</sup> In Type II, where one doublet couples to the up-type quarks and the other couples to the down-type quarks and leptons (or the Flipped model with the up- and down-type quarks swapped), there are enhancements in the  $b \to s \gamma$  decay rate. This is due to the constructive interference between SM diagrams, and 2HDM-II diagrams that have the charged Higgs running in the loop in place of  $W^{\pm}$  [240, 241]. The stringent constraints on the  $b \to s \gamma$  decay rate [201, 241] force the charged Higgs above a few hundred GeV in Type II/Flipped models. These constraints are much weaker for the 2HDM-I as the diagrams destructively interfere instead – allowing  $m_{H^{\pm}} \sim 150-350$  GeV alongside a light neutral scalar or pseudoscalar. Moreover, imposing the alignment limit

 $<sup>^{1}\</sup>mathrm{See}$  Refs. [234–238] for recent discussions of GW prospects in the 2HDM context.

<sup>&</sup>lt;sup>2</sup>FCNCs are interactions that change a fermion's flavour without changing its electric charge. These do not exist in the SM at tree level and are tightly constrained by data [239].

 $|\cos(\beta - \alpha)| \ll 1$  keeps the 125 GeV Higgs SM-like, while still permitting a new state at 95 GeV with suppressed couplings to heavy gauge bosons VV and enhanced loop-induced couplings to  $\gamma\gamma$  and  $\tau\tau$ .

In this chapter, we explore the scenario in which the pseudoscalar A is identified with the new 95 GeV resonance. This assignment provides a better fit to existing collider data compared to associating the scalar H with the resonance. The reason is as follows: In the  $m_H = 95$  GeV scenario, the CP-even scalar H couples to electroweak vector bosons at tree level. However, these couplings are constrained by the Higgs signal-strength sum rule<sup>1</sup> and by global fits to Higgs data (see e.g. [204]) which restrict the scalar mixing via  $|\cos(\beta - \alpha)| \lesssim 0.2$ . This suppression limits both the production cross section and the branching ratio into  $\gamma\gamma$ , making it difficult to account for either the LEP excess in the  $b\bar{b}$  channel [186] or the diphoton excess observed by CMS [204].

The Higgs sector of the 2HDM consists of two  $SU(2)_L$  doublets,  $\Phi_1$  and  $\Phi_2$ , with opposite charge under a  $\mathbb{Z}_2$  symmetry and hypercharge Y = 1/2. All right-handed SM fermions are taken to be even under the  $\mathbb{Z}_2$ , while  $\Phi_1$  is conventionally chosen to be odd, making it a fermiophobic<sup>2</sup> doublet. Thus the resulting Yukawa terms in the 2HDM remain the same as in the SM, except with  $\Phi_2$  taking the place of the SM Higgs doublet and coupling to the fermions. After electroweak symmetry breaking, the Higgs doublets can be parametrised in terms of the physical scalar degrees of freedom as follows [242]:

$$\Phi_1 = \begin{pmatrix} -H^+ \sin \beta + G^+ \cos \beta \\ \frac{1}{\sqrt{2}} (v \cos \beta - h \sin \alpha + H \cos \alpha - iA \sin \beta + iG^0 \cos \beta) \end{pmatrix}, \qquad (5.2.1)$$

<sup>&</sup>lt;sup>1</sup>As we will see later, the two neutral Higgs will have vector boson couplings that follow the sum rule  $(c_V^h)^2 + (c_V^H)^2 = 1$ , meaning they must combine to reproduce the SM Higgs coupling. If the Higgs signal strength is close to 1, and h is designated as the SM Higgs, this tightly constrains the coupling of H to V.

 $<sup>^2</sup>$ That is, it has substantially weaker couplings to fermions as they are only induced at loop level.

$$\Phi_2 = \begin{pmatrix} H^+ \cos \beta + G^+ \sin \beta \\ \frac{1}{\sqrt{2}} (v \sin \beta + h \cos \alpha + H \sin \alpha + iA \cos \beta + iG^0 \sin \beta) \end{pmatrix}.$$
 (5.2.2)

Here, h denotes the SM-like Higgs boson and is a CP-even scalar, accompanied by the conventionally heavier CP-even state H. The field A is the neutral CP-odd pseudoscalar, which we later associate with the 95 GeV resonance.

The  $H^{\pm}$  are a pair of charged Higgs bosons, while  $G^{\pm}$  and  $G^{0}$  are the Goldstone bosons. The SM Higgs vev is v=246 GeV. The vevs of the two doublets,  $v_{1}$  and  $v_{2}$ , are constrained by the requirement that  $v_{1}^{2}+v_{2}^{2}=v^{2}$ , and the angle  $\beta$  is defined via  $\tan \beta = v_{2}/v_{1}$ . The angle  $\alpha$  diagonalises the CP-even scalar mass matrix and determines the physical mass eigenstates [243].

We can define a new angle  $\delta = \beta - \alpha - \pi/2$  to relate the tree-level couplings between the physical resonances and the fermions,

$$c_f^h = \frac{\cos \alpha}{\sin \beta} = \cos \delta - \frac{\sin \delta}{\tan \beta}, \quad c_f^H = \frac{\sin \alpha}{\sin \beta} = -\sin \delta - \frac{\cos \delta}{\tan \beta}, \quad c_u^A = -c_{d,L}^A = \cot \beta,$$

$$(5.2.3)$$

as well as gauge bosons,

$$c_V^h = \sin(\beta - \alpha) = \sin\delta,$$
  $c_V^H = \cos(\beta - \alpha) = -\sin\delta$  (5.2.4)

where V = W, Z.

The couplings of the light Higgs boson h approach their SM values  $(c_f^h \to 1)$  in the limit  $\alpha \to 0$  and  $\beta \to \pi/2$ . In contrast, the heavier scalar H does not couple to fermions at  $\alpha = 0$ , and decouples from gauge bosons when  $\alpha = \beta \pm \pi/2$ . The latter condition corresponds to  $\cos(\beta - \alpha) = 0$ , known as the *alignment limit* of the model. In this limit, the light Higgs h has the same tree-level couplings to the gauge bosons as in the SM.

The tree-level potential for the Type I 2HDM is as follows:

$$V_H = m_{11}^2 \Phi_1^{\dagger} \Phi_1 + m_{22}^2 \Phi_2^{\dagger} \Phi_2 - m_{12}^2 \left( \Phi_1^{\dagger} \Phi_2 + \text{h.c.} \right) + \lambda_1 (\Phi_1^{\dagger} \Phi_1)^2$$
 (5.2.5)

$$+ \lambda_{2}(\Phi_{2}^{\dagger}\Phi_{2})^{2} + \lambda_{3}(\Phi_{1}^{\dagger}\Phi_{1})(\Phi_{2}^{\dagger}\Phi_{2}) + \lambda_{4}(\Phi_{1}^{\dagger}\Phi_{2})(\Phi_{2}^{\dagger}\Phi_{1}) + \frac{\lambda_{5}}{2} \left[ (\Phi_{1}^{\dagger}\Phi_{2})^{2} + \text{h.c.} \right],$$
(5.2.6)

where  $m_{11}$  and  $m_{22}$  are the masses of the doublets,  $m_{12}$  is the mixing parameter, and  $\lambda_1 \ldots, \lambda_5$  are quartic couplings. A fuller treatment of the potential would allow for the additional terms

$$V_H \supset \left(\lambda_6 \Phi_1^{\dagger} \Phi_1 + \lambda_7 \Phi_2^{\dagger} \Phi_2\right) \Phi_1^{\dagger} \Phi_2 + \text{h.c.}, \qquad (5.2.7)$$

however, these terms would not be permitted in the  $\mathbb{Z}_2$  symmetry, setting  $\lambda_6$ ,  $\lambda_7 = 0$ . This softly broken symmetry is desired as the non-observation of FCNCs requires that the fermions be coupled to a single Higgs doublet only, as mentioned before. This is only possible with the doublets and the fermions being charged under the  $\mathbb{Z}_2$  symmetry, thus forbidding the  $\lambda_6$ ,  $\lambda_7$  terms [244–247].  $m_{12}^2$  is permitted to be non-zero, softly breaking the  $\mathbb{Z}_2$  symmetry [244,247].

In the 2HDM, the background fields  $\phi_i$  are identified as the second, real components of the two Higgs doublets respectively,

$$\Phi_i \to \frac{1}{\sqrt{2}} \begin{pmatrix} 0 \\ \phi_i \end{pmatrix} + \Phi_i \,. \tag{5.2.8}$$

After the two Higgs doublets take these background field values, we arrive at the

<sup>&</sup>lt;sup>1</sup>This determines the difference between the inert doublet model and the 2HDM-I, as the inert doublet model has  $\mathbb{Z}_2$  as an exact symmetry of the theory.

scalar mass matrix for the heavy bosons  $\{W, Z, H, A, H^{\pm}, h, G^{0}, G^{\pm}\}$ :

$$M^{2} = \begin{pmatrix} M_{11}^{2} & 0 & 0 & 0 & M_{15}^{2} & 0 & 0 & 0 \\ 0 & M_{22}^{2} & 0 & 0 & 0 & M_{26}^{2} & 0 & 0 \\ 0 & 0 & M_{33}^{2} & 0 & 0 & 0 & M_{37}^{2} & 0 \\ 0 & 0 & 0 & M_{44}^{2} & 0 & 0 & 0 & M_{48}^{2} \\ M_{15}^{2} & 0 & 0 & 0 & M_{55}^{2} & 0 & 0 & 0 \\ 0 & M_{26}^{2} & 0 & 0 & 0 & M_{66}^{2} & 0 & 0 \\ 0 & 0 & M_{37}^{2} & 0 & 0 & 0 & M_{77}^{2} & 0 \\ 0 & 0 & 0 & M_{48}^{2} & 0 & 0 & 0 & M_{88}^{2} \end{pmatrix}, \tag{5.2.9}$$

where,

$$M_{11}^2 = m_{11}^2 + \frac{1}{2}(2\lambda_1\phi_1^2 + \lambda_-\phi_2^2), \qquad M_{22}^2 = m_{11}^2 + \frac{1}{2}(2\lambda_1\phi_1^2 + \lambda_3\phi_2^2), \qquad (5.2.10)$$

$$M_{33}^2 = m_{11}^2 + \frac{1}{2}(6\lambda_1\phi_1^2 + \lambda_+\phi_2^2), \qquad M_{44}^2 = M_{22}^2,$$
 (5.2.11)

$$M_{11}^{2} = m_{11}^{2} + \frac{1}{2}(2\lambda_{1}\phi_{1}^{2} + \lambda_{-}\phi_{2}^{2}), \qquad M_{22}^{2} = m_{11}^{2} + \frac{1}{2}(2\lambda_{1}\phi_{1}^{2} + \lambda_{3}\phi_{2}^{2}), \qquad (5.2.10)$$

$$M_{33}^{2} = m_{11}^{2} + \frac{1}{2}(6\lambda_{1}\phi_{1}^{2} + \lambda_{+}\phi_{2}^{2}), \qquad M_{44}^{2} = M_{22}^{2}, \qquad (5.2.11)$$

$$M_{55}^{2} = m_{22}^{2} + \frac{1}{2}(2\lambda_{2}\phi_{2}^{2} + \lambda_{-}\phi_{1}^{2}), \qquad M_{66}^{2} = m_{22}^{2} + \frac{1}{2}(2\lambda_{2}\phi_{2}^{2} + \lambda_{3}\phi_{1}^{2}), \qquad (5.2.12)$$

$$M_{77}^{2} = m_{22}^{2} + \frac{1}{2}(6\lambda_{2}\phi_{2}^{2} + \lambda_{+}\phi_{1}^{2}), \qquad M_{88}^{2} = M_{66}^{2}, \qquad (5.2.13)$$

$$M_{15}^{2} = -m_{12}^{2} + \lambda_{5}\phi_{1}\phi_{2}, \qquad M_{26}^{2} = -m_{12}^{2} + \frac{1}{2}(\lambda_{4} + \lambda_{5})\phi_{1}\phi_{2}, \qquad (5.2.14)$$

$$M_{77}^2 = m_{22}^2 + \frac{1}{2}(6\lambda_2\phi_2^2 + \lambda_+\phi_1^2), \qquad M_{88}^2 = M_{66}^2,$$
 (5.2.13)

$$M_{15}^2 = -m_{12}^2 + \lambda_5 \phi_1 \phi_2,$$
  $M_{26}^2 = -m_{12}^2 + \frac{1}{2}(\lambda_4 + \lambda_5)\phi_1 \phi_2,$  (5.2.14)

$$M_{37}^2 = -m_{12}^2 + \lambda_+ \phi_1 \phi_2, \qquad M_{48}^2 = M_{26}^2,$$
 (5.2.15)

and where we used the abbreviation  $\lambda_{\pm} = \lambda_3 + \lambda_4 \pm \lambda_5$ . To obtain the final mass eigenvalues, the diagonalisation of the mass matrix in Eq. (5.2.9) is conducted as in [220, 221].

In practice, we wish to calculate the Lagrangian parameters  $m_{11}^2, m_{22}^2, m_{12}^2, \lambda_1 \dots, \lambda_5$ from the physical mass inputs  $\{m_h, m_H, m_A, m_{H^{\pm}}\}$ , along with the input model angles  $\alpha, \beta$  and the input parameter  $m_{12}$ . Appendix B.2 in Ref. [221] features the tree-level relations to calculate the Lagrangian parameters, however for a more accurate analysis the one-loop renormalised parameters should be utilised instead. We describe the procedure of vacuum renormalisation in detail in Section 5.4.5 below and the Appendix B.2.

#### 5.3 Thermal Potential

To compute the temperature-dependent effective potential for the Type I 2HDM, we make use of high-temperature dimensional reduction, which we reviewed in Section 3.7.4 and which we recap briefly here. In the context of Lorentz scalar-driven transitions, this approach is well-suited for the high-temperature regime relevant to the transitions we study. As mentioned previously, this method features reduced theoretical uncertainties; in particular, it allows for a consistent inclusion of all large thermal corrections including two-loop thermal masses essential for renormalisation scale independence [134,248,249] which in turn is essential for theoretical consistency and ensuring physically meaningful results, but commonly not achieved.

As mentioned in Section 3.7.4, dimensional reduction utilises the thermal hierarchy of scales

$$\frac{g^2}{\pi}T \ll gT \ll \pi T, \tag{5.3.1}$$

with g representing a gauge coupling. The scale  $|p| \sim \pi T$  corresponds to the hard non-zero bosonic (fermionic) Matsubara modes [131],  $|p| \sim gT \sim m_D$  to the soft Debye screening modes, and  $|p| \sim g^2 T$  to the non-perturbative ultrasoft modes in the infrared (IR) [133]. By successively integrating out ultraviolet (UV) modes—see e.g. [250]— one obtains a sequence of dimensionally reduced EFTs. The final step yields a 3D EFT at the scale of bubble nucleation corresponding to  $g^2 T/\pi \ll |p| \ll gT$  [251], the so-called softer scale [249,252], since, in practice, the mass of the phase transition undergoing scalar will be parametrically larger than the ultrasoft scale. In this final EFT<sup>1</sup>, the long-distance dynamics of the transition is encoded in three spatial dimensions.

To compute the thermodynamics of a phase transition, one typically makes use of the effective potential at finite temperature. This potential is then computed in the final 3D EFT at the softer scale. To obtain the potential and the 3D EFT Lagrangian in practice, we utilise the thermal EFT matching software DRalgo [253], which we

<sup>&</sup>lt;sup>1</sup>In Appendix B.1, we discuss the choice of the scale for  $\bar{\mu}_{3US}$  which defines the softer scale.

cross-check via further in-house software in FORM [254], and apply qgraph [255] for diagram generation.

#### 5.3.1 The Dimensionally Reduced Effective Potential

The starting point for our analysis is the effective potential up to two-loop level in the softer 3D EFT. This corresponds to the functionalities of DRalgo v1.2.0. Since we are interested in tracking the phases in multi-field space, we refrain from integrating out further, potentially heavy vector fields [252]. By keeping the matching relations (which relate Lagrangian parameters between the hard, soft, and softer theories) at two-loop level, the options to compute the effective potential amount to its different loop orders, labelled via

[3D@NLO  $V_3$ @LO]: two-loop EFT matching, one-loop effective potential, (5.3.2)

[3D@NLO  $V_3$ @NLO]: two-loop EFT matching, two-loop effective potential. (5.3.3)

Here, we will focus on the former, namely [3D@NLO  $V_3$ @LO]. The reason for this is that the direct computation of the two-loop effective potential contains scalar contributions that, for some parts of the parameter space, should be counted as higher-order in comparison to the heavy vector contributions [256,257]. An artefact of this setup is the presence of logarithmically divergent terms in the two-loop potential, which are the result of negative mass eigenvalues in the logarithms coming mostly from sunset diagrams. The divergences lead to numerical issues when calculating the transitions; unphysical vacua are identified due to sharp discontinuous local minima, leading to unphysical phase transition parameters (such as bubble walls moving super-luminously;  $v_W > 1$ ). To avoid such issues we follow [258] and compute the one-loop potential with two loop matching relations. In the following, we refer to the setup in Eq. (5.3.2) as the two-loop improved one-loop potential.

<sup>&</sup>lt;sup>1</sup>See Ref. [249] for a similar application.

The final effective potential at the transition scale, is a function of the 3D effective fields  $\phi^{3D} = \{\phi_1^{3D}, \phi_2^{3D}\}^1$  and the temperature T.

The 4D effective thermal potential,  $V_4$ , can be calculated from the 3D potential via

$$V_4(\phi, T) = TV_3(\phi^{3D}, T)$$
 (5.3.4)

using the relation between field values in three- and four-dimensions  $\phi^{3D} \to \phi/\sqrt{T}$ . Henceforth, we suppress the 3D superscript for the fields in the 3D EFT.

#### 5.3.2 Higher Orders in the Effective Potential

In the effective potential at the softer scale, we utilise the NLO matching relations from DRalgo directly, based on the example file 2hdm.m.<sup>2</sup> Similar matching relations can also be found in [221].<sup>3</sup> For the corresponding vacuum renormalisation, see Sections 5.4.5 and B.2.

Up to two-loop order, the 3D effective potential is

$$V_3 = V_{0.3} + V_{1.3} + V_{2.3}, (5.3.5)$$

$$V_{1,3} = \sum_{i} n_i J_3(\overline{m}_i^2(\boldsymbol{\phi}, T)), \qquad (5.3.6)$$

where  $d = 3-2\epsilon$ ,  $V_{0,3}(\phi, T)$  is the three-dimensional version of the tree-level potential Eq. (5.2.5) [220, 221], and the degrees of freedom,  $n_i$ , are d-dependent. The corresponding mass eigenvalues  $\overline{m}_i$  of the dynamical fields  $i \in \{W, Z, H, A, H^{\pm}, h, G^0, G^{\pm}\}$  in the 3D EFT depend on the background fields for the two Higgs doublets, whose 4D analogues are seen in Eq. (5.2.1). We discussed the calculation of the mass eigenvalues from the mass matrix in Section 5.2.

Similarly to the 4D vacuum case and the corresponding Coleman-Weinberg poten-

<sup>&</sup>lt;sup>1</sup>These background fields are the 3D analogues of the background fields defined in Eq. (5.2.8). <sup>2</sup>See the DRalgo GitHub, https://github.com/DR-algo/DRalgo/blob/main/examples/2hdm.

<sup>&</sup>lt;sup>3</sup>In comparison with the matching relations of [221], scalar masses in our softer-scale matching relations are counted as higher-order inside of logarithmic terms for e.g.  $\overline{m}_{11}^2$ . Also, in Eq. (3.15) of [221],  $N_f$  should be the number of fermions and not the number of families.

tial [259], the one-loop 3D EFT potential,  $V_{1,3}$ , takes a closed form. The corresponding integrals are UV-finite and three-dimensional

$$J_3(m^2) = \frac{1}{2} \int_{\mathbf{p}} \ln(\mathbf{p}^2 + m^2) \stackrel{d=3-2\epsilon}{=} -\frac{1}{12\pi} (m^2)^{\frac{3}{2}}, \qquad (5.3.7)$$

where  $\int_{\mathbf{p}} = \int d^3\mathbf{p}/((2\pi)^3 \, 2E(\mathbf{p}))$ . The two-loop contributions,  $V_{2,3}$ , to the potential (5.3.5), as well as the two-loop 3D EFT matching relations, are directly adopted from DRalgo [253] and can also be taken from [260]. The parameters of this final 3D EFT are evolved to the 3D renormalisation group (RG) scale,  $\bar{\mu}_3$ , which we set to  $\bar{\mu}_3 = T$  in our analysis. The RG evolution and vacuum renormalisation procedures are detailed in Section 5.4.5 and Appendix B.2.

In Section 5.3.1, we argued that directly employing the two-loop effective potential, without integrating out heavy vector and temporal modes to induce the transition, can lead to pathological behaviour for some benchmark points along the transition path in the multi-dimensional field space. Since the preferred approach is therefore to use the [3D@NLO  $V_{\rm eff}$ @LO] prescription Eq. (5.3.2), one may wonder about the importance of omitting two-loop corrections in the effective potential while keeping them in the matching. These effects have been studied in [249,258], which concluded that the dominant uncertainties are associated with higher-order corrections in the matching. To investigate this and support our choice of using the setup Eqs. (5.3.3) for our scan, in Section 5.5 we examine a few benchmark points to assess the magnitude of uncertainty introduced by neglecting higher-order terms in the effective potential. These benchmark points are summarised in Table 5.2.

## 5.4 Phase Transition and GW signature

To find the phases, calculate phase transition properties and gravitational wave spectra from our 4D (DR) potential, we make use of the PhaseTracer2 package for C++ [261,262]. The package automates the pipeline from a 4D thermal potential to the gravitational wave spectrum parameters and signal-to-noise ratios (SNRs) for

proposed gravitational wave interferometers, such as LISA [21,22] and Taiji [233]. In this section, we provide a brief review of the computation performed by the package.

#### 5.4.1 Bubble Nucleation

First, it is important to identify the phases of the thermal potential. The phases are traced while the temperature T is adjusted for a defined temperature range, giving the full phase structure of the model. Thermal potentials which feature phase transitions will typically see a single minimum at high temperature, which represents the initial phase and the true vacuum at that temperature. As the universe cools, a second minimum will appear, initially with a higher potential value than the first phase.

The critical temperature,  $T_C$ , is defined as the temperature at which two phases are degenerate. Below this temperature, the new phase becomes the 'true vacuum', or the stable phase, whereas the initial phase becomes the false vacuum, or metastable phase. If a potential barrier exists between the false vacuum and the true vacuum, the phase transition will be first order, which requires bubbles of the new phase to nucleate via the tunnelling of the field configuration through the barrier, or via thermal fluctuations giving enough energy to the field to overcome the barrier. The nucleation and expansion of new bubbles of the true vacuum occur during the phase transition, which is considered to have ended when percolation has occurred.

#### Euclidean Action of the Transition Path

Bubbles can only nucleate when there is a viable transition path between the minima with a low enough action. After switching to Euclidean space, with  $t \to -i\tau$ , the transition path can be parametrised as  $\phi_1(\rho)$  and  $\phi_2(\rho)$  with  $\rho = \sqrt{\tau^2 + \mathbf{x}^2}$  being a radial parameter in space, indicating a spherically symmetric bubble.

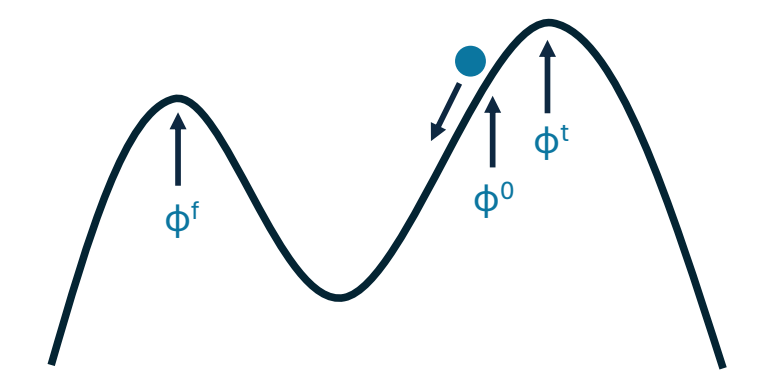


Figure 5.1: Illustration of an upturned potential showing the true vacuum  $\phi^t$ , the false vacuum  $\phi^f$ , and the 'release' of the classical particle at an initial position  $\phi^0$ .

The associated Euclidean action can be written as

$$S_d[\phi_1, \phi_2](T) = \Omega_{d-1} \int_0^\infty \rho^{d-1} \left\{ \frac{1}{2} (\dot{\phi_1}^2 + \dot{\phi_2}^2) + V(\phi_1, \phi_2, T) \right\} d\rho, \qquad (5.4.1)$$

with d being the number of dimensions of the O(d)-symmetric field configuration, and  $\Omega_n$  being the surface area of an n-dimensional sphere. While d=4 for nucleation by quantum tunnelling, d=3 for nucleation by thermal fluctuations.

The Euler-Lagrange equation provides the saddle point of this action, known as the bounce equation, given by [263]

$$\ddot{\phi}_i(\rho) + \frac{d-1}{\rho}\dot{\phi}_i(\rho) = \frac{\partial}{\partial\phi_i}V(\phi_1, \phi_2, T). \tag{5.4.2}$$

This equation is solved with the boundary conditions  $\dot{\phi}_i(0) = \dot{\phi}_i(\rho \to \infty) = 0$ , and  $\phi_i(\rho \to \infty) = \phi_i^f$ , where  $\phi_i^f$  is the value of the fields at the false vacuum (see [94,264] for a discussion of the appropriate boundary conditions for tunnelling). It is equivalent to the solution of a classical particle in an upturned potential, being released at an initial position  $\phi_i^0$  near the true vacuum (as shown in Fig. 5.1), until it comes to a rest exactly at the crest of the hill where the false vacuum resides. For a 1D field configuration calculating this solution requires the utilisation of the 'shooting method'. An initial guess for  $\phi^0 = \phi(0)$  is made, which is then evolved towards the false vacuum using the bounce equation. If the particle comes to rest at the crest of that hill, the bounce solution has been calculated. Otherwise, if it goes

beyond the crest of the hill, it overshot and the initial guess for  $\phi_0$  was too close to the true vacuum. If it doesn't make it to the crest of the hill, it has undershot and the initial guess was too close to the bottom of the valley in the upturned potential. A generalisation of this method for the multi-field case is used in the 'path deformation' algorithm, first utilised in the CosmoTransitions package [265] and then in PhaseTracer2 [262]. Here, the transition path may no longer be a trivial straight line path between the two minima, so the path must be perturbed in the direction that minimises the action, to find the path of least action at temperature T. Then, the action is calculated and checked against the nucleation/percolation criteria (see Section 5.4.1) to determine the temperature at which the a bubble has nucleated or the phase transition has percolated.

To examine how the path deformation works, we reparametrise the path  $\underline{\phi}(\rho) = \{\phi_1(\rho), \phi_2(\rho), \dots\}$  as  $\underline{\phi}(x)$  [265], where  $x = x(\rho)$  and x is defined such that  $|d\underline{\phi}/dx| = 1$  as in Ref. [262]. Next, we define  $d\underline{\phi}/dx = \hat{e}_t(x)$  as the unit tangent vector of the path.

This results in the splitting of the bounce equation 5.4.2 into parallel and perpendicular parts,

$$\frac{d^2x}{d\rho^2} + \frac{d-1}{\rho} \frac{dx}{d\rho} = (\hat{e}_t(x) \cdot \nabla) V(\underline{\phi}, T) = \frac{d}{dx} V(\underline{\phi}, T), \qquad (5.4.3)$$

$$\left(\frac{dx}{d\rho}\right)^2 \frac{d^2 \phi}{dx^2} = \nabla_{\perp} V(\underline{\phi}, T) , \qquad (5.4.4)$$

where  $\nabla_{\perp}$  indicates the perpendicular components of the gradient in field space<sup>1</sup>. Through the second equation, we see that we can quantify how far off a path guess is from the bounce solution using the normal force, defined as

$$F_n(x) = \left(\frac{dx}{d\rho}\right)^2 \frac{d^2\phi}{dx^2} - \nabla_{\perp}V(\underline{\phi}, T), \qquad (5.4.5)$$

and where this vanishes, the perpendicular part of the bounce equation is satisfied. Thus, a solution to Eq. 5.4.3 with a vanishing normal force is a solution to the

We use the notation  $V(\underline{\phi},T)$  instead of  $V(\phi_1,\phi_2,T)$  when referring to a generic multi-field potential.

bounce equation, and the path of least action has been found.

To conclude, the path deformation proceeds as follows:

- 1. An initial guess for the path  $\underline{\phi}(x)$  is made, typically a straight line connecting the minima in field space.
- 2. Next, the one dimensional shooting method is utilised to iteratively solve Eq. 5.4.3 to calculate a solution for  $x(\rho)$ .
- 3. The normal force  $F_n$  is calculated along the path using Eq. 5.4.4 to determine in what how much and in what direction the path needs to be perturbed towards the bounce solution.
- 4. A perturbed path is fed into Step 2 and then 3, until we calculate a path with vanishing  $F_n$  given some tolerance and a bounce solution has been found.

The action  $S_d(T)$  is then calculated for the bounce solution at temperature T.

As mentioned before,  $S_4$  is used to calculate nucleation via quantum tunnelling, which is the most important effect at zero temperature. For the EWPT which happens at high temperature, we thus use  $S_3$  instead to calculate nucleation by thermal fluctuations.

#### **Nucleation Criteria**

We define the onset of the phase transition through the following nucleation criterion [25, 266, 267]

$$\frac{S_3}{T_N} \simeq 141 + \ln\left(\frac{A}{T_N^4}\right) - 4\ln\left(\frac{T_N}{100 \,\text{GeV}}\right) - \ln\left(\frac{\bar{\beta}}{100 H_*}\right),$$
 (5.4.6)

where  $T_N$  is the nucleation temperature, considered to be the onset of the phase transition.  $\bar{\beta}/H_*$  is the inverse of the time taken for the phase transition to 'complete',

where  $H_*$  refers to the Hubble constant at the time of GW production. For the EWPT,  $\ln(A/T^4) \simeq -14$  [268].<sup>1</sup>

While this condition is phrased in terms of the Euclidean action, it is derived from the requirement that the nucleation rate per unit volume becomes significant in an expanding universe. More precisely, it approximates the point at which the probability of bubble nucleation in a Hubble volume becomes order unity. The full percolation criterion requires integrating the nucleation rate over spacetime to track the volume fraction of the false vacuum (see e.g. [132]). This criterion, which allows for the calculation of the percolation temperature,  $T_p$ , is provided by [271]

$$\frac{S_3}{T_p} \simeq 131 + \ln\left(\frac{A}{T_p^4}\right) - 4\ln\left(\frac{T_p}{100 \,\text{GeV}}\right) - 4\ln\left(\frac{\bar{\beta}}{100 H_*}\right) + 3\ln(v_W), \quad (5.4.7)$$

where we use an ansatz for  $\bar{\beta}/H_* = 10^4$ , justified in Section 5.5 and the bubble wall velocity  $v_W = 0.63$  justified in Section 5.4.3. The ansatzes are used as we can only calculate these quantities a posteriori. A more thorough calculation will iteratively solve for a self-consistent percolation temperature and gravitational wave spectrum, however this approximation should be appropriate for our purposes.

To summarise, as the temperature T is lowered, a bounce solution is found and its action calculated, which is then compared to the nucleation/percolation criteria until they are met and the  $T_N$  and/or  $T_p$  are found.

#### 5.4.2 Phase Transition Parameters

The phase transition can be characterised by the transition strength parameter,  $\bar{\alpha}$ , and the inverse time of transition,  $\bar{\beta}/H_*$ , which are vital for the computation of the gravitational wave spectrum. We use this notation to differentiate these parameters from the 2HDM model angles  $\alpha, \beta$ .

<sup>&</sup>lt;sup>1</sup>In practice, the nucleation rate receives higher-order corrections from fluctuations around the bounce solution, modifying the prefactor A(T) and the interpretation of  $S_3$ , and have recently been studied in detail using functional determinant methods [251, 269]. Public tools such as bubbleDet [270] enable the automated inclusion of these corrections, providing a more accurate estimate of the nucleation rate.

The trace anomaly difference of the energy-momentum tensor is

$$\Delta\theta = \left(V(\underline{\phi}, T_*) - \frac{T_*}{4} \frac{\partial}{\partial T} V(\underline{\phi}, T)|_{T_*}\right)\Big|_{\phi_*}^{\underline{\phi}_f}, \qquad (5.4.8)$$

where  $T_*$  is the gravitational wave production temperature, typically identified with the percolation temperature of the phase transition  $T_p$ .  $\Delta\theta$  quantifies the amount of energy available for conversion to spacetime shear stress, which is represented by the off-diagonal components of the stress-energy tensor  $T^{\mu\nu}$ , and is responsible for the generation of gravitational waves [272–274]. This is taken in the relativistic plasma limit and in practice receives further corrections if the broken-phase speed of sound squared differs from  $c_s^2 = 1/3$  [275, 276].

The ratio of the trace anomaly difference to the energy density in the plasma (approximated by the radiation energy density at the GW production temperature  $\rho_r = \pi^2 g_* T_p^4/30$ ), quantifies the energy available for gravitational wave production, and thus characterises the strength of the phase transition:<sup>1</sup>

$$\bar{\alpha} \equiv \frac{\Delta \theta}{\rho_r} \,. \tag{5.4.9}$$

Several alternative definitions of  $\bar{\alpha}$  exist in the literature. A commonly used one defines it as the ratio of vacuum energy difference to the radiation energy density,  $\bar{\alpha} = \Delta V_{\rm eff}/\rho_r$ , which neglects thermal effects [24]. Another popular definition comes from hydrodynamics, where  $\bar{\alpha} = \Delta \rho/(\rho + p)$  describes the energy injected into the plasma relative to its enthalpy [277]. A third definition is based on the *pseudo* trace anomaly definition [275], which approximates the energy available for shear stress using a simplified thermal treatment.

The definition used in this chapter includes both vacuum and thermal contributions and is particularly appropriate for models like the 2HDM, where no tree-level barrier is present and thermal corrections are essential for realizing a FOPT.

Next,  $\bar{\beta}/H_*$ , is derived from the truncated first order Taylor expansion of the bubble

 $<sup>^{1}\</sup>mathrm{As}$  above, we use barred notation for this parameter to differentiate it from the Lagrangian parameters in the 2HDM.

nucleation rate around  $t_*$ , the characteristic time of the GW production, [21,262,278]:

$$\Gamma_N = Ae^{-S_3/T} \approx \Gamma_N(t = t_p)e^{-\bar{\beta}(t - t_p)}, \qquad (5.4.10)$$

where  $\bar{\beta}$  clearly characterises the inverse time scale of the transition. Under the adiabatic assumption for the expansion of the universe, dT/dt = -HT with H being the Hubble parameter [21]. Thus we can derive  $\bar{\beta}/H_*$  through [262]

$$\bar{\beta} = \frac{d(S_3/T)}{dt} \bigg|_{t=t_*} = H_* T_* \left. \frac{d(S_3/T)}{dT} \right|_{T=T_*}.$$
 (5.4.11)

As before,  $t_* = t_p$  as it is typically associated with the time of percolation rather than nucleation.

#### 5.4.3 Gravitational Wave Spectrum

Early universe FOPTs give three main sources of gravitational waves:

- Sound waves induced by the expansion of bubbles into the surrounding plasma,
- Bubble collisions creating anisotropic stress directly [279],
- Turbulence in the plasma caused by bubble collision energy [23, 280].

Typically, the GW contribution from these three sources can be calculated from knowledge of the thermal parameters  $\bar{\alpha}, \bar{\beta}/H_*$  and  $v_W$  which is the bubble wall velocity. A thorough calculation of  $v_W$  can be achieved through hydrodynamical simulations of the phase transition, as in Refs. [281, 282], however these are time consuming and  $v_W$  is typically supplied as an input parameter [262, 283]. A general perturbative determination of  $v_W$  requires including out-of-equilibrium effects [284] as recently automated in Ref. [285].

It has been argued by Steinhardt [286] that  $v_W$  can be approximated by the Chapman-Jouguet velocity, typically used to describe explosive detonations:

$$v_W \approx v_{\rm CJ} = \frac{1}{1+\bar{\alpha}} \left( c_s + \sqrt{\bar{\alpha}^2 + \frac{2}{3}\bar{\alpha}} \right)$$
 (5.4.12)

where we take the speed of sound in the plasma to be  $c_s=1/\sqrt{3}$ . For the strongest transitions we find in Section 5.5 (which have  $\bar{\alpha}\approx 4\times 10^{-3}$ ) the Chapman-Jouguet velocity gives  $v_W\approx 0.63$ , justifying the ansatz used in Section 5.4.1, and the use of this value as an input to Eq. (5.4.7) in our numerical studies. However, Eq. (5.4.12) is valid only in a restricted regime. As noted in Refs. [283,287], the assumptions underlying the Chapman-Jouguet condition do not strictly apply to cosmological phase transitions due to the differences between chemical combustion and cosmological phase transitions. More accurate treatments bracket the true value of  $v_W$  between two physical limits: a ballistic limit, representing minimal interaction between the bubble wall and plasma [283], and a Local Thermal Equilibrium (LTE) limit, which assumes local entropy conservation and requires detailed thermodynamic input [283,288,289]. The LTE expression has been shown to match well with numerical simulations [290], but is computationally prohibitive for parameter scans. For simplicity, we adopt the Chapman-Jouguet approximation in this chapter.

The characteristic frequency of the GW spectrum  $f_*$  can be naively estimated by multiplying the redshift factor (from the time of GW production to today) with  $H_*$ . This rests on the approximation that the wavelength of the signal is set by the horizon scale at time of production.

In the following sections, we will discuss the fitting formulas for the three sources of gravitational waves that have been derived from numerical simulations.

#### Sound waves

Numerical simulations indicate that sound waves are typically the dominant source of GWs from FOPTs [291,292]<sup>1</sup>. Two length scales dictate the bounds of the power spectrum of the acoustic GW contribution, which are the mean distance between the bubbles,

$$R_* = (8\pi)^{1/3} v_W / \bar{\beta} \,, \tag{5.4.13}$$

<sup>&</sup>lt;sup>1</sup>This is indeed the case across the parameter space of this work, however see [293] for examples of exceptions.

and the thickness of the expanding sound shell in the plasma outside the bubble of the new phase,

$$\Delta R_* = R_* \frac{|v_W - c_s|}{c_s} \,. \tag{5.4.14}$$

The sound shell thickness  $\Delta R_*$  dictates the position of the peak of the power spectrum [294]. Hindmarsh et al derived an analytic fitting formula for the acoustic GW contribution [25, 292, 294], which we write here in the form used by PhaseTracer2 [262],

$$\Omega_{\rm sw}h^2(f) = 2.061 F_{gw,0} \Gamma^2 \bar{U}_f^4 S_{\rm sw}(f) \tilde{\Omega}_{\rm gw}h^2 \times \min(H_* R_* / \bar{U}_f, 1) (H_* R_*) , \qquad (5.4.15)$$

where  $\min(H_*R_*/\bar{U}_f, 1)(H_*R_*)$  accounts for the finite lifetime of the shear stress induced by the sound waves [292], and

$$F_{gw,0} = 3.57 \times 10^{-5} \left(\frac{100}{g_*}\right)^{1/3}$$
, (5.4.16)

$$S_{\rm sw}(f) = \left(\frac{f}{f_{\rm sw}}\right)^3 \left(\frac{7}{4+3\left(\frac{f}{f_{\rm sw}}\right)^2}\right)^{7/2},$$
 (5.4.17)

$$\frac{f_{\text{sw}}}{1\,\mu\text{Hz}} = \frac{2.6}{H_* R_*} \left(\frac{z_p}{10}\right) \left(\frac{T_*}{100\,\text{GeV}}\right) \left(\frac{g_*}{100}\right)^{1/6} \,. \tag{5.4.18}$$

Here,  $f_{\rm sw}$  is the peak frequency of the sound waves and  $S_{\rm sw}(f)$  is the spectral shape.  $\Gamma$  is the ratio of enthalpy to the energy density of the plasma, taken to be 4/3 for the early universe,  $\bar{U}_f$  is the enthalpy weighted root mean square fluid velocity of the plasma, and  $z_p \sim 10$  and  $\tilde{\Omega}_{\rm gw} \sim 0.012$  are parameters informed by the numerical simulations.

Thus, we see that  $\Gamma \bar{U}_f^2 = K_{\rm sw}$  is the ratio of kinetic energy in the fluid to its energy density. We can write this as

$$\Gamma \bar{U}_f^2 = K_{\text{sw}} = \frac{\kappa_{\text{sw}} \bar{\alpha}}{1 + \bar{\alpha}}, \qquad (5.4.19)$$

where  $\kappa_{sw}$  is an efficiency factor for the conversion of the latent energy of the phase transition into the acoustic kinetic energy of the fluid.

PhaseTracer2 employs the following fitting formula for  $\kappa_{\rm sw}$  when the wall velocity

is taken to be the Chapman-Jouguet velocity:

$$\kappa_{\rm sw} = \frac{\sqrt{\bar{\alpha}}}{0.135 + \sqrt{0.98 + \bar{\alpha}}} \,. \tag{5.4.20}$$

#### **Bubble Collisions**

Similar numerical simulations are used to inform fitting formulas for the GW contribution from bubble collisions. The envelope approximation [295], where bubble wall thicknesses are considered to be infinitesimal and are treated as non-existent in regions of overlap, is often employed to simplify these computations [295–299]. Here, we quote the fitting formulas used by PhaseTracer2 [262] based on the work in Ref. [300]:

$$\Omega_{\rm col}^{\rm env} h^2(f) = 1.67 \times 10^{-5} \Delta \left(\frac{g_*}{100}\right)^{-1/3} \left(\frac{\bar{\beta}}{H_*}\right)^{-2} K_{col}^2 S_{\rm env} \left(\frac{f}{f_{\rm env}}\right) , \qquad (5.4.21)$$

where

$$\Delta = \frac{0.48v_W^3}{1 + 5.3v_W^2 + 5v_W^4} \,. \tag{5.4.22}$$

As with the sound waves,

$$K_{\rm col} = \frac{\kappa_{\phi}\bar{\alpha}}{1+\bar{\alpha}} \tag{5.4.23}$$

represents the fraction of latent phase transition energy converting to kinetic energy in the fluid from collisions, where

$$\kappa_{\phi} = \frac{1}{1 + 0.715\bar{\alpha}} \left( 0.715\bar{\alpha} + \frac{4}{27} \sqrt{\frac{3\bar{\alpha}}{2}} \right) \tag{5.4.24}$$

is the efficiency factor [298].

The spectral shape is given by

$$S_{\text{env}}(r) = (0.064r^{-3} + 0.456r^{-1} + 0.48r)^{-1},$$
 (5.4.25)

and the peak collisional frequency is given by

$$\frac{f_{\text{env}}}{1\,\mu\text{Hz}} = 16.5 \left(\frac{f_*}{\bar{\beta}}\right) \left(\frac{g_*}{100}\right)^{1/6} \left(\frac{\bar{\beta}}{H_*}\right) \left(\frac{T_*}{100\,\text{GeV}}\right) \tag{5.4.26}$$

where

$$\frac{f_*}{\bar{\beta}} = \frac{0.35}{1 + 0.069v_W + 0.69v_W^4} \,. \tag{5.4.27}$$

#### Turbulence

Simulation based fitting formulas for the contribution from magnetohydrodynamic turbulence in the plasma, calculated in Refs. [23,149], are used as follows in PhaseTracer2 [262]:

$$\Omega_{\rm turb}h^2(f) = 3.35 \times 10^{-4} v_W \left(\frac{\bar{\beta}}{H_*}\right)^{-1} K_{\rm turb}^{3/2} \left(\frac{g_*}{100}\right)^{-1/3} \frac{r^3}{(1+r)^{11/3} (1+8\pi f/H_0)},$$
(5.4.28)

where

$$H_0 = 16.5 \left(\frac{g_*}{100}\right)^{1/6} \left(\frac{T_*}{100 \,\text{GeV}}\right) \,\mu\text{Hz}$$
 (5.4.29)

is the redshifted Hubble rate at the GW production temperature  $T_*$ , and

$$K_{\text{turb}} = \frac{\kappa_{\text{turb}}\bar{\alpha}}{1+\bar{\alpha}},\tag{5.4.30}$$

is the fraction of phase transition energy transferred to turbulence in the plasma. The efficiency factor  $\kappa_{\rm turb}$  can be taken to be in the range  $0.05 \lesssim \kappa_{\rm turb}/\kappa_{\rm sw} \lesssim 0.1$  [292].

The variable  $r = f/f_{\text{turb}}$  with peak frequency

$$f_{\text{turb}} = \frac{27}{v_W} \frac{\bar{\beta}}{H_*} \left(\frac{g_*}{100}\right)^{1/6} \left(\frac{T_*}{100 \,\text{GeV}}\right).$$
 (5.4.31)

#### **Total Spectrum**

Finally, we arrive at the total gravitational wave spectrum which is the sum of these three contributions,

$$\Omega_{\rm gw}h^2(f) = \Omega_{\rm sw}h^2(f) + \Omega_{\rm col}^{\rm env}h^2(f) + \Omega_{\rm turb}h^2(f). \qquad (5.4.32)$$

For high GW production temperatures  $T_* > 10 \,\text{GeV}$ , the contribution from bubble collisions is neglected in PhaseTracer2 [262] due to the sound wave contribution being significantly larger.

#### 5.4.4 LISA signal to noise ratios

The signal to noise ratios (SNRs) for LISA can be calculated through [25, 301]

$$SNR_{LISA} = \sqrt{\mathcal{T} \int_{f_{min}}^{f_{max}} df \left(\frac{h^2 \Omega_{gw}(f)}{h^2 \Omega_{sens}(f)}\right)^2},$$
 (5.4.33)

where  $\mathcal{T}$  is the length of time for data collection, and  $h^2\Omega_{\text{sens}}(f)$  is the frequency dependent sensitivity of the experiment. It is given by [301]

$$h^2 \Omega_{\text{sens}}(f) = \frac{4\pi^2}{3H_0^2} f^3 S_h(f)$$
 (5.4.34)

where the  $S_h(f)$  is the inverse noise weighted sensitivity to the spectral density,

$$S_h(f) \simeq \frac{20\sqrt{2}}{3} \left( \frac{S_I(f)}{(2\pi f)^4} + S_{II}(f) \right) \left( 1 + \left( \frac{3f}{4f_*} \right)^2 \right) .$$
 (5.4.35)

For LISA, the term involving

$$S_I(f) = 5.76 \times 10^{-48} \left( 1 + \left( \frac{f_1}{f} \right)^2 \right) \text{ Hz}^3$$
 (5.4.36)

where  $f_1 = 0.4 \,\text{mHz}$ , gives the acceleration noise associated with spurious forces on the test masses, for example those that occur due to the build up of electrostatic charge [302].

The term involving

$$S_{II}(f) = 3.6 \times 10^{-41} \,\mathrm{Hz}^{-1}$$
 (5.4.37)

corresponds to the noise from optical path length fluctuations. The characteristic LISA frequency  $f_* = c/(2\pi L)$ , where  $L = 2.5 \times 10^6$  km and c is the speed of light, relates to the distance that light travels between LISA sensors.

Useful quantities that can be taken from  $\Omega_{\rm gw}h^2$  include the frequency  $f_{\rm gw}$  for which the amplitude is greatest (the 'peak frequency'), and the peak amplitude  $\Omega_{\rm gw}h^2(f_{\rm gw})$  at that frequency.

#### 5.4.5 From the Effective Potential to Gravitational Waves

In the previous two sections, we have described our calculation of the 2HDM thermal potential and the dynamics of the first order phase transition with a light degree of freedom. We summarise the calculation pipeline with the following steps:

- 1. First, we take the physical input parameters  $\{m_h, m_H, m_A, m_{H^{\pm}}, \tan(\beta), \cos(\beta \alpha), m_{12}\}$  defined at the input RG scale  $\Lambda_0 = m_Z$ .
- 2. Next, we use these physical input parameters to calculate the one-loop renormalised 4D Lagrangian input parameters  $\{m_{11}^2, m_{22}^2, m_{12}^2, \lambda_1, \dots, \lambda_5, y_t, g_1^2, g_2^2, g_3^2\}$ .
- 3. Next, we use the beta functions (provided in Appendix B.1) to RG evolve these renormalised 4D Lagrangian parameters to the matching scale  $\bar{\mu}_4 = 4\pi e^{-\gamma_E}T$ , such that we have  $\{\bar{m}_{11}^2, \bar{m}_{22}^2, \bar{m}_{12}^2, \bar{\lambda}_1, \dots, \bar{\lambda}_5, \bar{y}_t, \bar{g}_1^2, \bar{g}_2^2, \bar{g}_3^2\}$ .
- 4. Using the soft 3D matching relations, we calculate the soft parameters

$$\{(m_{11}^{3D})^2, (m_{22}^{3D})^2, (m_{12}^{3D})^2, \lambda_1^{3D}, \dots, \lambda_7^{3D}, y_t^{3D}, (g_1^{3D})^2, (g_2^{3D})^2, (g_3^{3D})^2\}$$
 (5.4.38)

at the scale  $\bar{\mu}_3 = T$ . In the soft theory,  $\lambda_{6-7}^{3D}$  arise from integrating out the non-zero Matsubara modes, despite our model having as input  $\lambda_{6-7} = 0$ .

5. Using the softer matching relations, we calculate the softer parameters

$$\{(\bar{m}_{11}^{3\mathrm{D}})^2, (\bar{m}_{22}^{3\mathrm{D}})^2, (\bar{m}_{12}^{3\mathrm{D}})^2, \bar{\lambda}_1^{3\mathrm{D}}, \dots, \bar{\lambda}_7^{3\mathrm{D}}, \bar{y}_t^{3\mathrm{D}}, (\bar{g}_1^{3\mathrm{D}})^2, (\bar{g}_2^{3\mathrm{D}})^2, (\bar{g}_3^{3\mathrm{D}})^2\}$$
 (5.4.39)

at the softer matching scale  $\bar{\mu}_{3\text{US}} = \bar{\mu}_3$ .

- 6. The softer parameters serve as input to construct the 3D effective potential,  $V_3(\phi_1^{3D}, \phi_2^{3D}, T)$ . As mentioned previously, we find the 4D effective potential  $V_4(\phi_1, \phi_2, T)$  through Eq. 5.3.4.
- 7. Through  $V_4(\phi_1, \phi_2, T)$ , we can then,

Note that in this chapter and Appendix B we use the notation  $g_1 = g'$ ,  $g_2 = g$ , and  $g_3 = g_s$ .

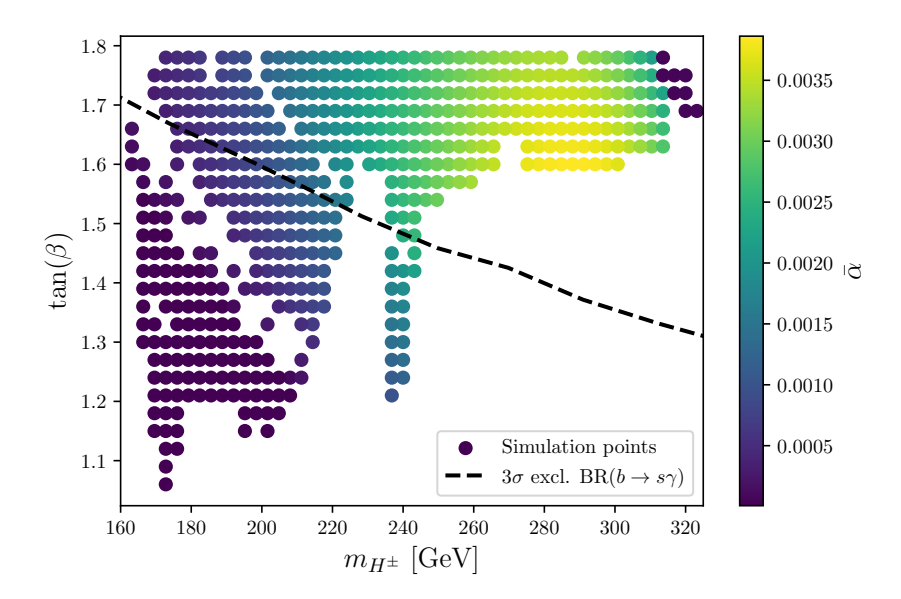


Figure 5.2: Computed phase transitions with a light pseudoscalar  $m_A = 95$  GeV in the region seen in Fig. 5 of Ref. [204]. We have fixed  $m_H = 160$  GeV and  $\cos(\beta - \alpha) = -0.2$ , with the other fixed values as in Table 5.1.

- (a) Find the minima of the potential, identifying when they co-exist and finding possible critical temperatures  $T_C$ .
- (b) Find possible transition paths between the minima and calculate the action S along the paths, comparing S/T to the percolation criterion in Eq. 5.4.7. This allows us to calculate the percolation temperature(s)  $T_p$ .
- (c) Calculate the transition parameters  $\bar{\alpha}$ ,  $\bar{\beta}/H_*$ , and then the peak gravitational wave frequencies and amplitudes associated with the transitions. From this, the signal-to-noise ratios (SNRs) for LISA or other experiments can be calculated.

### 5.5 Results

As explained previously, we work in the real 2HDM Type I, associating the 95 GeV resonance with the pseudoscalar A. The model features eight free parameters, of which we fix six to benchmark values informed by theoretical and experimental constraints (Table 5.1).

5.5. Results 167

In particular, we fix  $\tan \beta$  to be within the range necessary to fit both the diphoton signal and the ditau signal (see e.g. Ref. [204]). Interestingly, we have confirmed that the value of  $\tan(\beta)$  chosen here also optimises the strength of the EWPT as can be seen in Fig. 5.2. In this figure, we show the transition strength parameter  $\bar{\alpha}$  in the parameter space allowed by current constraints [204], fixing  $m_H = 160$  GeV and  $\cos(\beta - \alpha) = -0.2$  which will be motivated a posteriori. From this result it is seen that the value of  $\tan(\beta)$  chosen to fit both collider signals also leads to stronger phase transitions, when  $m_{H^{\pm}} \approx 290$  GeV. This also partially alleviates the tensions with flavour physics  $(b \to s\gamma)$ .

Lastly, we find little sensitivity to  $m_{12}$  below  $m_{12} \sim 10 \,\text{GeV}$ , and fix it at an arbitrary value of  $m_{12} = 1 \,\text{GeV}$  to represent that entire range. A preliminary scan in  $m_{12}$  up to  $10^2 \,\text{GeV}$  showed that  $\bar{\alpha}$  was strongest for  $m_{12} \approx 10^{1.35} \,\text{GeV}$ . An analysis with  $m_{12}$  fixed to this value showed no qualitative and only minor quantitative differences from the conclusions presented below (maximum SNR at LISA was found to be  $\mathcal{O}(10^{-6})$ ).

For supercooled transitions, it is also important to check that volume of space that is in the false vacuum is decreasing, along with checking the percolation condition in Eq. (5.4.7). This is because the condition can be met and yet the progression of the transition could be reversed. Since supercooling as quantified by the relative difference of  $\delta_{\rm SC} = (T_C - T_N)/T_N$  is never larger than  $\sim 20\%$  across the parameter space, the transitions are not strongly supercooled. Due to the absence of such large supercooling, the condition of shrinking false vacuum is also met for the investigated parameter space and no subsequent thermal inflation is observed [303, 304]. The observed mild values of supercooling result also in relatively small field values and no large separation of temperature scales in contrast to classically conformal models, where supercooling is large and one needs to utilise a more refined framework [305–307]. In turn, this gives credence to the validity of the high-temperature expansion for computing both the transition timescale and the strength within the 3D EFT framework.

Chapter 5. Phase Transition Phenomenology of the 95 GeV Resonance in the Two Higgs Doublet Model

Parameter	Value	Motivation
$\overline{m_A}$	95  GeV	Resonance mass
$m_h$	125  GeV	SM-like Higgs
$m_{H^{\pm}}$	$290~{\rm GeV}$	Alleviate $b \to s \gamma$ tension
$\tan \beta$	1.57	Fit $\gamma\gamma$ and $\tau\tau$ excesses
$m_{12}^{2}$	$1 \text{ GeV}^2$	Minimal impact on EWPT strength
$v = \sqrt{v_1^2 + v_2^2}$	$246~{\rm GeV}$	Electroweak vev

Table 5.1: Fixed inputs for our scan identifying A, H with the resonance respectively.

The remaining two parameters are varied as

$$\cos(\beta - \alpha) \in [-0.3, 0.3], \qquad m_H \in [130, 300] \text{ GeV}.$$
 (5.5.1)

We vary the temperature T between 300 and 20 GeV when finding the phases and identifying transitions. As we shall see, we do not expect that allowing for smaller  $m_H$  in our scan leads to different vacuum structures or stronger transitions.

These ranges are fully compatible with electroweak precision fits: by keeping  $m_H \in [130, 300]$  GeV (with near degenerate A and  $H^{\pm}$ ) and  $|\cos(\beta - \alpha)| \leq 0.3$ , the S and T parameters lie within the  $2\sigma$  allowed region of global fits. Moreover, the implied quartic couplings in the scalar potential remain  $\mathcal{O}(1)$ , well below the treelevel unitarity bounds (and safely perturbative), so all  $2 \to 2$  scalar-scalar amplitudes satisfy  $|a_0| < \frac{1}{2}$ , where  $a_0$  is the s-wave amplitude of the  $2 \to 2$  scattering.<sup>1</sup>

We show the results of our scan in Fig. 5.3. We find that the vacuum structure as a function of temperature depends on  $\cos(\beta - \alpha)$  and  $m_H$  as follows:

For small  $m_H \lesssim 200$  GeV and large  $\cos(\beta - \alpha) \gtrsim -0.1$ , the first vacuum away from the origin to appear does not give the SM-like resonance h a vev. The further, SM-like vacuum only appears later, and EWSB thus occurs through a two-step transition. Either of these transitions is weaker than the immediate transition to the SM-like vacuum, which occurs for a band of smaller  $\cos(\beta - \alpha)$ . This is because in this range, the electroweak gauge bosons couple more strongly to the SM-like state.

<sup>&</sup>lt;sup>1</sup>This condition is a result of the imposition of unitarity on the Legendre expansion of the scattering matrix, where  $a_j$  is the coefficient of the j-th Legendre polynomial  $P_j(\cos(\theta))$ , and  $a_0$  is real for a tree-level process. See Ref. [34] for a derivation of this constraint.

5.5. Results 169

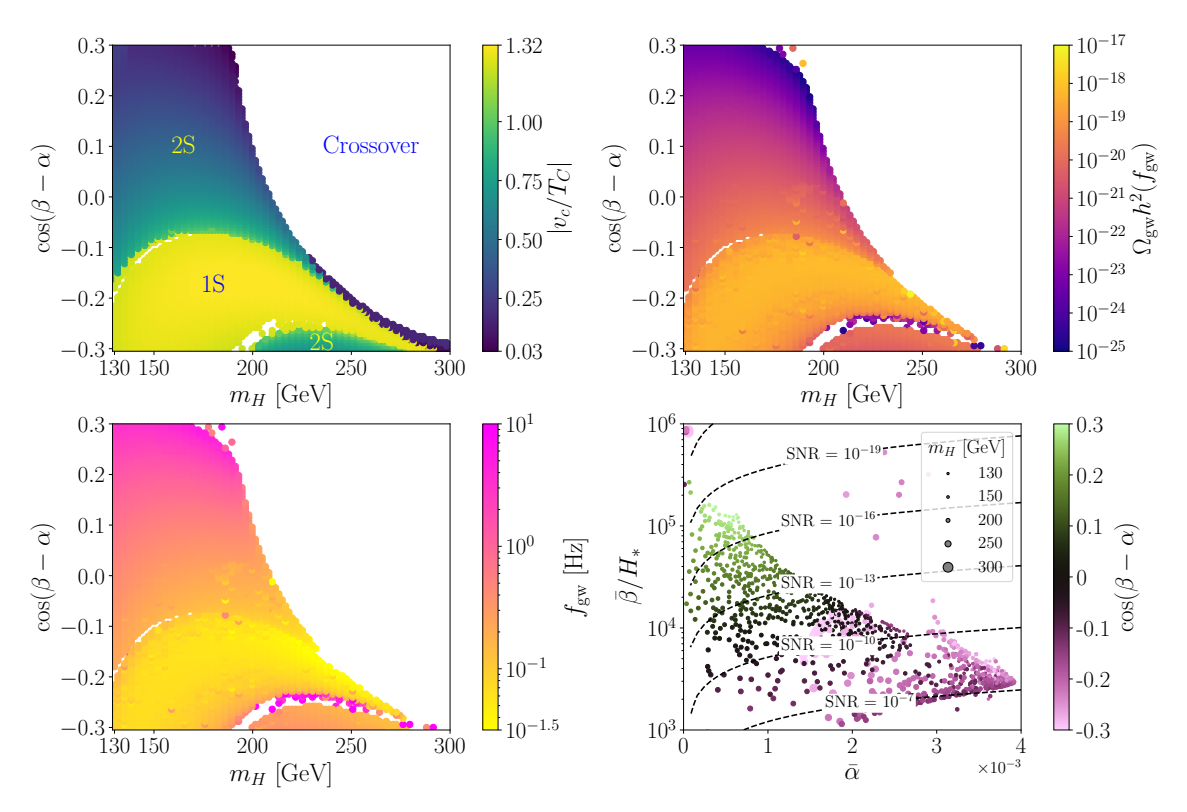


Figure 5.3: **Top Left Panel:** First order phase transitions in the  $m_H$  -  $\cos(\beta - \alpha)$  plane, with the colour showing the value of the largest  $|v_c/T_C|$  for that parameter point. Regions of two step (2S) and one step (1S) first order phase transitions are labelled, along with the region that has crossovers. Top Right Panel: As for top left, showing the peak amplitude  $\Omega_{\rm gw}h^2(f_{\rm gw})$  instead. Bottom Left Panel: As for top left, showing the peak frequency  $f_{gw}$  instead. Bottom Right Panel: Computed phase transitions for different parameter points plotted against transition parameters  $\bar{\alpha}$  and  $\beta/H_*$ . Only a randomly sampled selection (1 in 4) is chosen to be shown on the plot to make the trends clear. The value of  $\cos(\beta - \alpha)$  for each point is shown by the colour, whereas the value of  $m_H$  is shown by the size of the circle. We show LISA SNR curves for an ansatz transition temperature of 160 GeV, and an ansatz  $v_W = 0.63$ .

Chapter 5. Phase Transition Phenomenology of the 95 GeV Resonance 170 in the Two Higgs Doublet Model

BM	$m_H$	$\cos(\beta - \alpha)$	$\bar{\alpha}_{1\text{-loop}}$	$\bar{\alpha}_{2\text{-loop}}$	Error
2S	130	0	0.0017	0.0035	51%
1S	200	-0.2	0.00015	0.00019	21%

Table 5.2: The transition strength parameter  $\bar{\alpha}$  and relative errors for Benchmarks 2S and 1S at (2-loop improved) 1-loop [3D@NLO  $V_3$ @LO] and 2-loop [3D@NLO  $V_3$ @NLO]. Other parameters are fixed according to Table 5.1.

For lower  $\cos(\beta - \alpha)$  the transition again occurs in two steps. For large  $m_H$  and  $\cos(\beta - \alpha)$ , no barriers are created and EWSB occurs via a crossover.

In the second and third panel, we show the peak amplitude and frequency for the GW spectrum resulting from strongest transition. As expected, the largest amplitudes are found in the band where the transition occurs directly. However, the amplitudes throughout this parameter space are lower than can be probed by the anticipated GW experiments in the next decades. Moreover, the peak frequencies are typically outside of the range of space-based interferometers, reflecting the large  $\bar{\beta}/H_*$  parameters found in our scan.

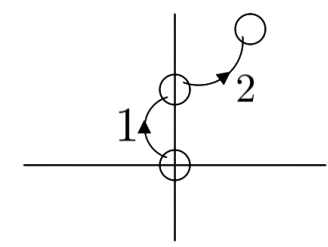
This is explicitly demonstrated in the last panel of Fig. 5.3, in which we show the predicted latent heat parameter  $\bar{\alpha}$  and inverse duration parameter  $\bar{\beta}/H_*$  for the range of models we scan over. We show contours of fixed SNR for the LISA experiment (calculated through Eq. 5.4.33) with dashed contours, where we assumed a transition temperature of 160 GeV which we found to be characteristic, and a wall speed of  $v_W = 0.63$ . No models in our scan reach SNR unity.

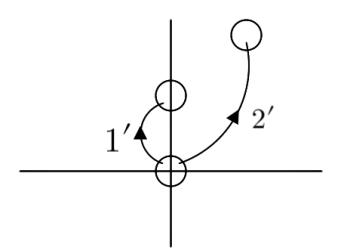
Finally, we attempt to quantify the error introduced by our use of the two-loop improved one-loop potential instead of the two-loop potential.<sup>1</sup>. We evaluate two benchmark points which are representative of the two step region (2S) and the one step region (1S), at both one and two loop, making use of the two loop matching relations in both cases.

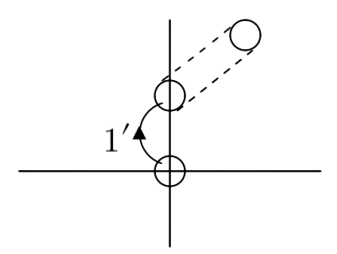
The results of these benchmark points are found in Table 5.2. We find that the

 $<sup>^1\</sup>mathrm{The}$  two-loop result was not used for our parameter scan due to the issues discussed in Section 5.3.1

5.5. Results 171







- (a) Benchmark 2S showing a 2-step transition at both 1- and 2-loop.
- (b) Benchmark 1S @ 1-loop, showing a direct transition labelled 2'. A weaker transition 1' (with a lower  $T_p$ ) is also calculated.
- (c) Benchmark 1S @ 2-loop, showing a direct transition labelled 1'. This is followed by a crossover to the zero-temperature minimum.

Figure 5.4: Illustrative phase diagrams for the benchmark points 1S and 2S in Table 5.2, with regions that contain 1S and 2S shown in Fig. 5.3.

differences in percolation temperatures are in agreement with the differences between the 1-loop and 2-loop calculations in Ref. [79], and that the differences in  $\bar{\alpha}$  are of order  $\mathcal{O}(0.1-1)$ . This means that while the 2-loop potential provides important quantitative contributions, the transition strengths are within the same order of magnitude, resulting in similarly weak SNRs. For benchmark 2S, the interim phase appears earlier than the SM-like vacuum, resulting in the 2-step transition (Fig. 5.4a). For benchmark 1S at 1-loop, the single step occurs directly from the origin to the SM-like vacuum (Fig. 5.4b), as the interim phase appears at a colder temperature than the SM-like vacuum, and disappears quickly. For the same benchmark at 2-loop, the interim phase and the further SM-like vacuum are not distinct and instead there is a crossover between them. Thus the transition happens to the field space location of the interim phase, and then the phase migrates to the location of the SM-like vacuum (Fig. 5.4c. As higher order corrections are known to change the type of phase transition [308], this is a source of the difference between the 1-loop and 2-loop results. We illustrate this phase structure in Fig. 5.4.

For benchmark 1S at 1-loop, we provide the  $\bar{\alpha}$  of transition 1' in Fig. 5.4b in the table, rather than the stronger transition 2'. This provides a more direct comparison to the 1' transition of 1S at 2-loop (see Fig. 5.4c).

#### 5.6 Conclusions

In this chapter, we identified the available parameter space for the implementation of the 95 GeV resonance into the real Type I 2HDM based on previous work, ensuring a simultaneous best fit for the  $b \to s \gamma$  branching ratio, and the  $\gamma \gamma$  and  $\tau \tau$  resonances. The constraints leave  $m_H$  and  $\cos(\beta - \alpha)$  as the parameters that are most free to change. After fixing the rest of the parameters in the model, we use the dimensionally reduced thermal effective potential to compute the transition parameters  $\bar{\alpha}$  and  $\bar{\beta}/H_*$ . We also compute the gravitational wave spectrum  $\Omega_{\rm gw}h^2(f)$ , its peak frequency  $f_{\rm gw}$  and peak amplitude  $\Omega_{\rm gw}h^2(f_{\rm gw})$ .

We find that in the  $m_H - \cos(\beta - \alpha)$  parameter space, there are regions of crossovers, one step, and two step first order transitions. The region with one step transitions predictably provides the strongest transitions, with  $\bar{\alpha} \sim 0.0035$ . These correspond to peak amplitudes of  $\sim 10^{-18}$  and  $f_{\rm gw} \sim 10^{-1.5}$ , resulting in the strongest SNRs for the LISA experiment being around  $10^{-7}$ , which are much weaker than the conventionally desired thresholds of SNR  $\sim 10$ . We conclude that a model that simultaneously seeks to explain the  $\gamma\gamma$ ,  $\tau\tau$  and LEP excesses in the 2HDM could only result in FOPTs that are too weak to be detected by LISA, and would require interferometers with much greater sensitivity to the cHz frequency band.

The modest strength of the EWPT observed in our scan can be attributed to the radiative origin of the barrier separating the vacua. In the parameter space compatible with identifying the 95 GeV excess as a light pseudoscalar, the scalar mass spectrum is relatively compressed, limiting the enhancement of thermal cubic terms that typically arise from large mass splittings. As a result, the barrier is primarily generated by gauge boson loops, similar to the Standard Model. The light pseudoscalar itself contributes only weakly to the thermal potential at high temperatures, and does not induce a significant enhancement of the barrier. This scenario contrasts with regions of the 2HDM where heavier scalars can radiatively strengthen the transition or where tree-level terms provide a barrier already at zero

5.6. Conclusions 173

temperature. In particular, previous studies have shown that large mass splittings, especially between the pseudoscalar and the heavy scalar or charged Higgs, can amplify scalar contributions to the thermal potential and lead to a strong first-order transition. Consequently, while the transition is generically first-order in our setup, it is not sufficiently strong to produce observable gravitational wave signals or support electroweak baryogenesis without additional model ingredients.

Another possibility for generating a large barrier via significant mass splitting is to treat the second, heavier scalar as a UV degree of freedom in the final EFT, and integrate it out during dimensional reduction. However, implementing this approach would require dynamically switching between different EFT hierarchies throughout the parameter scan [252]. We have therefore chosen to focus on the thermal mass hierarchy as outlined in our analysis, and defer the exploration of more intricate EFT hierarchies to future work.

Lastly, we comment on how additional degrees of freedom could alter the thermal history and potentially enhance the strength of the phase transition. In the 2HDM we discussed, the barrier between the high temperature and the low temperature vacuum is generated radiatively. A coupling of the Higgs sector to a scalar gauge singlet can introduce a tree-level barrier in the potential. Alternatively, fermionic extensions or higher-dimensional operators (e.g.  $(H^{\dagger}H)^3/\Lambda^2$ ) in the UV of the 4D theory [134] can enable viable electroweak baryogenesis. Additionally, higher-dimensional operators in the UV of the 3D EFT theory [309–311] can modify the shape of the potential at finite temperature, and thus the strength of the transition. These extensions may also shift the transition dynamics into a more strongly supercooled regime, lowering the percolation temperature and thus pushing the GW signal into the most sensitive frequency band of space-based interferometers. A systematic exploration of such scenarios within the dimensional reduction framework, including complementary constraints from colliders and electroweak precision studies (e.g. [278, 312]) is a promising direction for future work.

# Chapter 6

# Conclusion

Well, here at last, dear friends, on the shores of the Sea comes the end of our fellowship in Middle-earth.

from The Lord of the Rings by J.R.R. Tolkien

In this thesis, we have explored theoretical early universe phenomena tangentially connected by a link to the baryon asymmetry of the universe. These are: Hot Leptogenesis, and a first order electroweak phase transition in the Type I 2HDM. Particle physics at this scale requires finite temperature considerations, for example thermal statistics/thermodynamics in the analysis of hot leptogenesis, and dimensional reduction to calculate the thermal potential for the Type I 2HDM. We reviewed the Standard Model, cosmological, and finite temperature theoretical background in Chapters 2 and 3.

In Chapter 4, we discussed how the desire for naturalness in the Higgs sector imposes the Vissani bound on the lightest right-handed neutrino, such that  $m_{N_1} \lesssim 10^7 \,\mathrm{GeV}$ . This conflicts with the Davidson-Ibarra bound, the lower bound for sufficient baryon asymmetry generation, which generally requires  $m_{N_1} \gtrsim 10^{7-8} \,\mathrm{GeV}$ . Hot Leptogenesis is introduced as a model that can resolve these tensions with a hot sector filled with  $N_1$ , the lightest right-handed neutrino, and  $\phi$  a scalar particle that keeps the sector in kinetic equilibrium. The hot sector is identified as a natural consequence of

inequitable inflaton couplings to the hot sector vs the SM. The parameter space for the mass and Yukawa couplings of  $\phi$  are scanned over such that we clearly define regions of kinetic and chemical equilibrium in the hot sector, while ensuring no thermal contact with the SM sector. We elucidate the new Boltzmann equations for this setup, and calculate the baryon asymmetry  $\eta_B$  over part of the Casas-Ibarra parameter space. We demonstrate a factor  $\sim 50$  enhancement in the generated baryon asymmetry due to our model, and that there exist regions of the parameter space that provide the BAU without being finely-tuned. For a benchmark point, we find that we can produce the BAU with a Higgs sector fine-tuning of  $\Delta_H \approx 10.4\%$ , and neutrino sector fine-tuning of  $\Delta_{\nu} \approx 855\%$ , which is a substantial improvement on the finely-tuned parameter space for vanilla leptogenesis.

In Chapter 5, we investigate the electroweak phase transition in the real Type I 2HDM, where the physical degree of freedom A is identified with the reported 95 GeV di-gamma and di-tau excess. We define the constraints on the parameter space such that the most free parameters are  $m_H$  and  $\cos(\beta - \alpha)$ , which is the coupling of H to the gauge bosons. In order to calculate the 1-loop thermal potential (improved with 2-loop matching), we make use of the dimensional reduction method, which has been shown to have significantly reduced uncertainties in comparison to the more commonly used 4D methods with daisy resummation. The Mathematica package DRAlgo is used to compute the dimensionally reduced potential. This is then fed into a C++ script, and the PhaseTracer2 package is used to find the vacua, calculate the percolation temperature  $T_p$ , and calculate phase transition parameters  $\bar{\alpha}$  and  $\bar{\beta}/H_*$ . The gravitational wave spectrum  $\Omega_{\rm gw}h^2(f)$  is also computed, along with signal-tonoise ratios for the LISA experiment. We present this data as a parameter scan of the  $m_H - \cos(\beta - \alpha)$  plane, which shows regions with one-step and two-step first order phase transitions, as well as a crossover. We find that the highest signal-to-noise ratios are of order  $\sim 10^{-6}$ , and thus conclude that it is unlikely that the 95 GeV resonance explained by the 2HDM could provide a first order phase transition that is detectable by experiments in the near future.

# Appendix A

# Cross-Sections, Decay Rates and Thermal Averaging

In this appendix, we give details of the cross-sections, decay rates and thermal averaging we use in our computations.

## A.1 Cross-Sections and Decay Rates

In Section 4.3 we examine a number of processes that contribute to energy exchange (via elastic scattering) or particle number exchange (via number-changing processes). Here, we give the relevant cross-sections which we calculated with the help of FeynCalc [313].

The Feynman diagrams for the elastic scattering processes  $N_1N_{2,3} \rightarrow N_1N_{2,3}$  are given in Fig. 4.4 (a) and (b), and the cross-section is

$$\sigma_{N_1 N_{2,3} \to N_1 N_{2,3}}(s) = \frac{(y_{\phi}^1)^2 (y_{\phi}^{2,3})^2}{4\pi m_{\phi}^2 s^2 \left(m_{\phi}^2 + s\right)} \left[ s \left( 4m_{N_1}^2 \left( 4m_{N_{2,3}}^2 - m_{\phi}^2 \right) + m_{\phi}^2 \left( 2m_{\phi}^2 - 4m_{N_{2,3}}^2 + s \right) \right) + 2m_{\phi}^2 \left( m_{\phi}^2 + s \right) \left( m_{\phi}^2 - 2 \left( m_{N_1}^2 + m_{N_{2,3}}^2 \right) \right) \log \left( \frac{m_{\phi}^2}{m_{\phi}^2 + s} \right) \right], \quad (A.1.1)$$

where s is the squared centre-of-mass energy. This process is relevant for considering whether the SM and hot sectors come into equilibrium via elastic scattering.

Figure 4.4 (a), (b) and (c) contribute to the elastic scattering process  $N_1N_1 \to N_1N_1$ , leading to the cross-section

$$\sigma_{2N_1 \to 2N_1}(s) = \frac{(y_{\phi}^1)^4}{16\pi s^2 m_{\phi}^2 (m_{\phi}^2 - s)^2 (m_{\phi}^2 + s)(2m_{\phi}^2 + s)} \left[ m_{\phi}^2 (m_{\phi}^4 - s^2)(24m_{N_1}^4 (s - 2m\phi^2) + 16m_{N_1}^2 (5s^2 + 2m_{\phi}^2 s - 4m_{\phi}^4) + 16m_{\phi}^6 - 8m_{\phi}^4 s - 5m_{\phi}^2 s^2) \log \left( \frac{m_{\phi}^2}{m_{\phi}^2 + s} \right) + s(2m_{\phi}^2 + s)(16m_{N_1}^4 (6m_{\phi}^4 - 9m_{\phi}^2 s + 5s^2) - 8m_{N_1}^2 (4m_{\phi}^6 - 9m_{\phi}^4 s + 7m_{\phi}^2 s^2) + 8m_{\phi}^8 - 12m_{\phi}^6 s + 3m_{\phi}^4 s^2 + 3m_{\phi}^2 s^3) \right]. \quad (A.1.2)$$

This process can maintain kinetic equilibrium in the hot sector.

Now we will consider number-changing processes that can maintain chemical equilibrium. The decay rate for  $\phi \to 2N_1$  shown in Fig. 4.6 (a) in the  $\phi$  rest frame is given by

$$\Gamma^{0}_{\phi \to 2N_{1}} = \frac{(y_{\phi}^{1})^{2} (m_{\phi}^{2} - 4m_{N_{1}}^{2})^{\frac{3}{2}}}{8\pi m_{\phi}^{2}}.$$
(A.1.3)

The cross-section for  $2N_1 \rightarrow 2\phi$  shown in Fig. 4.6 (b) and (c) is

$$\begin{split} \sigma_{2N_1 \to 2\phi}(s) &= \frac{y_\phi^4}{64\pi s \left(s - 4m_{N_1}^2\right)} \left[ -\frac{2\sqrt{s - 4m_{N_1}^2} \left(16m_{N_1}^4 + 2m_{N_1}^2 \left(s - 8m_\phi^2\right) + 3m_\phi^4\right)}{m_{N_1}^2 \sqrt{s - 4m_\phi^2} + m_\phi^4} \right. \\ &\quad + \frac{\left(s^2 - 4m_\phi^2 s + 6m_\phi^4 - 32m_{N_1}^4 + 16m_{N_1}^2 \left(s - m_\phi^2\right)\right)}{\left(s - 2m_\phi^2\right)} \\ &\quad \left. \left(s - 2m_\phi^2\right) \right. \\ &\left. \log\left(\frac{\sqrt{\left(s - 4m_{N_1}^2\right) \left(s - 4m_\phi^2\right)} - 2m_\phi^2 + s}{\sqrt{\left(s - 4m_{N_1}^2\right) \left(s - 4m_\phi^2\right)} + 2m_\phi^2 - s}\right) \right]. \quad (A.1.4) \end{split}$$

The cross-section for the s-channel process  $2N_1 \rightarrow 3\phi$  shown in Fig. 4.6 (d) is [314]

$$\sigma_{2N_1 \to 3\phi}(s) = \frac{\lambda^2 m_{N_1}^2 y_{\phi}^2}{6144\pi^2 s^2 (m_{\phi} - \sqrt{s})^2 (m_{\phi} + \sqrt{s})^{3/2}} \sqrt{\frac{s(3m_{\phi} - \sqrt{s})}{s - 4m_{N_1}^2}} \left[ (m_{\phi} + \sqrt{s})(3m_{\phi}^2 + s)\tilde{E}(m_{\phi}, s) - (m_{\phi} - \sqrt{s})^2)(3m_{\phi} + \sqrt{s})\tilde{F}(m_{\phi}, s) \right],$$
(A.1.5)

where  $\tilde{E}(m_{\phi}, s)$  is defined as

$$\tilde{E}(m_{\phi}, s) = E\left(\arcsin\left(\frac{1}{4}\sqrt{\frac{\left(3m_{\phi} - \sqrt{s}\right)\left(m_{\phi} + \sqrt{s}\right)^{3}}{m_{\phi}^{3}\sqrt{s}}}\right), \frac{16m_{\phi}^{3}\sqrt{s}}{\left(3m_{\phi} - \sqrt{s}\right)\left(m_{\phi} + \sqrt{s}\right)^{3}}\right), \tag{A.1.6}$$

and E(x,y) is the incomplete elliptic integral of the second kind, and similarly for  $\tilde{F}(m_{\phi},s)$  where F(x,y) is the incomplete elliptic integral of the first kind and the arguments are related in the same way.

## A.2 Thermal Averaging

For the rates considered in Section 4.3.1 we need the thermally averaged cross-sections for the initial states  $2N_1$  and  $N_1N_{2,3}$ , where  $N_1$  and  $N_{2,3}$  are at different temperatures.

The thermal averaged cross-section for two identical incoming  $N_1$  particles is given in Ref. [315],

$$\langle \sigma v \rangle = \frac{1}{8m_{N_1}^4 T_{N_1} K_2^2 \left(\frac{m_{N_1}}{T_{N_1}}\right)} \int_{4m_{N_1}^2}^{\infty} ds \, \sigma(s) (s - 4m_{N_1}^2) \sqrt{s} K_1 \left(\frac{\sqrt{s}}{T_{N_1}}\right) , \qquad (A.2.1)$$

where  $K_1$  and  $K_2$  are modified Bessel functions of the first and second kind, respectively.

For two incoming particles of different masses and different temperatures, we generalise the results in Refs. [158, 315, 316]. For the case of the initial state  $N_1N_2$ , the

thermal average is given by

$$\langle \sigma \bar{v} \rangle = \frac{\int \sigma \bar{v} f_{N_1} f_{N_2} d^3 \mathbf{p}_{N_1} d^3 \mathbf{p}_{N_2}}{\int f_{N_1} f_{N_2} d^3 \mathbf{p}_{N_1} d^3 \mathbf{p}_{N_2}}$$
(A.2.2)

where  $\bar{v}$  is the Møller velocity. We then neglect quantum statistics and take the approximation that  $f_{N_1}$  and  $f_{N_2}$  are given by Maxwell-Boltzmann distributions. This assumption lets us perform the integrals analytically and introduces minimal errors in our results. We first compute the denominator,

$$\int f_{N_1} f_{N_2} d^3 \mathbf{p}_{N_1} d^3 \mathbf{p}_{N_2} = 16\pi^2 T_{N_1} T_{\text{SM}} m_{N_1}^2 m_{N_2}^2 K_2 \left(\frac{m_{N_1}}{T_{N_1}}\right) K_2 \left(\frac{m_{N_2}}{T_{\text{SM}}}\right) , \quad (A.2.3)$$

where we have used the fact that  $E dE = |\mathbf{p}| d|\mathbf{p}|$  to rewrite the integral. For the numerator we follow the computation in [317]. We change coordinates from  $E_{N_1}$  and  $E_{N_2}$  to  $x_{\pm} = \frac{E_N}{T_{N_1}} \pm \frac{E_{N_2}}{T_{\rm SM}}$ , where the upper limit of the  $x_-$  integration is

$$x_{-}^{\text{max}} = \frac{m_{N_1}^2 T_{\text{SM}}^2 x_{+} + \sqrt{(m_{N_1}^2 - s)^2 T_{\text{SM}} \left( m_{N_1}^2 (T_{N_1} - T_{\text{SM}}) + T_{\text{SM}} (T_{N_1} T_{\text{SM}} x_{+}^2 - s) \right)}}{m_{N_1}^2 T_{\text{SM}} (T_{\text{SM}} - T_{N_1}) + s T_{N_1}} . \tag{A.2.4}$$

Integration over  $x_{-}$  and  $x_{+}$  then leads to

$$\langle \sigma \bar{v} \rangle = D \int_{(m_{N_1} + m_{N_2})^2}^{\infty} ds \, \sigma(s) \frac{C}{B} \left( A(1+z)e^{-z} + C\sqrt{B}K_1(z) \right) \tag{A.2.5}$$

where

$$A = m_{N_1}^2 T_{\rm SM}^2 - m_{N_2}^2 T_{N_1}^2 \tag{A.2.6}$$

$$B = m_{N_2}^2 T_{N_1} (T_{N_1} - T_{SM}) + m_{N_1}^2 T_{SM} (T_{SM} - T_{N_1}) + s T_{N_1} T_{SM}$$
(A.2.7)

$$C = \sqrt{(s - (m_{N_1} - m_{N_2})^2)(s - (m_{N_1} + m_{N_2})^2)}$$
(A.2.8)

$$D^{-1} = 8m_{N_1}^2 m_{N_2}^2 K_2 \left(\frac{m_{N_1}}{T_{N_1}}\right) K_2 \left(\frac{m_{N_2}}{T_{SM}}\right), \tag{A.2.9}$$

$$z = \frac{\sqrt{B}}{T_{N_s} T_{\text{SM}}}.$$
 (A.2.10)

The thermally averaged cross-section for initial states  $N_1N_3$  is given by replacing  $N_2$  with  $N_3$ .

### Appendix B

#### Renormalisation of the 2HDM

#### B.1 Running and $\beta$ -functions

Electroweak resonances are typically measured at the Z-pole, meaning that the physical mass inputs will exist at an energy scale  $\mu=m_Z$ . Through the one-loop renormalisation relations, we can relate this input to Lagrangian parameters that also exist at the same energy scale. Next, we can RG evolve the Lagrangian parameters via the beta functions to the 4D scale  $\mu=\bar{\mu}_4$  of our theory, where they can then act as input for our model.

The renormalisation group equations listed below are associated with the parameters of the 2HDM and encode their running with respect to the four-dimensional  $\overline{\rm MS}$  renormalisation scale  $\bar{\mu}_4$  via the  $\beta$ -functions. To this end, we use

$$t \equiv \ln \bar{\mu}_4 \,, \tag{B.1.1}$$

where  $\bar{\mu}_4^2 \equiv 4\pi e^{-\gamma_E} \mu^2$ , and find at one-loop level:

$$\partial_t g_1^2 = \frac{7}{8\pi^2} g_1^4 \,, \tag{B.1.2}$$

$$\partial_t g_2^2 = -\frac{3}{8\pi^2} g_2^4 \,, \tag{B.1.3}$$

 $<sup>{}^{2}</sup>$ This relates the  $\overline{\rm MS}$  scale with that of the MS scheme.

$$\partial_t g_3^2 = -\frac{7}{8\pi^2} g_3^4 \,, \tag{B.1.4}$$

$$\partial_t y_t = \frac{1}{192\pi^2} y_t \left( -17g_1^2 - 27g_2^2 - 96g_3^2 + 54y_t^2 \right) , \qquad (B.1.5)$$

$$\partial_t m_{11}^2 = \frac{1}{32\pi^2} \left( -3m_{11}^2 (g_1^2 + 3g_2^2 - 8\lambda_1) + 4m_{22}^2 (2\lambda_3 + \lambda_4) \right) , \tag{B.1.6}$$

$$\partial_t m_{22}^2 = \frac{1}{32\pi^2} \left( -3m_{22}^2 (g_1^2 + 3g_2^2 - 4y_t^2 - 8\lambda_2) + 4m_{11}^2 (2\lambda_3 + \lambda_4) \right) , \tag{B.1.7}$$

$$\partial_t m_{12}^2 = \frac{1}{32\pi^2} m_{12}^2 \left( -3g_1^2 - 9g_2^2 + 6y_t^2 + 4(\lambda_3 + 2\lambda_4 + 3\lambda_5) \right) , \qquad (B.1.8)$$

$$\partial_t \lambda_1 = \frac{1}{128\pi^2} \left( 3g_1^4 + 9g_2^4 + 6g_1^2(g_2^2 - 4\lambda_1) - 72g_2^2 \lambda_1 \right)$$
(B.1.9)

$$+8(24\lambda_1^2+2\lambda_3^2+2\lambda_3\lambda_4+\lambda_4^2+\lambda_5^2)$$
, (B.1.10)

$$\partial_t \lambda_2 = \frac{1}{128\pi^2} \left( 3g_1^4 + 9g_2^4 + 6g_1^2(g_2^2 - 4\lambda_2) - 72g_2^2 \lambda_2 \right)$$
 (B.1.11)

+ 
$$96\lambda_2(y_t^2 + 2\lambda_2) + 8(-6y_t^4 + 2\lambda_3^2 + 2\lambda_3\lambda_4 + \lambda_4^2 + \lambda_5^2)$$
, (B.1.12)

$$\partial_t \lambda_3 = \frac{1}{64\pi^2} \left( 3g_1^4 + 9g_2^4 - 36g_2^2 \lambda_3 - 6g_1^2 (g_2^2 + 2\lambda_3) \right)$$
(B.1.13)

+ 
$$8(\lambda_3(3y_t^2 + 6(\lambda_1 + \lambda_2) + 2\lambda_3) + 2(\lambda_1 + \lambda_2)\lambda_4 + \lambda_4^2 + \lambda_5^2)$$
, (B.1.14)

$$\partial_t \lambda_4 = \frac{1}{16\pi^2} \left( 3g_1^2 (g_2^2 - \lambda_4) + 9g_2^2 \lambda_4 + 6y_t^2 \lambda_4 \right)$$
(B.1.15)

$$+4\lambda_4(\lambda_1+\lambda_2+2\lambda_3+\lambda_4)+8\lambda_5^2$$
, (B.1.16)

$$\partial_t \lambda_5 = \frac{1}{16\pi^2} \lambda_5 \left( -3g_1^2 - 9g_2^2 + 6y_t^2 + 4(\lambda_1 + \lambda_2 + 2\lambda_3 + 3\lambda_4) \right) , \qquad (B.1.17)$$

The renormalisation scale of the thermal transition is chosen as  $\bar{\mu}_4 = 4\pi e^{-\gamma_E} T$ , which lies close to the thermal scale and suppresses its contribution to the thermal logarithms. The scales of the soft and ultrasoft EFTs are set to  $\bar{\mu}_3 = \bar{\mu}_{3\text{US}} = BT$ , and for simplicity we choose B=1. We refer to this choice of the  $\bar{\mu}_{3\text{US}}$  scale as the 'softer' scale. In practice, the choice of  $\bar{\mu}_3$  can be made more rigorous by applying the principle of minimal sensitivity [318]. This principle entails minimising the dependence of  $\bar{\mu}_3$  or  $\bar{\mu}_{3\text{US}}$ , for example, in the effective potential, to determine an optimal scale  $\bar{\mu}_{\text{opt}}$ , as discussed in [319–321].

# B.2 Relations between $\overline{MS}$ -parameters and physical observables

The physical observables map to the  $\overline{\text{MS}}$ -parameters of the Lagrangian as,

$$(m_h, m_{H^{\pm}}, m_H, m_A, \cos(\beta - \alpha), \tan(\beta), m_W, m_Z, m_t, G_f, \alpha_s)$$

$$(m_{11}^2, m_{22}^2, m_{12}^2, \lambda_1, \lambda_2, \lambda_3, \lambda_4, \lambda_5, g_1, g_2, g_3, y_t).$$
(B.2.1)

The physical observables, along with  $m_{12}$ , serve as input parameters measured at the Z-pole,  $\mu = m_Z$ . We define the shorthand notation  $g_0^2 = 4\sqrt{2}G_f m_W^2$  for the tree-level coupling.

At tree-level, the vacuum relations for the gauge couplings are,

$$g_1^2 = g_0^2$$
,  $g_2^2 = g_0^2 \left( \left( \frac{m_Z}{m_W} \right)^2 - 1 \right)$ ,  $g_3^2 = \frac{g_0^2}{2} \left( \frac{m_t}{m_W} \right)^2$ . (B.2.2)

For the other Lagrangian parameters, we list the tree level relations given in Appendix B.2 of Ref. [221]:

$$m_{11}^2 = m_{12}^2 t_{\beta} - \frac{1}{2} \left( m_H^2 + (m_H^2 - m_H^2) c_{\beta - \alpha} (c_{\beta - \alpha} + s_{\beta - \alpha} t_{\beta}) \right),$$
 (B.2.3)

$$m_{22}^2 = m_{12}^2 t_{\beta}^{-1} - \frac{1}{2} \left( m_H^2 + (m_H^2 - m_H^2) c_{\beta - \alpha} (c_{\beta - \alpha} - s_{\beta - \alpha} t_{\beta}^{-1}) \right) , \qquad (B.2.4)$$

$$v^{2}\lambda_{1} = \frac{1}{2} \left( m_{H}^{2} + \Omega^{2} t_{\beta}^{2} - (m_{H}^{2} - m_{H}^{2}) \left( 1 - (s_{\beta-\alpha} + c_{\beta-\alpha} t_{\beta}^{-1})^{2} \right) t_{\beta}^{2} \right),$$
 (B.2.5)

$$v^{2}\lambda_{2} = \frac{1}{2} \left( m_{H}^{2} + \Omega^{2} t_{\beta}^{-2} - (m_{H}^{2} - m_{H}^{2}) \left( 1 - (s_{\beta-\alpha} - c_{\beta-\alpha} t_{\beta})^{2} \right) t_{\beta}^{-2} \right),$$
 (B.2.6)

$$v^{2}\lambda_{3} = 2m_{H^{\pm}} + \Omega^{2} - m_{H}^{2} - (m_{H}^{2} - m_{H}^{2}) \left( 1 + (s_{\beta-\alpha} + c_{\beta-\alpha}t_{\beta}^{-1})(s_{\beta-\alpha} - c_{\beta-\alpha}t_{\beta}) \right),$$
(B.2.7)

$$v^2 \lambda_4 = m_A^2 - 2m_{H^{\pm}} + m_H^2 - \Omega^2 \,, \tag{B.2.8}$$

$$v^2 \lambda_5 = m_H^2 - m_A^2 - \Omega^2 \,, \tag{B.2.9}$$

where we have defined  $\Omega^2 \equiv m_H^2 - m_{12}^2 (\tan(\beta) + \tan(\beta)^{-1})$  as in Ref. [221] <sup>1</sup>, and we use

<sup>&</sup>lt;sup>1</sup>Note that there is a difference in sign between our  $m_{12}^2$  and the one defined in that reference.

the notation  $c_{\beta-\alpha}=\cos(\beta-\alpha)$  (and likewise for the other trigonometric functions and angles). In Appendix A of [79], the one-loop  $\overline{\rm MS}$  renormalised expressions are provided with reference to the self-energies for the gauge bosons, top quark, and the scalars  $h, H, H^{\pm}$  and A. We make use of the self-energies calculated by the authors of [79], which have analytic expressions too unwieldy to quote here. Explicit expressions for the self-energies can be found in [322]. The one-loop renormalised Lagrangian parameters are also defined at  $\mu=m_Z$ , like the input physical observables. We then use the beta functions to run them to the thermal scale.

### Appendix C

# Integration of the DR EFT into

#### PhaseTracer2

The output of DRAlgo can be incredibly long and impractical for computation. With increasing loop orders, the number of binary operations in a single expression for the potential becomes too high for some compilers to parse and optimise.

Fortunately, techniques exist to optimise the expressions prior to inserting into code. In Mathematica, after running the dimensional reduction in DRAlgo, the Experimental' OptimizeExpression function can simplify expressions by identifying common sub-expressions and creating new 'Compile' variables to save on evaluation time. The subsequent expression that is composed of Compile variables is subsequently far shorter and can be parsed by compilers.

Additionally, the CForm function can allow for the conversion of this optimised expression into C code, with the StringReplace function allowing for the manipulation of the subsequent code strings so that they can be adapted for use in Python, C++, or any other programming language. Thus, a function can be created that compounds these operations together such that DRAlgo output can readily be used in a programme.

When interfacing the dimensionally reduced output with PhaseTracer2, particular care must be taken so that the package can handle divergences at low temperatures,

as this is beyond the validity of the EFT (we remind the reader that the vacuum structure is encoded in the Lagrangian parameters through the vacuum renormalisation of sec. B.2). The set\_t\_low and set\_t\_high functions in the PhaseFinder module allows for the temperature bounds to be set, such that phases are only identified between those temperatures and numerical issues can be avoided.

Finally, regarding the parameter scans: PhaseTracer2 does not come with an interface to set them up. However, it is relatively straightforward to wrap the PhaseTracer2 objects in a class that can be instantiated with the a new set of parameters. Parallelisation of the scan across multiple threads allows for increased efficiency when computing results, particularly on machines with numerous cores.

- [1] M. J. Baker, A. Bhatnagar, D. Croon and J. Turner, *Hot leptogenesis*, *JHEP*05 (2025) 082, [2409.09113].
- [2] A. Bhatnagar, D. Croon and P. Schicho, Interpreting the 95 GeV resonance in the Two Higgs Doublet Model: Implications for the Electroweak Phase Transition, 2025, [2506.20716].
- [3] A. Bhatnagar and D. Gajjar, Policy implications of artificial intelligence (AI), Rep. PN0708, UK Parliament, 2024. Available at: https://post.parliament.uk/research-briefings/post-pn-0708/.
- [4] ATLAS collaboration, G. Aad et al., Observation of a new particle in the search for the Standard Model Higgs boson with the ATLAS detector at the LHC, Phys. Lett. B 716 (2012) 1–29, [1207.7214].
- [5] CMS collaboration, S. Chatrchyan et al., Observation of a New Boson at a Mass of 125 GeV with the CMS Experiment at the LHC, Phys. Lett. B 716 (2012) 30-61, [1207.7235].
- [6] T. S. Kuhn, The Structure of Scientific Revolutions. University of Chicago Press, Chicago, 1962.
- [7] G. Galilei, Dialogo sopra i due massimi sistemi del mondo. Giovanni Battista Landini, Italy, 1632.
- [8] I. Newton, Philosophiæ Naturalis Principia Mathematica. Edmond Halley, England, 1687.

[9] J. C. Maxwell, A dynamical theory of the electromagnetic field, Phil. Trans.Roy. Soc. Lond. 155 (1865) 459–512.

- [10] M. Planck, On the Law of Distribution of Energy in the Normal Spectrum, Annalen Phys. 4 (1901) 553.
- [11] A. Einstein, Concerning a heuristic point of view toward the emission and transformation of light, Annalen Phys. 17 (1905) 132–148.
- [12] V. C. Rubin, W. K. Ford, Jr. and N. Thonnard, Rotational properties of 21 SC galaxies with a large range of luminosities and radii, from NGC 4605 (R=4kpc) to UGC 2885 (R=122kpc)., Astrophysical Journal 238 (June, 1980) 471–487.
- [13] C. Csaki, The Minimal supersymmetric standard model (MSSM), Mod. Phys. Lett. A 11 (1996) 599, [hep-ph/9606414].
- [14] S. Dimopoulos and H. Georgi, Softly broken supersymmetry and SU(5), Nuclear Physics B 193 (1981) 150–162.
- [15] G. Jungman, M. Kamionkowski and K. Griest, Supersymmetric dark matter, Physics Reports 267 (Mar., 1996) 195373.
- [16] M. Carena, M. Quirós and C. Wagner, Opening the window for electroweak baryogenesis, Physics Letters B 380 (July, 1996) 8191.
- [17] A. Canepa, Searches for Supersymmetry at the Large Hadron Collider, Rev. Phys. 4 (2019) 100033.
- [18] A. De Roeck, Dark matter searches at accelerators, Nuclear Physics B 1003 (2024) 116480.
- [19] G. Apollinari, I. Béjar Alonso, O. Brüning, P. Fessia, M. Lamont, L. Rossi et al., High-Luminosity Large Hadron Collider (HL-LHC): Technical Design Report V. 0.1, 2017.

[20] H. M. Gray, Future colliders for the high-energy frontier, Reviews in Physics6 (2021) 100053.

- [21] LISA COSMOLOGY WORKING GROUP collaboration, P. Auclair et al., Cosmology with the Laser Interferometer Space Antenna, Living Rev. Rel. 26 (2023) 5, [2204.05434].
- [22] K. Danzmann, LISA mission overview, Advances in Space Research 25 (2000) 1129–1136.
- [23] C. Caprini, R. Durrer and G. Servant, The stochastic gravitational wave background from turbulence and magnetic fields generated by a first-order phase transition, Journal of Cosmology and Astroparticle Physics 2009 (dec, 2009) 024.
- [24] C. Caprini, M. Hindmarsh, S. Huber, T. Konstandin, J. Kozaczuk, G. Nardini et al., Science with the space-based interferometer eLISA. II: gravitational waves from cosmological phase transitions, Journal of Cosmology and Astroparticle Physics 2016 (apr. 2016) 001.
- [25] C. Caprini, M. Chala, G. C. Dorsch, M. Hindmarsh, S. J. Huber, T. Konstandin et al., Detecting gravitational waves from cosmological phase transitions with LISA: an update, Journal of Cosmology and Astroparticle Physics 2020 (Mar., 2020) 024024.
- [26] K. Kajantie, M. Laine, K. Rummukainen and M. Shaposhnikov, Is There a Hot Electroweak Phase Transition at  $m_H \gtrsim m_W$ ?, Phys. Rev. Lett. 77 (Sep, 1996) 2887–2890.
- [27] F. Csikor, Z. Fodor and J. Heitger, End Point of the Hot Electroweak Phase Transition, Phys. Rev. Lett. 82 (Jan, 1999) 21–24.
- [28] M. D'Onofrio and K. Rummukainen, Standard model cross-over on the lattice, Phys. Rev. D 93 (Jan, 2016) 025003.

[29] M. Fukugita and T. Yanagida, Baryogenesis Without Grand Unification, Phys. Lett. B 174 (1986) 45–47.

- [30] F. Vissani, Do experiments suggest a hierarchy problem?, Phys. Rev. D 57 (1998) 7027–7030, [hep-ph/9709409].
- [31] G. Aad, T. Abajyan, B. Abbott, J. Abdallah, S. Abdel Khalek, A. Abdelalim et al., Observation of a new particle in the search for the Standard Model Higgs boson with the ATLAS detector at the LHC, Physics Letters B 716 (Sept., 2012) 129.
- [32] SUPER-KAMIOKANDE collaboration, Y. Fukuda, T. Hayakawa, E. Ichihara, K. Inoue, K. Ishihara, H. Ishino et al., Evidence for Oscillation of Atmospheric Neutrinos, Phys. Rev. Lett. 81 (Aug., 1998) 1562–1567.
- [33] Particle Data Group Collaboration collaboration, S. Navas,
   C. Amsler, T. Gutsche, C. Hanhart, J. J. Hernández-Rey, C. Lourenço et al.,
   Review of particle physics, Phys. Rev. D 110 (Aug, 2024) 030001.
- [34] M. D. Schwartz, Quantum Field Theory and the Standard Model. Cambridge University Press, 2013.
- [35] M. E. Peskin and D. V. Schroeder, An Introduction to quantum field theory. Addison-Wesley, Reading, USA, 1995, 10.1201/9780429503559.
- [36] E. Wigner, On Unitary Representations of the Inhomogeneous Lorentz Group, Annals of Mathematics 40 (1939) 149–204.
- [37] V. Bargmann and E. P. Wigner, Group Theoretical Discussion of Relativistic Wave Equations, Proc. Nat. Acad. Sci. 34 (1948) 211.
- [38] C. S. Wu, E. Ambler, R. W. Hayward, D. D. Hoppes and R. P. Hudson, Experimental Test of Parity Conservation in Beta Decay, Phys. Rev. 105 (Feb, 1957) 1413–1415.

[39] Y. Rodriguez, A New Pedagogical Way of Finding Out the Gauge Field Strength Tensor in Abelian and Non-Abelian Local Gauge Field Theories, 2016, [1512.03827].

- [40] P. W. Higgs, Broken Symmetries and the Masses of Gauge Bosons, Phys. Rev. Lett. 13 (Oct, 1964) 508–509.
- [41] F. Englert and R. Brout, Broken Symmetry and the Mass of Gauge Vector Mesons, Phys. Rev. Lett. 13 (Aug, 1964) 321–323.
- [42] G. S. Guralnik, C. R. Hagen and T. W. B. Kibble, Global Conservation Laws and Massless Particles, Phys. Rev. Lett. 13 (Nov, 1964) 585–587.
- [43] X. Fan, T. G. Myers, B. A. D. Sukra and G. Gabrielse, Measurement of the Electron Magnetic Moment, Phys. Rev. Lett. 130 (Feb, 2023) 071801.
- [44] T. Aoyama, M. Hayakawa, T. Kinoshita and M. Nio, Tenth-order electron anomalous magnetic moment: Contribution of diagrams without closed lepton loops, Physical Review D 91 (Feb., 2015).
- [45] J. C. Romão and J. P. Silva, A Resource for Signs and Feynman diagrams of the Standard Model, International Journal of Modern Physics A 27 (Oct., 2012) 1230025.
- [46] S. Deser and P. van Nieuwenhuizen, Nonrenormalizability of the Quantized Einstein-Maxwell System, Phys. Rev. Lett. 32 (1974) 245–247.
- [47] R. D. Peccei and H. R. Quinn, CP Conservation in the Presence of Pseudoparticles, Phys. Rev. Lett. 38 (Jun, 1977) 1440–1443.
- [48] SUPERNOVA SEARCH TEAM collaboration, A. G. Riess et al., Observational evidence from supernovae for an accelerating universe and a cosmological constant, Astron. J. 116 (1998) 1009–1038, [astro-ph/9805201].

[49] SUPERNOVA COSMOLOGY PROJECT collaboration, S. Perlmutter et al., Measurements of Ω and Λ from 42 High Redshift Supernovae, Astrophys. J. 517 (1999) 565–586, [astro-ph/9812133].

- [50] N. Aghanim, Y. Akrami, M. Ashdown, J. Aumont, C. Baccigalupi,
   M. Ballardini et al., Planck2018 results: VI. Cosmological parameters,
   Astronomy & Astrophysics 641 (Sept., 2020) A6.
- [51] H. M. Lee, Lectures on physics beyond the Standard Model, Journal of the Korean Physical Society 78 (May, 2021) 9851017.
- [52] F. Bezrukov, M. Y. Kalmykov, B. A. Kniehl and M. Shaposhnikov, Higgs boson mass and new physics, Journal of High Energy Physics 2012 (Oct., 2012).
- [53] P. D. Group, R. L. Workman, V. D. Burkert, V. Crede, E. Klempt, U. Thoma et al., Review of Particle Physics, Progress of Theoretical and Experimental Physics 2022 (08, 2022) 083C01, [https://academic.oup.com/ptep/articlepdf/2022/8/083C01/49175539/ptac097.pdf].
- [54] P. F. de Salas, D. V. Forero, S. Gariazzo, P. Martínez-Miravé, O. Mena, C. A. Ternes et al., 2020 global reassessment of the neutrino oscillation picture, JHEP 02 (2021) 071, [2006.11237].
- [55] S. Gariazzo, O. Mena and T. Schwetz, Quantifying the tension between cosmological and terrestrial constraints on neutrino masses, Phys. Dark Univ. 40 (2023) 101226, [2302.14159].
- [56] A. Einstein, The Field Equations of Gravitation, Sitzungsber. Preuss. Akad. Wiss. Berlin (Math. Phys.) 1915 (1915) 844–847.
- [57] J. A. Wheeler and K. Ford, Geons, black holes, and quantum foam: A life in physics. Norton & Company, 1998.

[58] N. Deruelle, J.-P. Uzan and P. de Forcrand-Millard, Relativity in Modern Physics. Oxford University Press, 08, 2018, 10.1093/oso/9780198786399.001.0001.

- [59] L. Perivolaropoulos and F. Skara, Challenges for ΛCDM: An update, New Astron. Rev. 95 (2022) 101659, [2105.05208].
- [60] A. G. Riess, W. Yuan, L. M. Macri, D. Scolnic, D. Brout, S. Casertano et al., A Comprehensive Measurement of the Local Value of the Hubble Constant with 1 km s1 Mpc1 Uncertainty from the Hubble Space Telescope and the SH0ES Team, The Astrophysical Journal Letters 934 (July, 2022) L7.
- [61] P. de Bernardis, P. A. R. Ade, J. J. Bock, J. R. Bond, J. Borrill, A. Boscaleri et al., A flat Universe from high-resolution maps of the cosmic microwave background radiation, Nature 404 (Apr., 2000) 955959.
- [62] A. H. Guth, Inflationary universe: A possible solution to the horizon and flatness problems, Phys. Rev. D 23 (Jan, 1981) 347–356.
- [63] M. Trodden and S. M. Carroll, TASI Lectures: Introduction to Cosmology, 2004, [astro-ph/0401547].
- [64] G. 't Hooft, Magnetic Monopoles in Unified Gauge Theories, Nucl. Phys. B 79 (1974) 276–284.
- [65] A. M. Polyakov, Particle Spectrum in Quantum Field Theory, JETP Lett. 20 (1974) 194–195.
- [66] R. B. Tully, H. Courtois, Y. Hoffman and D. Pomarède, The Laniakea supercluster of galaxies, Nature 513 (2014) 71, [1409.0880].
- [67] R. P. Kirshner, A. Oemler, Jr., P. L. Schechter and S. A. Shectman, A Survey of the Bootes Void, Astrophysical Journal 314 (Mar., 1987) 493.
- [68] A. R. Liddle and D. H. Lyth, Cosmological Inflation and Large-Scale Structure. Cambridge University Press, 2000.

[69] V. Barger, P. Langacker, M. McCaskey, M. J. Ramsey-Musolf and G. Shaughnessy, CERN LHC phenomenology of an extended standard model with a real scalar singlet, Phys. Rev. D 77 (Feb, 2008) 035005.

- [70] S. Profumo, M. J. Ramsey-Musolf and G. Shaughnessy, Singlet Higgs phenomenology and the electroweak phase transition, Journal of High Energy Physics 2007 (aug, 2007) 010.
- [71] P. H. Damgaard, A. Haarr, D. OConnell and A. Tranberg, Effective field theory and electroweak baryogenesis in the singlet-extended Standard Model, Journal of High Energy Physics 2016 (Feb., 2016).
- [72] V. Vaskonen, Electroweak baryogenesis and gravitational waves from a real scalar singlet, Phys. Rev. D 95 (Jun, 2017) 123515.
- [73] A. Beniwal, M. Lewicki, J. D. Wells, M. White and A. G. Williams, Gravitational wave, collider and dark matter signals from a scalar singlet electroweak baryogenesis, Journal of High Energy Physics 2017 (Aug., 2017).
- [74] C.-Y. Chen, J. Kozaczuk and I. M. Lewis, Non-resonant collider signatures of a singlet-driven electroweak phase transition, Journal of High Energy Physics 2017 (Aug., 2017).
- [75] M. Aboudonia, C. Balazs, A. Papaefstathiou and G. White, Investigating the Electroweak phase transition with a real scalar singlet at a muon collider, Journal of High Energy Physics 2025 (Apr., 2025).
- [76] J. M. Cline and P.-A. Lemieux, Electroweak phase transition in two Higgs doublet models, Phys. Rev. D 55 (Mar, 1997) 3873–3881.
- [77] L. Fromme, S. J. Huber and M. Seniuch, Baryogenesis in the two-Higgs doublet model, Journal of High Energy Physics 2006 (nov, 2006) 038.
- [78] G. C. Dorsch, S. J. Huber and J. M. No, A strong electroweak phase transition in the 2HDM after LHC8, Journal of High Energy Physics 2013 (Oct., 2013).

[79] K. Kainulainen, V. Keus, L. Niemi, K. Rummukainen, T. V. I. Tenkanen and V. Vaskonen, On the validity of perturbative studies of the electroweak phase transition in the Two Higgs Doublet model, Journal of High Energy Physics 2019 (June, 2019).

- [80] J.-M. Yang, M. S. Turner, G. Steigman, D. N. Schramm and K. A. Olive, Primordial Nucleosynthesis: A Critical Comparison of Theory and Observation, Astrophys. J. 281 (1984) 493–511.
- [81] A. H. Kazi, N. C. Rasmussen and H. Mark, Measurement of the Deuteron Binding Energy using a Bent-Crystal Spectrograph, Phys. Rev. 123 (Aug, 1961) 1310–1315.
- [82] N. Schöneberg, The 2024 BBN baryon abundance update, Journal of Cosmology and Astroparticle Physics 2024 (jun, 2024) 006.
- [83] E. W. Kolb and M. S. Turner, The Early Universe, vol. 69. Taylor and Francis, 5, 2019, 10.1201/9780429492860.
- [84] G. Steigman, Observational Tests of Antimatter Cosmologies, Annual Review of Astronomy and Astrophysics 14 (1976) 339–372.
- [85] L. Canetti, M. Drewes and M. Shaposhnikov, Matter and antimatter in the universe, New Journal of Physics 14 (sep, 2012) 095012.
- [86] F. Stecker, On the nature of the baryon asymmetry, Nuclear Physics B 252 (1985) 25–36.
- [87] G. Steigman, When clusters collide: constraints on antimatter on the largest scales, Journal of Cosmology and Astroparticle Physics 2008 (oct, 2008) 001.
- [88] A. G. Cohen and A. D. Rujula, Scars on the CBR?, 1997, [astro-ph/9709132].
- [89] A. G. Cohen, A. De Rújula and S. L. Glashow, A Matter-Antimatter Universe?, The Astrophysical Journal 495 (mar, 1998) 539.

[90] A. D. Sakharov, Violation of CP Invariance, C asymmetry, and baryon asymmetry of the universe, Pisma Zh. Eksp. Teor. Fiz. 5 (1967) 32–35.

- [91] J. S. Bell and R. Jackiw, A PCAC puzzle:  $\pi^0 \to \gamma \gamma$  in the  $\sigma$  model, Nuovo Cim. A **60** (1969) 47–61.
- [92] S. L. Adler, Axial-Vector Vertex in Spinor Electrodynamics, Phys. Rev. 177 (Jan, 1969) 2426–2438.
- [93] G. 't Hooft, Symmetry Breaking through Bell-Jackiw Anomalies, Phys. Rev. Lett. 37 (Jul, 1976) 8–11.
- [94] D. Croon, TASI lectures on Phase Transitions, Baryogenesis, and Gravitational Waves, PoS TASI2022 (2024) 003, [2307.00068].
- [95] M. E. Shaposhnikov, Anomalous fermion number nonconservation, in Summer School in High-energy Physics and Cosmology, pp. 338–374, 11, 1991.
- [96] C. Callan, R. Dashen and D. Gross, The structure of the gauge theory vacuum, Physics Letters B 63 (1976) 334–340.
- [97] R. Jackiw and C. Rebbi, Vacuum Periodicity in a Yang-Mills Quantum Theory, Phys. Rev. Lett. 37 (Jul, 1976) 172–175.
- [98] F. R. Klinkhamer and N. S. Manton, A saddle-point solution in the Weinberg-Salam theory, Phys. Rev. D 30 (Nov, 1984) 2212–2220.
- [99] C. Balazs, Baryogenesis: A small review of the big picture, 2014, [1411.3398].
- [100] J. A. Harvey and M. S. Turner, Cosmological baryon and lepton number in the presence of electroweak fermion-number violation, Phys. Rev. D 42 (Nov, 1990) 3344–3349.
- [101] C. Jarlskog, Commutator of the Quark Mass Matrices in the Standard Electroweak Model and a Measure of Maximal CP Nonconservation, Phys. Rev. Lett. 55 (Sep, 1985) 1039–1042.

[102] L. Covi, E. Roulet and F. Vissani, CP violating decays in leptogenesis scenarios, Phys. Lett. B 384 (1996) 169–174, [hep-ph/9605319].

- [103] L. Covi and E. Roulet, Baryogenesis from mixed particle decays, Phys. Lett. B 399 (1997) 113–118, [hep-ph/9611425].
- [104] A. Pilaftsis, CP violation and baryogenesis due to heavy Majorana neutrinos, Phys. Rev. D **56** (1997) 5431–5451, [hep-ph/9707235].
- [105] P. Minkowski,  $\mu \to e \gamma$  at a Rate of One Out of 10<sup>9</sup> Muon Decays?, Phys. Lett. B **67** (1977) 421–428.
- [106] T. Yanagida, Horizontal gauge symmetry and masses of neutrinos, Conf. Proc. C 7902131 (1979) 95–99.
- [107] M. Gell-Mann, P. Ramond and R. Slansky, Complex Spinors and Unified Theories, Conf. Proc. C790927 (1979) 315–321, [1306.4669].
- [108] R. N. Mohapatra and G. Senjanovic, Neutrino Mass and Spontaneous Parity Nonconservation, Phys. Rev. Lett. 44 (1980) 912.
- [109] J. A. Casas and A. Ibarra, Oscillating neutrinos and  $\mu \rightarrow e, \gamma$ , Nucl. Phys. B **618** (2001) 171–204, [hep-ph/0103065].
- [110] W. Buchmuller, P. Di Bari and M. Plumacher, Leptogenesis for pedestrians, Annals Phys. 315 (2005) 305–351, [hep-ph/0401240].
- [111] A. Pilaftsis, The little review on leptogenesis, Journal of Physics: Conference Series 171 (June, 2009) 012017.
- [112] S. Khlebnikov and M. Shaposhnikov, The statistical theory of anomalous fermion number non-conservation, Nuclear Physics B 308 (1988) 885–912.
- [113] M. Laine and M. Shaposhnikov, Remark on sphaleron erasure of baryon asymmetry, Physical Review D 61 (May, 2000).

[114] H. Dreiner and G. Ross, Sphaleron erasure of primordial baryogenesis, Nuclear Physics B 410 (1993) 188–216.

- [115] J. M. Cline, K. Kainulainen and K. A. Olive, Protecting the primordial baryon asymmetry from erasure by sphalerons, Phys. Rev. D 49 (1994) 6394–6409, [hep-ph/9401208].
- [116] R. Barbieri, P. Creminelli, A. Strumia and N. Tetradis, *Baryogenesis through leptogenesis*, *Nucl. Phys.* **B575** (2000) 61–77, [hep-ph/9911315].
- [117] E. Nardi, Y. Nir, J. Racker and E. Roulet, On Higgs and sphaleron effects during the leptogenesis era, Journal of High Energy Physics 2006 (Jan., 2006) 068068.
- [118] A. Abada, S. Davidson, F.-X. Josse-Michaux, M. Losada and A. Riotto, Flavour issues in leptogenesis, Journal of Cosmology and Astroparticle Physics 2006 (Apr., 2006) 004004.
- [119] A. Pilaftsis, Resonant τ Leptogenesis with Observable Lepton Number Violation, Phys. Rev. Lett. 95 (Aug, 2005) 081602.
- [120] A. Pilaftsis and T. E. J. Underwood, Electroweak-scale resonant leptogenesis, Phys. Rev. D 72 (Dec, 2005) 113001.
- [121] T. Endoh, T. Morozumi and Z. Xiong, Primordial Lepton Family Asymmetries in Seesaw Model, Progress of Theoretical Physics 111 (Jan., 2004) 123149.
- [122] O. Vives, Flavor dependence of CP asymmetries and thermal leptogenesis with strong right-handed neutrino mass hierarchy, Phys. Rev. D 73 (Apr, 2006) 073006.
- [123] S. Davidson and A. Ibarra, A Lower bound on the right-handed neutrino mass from leptogenesis, Phys. Lett. B 535 (2002) 25–32, [hep-ph/0202239].

[124] A. Pilaftsis and T. E. J. Underwood, Resonant leptogenesis, Nucl. Phys. B 692 (2004) 303–345, [hep-ph/0309342].

- [125] M. Flanz, E. A. Paschos and U. Sarkar, Baryogenesis from a lepton asymmetric universe, Physics Letters B 345 (Feb., 1995) 248252.
- [126] L. Covi, E. Roulet and F. Vissani, CP violating decays in leptogenesis scenarios, Physics Letters B 384 (Sept., 1996) 169174.
- [127] A. Pilaftsis, CP violation and baryogenesis due to heavy Majorana neutrinos, Physical Review D 56 (Nov., 1997) 54315451.
- [128] M. Breitbach, Gravitational Waves from Cosmological Phase Transitions, 2022, [2204.09661].
- [129] E. J. Weinberg, Radiative Corrections as the Origin of Spontaneous Symmetry Breaking, 2005, [hep-th/0507214].
- [130] C. Delaunay, C. Grojean and J. D. Wells, Dynamics of non-renormalizable electroweak symmetry breaking, Journal of High Energy Physics 2008 (apr, 2008) 029.
- [131] T. Matsubara, A New approach to quantum statistical mechanics, Prog. Theor. Phys. 14 (1955) 351–378.
- [132] M. B. Hindmarsh, M. Lüben, J. Lumma and M. Pauly, Phase transitions in the early universe, SciPost Phys. Lect. Notes 24 (2021) 1, [2008.09136].
- [133] A. Linde, Infrared problem in the thermodynamics of the Yang-Mills gas, Physics Letters B **96** (1980) 289–292.
- [134] D. Croon, O. Gould, P. Schicho, T. V. I. Tenkanen and G. White, Theoretical uncertainties for cosmological first-order phase transitions, Journal of High Energy Physics 2021 (Apr., 2021).

[135] P. Arnold and O. Espinosa, Effective potential and first-order phase transitions: Beyond leading order, Phys. Rev. D 47 (Apr, 1993) 3546–3579.

- [136] D. Curtin, P. Meade and H. Ramani, Thermal resummation and phase transitions, The European Physical Journal C 78 (Sep. 2018).
- [137] P. H. Ginsparg, First Order and Second Order Phase Transitions in Gauge Theories at Finite Temperature, Nucl. Phys. B 170 (1980) 388–408.
- [138] T. Appelquist and R. D. Pisarski, High-Temperature Yang-Mills Theories and Three-Dimensional Quantum Chromodynamics, Phys. Rev. D 23 (1981) 2305.
- [139] S. Nadkarni, Dimensional Reduction in Hot QCD, Phys. Rev. D 27 (1983)917.
- [140] N. P. Landsman, Limitations to Dimensional Reduction at High Temperature, Nucl. Phys. B 322 (1989) 498–530.
- [141] K. Kajantie, M. Laine, K. Rummukainen and M. Shaposhnikov, Generic rules for high temperature dimensional reduction and their application to the standard model, Nuclear Physics B 458 (Jan., 1996) 90136.
- [142] E. Braaten and A. Nieto, Effective field theory approach to high-temperature thermodynamics, Physical Review D 51 (June, 1995) 69907006.
- [143] E. Braaten and A. Nieto, Free energy of QCD at high temperature, Phys. Rev. D 53 (1996) 3421–3437, [hep-ph/9510408].
- [144] O. Gould, J. Kozaczuk, L. Niemi, M. J. Ramsey-Musolf, T. V. I. Tenkanen and D. J. Weir, Nonperturbative analysis of the gravitational waves from a first-order electroweak phase transition, Phys. Rev. D 100 (Dec, 2019) 115024.
- [145] P. M. Schicho, T. V. I. Tenkanen and J. Österman, Robust approach to thermal resummation: Standard Model meets a singlet, Journal of High Energy Physics 2021 (June, 2021).

[146] B. Abbott, R. Abbott, T. Abbott, M. Abernathy, F. Acernese, K. Ackley et al., Observation of Gravitational Waves from a Binary Black Hole Merger, Physical Review Letters 116 (Feb., 2016).

- [147] E. E. Flanagan and S. A. Hughes, The basics of gravitational wave theory, New Journal of Physics 7 (sep, 2005) 204.
- [148] H. Araújo, P. Cañizares, M. Chmeissani, A. Conchillo, M. Díaz-Aguiló,
  E. García-Berro et al., Milli-Hertz Gravitational Waves: LISA and LISA
  PathFinder, Journal of Physics: Conference Series 314 (sep, 2011) 012014.
- [149] P. Binétruy, A. Bohé, C. Caprini and J.-F. Dufaux, Cosmological backgrounds of gravitational waves and eLISA/NGO: phase transitions, cosmic strings and other sources, Journal of Cosmology and Astroparticle Physics 2012 (jun, 2012) 027.
- [150] J. R. Gair, S. Babak, A. Sesana, P. Amaro-Seoane, E. Barausse, C. P. L. Berry et al., Prospects for observing extreme-mass-ratio inspirals with LISA, Journal of Physics: Conference Series 840 (may, 2017) 012021.
- [151] K. Szekerczes, S. Noble, C. Chirenti and J. I. Thorpe, Imaging the Milky Way with Millihertz Gravitational Waves, The Astronomical Journal 166 (jun, 2023) 17.
- [152] ESA, "Capturing the ripples of spacetime: LISA gets go-ahead."

  https://www.esa.int/Science\_Exploration/Space\_Science/LISA/
  Capturing\_the\_ripples\_of\_spacetime\_LISA\_gets\_go-ahead, 2024.
- [153] A. Klein, E. Barausse, A. Sesana, A. Petiteau, E. Berti, S. Babak et al., Science with the space-based interferometer eLISA: Supermassive black hole binaries, Phys. Rev. D 93 (Jan, 2016) 024003.
- [154] N. Bernal and C. S. Fong, Hot Leptogenesis from Thermal Dark Matter, JCAP 10 (2017) 042, [1707.02988].

[155] J. D. Clarke, R. Foot and R. R. Volkas, Electroweak naturalness in the three-flavor type I seesaw model and implications for leptogenesis, Phys. Rev. D 91 (2015) 073009, [1502.01352].

- [156] K. Moffat, S. Pascoli, S. T. Petcov, H. Schulz and J. Turner, Three-flavored nonresonant leptogenesis at intermediate scales, Phys. Rev. D 98 (2018) 015036, [1804.05066].
- [157] L. Kofman, A. Linde and A. A. Starobinsky, Reheating after Inflation, Physical Review Letters 73 (Dec., 1994) 31953198.
- [158] M. Cannoni, Relativistic  $\langle \sigma v_{rel} \rangle$  in the calculation of relics abundances: a closer look, Phys. Rev. D 89 (2014) 103533, [1311.4494].
- [159] A. D. Linde, Chaotic Inflation, Phys. Lett. B 129 (1983) 177–181.
- [160] D. S. Salopek, Consequences of the COBE satellite for the inflationary scenario, Phys. Rev. Lett. 69 (1992) 3602–3605.
- [161] G. Lazarides and Q. Shafi, Origin of matter in the inflationary cosmology, Phys. Lett. B 258 (1991) 305–309.
- [162] G. F. Giudice, M. Peloso, A. Riotto and I. Tkachev, Production of massive fermions at preheating and leptogenesis, JHEP 08 (1999) 014, [hep-ph/9905242].
- [163] T. Asaka, K. Hamaguchi, M. Kawasaki and T. Yanagida, Leptogenesis in inflaton decay, Phys. Lett. B 464 (1999) 12–18, [hep-ph/9906366].
- [164] T. Asaka, K. Hamaguchi, M. Kawasaki and T. Yanagida, Leptogenesis in inflationary universe, Phys. Rev. D 61 (2000) 083512, [hep-ph/9907559].
- [165] V. N. Senoguz and Q. Shafi, GUT scale inflation, nonthermal leptogenesis, and atmospheric neutrino oscillations, Phys. Lett. B 582 (2004) 6–14, [hep-ph/0309134].

[166] F. Hahn-Woernle and M. Plumacher, Effects of reheating on leptogenesis, Nucl. Phys. B 806 (2009) 68–83, [0801.3972].

- [167] B. Garbrecht and P. Schwaller, Spectator Effects during Leptogenesis in the Strong Washout Regime, JCAP 10 (2014) 012, [1404.2915].
- [168] M. Hufnagel and M. H. G. Tytgat, The domain of a cannibal dark matter, JCAP 09 (2023) 012, [2212.09759].
- [169] A. Ghosh, S. Gope and S. Mukhopadhyay, Cannibal dark matter decoupled from the standard model: Cosmological constraints, Phys. Rev. D 106 (2022) 103515, [2206.11046].
- [170] A. Abada, S. Davidson, F.-X. Josse-Michaux, M. Losada and A. Riotto, Flavor issues in leptogenesis, JCAP **04** (2006) 004, [hep-ph/0601083].
- [171] A. De Simone and A. Riotto, On the impact of flavour oscillations in leptogenesis, JCAP 0702 (2007) 005, [hep-ph/0611357].
- [172] S. Blanchet, P. Di Bari and G. G. Raffelt, Quantum Zeno effect and the impact of flavor in leptogenesis, JCAP 0703 (2007) 012, [hep-ph/0611337].
- [173] S. Blanchet, P. Di Bari, D. A. Jones and L. Marzola, Leptogenesis with heavy neutrino flavours: from density matrix to Boltzmann equations, JCAP 1301 (2013) 041, [1112.4528].
- [174] A. Abada, S. Davidson, A. Ibarra, F. X. Josse-Michaux, M. Losada and A. Riotto, Flavour Matters in Leptogenesis, JHEP 09 (2006) 010, [hep-ph/0605281].
- [175] A. Granelli, K. Moffat, Y. Perez-Gonzalez, H. Schulz and J. Turner, ULYSSES: Universal LeptogeneSiS Equation Solver, Computer Physics Communications 262 (May, 2021) 107813.

[176] A. Granelli, C. Leslie, Y. F. Perez-Gonzalez, H. Schulz, B. Shuve, J. Turner et al., ULYSSES, universal LeptogeneSiS equation solver: Version 2, Comput. Phys. Commun. 291 (2023) 108834, [2301.05722].

- [177] J. Lopez-Pavon, S. Pascoli and C.-f. Wong, Can heavy neutrinos dominate neutrinoless double beta decay?, Phys. Rev. D 87 (2013) 093007, [1209.5342].
- [178] I. Esteban, M. C. Gonzalez-Garcia, M. Maltoni, I. Martinez-Soler and T. Schwetz, Updated fit to three neutrino mixing: exploring the accelerator-reactor complementarity, JHEP 01 (2017) 087, [1611.01514].
- [179] I. Esteban, M. C. Gonzalez-Garcia, M. Maltoni, T. Schwetz and A. Zhou, The fate of hints: updated global analysis of three-flavor neutrino oscillations, JHEP 09 (2020) 178, [2007.14792].
- [180] T. H. Yeh, J. Shelton, K. A. Olive and B. D. Fields, Probing physics beyond the standard model: limits from BBN and the CMB independently and combined, JCAP 10 (2022) 046, [2207.13133].
- [181] F. Hahn-Woernle, M. Plumacher and Y. Y. Y. Wong, Full Boltzmann equations for leptogenesis including scattering, JCAP 08 (2009) 028, [0907.0205].
- [182] CMS collaboration, A. M. Sirunyan et al., Search for a standard model-like Higgs boson in the mass range between 70 and 110 GeV in the diphoton final state in proton-proton collisions at √s = 8 and 13 TeV, Phys. Lett. B 793 (2019) 320–347, [1811.08459].
- [183] CMS collaboration, A. Hayrapetyan et al., Search for a standard model-like Higgs boson in the mass range between 70 and 110 GeV in the diphoton final state in proton-proton collisions at s=13 TeV, Phys. Lett. B 860 (2025) 139067, [2405.18149].

[184] ATLAS collaboration, T. A. Collaboration, Search for diphoton resonances in the 66 to 110 GeV mass range using 140 fb<sup>-1</sup> of 13 TeV pp collisions collected with the ATLAS detector, rep., CERN, Geneva, 2023. All figures including auxiliary figures are available at https://atlas.web.cern.ch/Atlas/GROUPS/PHYSICS/CONFNOTES/ATLAS-CONF-2023-035.

- [185] CMS collaboration, A. Tumasyan et al., Searches for additional Higgs bosons and for vector leptoquarks in ττ final states in proton-proton collisions at √s = 13 TeV, JHEP 07 (2023) 073, [2208.02717].
- [186] ALEPH, DELPHI, L3, OPAL, LEP WORKING GROUP FOR HIGGS BOSON SEARCHES collaboration, S. Schael et al., Search for neutral MSSM Higgs bosons at LEP, Eur. Phys. J. C 47 (2006) 547–587, [hep-ex/0602042].
- [187] A. Belyaev, R. Benbrik, M. Boukidi, M. Chakraborti, S. Moretti and S. Semlali, Explanation of the hints for a 95 GeV Higgs boson within a 2-Higgs doublet model, Journal of High Energy Physics 2024 (2024) 1–21.
- [188] J. Cao, X. Guo, Y. He, P. Wu and Y. Zhang, Diphoton signal of the light Higgs boson in natural NMSSM, Phys. Rev. D 95 (Jun, 2017) 116001.
- [189] S. Heinemeyer, C. Li, F. Lika, G. Moortgat-Pick and S. Paasch, Phenomenology of a 96 GeV Higgs boson in the 2HDM with an additional singlet, Physical Review D 106 (2022) 075003.
- [190] T. Biekötter, M. Chakraborti and S. Heinemeyer, A 96 GeV Higgs boson in the N2HDM, The European Physical Journal C 80 (Jan., 2020).
- [191] T. Biekötter and M. O. Olea-Romacho, Reconciling Higgs physics and pseudo-Nambu-Goldstone dark matter in the S2HDM using a genetic algorithm, Journal of High Energy Physics 2021 (Oct., 2021).
- [192] T. Biekötter, A. Grohsjean, S. Heinemeyer, C. Schwanenberger andG. Weiglein, Possible indications for new Higgs bosons in the reach of the

LHC: N2HDM and NMSSM interpretations, The European Physical Journal C 82 (Feb., 2022) .

- [193] T. Biekötter, S. Heinemeyer and G. Weiglein, Mounting evidence for a 95 GeV Higgs boson, Journal of High Energy Physics 2022 (Aug., 2022).
- [194] T. Biekötter, S. Heinemeyer and G. Weiglein, Excesses in the low-mass Higgs-boson search and the W-boson mass measurement, The European Physical Journal C 83 (May, 2023).
- [195] T. Biekötter, S. Heinemeyer and G. Weiglein, The CMS di-photon excess at 95 GeV in view of the LHC Run 2 results, Physics Letters B 846 (Nov., 2023) 138217.
- [196] T. Biekötter, S. Heinemeyer and G. Weiglein, 95.4 GeV diphoton excess at ATLAS and CMS, Physical Review D 109 (Feb., 2024).
- [197] J. Cao, X. Jia, Y. Yue, H. Zhou and P. Zhu, 96 GeV diphoton excess in seesaw extensions of the natural NMSSM, Phys. Rev. D 101 (Mar, 2020) 055008.
- [198] S. Iguro, T. Kitahara and Y. Omura, Scrutinizing the 95100 GeV di-tau excess in the top associated process, The European Physical Journal C 82 (Nov., 2022).
- [199] W. Li, H. Qiao and J. Zhu, Light Higgs boson in the NMSSM confronted with the CMS di-photon and di-tau excesses\*, Chinese Physics C 47 (dec, 2023) 123102.
- [200] J. M. Cline and T. Toma, Pseudo-Goldstone dark matter confronts cosmic ray and collider anomalies, Physical Review D 100 (Aug., 2019).
- [201] A. Crivellin, J. Heeck and D. Müller, Large  $h \to bs$  in generic two-Higgs-doublet models, Physical Review D 97 (Feb., 2018) .

[202] G. Cacciapaglia, A. Deandrea, S. Gascon-Shotkin, S. Le Corre, M. Lethuillier and J. Tao, Search for a lighter Higgs boson in Two Higgs Doublet Models, Journal of High Energy Physics 2016 (Dec., 2016).

- [203] A. A. Abdelalim, B. Das, S. Khalil and S. Moretti, Di-photon decay of a light Higgs state in the BLSSM, Nuclear Physics B 985 (2022) 116013.
- [204] D. Azevedo, T. Biekötter and P. M. Ferreira, 2HDM interpretations of the CMS diphoton excess at 95 GeV, JHEP 11 (2023) 017, [2305.19716].
- [205] R. Benbrik, M. Boukidi and S. Moretti, Superposition of CP-even and CP-odd Higgs resonances: Explaining the 95 GeV excesses within a two-Higgs-doublet model, Phys. Rev. D 110 (Dec, 2024) 115030.
- [206] A. Arhrib, K. H. Phan, V. Q. Tran and T.-C. Yuan, When the Standard Model Higgs meets its lighter 95 GeV twin, Nuclear Physics B 1015 (2025) 116909.
- [207] J. A. Aguilar-Saavedra, H. B. Câmara, F. R. Joaquim and J. F. Seabra, Confronting the 95 GeV excesses within the U(1) extended next-to-minimal 2HDM, Phys. Rev. D 108 (Oct, 2023) 075020.
- [208] S. Semlali, A. Belyaev, R. Benbrik, M. Boukidi, M. Chakraborti and S. Moretti, Probing 95 GeV Higgs in the 2HDM Type-III, in Proceedings of The Eleventh Annual Conference on Large Hadron Collider Physics PoS(LHCP2023), LHCP2023, p. 299, Sissa Medialab, Jan., 2024, DOI.
- [209] J. M. Cline, K. Kainulainen and A. P. Vischer, Dynamics of two Higgs doublet CP violation and baryogenesis at the electroweak phase transition, Phys. Rev. D 54 (1996) 2451–2472, [hep-ph/9506284].
- [210] I. P. Ivanov, Thermal evolution of the ground state of the most general 2HDM, Acta Phys. Polon. B 40 (2009) 2789–2807, [0812.4984].

[211] I. F. Ginzburg, I. P. Ivanov and K. A. Kanishev, The Evolution of vacuum states and phase transitions in 2HDM during cooling of Universe, Phys. Rev. D 81 (2010) 085031, [0911.2383].

- [212] P. Basler, M. Krause, M. Muhlleitner, J. Wittbrodt and A. Wlotzka, Strong First Order Electroweak Phase Transition in the CP-Conserving 2HDM Revisited, JHEP 02 (2017) 121, [1612.04086].
- [213] G. C. Dorsch, S. J. Huber, T. Konstandin and J. M. No, A Second Higgs Doublet in the Early Universe: Baryogenesis and Gravitational Waves, JCAP 05 (2017) 052, [1611.05874].
- [214] W. Grimus, L. Lavoura, O. M. Ogreid and P. Osland, A Precision constraint on multi-Higgs-doublet models, J. Phys. G 35 (2008) 075001, [0711.4022].
- [215] H. E. Haber and D. O'Neil, Basis-independent methods for the two-Higgs-doublet model III: The CP-conserving limit, custodial symmetry, and the oblique parameters S, T, U, Phys. Rev. D 83 (2011) 055017, [1011.6188].
- [216] G. Funk, D. O'Neil and R. M. Winters, What the Oblique Parameters S, T, and U and Their Extensions Reveal About the 2HDM: A Numerical Analysis, Int. J. Mod. Phys. A 27 (2012) 1250021, [1110.3812].
- [217] H. E. Haber and H. E. Logan, Radiative corrections to the Z b anti-b vertex and constraints on extended Higgs sectors, Phys. Rev. D 62 (2000) 015011, [hep-ph/9909335].
- [218] M. Jung, A. Pich and P. Tuzon, Charged-Higgs phenomenology in the Aligned two-Higgs-doublet model, JHEP 11 (2010) 003, [1006.0470].
- [219] J. O. Andersen, T. Gorda, A. Helset, L. Niemi, T. V. I. Tenkanen,A. Tranberg et al., Nonperturbative Analysis of the Electroweak Phase

- Transition in the Two Higgs Doublet Model, Phys. Rev. Lett. **121** (2018) 191802, [1711.09849].
- [220] A. Helset, Dimensional reduction of the Two-Higgs Doublet Model with a softly broken Z2 symmetry at one-loop, Master's thesis, Norwegian U. Sci. Tech., 6, 2017.
- [221] T. Gorda, A. Helset, L. Niemi, T. V. I. Tenkanen and D. J. Weir, Three-dimensional effective theories for the two Higgs doublet model at high temperature, JHEP 02 (2019) 081, [1802.05056].
- [222] M. Losada, High temperature dimensional reduction of the MSSM and other multiscalar models, Phys. Rev. D 56 (1997) 2893–2913, [hep-ph/9605266].
- [223] J. O. Andersen, Dimensional reduction of the two Higgs doublet model at high temperature, Eur. Phys. J. C 11 (1999) 563–570, [hep-ph/9804280].
- [224] M. Laine and K. Rummukainen, Two Higgs doublet dynamics at the electroweak phase transition: A Nonperturbative study, Nucl. Phys. B 597 (2001) 23–69, [hep-lat/0009025].
- [225] M. Laine, M. Meyer and G. Nardini, Thermal phase transition with full 2-loop effective potential, Nuclear Physics B 920 (July, 2017) 565600.
- [226] I. K. Banerjee, U. K. Dey and S. Khalil, Primordial Black Holes and Gravitational Waves in the  $U(1)_{B-L}$  extended inert doublet model: a first-order phase transition perspective, JHEP 12 (2024) 009, [2406.12518].
- [227] S. Jiang, F. P. Huang and X. Wang, Bubble wall velocity during electroweak phase transition in the inert doublet model, Phys. Rev. D 107 (2023) 095005, [2211.13142].
- [228] K. Kajantie, M. Laine, K. Rummukainen and M. E. Shaposhnikov, A Nonperturbative analysis of the finite T phase transition in SU(2) x U(1) electroweak theory, Nucl. Phys. B 493 (1997) 413–438, [hep-lat/9612006].

[229] M. Gurtler, E.-M. Ilgenfritz and A. Schiller, Where the electroweak phase transition ends, Phys. Rev. D 56 (1997) 3888–3895, [hep-lat/9704013].

- [230] L. Niemi, M. J. Ramsey-Musolf, T. V. I. Tenkanen and D. J. Weir, Thermodynamics of a Two-Step Electroweak Phase Transition, Phys. Rev. Lett. 126 (2021) 171802, [2005.11332].
- [231] G. M. Harry, P. Fritschel, D. A. Shaddock, W. Folkner and E. S. Phinney, Laser interferometry for the big bang observer, Class. Quant. Grav. 23 (2006) 4887–4894.
- [232] S. Kawamura et al., The Japanese space gravitational wave antenna: DECIGO, Class. Quant. Grav. 28 (2011) 094011.
- [233] W.-H. Ruan, Z.-K. Guo, R.-G. Cai and Y.-Z. Zhang, Taiji program: Gravitational-wave sources, Int. J. Mod. Phys. A 35 (2020) 2050075, [1807.09495].
- [234] M. J. Ramsey-Musolf, V. Q. Tran and T.-C. Yuan, Gravitational waves and dark matter in the gauged two-Higgs doublet model, JHEP 01 (2025) 129, [2408.05167].
- [235] S. Lee, D. Kim, J.-H. Cho, J. Kim and J. Song, Multi-step Strong First-Order Electroweak Phase Transitions in the Inverted Type-I 2HDM: Parameter Space, Gravitational Waves, and Collider Phenomenology, 6, 2025, [2506.03260].
- [236] D. Gonçalves, A. Kaladharan and Y. Wu, Gravitational waves, bubble profile, and baryon asymmetry in the complex 2HDM, Phys. Rev. D 108 (2023) 075010, [2307.03224].
- [237] R. Zhou and L. Bian, Gravitational wave and electroweak baryogenesis with two Higgs doublet models, Phys. Lett. B 829 (2022) 137105, [2001.01237].

[238] T. Biekötter, S. Heinemeyer, J. M. No, M. O. Olea-Romacho and G. Weiglein, The trap in the early Universe: impact on the interplay between gravitational waves and LHC physics in the 2HDM, JCAP 03 (2023) 031, [2208.14466].

- [239] A. de Jesus, S. Kovalenko, T. de Melo, J. Neto, Y. Oviedo-Torres, F. Queiroz et al., On the role of LHC and HL-LHC in constraining flavor changing neutral currents, Physics Letters B 849 (2024) 138419.
- [240] Z. Xiao, C. S. Li and K.-T. Chao, Charm multiplicity and the branching ratios of inclusive charmlessbquark decays in the general two-Higgs-doublet models, Physical Review D 62 (Oct., 2000).
- [241] M. Misiak and M. Steinhauser, Weak radiative decays of the B meson and bounds on  $M_{H^\pm}$  in the Two-Higgs-Doublet Model, Eur. Phys. J. C 77 (2017) 201, [1702.04571].
- [242] P. J. Fox and N. Weiner, Light Signals from a Lighter Higgs, JHEP 08 (2018) 025, [1710.07649].
- [243] G. Branco, P. Ferreira, L. Lavoura, M. Rebelo, M. Sher and J. P. Silva, Theory and phenomenology of two-Higgs-doublet models, Physics Reports 516 (July, 2012) 1102.
- [244] A. Bernal, J. A. Casas and J. M. Moreno, Fine-tuning in the 2HDM, Eur. Phys. J. C 82 (2022) 950, [2202.09103].
- [245] S. L. Glashow and S. Weinberg, Natural Conservation Laws for Neutral Currents, Phys. Rev. D 15 (1977) 1958.
- [246] E. A. Paschos, Diagonal Neutral Currents, Phys. Rev. D 15 (1977) 1966.
- [247] J. Bernon, J. F. Gunion, H. E. Haber, Y. Jiang and S. Kraml, Scrutinizing the alignment limit in two-Higgs-doublet models: m<sub>h</sub>=125 GeV, Phys. Rev. D 92 (2015) 075004, [1507.00933].

[248] O. Gould and T. V. I. Tenkanen, On the perturbative expansion at high temperature and implications for cosmological phase transitions, JHEP 06 (2021) 069, [2104.04399].

- [249] M. Lewicki, M. Merchand, L. Sagunski, P. Schicho and D. Schmitt, Impact of theoretical uncertainties on model parameter reconstruction from GW signals sourced by cosmological phase transitions, Phys. Rev. D 110 (2024) 023538, [2403.03769].
- [250] J. Hirvonen, Intuitive method for constructing effective field theories, 5, 2022, [2205.02687].
- [251] O. Gould and J. Hirvonen, Effective field theory approach to thermal bubble nucleation, Phys. Rev. D 104 (2021) 096015, [2108.04377].
- [252] O. Gould and T. V. I. Tenkanen, Perturbative effective field theory expansions for cosmological phase transitions, JHEP **01** (2024) 048, [2309.01672].
- [253] A. Ekstedt, P. Schicho and T. V. Tenkanen, DRalgo: A package for effective field theory approach for thermal phase transitions, Computer Physics Communications 288 (July, 2023) 108725.
- [254] B. Ruijl, T. Ueda and J. Vermaseren, FORM version 4.2, 7, 2017, [1707.06453].
- [255] P. Nogueira, Automatic Feynman Graph Generation, J. Comput. Phys. 105 (1993) 279–289.
- [256] A. Ekstedt, O. Gould and J. Löfgren, Radiative first-order phase transitions to next-to-next-to-leading order, Phys. Rev. D 106 (2022) 036012, [2205.07241].
- [257] A. Ekstedt, P. Schicho and T. V. I. Tenkanen, Cosmological phase transitions at three loops: The final verdict on perturbation theory, Phys. Rev. D 110 (2024) 096006, [2405.18349].

[258] P. Schicho, T. V. I. Tenkanen and G. White, Combining thermal resummation and gauge invariance for electroweak phase transition, JHEP 11 (2022) 047, [2203.04284].

- [259] S. R. Coleman and E. J. Weinberg, Radiative Corrections as the Origin of Spontaneous Symmetry Breaking, Phys. Rev. D 7 (1973) 1888–1910.
- [260] L. Niemi, P. Schicho and T. V. I. Tenkanen, Singlet-assisted electroweak phase transition at two loops, Phys. Rev. D 103 (2021) 115035, [2103.07467].
- [261] P. Athron, C. Balázs, A. Fowlie and Y. Zhang, PhaseTracer: tracing cosmological phases and calculating transition properties, The European Physical Journal C 80 (June, 2020).
- [262] P. Athron, C. Balazs, A. Fowlie, L. Morris, W. Searle, Y. Xiao et al., PhaseTracer2: from the effective potential to gravitational waves, 2025, [2412.04881].
- [263] S. Coleman, Fate of the false vacuum: Semiclassical theory, Phys. Rev. D 15 (May, 1977) 2929–2936.
- [264] A. Andreassen, D. Farhi, W. Frost and M. D. Schwartz, Precision decay rate calculations in quantum field theory, Phys. Rev. D 95 (2017) 085011, [1604.06090].
- [265] C. L. Wainwright, CosmoTransitions: Computing cosmological phase transition temperatures and bubble profiles with multiple fields, Computer Physics Communications 183 (Sept., 2012) 20062013.
- [266] A. H. Guth and S. H. H. Tye, Phase Transitions and Magnetic Monopole Production in the Very Early Universe, Phys. Rev. Lett. 44 (1980) 631.
- [267] A. H. Guth and E. J. Weinberg, Cosmological Consequences of a First Order Phase Transition in the SU(5) Grand Unified Model, Phys. Rev. D 23 (1981) 876.

[268] M. E. Carrington and J. I. Kapusta, Dynamics of the electroweak phase transition, Phys. Rev. D 47 (Jun, 1993) 5304–5315.

- [269] A. Ekstedt, Higher-order corrections to the bubble-nucleation rate at finite temperature, Eur. Phys. J. C 82 (2022) 173, [2104.11804].
- [270] A. Ekstedt, O. Gould and J. Hirvonen, BubbleDet: a Python package to compute functional determinants for bubble nucleation, JHEP 12 (2023) 056, [2308.15652].
- [271] K. Enqvist, J. Ignatius, K. Kajantie and K. Rummukainen, Nucleation and bubble growth in a first order cosmological electroweak phase transition, Phys. Rev. D 45 (1992) 3415–3428.
- [272] E. Witten, Cosmic separation of phases, Phys. Rev. D 30 (Jul, 1984) 272–285.
- [273] C. J. Hogan, Gravitational radiation from cosmological phase transitions, Mon. Not. Roy. Astron. Soc. 218 (1986) 629–636.
- [274] D. Cutting, E. G. Escartin, M. Hindmarsh and D. J. Weir, Gravitational waves from vacuum first-order phase transitions. II. From thin to thick walls, Physical Review D 103 (Jan., 2021).
- [275] F. Giese, T. Konstandin and J. van de Vis, Model-independent energy budget of cosmological first-order phase transitions—A sound argument to go beyond the bag model, JCAP 07 (2020) 057, [2004.06995].
- [276] T. V. I. Tenkanen and J. van de Vis, Speed of sound in cosmological phase transitions and effect on gravitational waves, JHEP 08 (2022) 302, [2206.01130].
- [277] J. R. Espinosa, T. Konstandin, J. M. No and G. Servant, Energy Budget of Cosmological First-order Phase Transitions, JCAP 06 (2010) 028, [1004.4187].

[278] M. J. Ramsey-Musolf, T. V. I. Tenkanen and V. Q. Tran, Refining Gravitational Wave and Collider Physics Dialogue via Singlet Scalar Extension, 2024, [2409.17554].

- [279] A. Kosowsky, M. S. Turner and R. Watkins, Gravitational radiation from colliding vacuum bubbles, Phys. Rev. D 45 (1992) 4514–4535.
- [280] A. Roper Pol, S. Mandal, A. Brandenburg, T. Kahniashvili and A. Kosowsky, Numerical simulations of gravitational waves from early-universe turbulence, Phys. Rev. D 102 (2020) 083512, [1903.08585].
- [281] X. Wang, C. Tian and C. Balázs, Self-consistent prediction of gravitational waves from cosmological phase transitions, 2024, [2409.06599].
- [282] C. Tian, X. Wang and C. Balázs, Gravitational waves from cosmological first-order phase transitions with precise hydrodynamics, 2024, [2409.14505].
- [283] W.-Y. Ai, B. Laurent and J. van de Vis, Model-independent bubble wall velocities in local thermal equilibrium, Journal of Cosmology and Astroparticle Physics 2023 (July, 2023) 002.
- [284] B. Laurent and J. M. Cline, First principles determination of bubble wall velocity, Phys. Rev. D 106 (2022) 023501, [2204.13120].
- [285] A. Ekstedt, O. Gould, J. Hirvonen, B. Laurent, L. Niemi, P. Schicho et al., How fast does the WallGo? A package for computing wall velocities in first-order phase transitions, JHEP 04 (2025) 101, [2411.04970].
- [286] P. J. Steinhardt, Relativistic detonation waves and bubble growth in false vacuum decay, Phys. Rev. D 25 (Apr, 1982) 2074–2085.
- [287] M. Laine, Bubble growth as a detonation, Phys. Rev. D 49 (Apr, 1994) 3847–3853.

[288] W.-Y. Ai, B. Garbrecht and C. Tamarit, Bubble wall velocities in local equilibrium, Journal of Cosmology and Astroparticle Physics 2022 (Mar, 2022) 015.

- [289] W.-Y. Ai, B. Laurent and J. van de Vis, Bounds on the bubble wall velocity, JHEP 02 (2025) 119, [2411.13641].
- [290] T. Krajewski, M. Lewicki and M. Zych, Bubble-wall velocity in local thermal equilibrium: hydrodynamical simulations vs analytical treatment, Journal of High Energy Physics 2024 (May, 2024).
- [291] M. Hindmarsh, S. J. Huber, K. Rummukainen and D. J. Weir, Gravitational Waves from the Sound of a First Order Phase Transition, Phys. Rev. Lett. 112 (Jan, 2014) 041301.
- [292] M. Hindmarsh, S. J. Huber, K. Rummukainen and D. J. Weir, Numerical simulations of acoustically generated gravitational waves at a first order phase transition, Phys. Rev. D 92 (Dec, 2015) 123009.
- [293] J. Ellis, M. Lewicki, J. M. No and V. Vaskonen, Gravitational wave energy budget in strongly supercooled phase transitions, JCAP 06 (2019) 024, [1903.09642].
- [294] M. Hindmarsh, S. J. Huber, K. Rummukainen and D. J. Weir, Shape of the acoustic gravitational wave power spectrum from a first order phase transition, Phys. Rev. D 96 (Nov, 2017) 103520.
- [295] A. Kosowsky, M. S. Turner and R. Watkins, Gravitational radiation from colliding vacuum bubbles, Phys. Rev. D 45 (Jun, 1992) 4514–4535.
- [296] A. Kosowsky, M. S. Turner and R. Watkins, Gravitational waves from first-order cosmological phase transitions, Phys. Rev. Lett. 69 (Oct, 1992) 2026–2029.

[297] A. Kosowsky and M. S. Turner, Gravitational radiation from colliding vacuum bubbles: Envelope approximation to many-bubble collisions, Phys. Rev. D 47 (May, 1993) 4372–4391.

- [298] M. Kamionkowski, A. Kosowsky and M. S. Turner, Gravitational radiation from first-order phase transitions, Phys. Rev. D 49 (Mar, 1994) 2837–2851.
- [299] S. J. Huber and T. Konstandin, Gravitational wave production by collisions: more bubbles, Journal of Cosmology and Astroparticle Physics 2008 (sep, 2008) 022.
- [300] R. Jinno and M. Takimoto, Gravitational waves from bubble collisions: An analytic derivation, Phys. Rev. D 95 (Jan, 2017) 024009.
- [301] T. L. Smith and R. R. Caldwell, LISA for cosmologists: Calculating the signal-to-noise ratio for stochastic and deterministic sources, Physical Review D 100 (Nov., 2019).
- [302] T. J. Sumner, G. Mueller, J. W. Conklin, P. J. Wass and D. Hollington, Charge induced acceleration noise in the LISA gravitational reference sensor, Classical and Quantum Gravity 37 (Jan., 2020) 045010.
- [303] D. H. Lyth and A. Riotto, Particle physics models of inflation and the cosmological density perturbation, Phys. Rept. 314 (1999) 1–146, [hep-ph/9807278].
- [304] L. Sagunski, P. Schicho and D. Schmitt, Supercool exit: Gravitational waves from QCD-triggered conformal symmetry breaking, Phys. Rev. D 107 (2023) 123512, [2303.02450].
- [305] M. Kierkla, A. Karam and B. Swiezewska, Conformal model for gravitational waves and dark matter: a status update, JHEP 03 (2023) 007, [2210.07075].
- [306] M. Kierkla, B. Swiezewska, T. V. I. Tenkanen and J. van de Vis, Gravitational waves from supercooled phase transitions: dimensional

transmutation meets dimensional reduction, JHEP **02** (2024) 234, [2312.12413].

- [307] M. Kierkla, P. Schicho, B. Swiezewska, T. V. I. Tenkanen and J. van de Vis, Finite-temperature bubble nucleation with shifting scale hierarchies, 3, 2025, [2503.13597].
- [308] O. Gould and C. Xie, Higher orders for cosmological phase transitions: a global study in a Yukawa model, JHEP 12 (2023) 049, [2310.02308].
- [309] M. Chala, J. C. Criado, L. Gil and J. L. Miras, Higher-order-operator corrections to phase-transition parameters in dimensional reduction, JHEP 10 (2024) 025, [2406.02667].
- [310] M. Chala and G. Guedes, The High-Temperature Limit of the SM(EFT), 3, 2025, [2503.20016].
- [311] F. Bernardo, P. Klose, P. Schicho and T. V. I. Tenkanen, Higher-dimensional operators at finite-temperature affect gravitational-wave predictions, 3, 2025, [2503.18904].
- [312] L. S. Friedrich, M. J. Ramsey-Musolf, T. V. I. Tenkanen and V. Q. Tran, Addressing the Gravitational Wave - Collider Inverse Problem, 3, 2022, [2203.05889].
- [313] V. Shtabovenko, R. Mertig and F. Orellana, New Developments in FeynCalc 9.0, Comput. Phys. Commun. 207 (2016) 432–444, [1601.01167].
- [314] J. C. R. ao, Integration of three body phase space: The 3BodyXSections and 3BodyDecays packages, 2023.
- [315] P. Gondolo and G. Gelmini, Cosmic abundances of stable particles: Improved analysis, Nucl. Phys. B 360 (1991) 145–179.
- [316] J. Edsjö and P. Gondolo, Neutralino relic density including coannihilations, Physical Review D 56 (Aug., 1997) 18791894.

[317] A. Cheek, L. Heurtier, Y. F. Perez-Gonzalez and J. Turner, Primordial black hole evaporation and dark matter production. II. Interplay with the freeze-in or freeze-out mechanism, Physical Review D 105 (Jan., 2022).

- [318] P. M. Stevenson, Optimized Perturbation Theory, Phys. Rev. D 23 (1981) 2916.
- [319] S.-z. Huang and M. Lissia, The Relevant scale parameter in the high temperature phase of QCD, Nucl. Phys. B 438 (1995) 54–66, [hep-ph/9411293].
- [320] M. Laine and Y. Schroder, Two-loop QCD gauge coupling at high temperatures, JHEP 03 (2005) 067, [hep-ph/0503061].
- [321] I. Ghisoiu, J. Moller and Y. Schroder, Debye screening mass of hot Yang-Mills theory to three-loop order, JHEP 11 (2015) 121, [1509.08727].
- [322] S. Kanemura, M. Kikuchi and K. Yagyu, Fingerprinting the extended Higgs sector using one-loop corrected Higgs boson couplings and future precision measurements, Nucl. Phys. B 896 (2015) 80–137, [1502.07716].